Study of magnetic relaxation dynamics in soft matter nanoparticle composite systems

Von der Fakultät für Physik der Universität Duisburg-Essen
zur Erlangung des akademischen Grades eines Doktors
der Naturwissenschaften (Dr. rer. nat.)
genehmigte Dissertation

von

Joachim Landers

aus

Mülheim an der Ruhr

Datum der Disputation: **07. November 2016**

1. Gutachter:	**Prof. Dr. Heiko Wende**
2. Gutachter:	**PD Dr. Frank Ludwig**
3. Gutachter:	**Prof. Dr. Annette Schmidt**

Abstract

This thesis focuses on magnetic relaxation phenomena of iron oxide nanoparticles incorporated in different viscous and viscoelastic composite materials and their response to external stimuli. The combination of magnetic nanoparticles and deformable matrix materials offers a wide range of possible applications, each requiring a specific response of the composite system to its environment, which is primarily determined by the magnetization dynamics of the embedded particles. Therefore, the main point of interest is the influence of the nanostructure of the surrounding medium and of particle-matrix interaction on nanoparticle magnetization dynamics in the soft matter system. To obtain comparable results on different length and time scales, AC-susceptometry (ACS) was applied supplementarily to Mössbauer spectroscopy (MS) experiments. Additional information on the magnetic particle structure and relaxation phenomena was obtained by X-ray diffraction (XRD), Ferromagnetic Resonance (FMR) experiments and SQUID-magnetometry.

To clarify the influence of interparticle interaction on Néel relaxation, which is the primary relaxation mechanism in small nanoparticles, 6 nm iron oxide nanoparticles with different capping thicknesses have been studied regarding their relaxation behavior. It could be demonstrated that the capping had minor influence on the static magnetic structure of the particles', while dramatically modifying the rate of Néel relaxation. Comparing capped magnetite nanoparticles of 6 - 26 nm in glycerol solution the transition from superparamagnetism originating from Néel relaxation to (pseudo-)superparamagnetism caused by Brownian motion could be observed, providing the ability to study both processes upon varying temperature and external magnetic field. By this approach, parameter sets of both relaxation mechanisms have been determined for the first time simultaneously from Mössbauer experiments.

In a detailed investigation on hematite nanospindles in ferrohydrogels, information on the particle containment, i.e., the reduction in particle mobility depending on the hydrogel crosslinkage, was obtained by direct comparison of Mössbauer spectroscopy and AC-susceptometry, the latter showing no sign of relaxation. This apparent contradiction could be clarified in terms of constrained diffusive motion in spatially limited polymer meshes observed on different time scales, considering the type of relaxation and the timescale both techniques are sensitive to. A similar method was utilized to quantify the Brownian motion of oleic-acid coated magnetite particle clusters incorporated in two types of polymer compounds for remote melting applications. By examining their magnetic structure and diffusion dynamics as a starting point, effects of Néel relaxation and Brownian motion visible in a detailed AC-susceptometry study could be identified and interpreted, whereby the particle cluster size in the molten polymer could be extracted.

Kurzzusammenfassung

Die vorliegende Arbeit behandelt magnetische Relaxationsphänomene von Eisenoxid-Nanopartikeln, eingebracht in verschiedene viskose und viskoelastische Kompositmaterialien, und deren Reaktion auf externe Stimuli. Die Kombination magnetischer Nanopartikel und verformbaren Matrixmaterials eröffnet eine Vielzahl möglicher Anwendungen, von denen jede eigene Anforderungen an die Reaktion des Komposits auf seine Umgebung hat, welche durch die Magnetisierungsdynamik der eingebetteten Nanopartikel bestimmt wird. Daher liegt das Hauptaugenmerk auf dem Einfluss der Nanostruktur des umgebenden Mediums und der Partikel-Matrix Wechselwirkung auf das dynamische Magnetisierungsverhalten der Partikel im Soft-Matter Komposit. Um einen Vergleich dieser Größen auf verschiedenen Längen- und Zeitskalen zu ermöglichen, wurde AC-Suszeptometrie (ACS) ergänzend zur Mössbauerspektroskopie (MS) durchgeführt. Weitere Informationen über magnetische Struktur und Relaxationseigenschaften der Partikel ergaben sich aus Röntgenbeugungsexperimenten (XRD), Ferromagnetischer Resonanz (FMR) und SQUID-Magnetometrie.

Um den Einfluss interpartikulärer Wechselwirkung auf Néelsche Relaxation als primären Relaxationsmechanismus kleiner Nanopartikel zu untersuchen, wurde das Relaxationsverhalten verschieden dick beschichteter 6 nm Eisenoxidpartikel verglichen. Neben einem geringen Effekt der Beschichtung auf die statische magnetische Struktur der Partikel konnte eine deutliche Änderung der Néelschen Relaxationsrate nachgewiesen werden. Im Vergleich beschichteter Magnetitpartikel von 6 - 26 nm in Glycerollösung konnte der Übergang von Néelschem Superparamagnetismus zum (Pseudo-)Superparamagnetismus hervorgerufen durch Brownsche Bewegung beobachtet werden, was es ermöglichte beide Prozesse bei verschiedenen Temperaturen und externen Magnetfeldern zu studieren. Auf diese Weise konnten zum ersten Mal Parameter beider Relaxationsmechanismen gleichzeitig mittels Mössbauerspektroskopie ermittelt werden. Im direkten Vergleich von Mössbauerspektroskopie- und AC-Suszeptometriemessungen wurde in eingehenden Untersuchungen von Hämatitnanospindeln in Ferrohydrogelen die Einschränkung der Partikelmobilität abhängig von der Vernetzungsdichte des Hydrogels untersucht, wobei in den letztgenannten ACS-Experimenten keine Anzeichen magnetischer Relaxation erkennbar waren. Dieser scheinbare Widerspruch konnte unter Berücksichtigung eingeschränkter Partikelbewegung in räumlich begrenzten Polymermaschen und den beiden Techniken zugänglichen Zeitskalen und Relaxationsarten erklärt werden. Ein ähnlicher Ansatz wurde genutzt, um die Brownsche Bewegung Ölsäure-beschichteter Magnetit-Partikelcluster in verschiedenen Polymerarten quantitativ zu bestimmen. Aufbauend auf der Analyse der magnetischen Struktur und Diffusionsbewegung wurden Beiträge Néelscher und Brownscher Relaxation in detaillierten AC-Suszeptometriemessungen identifiziert und interpretiert, was zudem die Abschätzung der hydrodynamischen Clustergröße ermöglichte.

Contents

1 Introduction

Magnetic nanoparticles exhibit a broad spectrum of exceptional properties, which originate either from their limited size or from their high surface-to-volume ratio. In addition to superparamagnetism by Néel superspin fluctuation, also the decrease of transition temperatures in nanoparticles results from their limited size or volume, respectively [1]. On the other hand, the high specific surface of nanoparticles results in their suitability for catalysis, allows particle surface functionalization by adding ligand molecules and, furthermore, gives rise to canted surface spin structures, essentially influencing the nanoparticles' magnetic anisotropy [2, 3].

Motivated by these phenomena, widespread efforts have been made in recent years to create magnetic nanoparticle compound materials, where the particles can be utilized as a probe for the state of the matrix, which can then be read out by experimental techniques sensitive to the particle magnetism, or are incorporated as an active 'device' transferring external stimuli to the matrix, or vice versa. Especially the latter approach, combining the peculiar magnetic characteristics of the nanoparticles with the macroscopic properties of the surrounding materials, has resulted in a variety of different particle-compound systems, including ferro(hydro)gels, nanoparticle-polymer composites, ferrofluids and magnetorheological fluids for medical applications, engineering, material science and sensor development.

We encounter applications of such systems in daily life, ranging from adjustable shock absorbers in vehicles, based on field-controlled viscosity tuning of magnetorheological fluids, to ferrofluids utilized to improve the cooling and performance of voice coils in loudspeakers [4, 5, 6]. Held in position by small permanent magnets, ferrofluids also are used for the sealing of crank shafts or other moving devices [7]. Two of the most prominent concepts regarding magnetic ferrofluids in medical application are hyperthermia cancer treatment, converting the energy of an external AC magnetic field to localized tissue heating, and field-controlled drug targeting [8, 9, 10].

Embedded in viscoelastic or elastic media instead of fluids, magnetic nanoparticles can be utilized to vary the macroscopic shape or nanostructure of these matrices in external magnetic fields in addition to effects reported in ferrofluids. Such particle composites can serve as fine actuators or sensors, as well as 'motors' driving the overall movement of the device they are incorporated in [11, 12, 13]. Creating a macroscopic deformation of the compounds' shape, they can also be used for filter applications or flow control, e.g., by tuning the diameters of soft matter capillaries [14].

In soft matter nanoparticle compounds in general, meaning here magnetic nanoparticles incorporated in a deformable medium also including fluids, these different approaches, applications and processes are based on two critical mechanisms: The dynamical intrinsic fluctuation of the particle moment and the response of the particles to an external magnetic field, i.e., forced reorientation of magnetic moments. Both effects have been intensively studied by standard

magnetometry and/or AC-susceptibility methods, if possible in transparent media by optical absorption techniques, e.g., dynamic light scattering (DLS), and more sophisticated methods including magnetic particle imaging (MPI) and X-ray absorption techniques [15, 16, 17]. However, relatively few reports on the study of magnetic relaxation phenomena by Mössbauer spectroscopy can be found that focus on soft matter particle compounds. This is surprising, as Mössbauer spectroscopy is one of the most prominent techniques for the evaluation of the Néel relaxation process leading to superparamagnetism. Only few studies of Brownian particle motion in ferrofluids by Mössbauer spectroscopy are reported in the literature as outlined in section 3.1. Mössbauer spectroscopy is a well-suited technique for many types of magnetic characterization, as it is element-specific, here used to study ^{57}Fe, sensitive to the local magnetic moment of iron atoms, and is also a 'fast' method with a characteristic time window in the nanosecond regime.

Therefore, Mössbauer spectroscopy is utilized in this thesis to analyze magnetic relaxation phenomena in different compound materials, providing valuable information on magnetic anisotropy, magnetic structure and Néel relaxation times of the particles as well as on the dynamic viscosity in fluids and, furthermore, constrained particle movement in nanostructured ferrohydrogels. The latter studies result in a better understanding of the particle-matrix interaction on the nanoscale, especially by using Mössbauer spectroscopy in combination with AC-susceptometry and standard magnetometry protocols, as these techniques display highly different time windows, leading to additional insight on time-dependent phenomena in Néel superparamagnetism as well as in constrained Brownian motion in inhomogeneous nanostructures. On that basis, the following topics are treated in the present thesis:

- In the first chapters of the thesis a basic understanding of magnetic relaxation phenomena and the applied experimental techniques shall be imparted. This includes an illustrative introduction to diffusional Brownian motion and Néel superspin relaxation and nanoparticle magnetism in general, but also to fundamentals of the angular dependent γ-ray absorption process, the shape of the Mössbauer spectrum as well as to 'custom-built' theoretical models for Mössbauer spectroscopy and AC-susceptibility analysis.

- In chapter 4, the influence of interparticle interaction on the Néel relaxation mechanism shall be clarified, which is critical in compounds formed by larger particles with a high magnetic moment and a strong magnetic stray field, or in case of high particle concentrations. To ensure variation of the interaction strength only, capped particles with different capping materials and thicknesses were studied, tuning the average core-to-core particle distance and, therefore, the interaction energy.

- Chapter 5 focuses on ferrofluids of 6 - 26 nm iron oxide nanoparticles incorporated in glycerol solution. By means of Mössbauer spectroscopy and AC-susceptometry the question is tackled, to which extent Brownian motion and Néel relaxation parameters can be extracted from the same set of measurements, and whether sufficient consistency can be found for both phenomena using techniques working on very different timescales and based on different detection mechanisms. Also the region of ultrahigh viscosities close to the glass transition temperature is examined more closely.

- In chapter 6, hematite nanospindles in different matrices are studied in terms of their magnetic structure, constrained movement, orientational behavior and shape effects in comparison to spherically shaped particles. The hematite particles are embedded in crosslinked ferrohydrogels of different crosslinking density, resulting in varying range of motion. To analyze not only the containment effect itself, but also the influence of the type of particle-matrix interaction on particle mobility, the nanospindles were incorporated in a second set of particle-crosslinked ferrohydrogels, where the particle movement is limited not by a surrounding cage of polymer chains, but directly by these chains that are attached to the particle surface, anchoring the particles to each other. Here, the major issue regarding viscoelastic ferrohydrogels is in which way the change in particle-matrix coupling mechanism modifies the particles' mobility and demagnetization behavior and to which extent these are affected by particle containment on different time- and length scales.

- The main focus in chapter 7 is on the effect of magnetically induced heating, used for the preparation of remotely meltable composites. 'Raspberry' structured particle clusters are embedded in two types of polymer compounds of different melting point and viscosity in the liquid state. By the combination of Mössbauer spectroscopy and extensive field- and temperature-dependent mapping of the magnetic AC-susceptibility, relaxation times of Néel fluctuation and Brownian motion are investigated and the distribution of hydrodynamic diameters of particle clusters in the polymer melt is extracted.

- In chapter 8 the essential results and conclusions drawn are summarized, especially referring to the core issues introduced above. In parallel, future prospects and promising experimental approaches are discussed accordingly.

2 Basic theory of nanoparticle magnetism and relaxation dynamics

2.1 Iron oxides

Experiments, as they are described and illustrated in the scope of this thesis, were performed on different types of iron oxide nanoparticles, as these are by far the most frequently produced and utilized magnetic nanoparticles in research as well as in medical and engineering applications. An overview on iron oxide mineralic phases, possible oxidation processes and relevant temperature ranges may be gained from figure 2.1. They stand out due to their biocompatibility and the abundance of precursor materials, but differ widely in their structural and magnetic properties.

The ferrimagnetic iron oxides magnetite and maghemite, for instance, exhibit a high saturation magnetization and low magnetic anisotropy and, accordingly, display orientational behavior strongly dependent on external magnetic fields. Therefore, nanoparticles of these minerals are well suited for compound materials, where the mechanical properties of the compound will be tuned by variation of external magnetic stimuli. Following this approach, (partially oxidized) magnetite nanoparticles are used in chapters 4, 5 and 7. Hematite, on the other hand, exhibits a nearly ideal antiferromagnetic order, as is illustrated in further detail below, resulting in a minimum net magnetic moment. For that reason, hematite nanospindles are utilized in chapter 6 to study the results of a mechanical nanoparticle containment without effects of considerable magnetic dipole interaction on nanoparticle movement or positioning in the hydrogel, inevitable for ferrimagnetic particles of similar size. The most relevant characteristics of the iron oxides studied here, i.e., magnetite (Fe_3O_4), maghemite (γ-Fe_2O_3) and hematite (α-Fe_2O_3), are briefly presented below.

Magnetite & Maghemite

The iron oxide phase magnetite (Fe_3O_4) crystallizes in the (inverse) spinel structure, corresponding to space group $Fd\overline{3}m$. Its unit cell and ferrimagnetic structure are illustrated in figure 2.2 (a). The cubic unit cell with a lattice constant of 0.8396 nm contains 8 formula units with 8 iron ions in a tetrahedral configuration with 4 oxygen next neighbors (A-site) and 16 iron atoms in octahedral configuration with 6 oxygen next neighbors (B-site) [19]. Half of the Fe^{2+} ions are positioned on B-sites, wherefore magnetite is considered as an inverse spinel, characterized by $[Fe^{3+}]_A[Fe^{2+}Fe^{3+}]_BO_4$.

A- and B-sites display antiferromagnetic coupling, leading to net ferrimagnetic behavior, which magnetite conserves up to the Curie temperature T_C of 858 K, while maghemite becomes paramagnetic above $T_C \approx 900$ K. Both Curie temperatures are hard to measure due to the

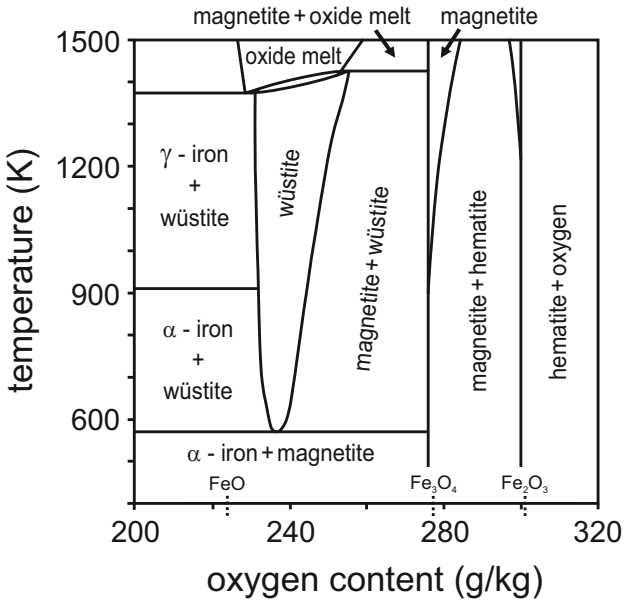

Figure 2.1: Phase diagram of iron oxides. Figure adapted from Ref. [18].

oxidation of magnetite to maghemite above 500 K and the inversion of maghemite to hematite at 500 - 900 K [19]. In magnetite, one can estimate a magnetic moment of $5\mu_B$ per Fe^{3+} ion with an electronic configuration of $[Ar]3d^5$, and $4\mu_B$ for Fe^{2+} with $[Ar]3d^6$-configuration, following Hund's rules. Since the magnetic moments of the antiferromagnetically coupled Fe^{3+} ions on A- and B-site cancel each other, the theoretical net magnetic moment of 4 μ_B results mainly from the Fe^{2+} ions in octahedral configuration, as demonstrated in figure 2.3. Experimentally, a saturation magnetization of about 510 kA/m or 98 emu/g was determined, corresponding to ca. 4.1 μ_B per formula unit, in good agreement with the theoretical calculation [20].

Maghemite (γ-Fe_2O_4) exhibits the magnetite spinel structure with 1/3 vacancy on octahedral B-sites per formula unit to compensate the deficiency in iron compared to (Fe_3O_4). The presence of vacancies leads to a volume contraction and, correspondingly, to a reduced lattice constant of 0.8337 nm [19]. In bulk maghemite and large particles, vacancy ordering can be detected by the emergence of additional superstructure peaks in diffraction patterns [22]. On the contrary, in the majority of small maghemite nanoparticles in the literature no evidence of vacancy ordering is detected, probably due to poor crystalline structure or random occupation of B-sites by iron ions at elevated temperatures during the nanoparticle synthesis.

By comparing sublattice magnetizations of magnetite and maghemite in figure 2.3, it can be easily understood that vacancies on octahedral B-sites lead to a reduction in the magnetization of the dominant B-sublattice, and, therefore, to a reduce in net magnetization of ca. 20 % relative to magnetite, i.e., to 83.5 emu/g or about 3.18 μ_B per formula unit [20].

At ambient conditions, i.e., room temperature and standard pressure, magnetite is no stable iron oxide phase. By oxidation of the first monolayers exposed to air, bodies of magnetite develop a thin passivation layer of maghemite, which again slows down further oxidation. While

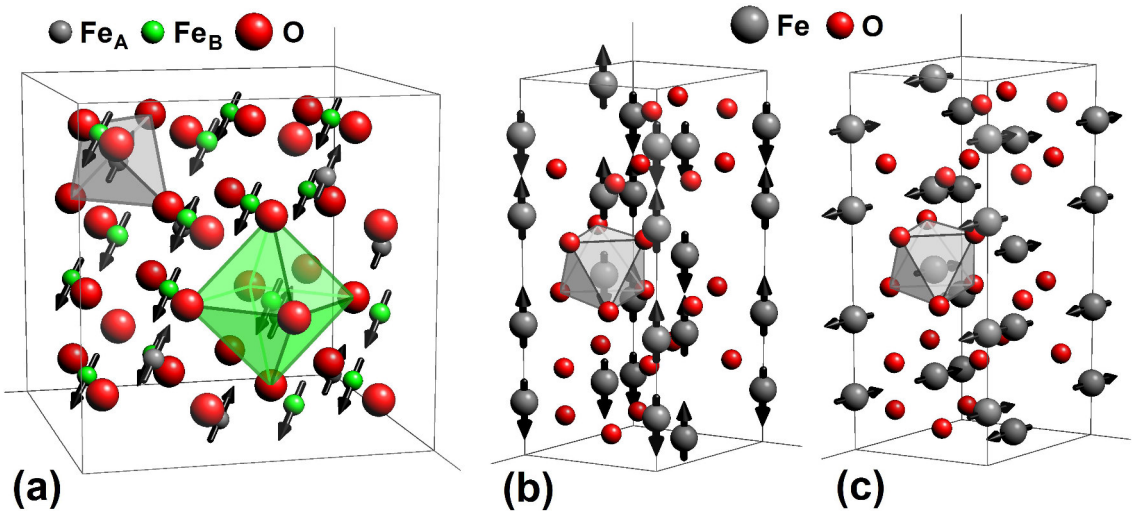

Figure 2.2: Crystalline and magnetic structure of magnetite (a) and hematite below (b) and above the Morin transition (c), adapted from [21]. Octahedral B- and tetrahedral A-sites of iron in magnetite are highlighted exemplarily.

maghemite passivation layers of up to 2 nm form quasi instantaneously, further growth of the layer thickness up to 4 - 5 nm may last several months [23]. Obviously, the speed of the oxidation process is critical in terms of iron oxide nanoparticle synthesis and application, as typical nanoparticle diameters in the range of 5 - 15 nm will correspond to completely different amounts of remaining magnetite. The oxidation rate of nanoparticles can be further decreased by usage of an appropriate coating material, suppressing oxide diffusion to the particle core material [24, 25]. Additionally, particle coating is exploited in ferrofluidic systems to minimize particle agglomeration and interaction. Often-utilized shell materials are, e.g., silica or dextran; the ability of silica shells to conserve the original nanoparticle state has been outlined in Ref. [26].

To distinguish between magnetite and maghemite in a given sample raises a serious problem, as both ferrimagnetic iron oxides have the same crystal structure and similar magnetic properties, including the saturation magnetization M_S. While diffraction techniques are often the most promising approach to identify similar minerals, e.g., by small differences in their lattice parameters, the broadening of diffraction lines in small nanoparticles and the absence of the maghemite superstructure attributed to vacancy ordering make an unambiguous identification for particle diameters D $\leq$ 15 nm quite difficult. Additionally, the difference of about 20 % in saturation magnetization may be obscured by size effects and the reduction in magnetic particle moment by surface canting, as described in the next section dealing with nanoparticle magnetism. All in all, neither diffraction techniques nor measurements of the saturation magnetization represent a promising method to clarify which iron oxide is present in a given sample of small nanoparticles.

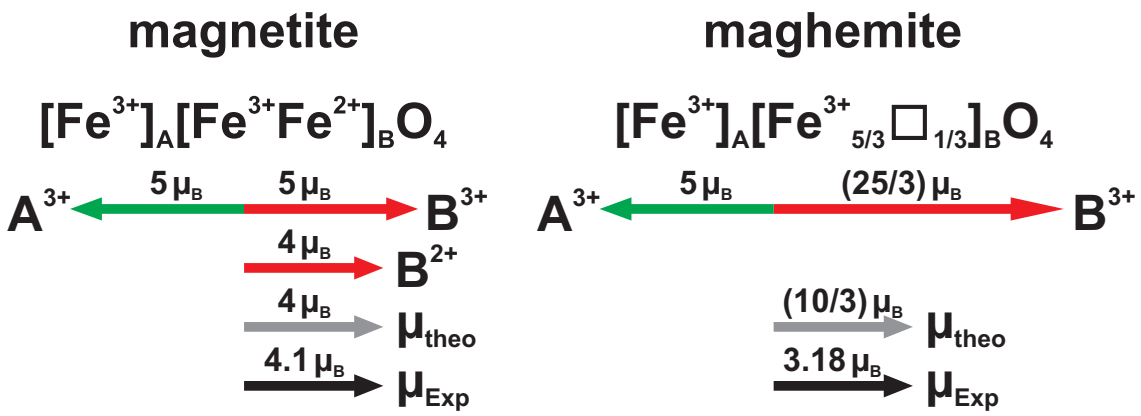

Figure 2.3: Schematic spin arrangement and net magnetic moments per formula unit in the ferrimagnetic iron oxides magnetite and maghemite. Experimental values μ_{Exp} of the magnetic moment are calculated from literature values of the saturation magnetization given in the text.

On the other hand, there are element-specific and even site-specific techniques, i.e., Mössbauer spectroscopy and X-ray absorption techniques, which allow a statement on the presence and quantity of magnetite in an iron oxide volume, based on the Fe^{2+} signal amplitude. However, in some cases an identification by basic magnetometry, requiring much less effort, is possible due to characteristic phase transitions of the different iron oxides:

In 1939, E. Verwey discovered a spontaneous increase in magnetite conductivity by several orders of magnitude upon exceeding a temperature of 123 K, henceforth known as Verwey temperature T_{Verwey} [27]. Further investigations assigned this effect to a dramatic increase in electronic mobility by electron hopping between Fe^{3+}- and Fe^{2+}-sites, or explained it by more sophisticated models including charge-orbital ordering [28, 29]. To measure the electrical conductivity of a single nanoparticle or nanoparticles embedded in a solid matrix is a matter of considerable experimental effort. However, as the Verwey transition is accompanied by a clearly visible feature in the temperature-dependent magnetization, the observation of a discontinuity close to the Verwey temperature of about 123 K, as it can be found in figure 5.2, clearly implies the presence of magnetite in the iron oxide sample at hand.

Hematite

Hematite (α-Fe_2O_3) is the most stable form of iron oxide at ambient conditions. Thereby, it is the final product of several of geochemical reactions leading to its rich occurrence in minerals forming under sufficient oxygen provision, e.g., when exposed to atmosphere. It exhibits the corundum crystal structure, which can be approximated by a hexagonal lattice, as is shown in figure 2.2.

Below the so-called Morin transition temperature T_{Morin}, which can be found in bulk hematite

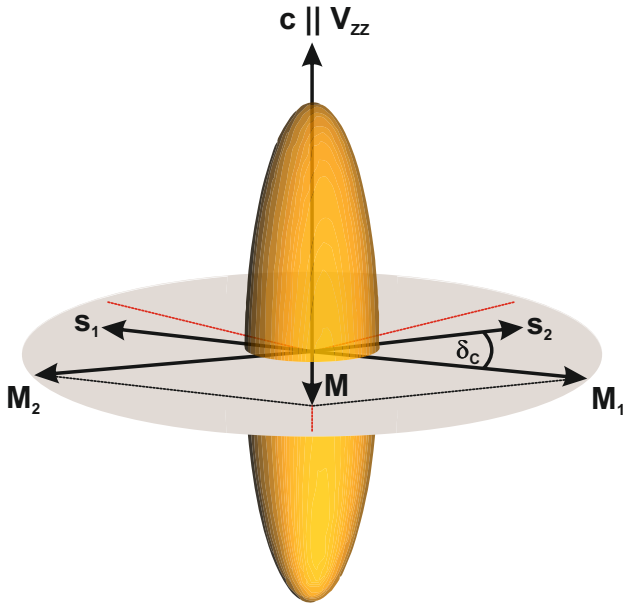

Figure 2.4: Canted antiferromagnetic structure of spins s_1 and s_2, and sublattice magnetizations M_1 and M_2 in hematite above T_{Morin}, and the resulting net magnetization M. The canting angle δ_C is exaggerated in the drawing. Red dashed lines mark the triaxial anisotropy axes in the basal plane, which is perpendicular to the c-axis. In spindle-shaped nanoparticles, as studied in chapter 6, the long particle axis is parallel to the c-axes, i.e., to the main component of the electric field gradient V_{zz}.

at ca. 263 K [30], α-Fe_2O_3 displays ideal collinear antiferromagnetic ordering with spins aligned coaxial to the hexagonal c-axis. At elevated temperatures above T_{Morin}, a spin-flop transition to canted antiferromagnetism due to the Dzialoshinskii-Moriya interaction can be observed, where sublattice magnetizations and the net magnetization resulting from the canting angle δ_C are situated in the hexagonal basal plane. In this 'weakly ferromagnetic' state, the canting angle δ_C has been reported to be ca. 0.13°, corresponding to a net magnetization of about 0.35 - 0.4 emu/g [31]. The basal plane can be considered as an easy magnetic plane due to pronounced uniaxial magnetocrystalline anisotropy, with the hexagonal c-axis as the hard magnetic direction. Within the basal plane, additional minor contributions of a triaxial anisotropy have been reported, with magnetocrystalline anisotropy energy densities in the range of 10 - 100 Jm^{-3} [32]. The configuration of anisotropy axes and canted antiferromagnetic spin arrangement is visualized in figure 2.4.

Early studies of the net magnetization and the canting angle in hematite were carried out by magnetometry experiments and Mössbauer spectroscopy [33]. In field dependent magnetization curves of hematite nanoparticles, sharp hysteresis loops are found in the low-field regime corresponding to the orientation of the spontaneous magnetization of about 0.35 emu/g, while an increase in magnetization is found at higher field amplitudes presumably due to widening of the antiferromagnetic canting angle δ_C [34]. If the measurement takes place at temperatures below T_{Morin} in the ideal collinear antiferromagnetic state, the spin-flop transition can also be driven by the magnetic field, leading to weakly ferromagnetic behavior above a critical magnetic field amplitude [33]. In Mössbauer spectroscopy, the spin-flop transition at T_{Morin} is easily observable, as the reorientation of spins from parallel- to perpendicular alignment relative to

the c-axis, the latter being coaxial to the main axis of the electric field gradient V_{zz}, results in a characteristic shift in absorption line positions, as explained in chapter 6 in detail [35].

2.2 Basics of nanoparticle magnetism

The tendency of a medium with non-zero spontaneous magnetization, i.e., ferro- or ferrimagnets, to display magnetically hard and easy directions can be described in terms of magnetic anisotropy, closely correlated to the coercive field H_C. In 3D-systems, usually the most important contribution to magnetic anisotropy originates from spin-orbit coupling and is denominated as magnetocrystalline anisotropy. Essentially, the magnetic moment can be assigned primarily to the spin angular momentum $\vec{S}$ of the unpaired electrons in the system, while the orbital angular momentum $\vec{L}$ is correlated to the crystal axes, representing positions of high electron probability density. Therefore $\vec{S}$-$\vec{L}$ (spin-orbit) coupling results in a contribution to the systems internal energy depending on the orientation of the magnetization vector relative to the symmetry axes of the crystal lattice. One of the most common types of magnetocrystalline anisotropy is uniaxial anisotropy, often to be found in systems with a single axis of high symmetry, e.g., the approximately hexagonal hematite structure, whose energy is described by equation (2.1). Here, θ is the angle between magnetization vector $\vec{M}$ and the symmetry axis, e.g., the hexagonal hematite c-axis, and K_{u1} and K_{u2} are anisotropy energy densities.

$$E_{uni} = VK_{u1}\sin^2(\theta) + VK_{u2}\sin^4(\theta) + ... \tag{2.1}$$

More generally, anisotropy energies are described in terms of the direction cosines $\alpha_i = \frac{\vec{M}}{M}\vec{e_i}$ of the normalized magnetization vector relative to the symmetry axes of the crystal lattice. For materials of cubic symmetry, e.g., minerals of the spinel group, the angular dependent contribution of anisotropy energy can be estimated from equation (2.2) [19]. For magnetite, magnetic anisotropy constants of $K_1 \approx$ -12 kJm^{-3} and $K_2 \approx$ -3 kJm^{-3} have been found at room temperature, resulting in the cubic [111]-directions being the easy magnetic axes [36, 37]. More complex types of magnetocrystalline anisotropy will be introduced in the corresponding sections of this thesis, if required.

$$E_{cub} = VK_1(\alpha_1^2\alpha_2^2 + \alpha_1^2\alpha_3^2 + \alpha_2^2\alpha_3^2) + VK_2(\alpha_1^2\alpha_2^2\alpha_3^2) + ... \tag{2.2}$$

Another source of magnetic anisotropy originates from the shape of the particles, correspondingly named shape anisotropy E_{Shape}. Elongated particles usually display a preferred magnetic orientation along the long particle axis, due to the combined long-range dipolar interaction of all individual magnetic moments integrated over the whole particle volume. The shape anisotropy energy is given by equation (2.3), introducing the diagonalized demagnetization tensor $\underline{N}$ with $\sum N_i = 1$. The elements of the demagnetization vector depend on the shape of the individual

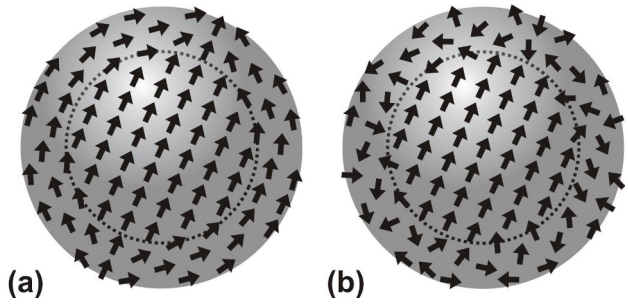

Figure 2.5: Schematic types of surface spin structure with preferred spin alignment parallel to the particle surface (a) and displaying a frustrated surface spin structure (b).

particle, yielding $N_i = 1/3$ for spherical particles without preferred magnetization direction. The majority of particles discussed in this thesis is of spherical nature, except for hematite nanospindles embedded in ferrohydrogels, shown in chapter 6, whose shape anisotropy is calculated in section A.5 of the appendix.

$$E_{Shape} = V\frac{\mu_0}{2}\vec{M}\underline{N}\vec{M} = V\frac{\mu_0}{2}\sum_i N_i M_i^2 \tag{2.3}$$

In small magnetic particles of core diameter D_C, the majority of atoms is positioned in proximity to the particle surface, leading to the emergence of a surface anisotropy E_S. Neglecting the curvature of the particle, they can be visualized as surface atoms in a thin film sample, preferring an in-plane orientation of magnetic moments due to predominant surface anisotropy $E_S = \frac{6K_S}{D_C}$, but reports on surface spin structures showing magnetic moments with out of plane orientation can also be found in the literature, as follows. The competition between surface alignment and magnetocrystalline anisotropy is well known as a potential source of frustrated spin structures, where pinned magnetic moments correspond to very high magnetic anisotropies. Different types of spin geometries can manifest, depending on the individual crystalline and magnetic structure, the shape of the particles, magnetocrystalline anisotropy and the presence of lattice defects [2, 38]. Two possible spin structures are visualized in figure 2.5, where surface spins are either aligned preferably parallel to the surface or show a frustrated state. Pinned magnetic moments in such surface structures are often referred to as 'magnetically dead layers' [39, 40], as huge magnetic field amplitudes are required to obtain at least partial alignment of these regions. However, different types of spin structures are hard to distinguish, if they result in the same reduction in net magnetic particle moment. This problem can be solved to some extent by applying experimental techniques sensitive to the *local* spin orientation or by combining methods of different surface sensitivity.

The total anisotropy energy of such a particle often is described in terms of an effective magnetic anisotropy K_{eff}, containing contributions of shape, magnetocrystalline and surface anisotropy. In particles smaller than 10 - 20 nm the magnetocrystalline anisotropy may pose the less important source of total anisotropy energy. This can be demonstrated by comparing the cubic anisotropy constants of magnetite ($K_1 \approx$ -12 kJm^{-3}, $K_2 \approx$ -3 kJm^{-3}) with effective

anisotropies of $K_{eff} > 20$ kJm^{-3} found in Fe_3O_4 particles smaller than ca. 12 nm, whereby the magnetic orientation is determined primarily by the combination of shape and surface anisotropy [41, 42, 43]. As even minor deviations from the ideal spherical shape are known to give rise to an uniaxial anisotropy contribution parallel to the elongated particle axis, equation (2.4) has been reported to be an adequate estimation of the effective anisotropy energy [1].

$$E_A = V K_{eff} \sin^2(\theta) \tag{2.4}$$

In addition to these intrinsic particle properties, the magnetic orientation also is affected by interparticular interactions. First to name here is the magnetic dipolar interaction between net magnetic moments of different particles, as interparticle exchange interaction is limited to very small contact areas and nullified by particle coating used in most ferrofluids and compounds. The total energy of magnetic dipole interaction is determined by the magnetic properties of the interacting particles and even more by their local configuration. Nevertheless, the simple expression (2.5) can be found for the maximum dipolar interaction energy of two interacting particles with core-to-core distance D and net magnetic moment μ_{NP} [44].

$$E_{dip} \approx \frac{\mu_0 \mu_{NP}^2}{4\pi D^3} \tag{2.5}$$

The high surface-to-volume ratio in magnetic nanoparticles affects not only the magnetic anisotropy. For many applications nanoparticles containing 3d-elements are utilized, which exhibit high Curie temperature and also relatively high saturation magnetization. However, these materials are also vulnerable to oxidation. While in magnetite particles this may be considered of less importance, as the oxidation from magnetite to maghemite will result in minor modifications of magnetic structure, saturation magnetization and anisotropy, it is highly critical in pure 3d-elements. E.g., iron particles exposed to oxygen will react to different types of iron oxides of ferri- or antiferromagnetic long-range order, which will modify their magnetic structure and, consequently, their net magnetic moment. This may also lead to exchange-bias effects due to competing ferro-antiferromagnetic interactions at the iron to iron oxide interface, further changing the magnetic behavior of the particles. Thus, capping layers in current nanoparticle compounds are applied not only to prevent particle agglomeration, but also to minimize oxygen transport to the reactive material of the particle core. On the other hand, the high specific surface area in nanoparticle powders makes them highly suitable for catalytic applications, for which, however, non-magnetic particles are used more frequently.

While surface effects on particle magnetism are prominent, consequences of the limited particle size and volume are even more significant in terms of magnetization dynamics. One of these is the phenomenon of thermally excited fluctuation of the particle superspin, which usually is denominated as superparamagnetism. As this is one of the major topics of this study, its origin,

temperature dependence and superspin relaxation time are discussed in the following section in more detail. Apart from superparamagnetism, the particle size also strongly affects magnetic transition temperatures. Considering, e.g., the Curie temperature as the transition point from the ferromagnetically coupled to the paramagnetic state, the critical effect of particle size D_C on T_C is obvious, if D_C deceeds the magnetic correlation length, that usually diverges at T_C. At particle diameters this low, an artificial limit of the correlation length is set, resulting in a corresponding decrease in the Curie temperature [45]. Not only Curie- and Néel temperatures, marking the transition to paramagnetic behavior, but also several further magnetic transition temperatures have been reported to display a noticeable drop upon decreasing particle sizes, including the Verwey transition temperature T_{Verwey} in magnetite and the Morin spin-flop transition in hematite [46, 47]. For ultrasmall particles these transitions have not been detected in common experimental temperature ranges, wherefore it remains unclear, whether they do not occur below a critical particle diameter or drop below the attainable temperature interval.

2.3 Superparamagnetism: Néel relaxation

In the previous section the concept of magnetic anisotropy has been introduced. Now, considering small single-domain particles instead of a macroscopic sample, the magnetic anisotropy energy $E_A = K_{eff}V_C$ can be found to be comparable to the thermal energy $E_{th} = k_BT$, due to the limited particle core volume V_C. This can be illustrated using the Stoner-Wohlfarth model assuming non-interacting nanoparticles with uniaxial magnetic anisotropy [48]. This model does not only benefit of relatively simple analytical expressions describing two antiparallel easy magnetic axes, but is also experimentally reasonable, since even slight deviations from the ideal spherical shape of the particles may lead to a dominant uniaxial contribution of magnetic shape anisotropy.

Using the angular dependence in anisotropy energy given by equation (2.4), one finds two antiparallel minima in $E_A(\theta)$, separated by an energy barrier E_A as illustrated in figure 2.6. In the simple model proposed by Néel, thermal excitation results in random fluctuation of the magnetic particle moment within this energy landscape, as described by the Néel equation (2.6), switching between antiparallel orientations on a short time scale [49]. Regarding the particles as ferromagnetic and single-domain, this process is a coherent fluctuation of all ferromagnetically coupled magnetic moments within a particle, henceforth denominated for reasons of simplicity as particle moment or 'superspin'. One can establish an intrinsic time constant or 'attempt time' τ_0, in which the superspin can change its direction. Therefore, τ_0 would be the shortest possible relaxation time, attainable only in the case of a negligible magnetic anisotropy energy barrier, and τ_0^{-1} the fastest possible rate of superspin flips ('attempt frequency'). For higher anisotropy energies E_A the Néel equation predicts an Arrhenius-like dependence of the superspin

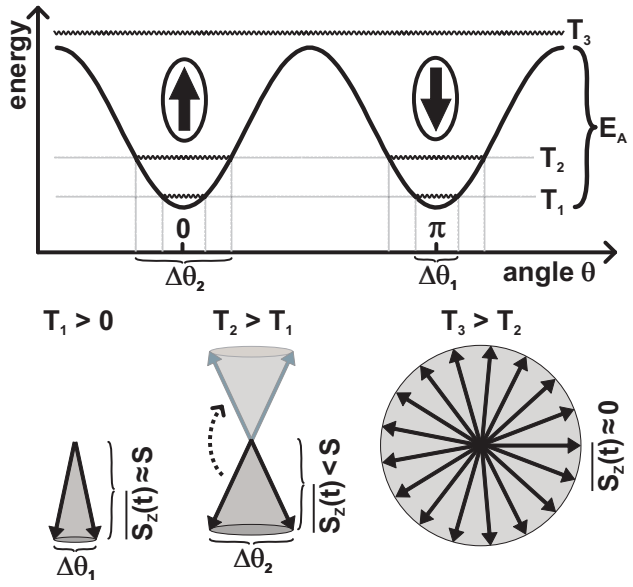

Figure 2.6: Schematic illustration of the superparamagnetic relaxation process assuming uniaxial magnetic anisotropy. At low temperatures $k_B T_1 \ll E_A$, thermal energy is insufficient to allow superspin flips. Instead, collective spin excitations in the current energy minimum occur. At $T_2 > T_1$ collective excitation at higher angular displacements may be accompanied by superspin flips. At even higher temperatures of $k_B T_3 \gg E_A$, free superspin fluctuation is observed, corresponding to completely superparamagnetic behavior.

relaxation rate on temperature, as is typical for thermally excited processes, where an activation energy has to be overcome. The relaxation time constant directly determines the time-averaged superspin S_z(t) and whether a specific experimental technique observes magnetically blocked or superparamagnetic behavior.

$$\tau_{Neel} = \tau_0 \exp\left(\frac{K_{eff} V}{k_B T}\right) \tag{2.6}$$

An ensemble of magnetic nanoparticles, which displays the above mentioned Néel relaxation, will be considered as a paramagnetic medium by techniques sensitive to the net magnetic moment, if only the superspin relaxation time τ_{Neel} is sufficiently short. Its temperature- and field-dependent magnetization can then be described in accordance with the theory of paramagnetism, except for its magnetic moment, that can exceed $10^5 \mu_B$, depending on the particle diameter. This elucidates the term of superparamagnetism: The particle moment experiences thermally induced fluctuations as in standard paramagnetism but with a much higher magnetic moment only limited by the particle volume.

An iron oxide nanoparticle of ca. 7 nm in diameter has a net magnetic moment of about $10^4 \mu_B$. Inserting this value in the Langevin equation (3.26), one finds saturation behavior at external magnetic fields several orders of magnitude smaller than in the case of a paramagnetic medium at the same temperature. This is an essential and peculiar property of superparamagnetic nanoparticles, meaning that by tuning its volume the particle can be designed to display either long-range magnetic order or quasi-paramagnetic behavior at a specific temperature, explaining the widespread application of magnetic nanoparticles in technology.

In common literature, one often reads the opposing terms 'superparamagnetic' and 'magnetically blocked', to define whether the particle moment can perform free fluctuation or is fixed in its current position. Although these notions are reasonable, they have to be used with care, as a reader could get the impression of superparamagnetism as a state in terms of thermodynamics. One has to mention that no thermodynamic phase transition takes place by reaching the superparamagnetic 'state'. Instead, the transition is a steady one, with a continuous increase in relaxation rate upon rising temperature, and the system is considered as superparamagnetic, when the relaxation rate exceeds the maximum time resolution of the applied technique:

In general, a nanoparticle is considered magnetically blocked, if no considerable deviation to static behavior is observed. In this case, the relaxation time τ_{Neel} is much longer then the specific time window τ_M of the method used. For $\tau_{Neel} \ll \tau_M$ instead, purely superparamagnetic behavior at a high relaxation rate is observed. Therefore, to characterize this transition from the magnetically blocked to the superparamagnetic regime, the majority of literature reports defines the so-called 'blocking temperature' T_B by the equality of the temperature dependent Néel relaxation rate τ_{Neel} and the time scale τ_M. To calculate T_B, equation (2.6) can be rearranged, resulting in

$$T_B = \frac{K_{eff}V}{k_B\Phi}, \quad \Phi = \ln\left(\frac{\tau_M}{\tau_0}\right) \tag{2.7}$$

The time scales τ_M of specific types of measurement can differ by several orders of magnitude. E.g., standard SQUID magnetometry requires ca. 10 s for an individual measurement of the net magnetic moment in the field direction, while in AC-susceptometry experiments, the time scale is determined by the AC-frequency of the applied magnetic field, resulting in τ_M down to microseconds. In Mössbauer spectroscopy, the inverse nuclear angular Larmor precession frequency ω_{Larmor}^{-1} of about 5 ns in case of iron oxide is the relevant time scale τ_M. Equation (2.7) can be further simplified by introducing the time factor Φ, which is inversely proportional to the blocking temperature T_B. As for the above mentioned examples, a parameter Φ of ca. 30 can be found for SQUID-magnetometry, resulting in low blocking temperatures, while 'fast' techniques with short time windows such as Mössbauer spectroscopy (MS), ferromagnetic resonance (FMR) or X-ray absorption spectroscopy (XAS) display blocking temperatures several times higher. The correct understanding of this dependence of T_B on τ_M is essential, when it comes to comparing blocking temperatures obtained by different techniques.

Using Néel's simple approach to model relaxation dynamics as a starting point, further concepts were established, e.g., by Brown [50], which made some effort to include a valid estimation of the relaxation prefactor τ_0 and its temperature dependence, which is neglected in Néel's model. In the literature, values of τ_0 in the range of $10^{-12} - 10^{-9}$ s are often used, dependent on the type of individual nanoparticles and the temperature [44]. Additionally, a wide range of experimental

reports is accessible, dealing with the influence of other parameters, i.e., the amplitude of an external DC or AC magnetic field, the degree of magnetic order of the nanoparticles and interparticle interaction, first of all magnetic dipole interaction [51, 52].
In the scope of this thesis, relaxation times were calculated, based on Néel's model, to gain comparable results for very different sets of nanoparticle ensembles. Nevertheless, as the topic of interparticular interaction will be examined more closely in chapter 4 and is also important in terms of ferrofluidic stability against agglomeration, the most frequently used model shall be summarized here shortly.
In literature reports on nanoparticles experiencing interaction of different types and strengths, as is realized by variation of the average core-to-core distance in chapter 4, magnetic dipole interaction has often been found to be accompanied by an increase in blocking temperature or a decrease in relaxation rate [53, 54, 55], while in some cases lowered energy barriers and blocking temperatures are reported [56]. Obviously, interparticle interaction introduces complex effects to the system's relaxation behavior, which are difficult to describe by a single specific model.
For a given configuration of adjacent nanoparticles, one can achieve the average magnetic stray field by adding up the contributions from each magnetic particle moment. The Zeeman energy, corresponding to the total stray field, will deform the energy landscape of the angular dependent anisotropy energy E_A. It seems reasonable to assume a decrease *or* increase in effective anisotropy barrier, depending on the individual configuration of two interacting particle moments being either parallel or perpendicular to the easy magnetic axes. However, this leads to an overall increase in effective anisotropy energy in most cases. A quantitative description of this phenomenon is the so-called Vogel-Fulcher equation (2.8), which is an empirical extension of the Néel equation (2.6).

$$\tau_{Neel} = \tau_0 \exp\left(\frac{K_{eff}V}{k_B(T-T_0)}\right), T_0 = \frac{E_{dip}}{k_B} \approx \frac{\mu_0\mu_{NP}^2}{4\pi D^3 k_B} \tag{2.8}$$

Here, μ_{NP} is the magnetic nanoparticle moment and D the core-to-core distance of the interacting nanoparticles. The newly introduced parameter T_0 represents a temperature-analog of the dipolar interaction energy E_{dip}. Equation (2.8) states divergence of the relaxation time τ_{Neel} at the temperature T_0, resulting in the observation of magnetically blocked behavior independent of the experimental method, corresponding to a magnetically frozen state. Systems with weak interparticle interaction are regarded as superparamagnetic or quasi-superparamagnetic in literature and can be analyzed by this method.
If the particles studied are in close contact and/or relatively large, leading to magnetic interaction energies comparable or larger than thermal and anisotropy energies, a continuous transition to a magnetic behavior governed by a multitude of metastable states of frustrated magnetic moments takes place, for which the name of 'spin-glass' or 'cluster-glass' behavior has

been established. This has been initially observed for systems of separated, frustrated magnetic moments in nonmagnetic matrices (spin glasses). However, characteristic aging and memory effects, indicative for spin glasses, have also been found in systems, where strongly interacting superparamagnetic particles were studied in place of single magnetic moments [57]. The superspins displayed frustrated orientational behavior upon cooling, denominated as 'super spin glass', thinking of a spin glass realized by superspins.

Although the transition from superparamagnets to super spin glasses is a continuous one and not well defined, a more detailed discussion of spin glass phenomena will not be included here, as no indication of spin glass effects could be observed in the present nanoparticular samples discussed in chapter 4 - 7.

2.4 Basics of Brownian motion and fluid dynamics

Superparamagnetic behavior, which can be understood as free coherent reorientation of the magnetic particle moment, is not limited to the Néel relaxation mechanism. While the latter deals with the superspin reorientation process within a spatially fixed nanoparticle, free 'motion' of the magnetic moment can also be achieved by the rotation of the nanoparticle with its fixed magnetic moment within a viscous medium at sufficiently high rotational frequencies. This effect takes place in ferrofluidic and related systems, where nanoparticles perform diffusive translational and rotational Brownian motion, caused by collisions with fluid molecules in ultrafast succession.

Although both phenomena have a similar effect on the net magnetization, they are of completely different physical origin. Because of that, the dynamical behavior of a ferrofluidic system without net magnetization is sometimes denominated as 'pseudo-superparamagnetism' [58]. For reasons of simplicity, relaxation phenomena of Néel superspin relaxation as well as by Brownian rotation will be denominated as superparamagnetism, but commented for clarity with an adequate description of the current relaxation mechanism.

A quantitative description of the process of Brownian motion was found by A. Einstein as early as 1905 by solving the Focker-Planck-equation to determine the time dependent progression of the probability function of a separate particle [59]. The effect was also modeled by M. von Smoluchowski in 1906 by studying the step-length of Brownian motion on different time scales with successive change in particle propagation direction by collisions with fluid molecules [60]. However, an approach, which seems more simple and illustrative, also leading to Einstein's equation for the mean square displacement, was established by P. Langevin by adding a randomly directed 'complementary force' to the equation of particle motion, representing the effect of molecule collisions on the particle surface [61]. This intuitive model will be used here as a starting point to describe superparamagnetism caused by Brownian motion.

Quantitative description of Brownian motion

In the simple approximation of a spherical particle in a Newtonian fluid and thermal equilibrium, one finds the same energy of $k_BT/2$ per degree of motional freedom according to the equipartition theorem. As a result, the mean square velocity $\overline{v^2}$ of a particle of mass m_{NP} in the fluid is

$$\overline{v^2} = \sqrt{\frac{3k_BT}{m_{NP}}}. \tag{2.9}$$

For an iron oxide nanoparticle with the hydrodynamic radius R_{Hyd} of 10 nm moving in water, one finds $\sqrt{\overline{v^2}} \approx 1$ m/s as an estimate of the mean velocity from equation (2.9), while a velocity of about 600 m/s is obtained for the much smaller and lighter water molecules itself. By comparing these high velocities of ballistic motion with the very moderate velocity of diffusive particle motion, as it can be observed on microparticles directly by usage of an optical microscope, the mechanism that takes place can be understood intuitively:

Although the ballistic velocity of the particle is relatively high, it can be considered as quasi-static for the much faster water molecules, wherefore the motion of the particles can be ignored in the following model. Each impact of a water molecule on the particle surface mediates a miniscule momentum, changing the particle propagation direction and velocity barely noticeable. However, the fluid molecules collide with the particle surface at extremely high rates, which can, dependent on the size of the particle, exceed 10^{15} s^{-1}. Although the probability of molecule-to-particle collisions is the same for each direction, statistically emerging accumulations of collisions with a small preference in one directions then cause the quite complex shivering particle motion on longer time scales, with ranges of free ballistic motion much smaller than the particle diameter of some nanometers.

Here, we assume that the rate of randomly directed transferred momentum of the particle can be considered as a continuous force by a surrounding medium on time scales, which are long compared to the time scale of molecule collisions, but still much shorter than the time intervals relevant for diffusive motion. Then, the particles experience an acceleration given by the equation of particle motion, which is defined by the Stokes frictional force being proportional to the particle velocity and the time-wise uncorrelated 'exciting' force [1].

The Stokes friction term can be simplified by usage of the translational friction coefficient γ_t of the fluid on the particle surface opposed to the propagation direction, which is then $\gamma_t = 6\pi\eta R_H$. The equation of motion is given by equation (2.10). To calculate the diffusive motion of more complex particle shapes, which cannot be well approximated by spherical shape, a more detailed description of friction coefficients may be found in section A.7 of the appendix.

$$m\frac{d^2x}{dt^2} = -6\pi\eta R_H\frac{dx}{dt} + F_X = -\gamma_t\frac{dx}{dt} + F_X \tag{2.10}$$

[1] Langevin named it 'complementary force' in his original publication [61]

By averaging equation (2.10) for a large number of particles, the randomly directed force F_X tends towards zero, whereby a simple exponential function can be found to solve the differential equation. By this way, one yields the following expression for the mean square displacement within a time interval τ in agreement with Einstein's theory:

$$\overline{\Delta x^2} = \frac{k_B T}{3\pi\eta R_H} \cdot \tau \tag{2.11}$$

$$= \frac{2k_B T}{\gamma_t} \cdot \tau \tag{2.12}$$

Equation (2.12) can be further simplified by usage of the translational diffusion coefficient D_t of a spherical body, which is given by the ratio of thermal energy to the translational friction coefficient. Considering movement in three dimensions, this yields

$$D_t = \frac{k_B T}{6\pi\eta R_H} = \frac{k_B T}{\gamma_t} \tag{2.13}$$

$$\overline{\Delta r^2} = \frac{6k_B T}{\gamma_t} \cdot \tau = 6D_t\tau \tag{2.14}$$

Regarding $\sqrt{\overline{r^2}}$ as a measure for the average 3-dimensional distance a particle travels within the time interval τ, one yields a distance of only 0.4 nm covered within one nanosecond by putting in the parameters of the above mentioned example of a sphere of $R_H = 10$ nm moving in water of viscosity $\eta \approx 10^{-3}$ Pas. By analogy, the particle requires a time of several microseconds to travel a distance corresponding to its own diameter. A motion of the particle on macroscopic length scales, as suggested by the high instantaneous velocity, is, therefore, impossible in time scales accessible without sophisticated experimental techniques. Furthermore, equation (2.14) indicates that, unlike ballistic motion, diffusion covers a mean path length $\sqrt{\overline{r^2}}$ proportional to $\sqrt{\tau}$ instead of τ. Also, it is noticeable that by the transition from ballistic to diffusive motion the particle mass no longer influences the particle velocity. Instead, the traveled path length only depends on the thermal energy driving the movement, the fluid's dynamic viscosity and the size of the particle, which determine the decelerating Stokes friction force.

Up until now, the theory is limited to translational particle motion. But naturally, randomly directed collisions with the particle surface will not only transfer a momentum, but also a torque on the particle, resulting in translational as well as rotational motion. It can be shown that the mean square angle $\overline{\Delta\theta^2}$, by which the particle turns within a time interval τ, can be calculated similarly to the mean square displacement [62]. By analogy to equation (2.14), $\overline{\Delta\theta^2}$ can be calculated by equations (2.15) and (2.16), introducing the rotational friction coefficient γ_{rot} and the rotational diffusion coefficient D_{rot}.

$$D_{rot} = \frac{k_B T}{8\pi\eta R_H^3}, \gamma_{rot} = 8\pi\eta R_H^3 \tag{2.15}$$

$$\overline{\Delta\theta^2} = \frac{6k_B T}{8\pi\eta R_H^3} \cdot \tau = 6D_{rot}\tau \tag{2.16}$$

To link this descriptive model of Brownian motion to the phenomenon of superparamagnetism, a characteristic Brownian rotation time τ_{rot} can be defined, which determines how 'fast' the orientation of the particle will change by rotational diffusion. By analogy to the Néel relaxation mechanism and the Néel relaxation time τ_{Neel}, τ_{rot} in equation (2.17) then is a measure for the time dependent decay of a sample's net magnetic moment from a completely aligned state to zero.

$$\tau_{rot} = \frac{1}{2D_{rot}} = \frac{4\pi\eta R_{Hyd}^3}{k_B T} \tag{2.17}$$

Dynamic viscosity and the glass transition

As mentioned above, the velocity of Brownian motion strongly depends on the friction coefficients γ_t and γ_{rot}. These are determined, apart from the fixed hydrodynamic diameter D_{Hyd} of the nanoparticle, by the dynamic viscosity η of the surrounding fluid. η characterizes the frictional force of a fluid acting on the surface of a moving particle and, therefore, is an important coupling element between the movement on the nanoscale and the macroscopic fluid properties. As in chapters 5 - 7 ferrofluids of very different viscosities and also nanostructured compounds are studied, which will then be discussed in terms of a more complex 'nanoviscosity', the topic shall be elucidated here shortly in the more simple model of a classical, Newtonian fluid. The term 'Newtonian' fluid describes a liquid, which responds to an acting shear stress by displaying a proportional shear rate or, put in another way, which exhibits a viscosity that is independent of the shear stress.

On a daily basis, one encounters a wide range of fluids of different viscosities. Some examples valid at ambient temperature can be found in figure 2.7. It has to be mentioned that a lot of 'fluids' known from everyday life, be it blood, mayonnaise, toothpaste, etc. are more complex non-Newtonian fluids, which should not be compared directly with the examples in figure 2.7, as their viscosity may depend on the shear stress and further parameters. The most common fluid, for sure, is water with a dynamic viscosity of 10^{-3} Pas at ambient conditions. At higher viscosities, an increasing resistance towards external forces and distinctively decelerated flow behavior can be observed. For even larger values of $\eta \gg 10^6$ Pas, the material may be hardly regarded a fluid any longer, as illustrated by the famous pitch drop experiment, showing the growth and fall of only one drop in several years [63].

Reference values of η are consciously given at room temperature, as they may display a different and distinct temperature dependence for each type of fluid , as shown, e.g., by liquified asphalt or glass melts formed upon heating to about 1000 K. However, for a large number of Newtonian fluids the so-called Andrade equation (2.18) has been proven to be a valid approximation for

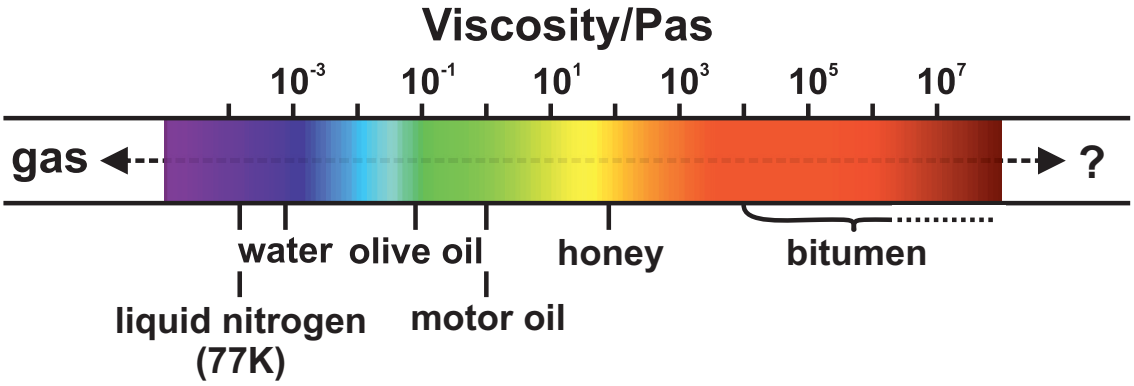

Figure 2.7: Some examples representing the wide range of dynamic viscosities one experiences in daily life. Unless described otherwise, values of η are given at room temperature [64].

the temperature dependence of the dynamic viscosity within limited temperature intervals:

$$\eta = \eta_0 \exp\left(\frac{E_{act}}{RT}\right), \tag{2.18}$$

where η_0 is a material parameter, R the molar gas constant and E_{act} the activation energy density, which has to be overcome for fluid molecules to switch places. From this, an important question emerges, regarding the high viscosity range on the right hand side of figure 2.7:
'Of which type is the behavior of a liquid on the molecular level in the regime of ultrahigh viscosity, where it is no longer macroscopically considered to be a fluid?'
It seems natural to assume that by the divergence in η one would reach parameters known from solid-state physics, even without crystallization of the fluid, i.e., being an *amorphous* solid. In fact, materials as shown in the pitch drop experiment, which are at the limit of what one would consider a fluid and behave as solids on normal time scales, may be either described by the shear modulus established for elastic solids just as well as by a dynamical viscosity.
While the process of crystallization is a thermodynamic phase transition, the transition from highly viscous liquids to amorphous solids upon decreasing temperature is not well defined, but instead, similar to the phenomenon of Néel superparamagnetism, is a continuous change in its macroscopic behavior and molecular motion. During this process, the mobility of fluid molecules decreases to a point, where it is comparable to that in crystalline materials. However, no long range ordering emerges, wherefore this process is known as the 'glass transition'. The characteristic glass transition temperature T_G is defined material-independently and relatively arbitrarily by the temperature, at which the dynamic viscosity η exceeds ca. 10^{12} Pas. By comparing this value with the example made by the pitch drop experiment, it is clear that a material of $\eta \approx 10^{12}$ Pas surely can be considered a solid on regular time scales.
Let one assume the glass transition to be a continuous transition considering the viscosity η as an 'order parameter'. Then, it is reasonable to expect that nanoscale dynamics in the fluid take

place unalteredly, but of course on longer time scales, i.e., for the translation and rotation of fluid molecules as well as for the movement of the reference nanoparticle. Evaluating equation (2.14) for the movement of a water molecule with an effective diameter of about 0.3 nm in a time interval $\tau \approx 1$ s, yields a covered path length of about 2 μm. A molecule of similar size in a hypothetical fluid at the glass transition with $\eta \approx 10^{12}$ Pas would travel only ca. $7 \cdot 10^{-14}$ m in the same time. This approach may provide an illustrative explanation for the existence of quasi-stable glasses at low temperatures, i.e., why some liquids display crystallization upon decreasing temperature, while others do not.

By cooling down a hypothetical liquid, instable crystallization seeds will form and dissolve again, if they do not grow large enough to be stable within sufficiently short time. The lower the temperature of the liquid, the smaller is the required seed size to be considered as stable. Then, the growth rate of the seeds by attaching new fluid molecules to its surface exceeds the degradation rate due to thermal energy. However, to be incorporated in the lattice structure of the crystallization seed, the molecules have to adopt a fitting surface position with the correct orientation. Now, if the liquid is cooled down very fast to far below its freezing temperature, where crystallization seeds start to form, one reaches the region of higher viscosity, where molecular dynamics slow down so far that molecules cannot adopt a fitting position and orientation within regularly observable time scales [65]. In this way the freezing of the fluid is suppressed, wherefore it is denominated a 'supercooled' liquid. Nevertheless, if the final liquid temperature is not sufficiently low, remaining molecular motion may allow spontaneous crystallization.

As the growth rate of crystallization seeds depends on material properties of the individual liquid, they also determine the limit of sufficiently fast cooling rates to attain the metastable glass state before spontaneous recrystallization takes place. Thereby, it is very difficult for some liquids to reach the glassy state, while others, e.g., glycerol and glycerol solutions, are known as good glass formers, attaining glassy states without freezing even at very slow cooling rates [66]. This phenomenon also affects glycerol-based ferrofluids discussed in chapter 5, where glass forming is indicated indirectly from temperature dependent measurement of the Brownian relaxation dynamics.

Glass formers display a temperature dependent viscosity that deviates from the simple behavior predicted by equation (2.18), and shows even faster increase in η upon decreasing temperature. For a multitude of glass-forming fluids it has been demonstrated that at temperatures closely above the glass transition temperature T_G, $\eta(T)$ can be well approximated by the Vogel-Fulcher law (2.8), which has been introduced before to describe the Néel fluctuation frequency in presence of interparticle interaction. In literature reports on fluid dynamics, one may find this law denominated as Vogel-Fulcher-Tammann-Hesse equation (2.19) (VFTH-equation), instead [67, 68, 69]:

Previously, T_0 had been introduced to describe the temperature analog of the interaction energy E_{dip} or the temperature, at which the relaxation time diverges and superspin fluctuation is 'frozen'. By analogy, here the Vogel-Fulcher temperature T_{VF} represents the point of freezing molecular dynamic motion, where the (rotational) Brownian relaxation time and the dynamic viscosity diverge. Relatively independent of the material at hand, T_{VF} has been found to be ca. 50 K below the glass transition temperature T_G [70, 71].

$$\eta = \eta_0 \exp\left(\frac{E_{act}}{R(T - T_{VF})}\right) \tag{2.19}$$

Comparison of Brownian and Néel dynamics and relaxation times

In addition to the Néel relaxation mechanism, now the rotational Brownian motion has been demonstrated to result in superparamagnetic behavior on sufficiently long time scales, too. However, although the underlying physical process is different, a number of similarities can be noticed for these two phenomena upon closer inspection.

- While the diffusive character of Brownian motion is evident, with some consideration the Néel relaxation process may be understood as the diffusive motion of the superspin direction. The relaxation prefactor τ_0 then represents the time required for a single diffusion 'step' with random direction in the energy landscape of angular dependent anisotropy energy $E_A(\theta)$ characterized by equation (2.4). The underlying process may be visualized as particle diffusion on a shaped surface with minima given by the two antiparallel easy magnetic directions. This model is applied in the simulation of Mössbauer spectra recorded on Néel-type superparamagnetic nanoparticles using the Jones-Srivastava many-state model, explained in detail in section 3.1 [72].

- For non-interacting particles the Néel relaxation time $\tau_{Neel}(T)$ can be estimated from equation (2.6), which displays the same type of function as equation (2.18), the latter describing a fluid's dynamic temperature dependence of the viscosity.

- If considerable interparticle interaction is present, τ_{Neel} may diverge at low temperatures and is then described by the more complex equation (2.8) instead of equation (2.6). Again, the same functional dependence may now be applied to describe the temperature-dependent dynamic viscosity of a glass-forming liquid, eq. (2.19). The latter is noticeable, as the term 'glass' originates from the material of the same name with metastable mechanical configuration without long-range ordering, while the corresponding term 'spin-glass' is defined as a metastable state, where again long-range ordering is desirable to access a state of minimum interaction energy for the magnetic moment, but is never reached due to spin frustration.

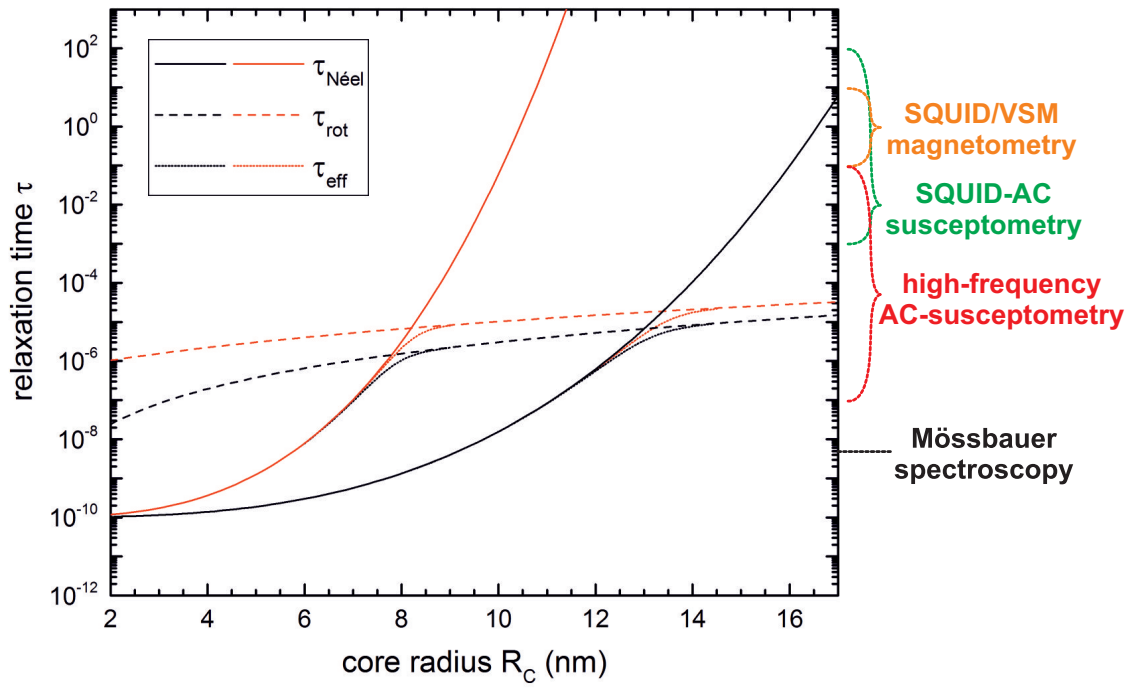

Figure 2.8: Néel relaxation times τ_{Neel} and Brownian rotation times τ_{rot} calculated from equations (2.6) and (2.17) versus particle core radius R_C. τ_{Neel} was determined for T = 300 K, $\tau_0 = 10^{-10}$ s and $K_{eff} = 5$ kJm^{-3} (black solid line) respectively $K_{eff} = 20$ kJm^{-3} (red solid line). τ_{rot} was estimated for $\eta = 10^{-3}$ Pas and particles with a 5 nm coating layer (red dashed line) or uncoated particles (black dashed line). Dotted lines are effective relaxation times calculated from equation (2.20). Time scales accessible to different magnetic measurement techniques or setups are highlighted.

- For both phenomena, the relaxation time diverges at low temperatures, as the thermal energy is insufficient to exceed the molecular activation energy in a fluid, or the energy barrier of magnetic anisotropy.

On the other hand, the most prominent difference in Néel and Brownian relaxation processes are the characteristic relaxation times in nanoparticles of different sizes. The Brownian rotation time τ_{rot} is proportional to the particle volume. Assuming a water-based ferrofluid with $\eta \approx$ 1 mPas, τ_{rot} can be estimated to be of constant magnitude in the range of microseconds for nanoscale particles, as illustrated in figure 2.8. Unlike the Néel relaxation, the Brownian motion varies with the hydrodynamic radius instead of the particle core radius, wherefore changes in coating shell thickness will additionally alter the rotation time.

However, the Néel relaxation time changes dramatically depending on the particle core diameter R_C and the effective magnetic anisotropy constant K_{eff}, due to the exponential correlation. As visible in figure 2.8, where typical time windows of experimental techniques are displayed comparatively, Brownian dynamics can be analyzed for ferrofluids of different particle sizes

by a single method, while the Néel relaxation mechanism covers several orders of magnitude in relaxation time. For this reason, a thorough analysis of the Néel relaxation process under variation of the particle core diameter requires the usage of experimental methods of vastly different time windows. As a consequence, Néel-type superspin relaxation is often studied by tuning the relaxation time via temperature variation, which is necessary for the study of Brownian motion and, therefore, less common in this field.

For system parameters as given in the exemplary figure 2.8, there is an intersection of τ_{Neel} and τ_{rot} at about 1 μs, defined primarily by the less size-dependent Brownian rotation time. An estimation of the total relaxation time in nanoparticles experiencing rotation and superspin relaxation simultaneously can then be accomplished by the following approach: Assuming both effects to be independent, the total rate of change in magnetization direction is the sum of relaxation frequencies, which easily leads to equation (2.20) for the effective relaxation time:

$$\tau_{eff} = \frac{\tau_N \cdot \tau_{rot}}{\tau_N + \tau_{rot}} \tag{2.20}$$

Obviously, the usage of τ_{eff} is only necessary close to the relaxation time intersection. For the majority of systems, given a specific nanoparticle diameter, the rotation and relaxation times differ by several orders of magnitude, except in a very sharp particle size interval of, e.g., 7 - 9 nm core radius for $K_{eff} = 20$ kJm^{-3} in the exemplary figure 2.8. Furthermore, it has to be considered that most of the available nanoparticle samples, be it commercial ones or laboratory-made for research, exhibit a more or less broad size distribution, which is of log-normal shape in general, following equation (2.21).

$$p(R_C) = \frac{1}{\sqrt{2\pi}\sigma R_C} \exp\left(-\frac{(\ln(R_C) - \mu)^2}{2\sigma^2}\right) \tag{2.21}$$

$$\overline{R_C} = \exp(\mu + \frac{\sigma^2}{2}) \tag{2.22}$$

In this context, a log-normal distribution with standard deviation $\sigma = 0.3$ is still regarded as monodisperse. And while this distribution in hydrodynamic particle diameters will not alter the Brownian rotation time considerably, the corresponding distribution p(τ_{Neel}) in superspin relaxation time will cover several orders of magnitude [73, 74]. This makes the usage of a discrete τ_{Neel} impracticable and the calculation of an effective relaxation time rather pointless, unless highly monodisperse particles are used.

Dynamics in soft matter compound systems

The straightforward description of relaxation dynamics as given above is valid assuming a particle surrounded by a homogenous Newtonian fluid and can be applied to model effects, e.g., in ferrofluids with low particle concentration.

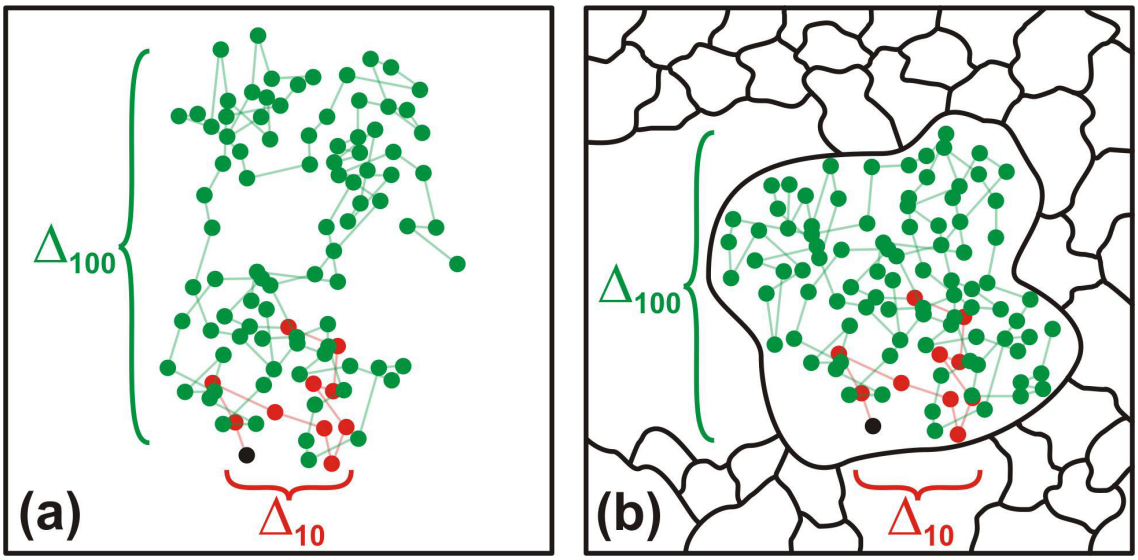

Figure 2.9: Free diffusive motion (a) in contrast to trapped motion of a confined nanoparticle with limited area of freedom (b). Dots mark the traveled distance of the particle per step: starting position (black), first 10 steps (red) and first 100 steps (green).

Recently, however, a broad range of different soft matter compound systems containing (magnetic) particles has been established, designed for a wide spectrum of technological and medical applications as outlined in chapter 1. Such materials often exhibit an inhomogeneous structure on the micro- or the nanoscale and may be realized by embedding the particles in some elastic matrix or trapping them in a rigid structure with limited range for free particle motion.

The original definition of the viscosity η becomes insufficient to describe the systems behavior, as in these compounds the particle mobility may depend on the direction or on external stimuli, or remain unaltered only at short distances from the particle's resting position. The free diffusive movement in contrast to trapped motion within a rigid confinement is illustrated in figure 2.9. In figure 2.9 (a), red dots mark the first 10 steps of free diffusive motion and green dots the movement until step 100. Representative values of the traveled path length after 10 and 100 steps are Δ_{10} and Δ_{100}, respectively. It can be seen that for free diffusive motion the mean square displacement increases proportionally to the step number (or traveled time τ), in agreement with equation (2.14). For the diffusive motion of the confined particle in figure 2.9 (b), similar behavior as in (a) is observed for the first steps, respectively on short time scales. In the region of 10 to 100 steps, the particle gets in contact with the confinement, blocking its path. This confinement could represent a rigid matrix structure as well as a blockade for particle motion by 'elastic' polymer strings in this simple schematic picture.

Since the movement of the nanoparticle is restricted to the area respectively volume of the confinement, we observe a decrease of Δ_{100} relative to free Brownian motion. On even longer time scales, the mean square displacement will, without question, saturate, wherefore a higher

effective viscosity will be detected by, e.g., magnetic techniques, sensing the particle motion on a longer time scale. 'Faster' techniques, on the other hand, will observe the 'real' viscosity of the medium within the confinement the particle is moving in. The behavior characterized by effective viscosities, dependent on the spatial and time window of the applied technique, is the subject of nanorheology and often named 'nanoviscosity' respectively 'microviscosity' [75, 76]. Following this concept, homogeneous as well as nanostructured materials will be studied within the scope of this thesis by techniques of different time constants τ_M to examine the influence of the nanoviscosity on relaxation dynamics.

3 Experimental techniques and theoretical models

3.1 Mössbauer spectroscopy

Mössbauer spectroscopy is a non-destructive, high-sensitivity technique to analyze the magnetic structure of materials based on the spectral structure of the absorption/emission spectrum of γ-quanta by the ^{57}Fe nucleus, providing a method of virtually unrivaled energy resolution as illustrated in the following paragraphs. It utilizes the effect of recoil-free nuclear resonant absorption discovered by R. L. Mössbauer in 1957, later on denominated as 'Mössbauer effect'. While the effect was originally discovered on ^{191}Ir, it has been observed in more than 100 isotopes so far. However, only about a dozen of these isotopes, including, e.g., ^{57}Fe, ^{119}Sn, ^{121}Sb, ^{125}Te and several lanthanides (^{151}Eu, ^{155}Gd, ^{161}Dy, ^{170}Yb), are used extensively, due to their convenient natural linewidths, absorption energies and the half life of their source materials. Being a technique highly suitable for magnetic studies, the vast majority of publications on Mössbauer spectroscopy deals with ^{57}Fe-based samples.

Depending on the individual experimental protocol in use, Mössbauer spectroscopy can also be applied to obtain information on structural, chemical and thermodynamic properties, wherefore, additionally to its usage in physical and chemical characterization, it is a prominent technique in the fields of geology and mineralogy [77], metallurgy [78], archeology [79, 80, 81] and astrophysics [82, 83, 84]. Realizing the impact of this newly established method, R. L. Mössbauer was awarded the Nobel prize in 1961 at the age of 32.

Introduction

In the following, a basic introduction will be given exemplarily for ^{57}Fe-Mössbauer spectroscopy. However, the same theory and calculations can be applied to alternative Mössbauer isotopes, based on the individual radioactive decay scheme.

^{57}Co is used as radioactive source material providing a discrete γ-ray energy for resonant absorption by ^{57}Fe, as shown in figure 3.1. ^{57}Co decays to ^{57}Fe with a half life $t_{1/2}$ of about 270 days, leading to a practical overall lifetime of a ^{57}Co-source of several years. Comparing ^{57}Co to ^{57}Mn as an alternative source material with a $t_{1/2}$ of about 2 min, it is clear that the half life is one of the most essential criteria defining the applicability of a Mössbauer isotope.

Additional criteria are the energy of the observed transition and its natural linewidth. The decay of, e.g., $^{57}_{27}$Co to the excited ^{57}Fe $I_{5/2}$ state leads either to the direct transition to the ground state with a transition energy of 136 keV or to the decay to the $I_{3/2}$ state, followed by the transition to the ground state, emitting γ-quanta of $E_\gamma = 14.4$ keV. The latter can be detected with high efficiency using a standard proportional counter, while energies above ca.

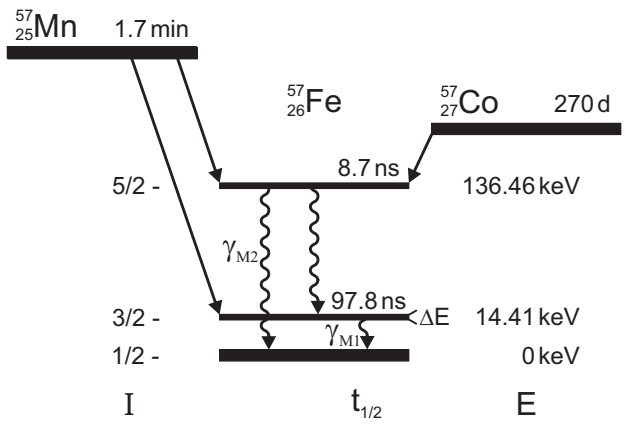

Figure 3.1: Decay scheme of $^{57}_{25}$Mn and $^{57}_{27}$Co nuclei into excited $^{57}_{26}$Fe nuclear states. Angular momentum quantum numbers and energies of the nuclear states are labeled. In general, the M1 transition from the excited $I_{3/2}$- to the $I_{1/2}$-ground state is used in Mössbauer spectroscopy. Adapted from [85]

100 keV require the usage of, e.g., scintillation counters or semiconductor detectors.

$$\Delta E \Delta t \geq \frac{\hbar}{2} \tag{3.1}$$

The half life of the $I_{3/2}$ state corresponds to a natural linewidth Γ_{nat} of about 5 neV of the emitted γ-quanta, using the time-energy uncertainty relation eq. (3.1). This value of Γ_{nat} is very convenient, as it is small compared to the energy scale of the relevant spectral features one is interested in and still big enough to be easily resolved with common electronics as described below. Half lifes $t_{1/2}$ smaller than 10 ns, as in the case of the excited $I_{5/2}$ state with about 8.7 ns, would produce a superposition of broad spectral features, obstructing the individual fine structure, while longer half lifes would correspond to absorption lines too sharp to be energetically resolved with acceptable effort.

Now, to illustrate the Mössbauer effect of recoilless absorption, we consider the simple example of a free iron atom of mass M and velocity $\vec{v}$, emitting a γ-quantum of the energy $E_0 \approx 14.41$ keV, corresponding to the $I_{3/2\rightarrow 1/2}$ transition. By emitting the γ-quantum, not only its energy is transferred, when the iron nucleus decays from the initial (i) $I_{3/2}$ state to the final (f) $I_{1/2}$ state, but also the momentum $\vec{p}$ of the free iron atom is decreased by the momentum of the emitted γ-quantum of $\hbar\vec{k}$, as described by the equations (3.2) - (3.4):

$$E_i = E_{3/2} + \frac{\vec{p}^2}{2M}, \tag{3.2}$$

$$E_f = E_{1/2} + \frac{(\vec{p} - \hbar\vec{k})^2}{2M}, \tag{3.3}$$

$$E_i - E_f = \underbrace{E_{3/2} - E_{1/2}}_{E_0} + \underbrace{\hbar(\vec{k}\cdot\vec{v})}_{E_D} - \underbrace{\frac{\hbar^2 k^2}{2M}}_{E_R} \tag{3.4}$$

Inserting the mass M of 57 atomic units and the angular wavenumber $|\vec{k}|$ corresponding to E_0 of about $7.29 \cdot 10^{10}$ m^{-1}, one finds a shift in transition energy by the recoil energy $E_R \approx 1.96$ meV relative to the 'original' transition energy E_0. Additionally, the transition is broadened by the

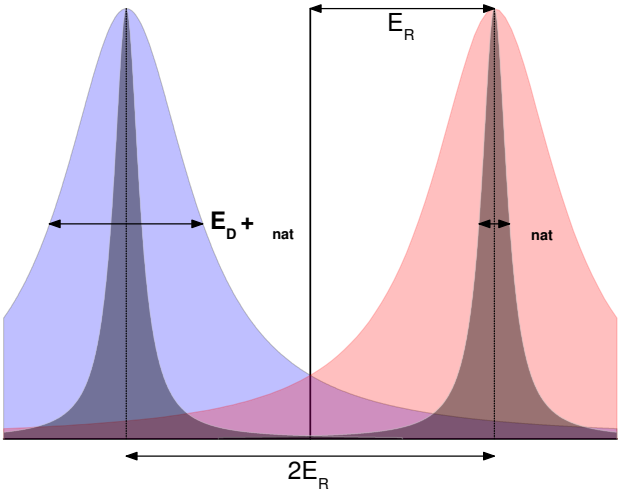

Figure 3.2: Superposition of emission (blue) and absorption line (red) of two free iron atoms, shifted by the recoil energy E_R. Doppler-broadened lines display considerable superposition (purple region). Lines of natural linewidth Γ_{nat} show negligible superposition, corresponding to minimal probability for resonant absorption.

Doppler-term E_D, dependent on the velocity of the free iron atom. Superposition of emission and absorption lines, with lineshapes given by the Breit-Wigner-equation (3.5), considering these energy contributions, is visualized in figure 3.2. As both line positions are shifted by the recoil energy $E_R \gg \Gamma_{nat}$, resonant absorption by the free iron atom would be unlikely. Obviously, resonant absorption of the γ-quanta requires recoil energies small compared to the total linewidth Γ.

$$I(E) \propto \frac{\Gamma^2}{4(E - E_0)^2 + \Gamma^2} \tag{3.5}$$

The natural solution for this problem is the incorporation of the previously free atom in a solid, e.g., crystalline medium. However, the question emerges, in which form an atom embedded in a crystal lattice absorbs the γ-quantum momentum, as it cannot perform free motion with macroscopic velocities, but only phononic oscillation. A first approach to tackle this question was presented by Shapiro [86] within classical theory of electrodynamics and further elucidated, e.g., in Ref. [85] and [87]. Using the vector potential of the excited iron nucleus, emitting a γ-quantum of angular wavenumber k, as a starting point, equation (3.6) is found to be a valid approximation the ratio of resonant to non-resonant absorption processes, where x_0 is the distance to the excited nucleus [85].

$$\ln(f) \approx 2 \ln\left(1 - \frac{k^2 x_0^2}{4}\right) \approx \frac{-k^2 x_0^2}{2} \tag{3.6}$$

With $\overline{x^2} = x_0^2/2$ being the mean square atomic displacement, one finds the simple formula

$$f \approx \exp(-k^2 \overline{x^2}). \tag{3.7}$$

The parameter f is denominated as the Lamb-Mössbauer factor and is in general directly proportional to the resonant area in the Mössbauer spectrum. f is often synonymously called Debye-Waller factor, which is the equivalent parameter in X-ray scattering theory. Considering the exponential behavior of equation (3.7), the probability of resonant absorption decreases,

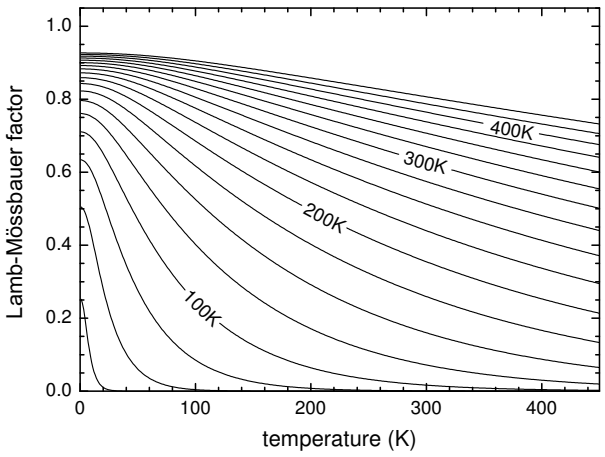

Figure 3.3: Temperature dependence of the Lamb-Mössbauer factor as calculated by equation (3.9) for Debye temperatures θ_D up to 450K, adapted from [87].

if the wave length λ is small compared to the region of about $\sqrt{\overline{x^2}}$ the γ-quantum originates from. This leads to the conclusion, that for large values of $\overline{x^2}$, as found in gases or liquids, no resonant absorption will be observed.

While equation (3.7) already is a practical estimation for the Lamb-Mössbauer factor, it yields $f \approx 1$ for small atomic displacements, neglecting the zero-point energy of the system. Using a quantum theoretical approach to describe the vibrational modes of a solid consisting of N atoms, one finds an expression for the Lamb-Mössbauer factor, valid also at low temperatures:

$$f = \exp\left(-\frac{2E_R}{3N\hbar}\int_0^{\omega_{max}}\left[n(\omega)+\frac{1}{2}\right]\frac{\rho(\omega)d\omega}{\omega}\right) \tag{3.8}$$

Here, $\rho(\omega)$ is the distribution of frequencies of the vibrational modes. In the Debye model, $\rho(\omega)$ is given by $9N\omega^2\omega_D^{-3}$ and cut off at the limiting Debye frequency ω_D. Inserting this into equation (3.8) yields

$$f = \exp\left(-\frac{3E_R}{2k_B\theta_D}\left[1+4\left(\frac{T}{\theta_D}\right)^2\int_0^{\theta_D/T}\frac{xdx}{\exp(x)-1}\right]\right) \tag{3.9}$$

The cut-off Debye frequency is given by $\hbar\omega_D = k_B\theta_D$, where θ_D is the Debye-temperature. θ_D is a well known thermodynamic quantity, which characterizes the 'softness' of phonon modes in a solid, i.e., the average thermal energy needed for phonon excitation. Although it has been demonstrated, that the continuous function $\rho(\omega)$ used in the Debye model only is a rough approximation of the phonon spectrum, it represents a valid approach for several thermodynamic quantities, e.g., the Lamb-Mössbauer factor f. The temperature dependence of equation (3.9) is exemplarily depicted in figure 3.3 for some values of θ_D, showing saturation in the low temperature regime and an exponential decrease in f at $T \gtrsim \theta_D/2$. Debye temperatures measured in bulk metals and oxides often are in the region of 300 - 500 K, but can be considerably smaller in nanoparticle systems.

Comparing the temperature dependent change in $f(\theta_D, T)$, representing the resonant area of the Mössbauer spectrum, only minor changes in f occur up to ambient temperatures for Debye

temperatures $\theta_D > 300$K, while for smaller values of θ_D room temperature spectra may display considerably decreased intensity. Therefore, low-temperature spectra are often required for a thorough analysis of nanoparticle samples or materials with a high number of soft phonon modes, to yield sufficient spectral area.

Up until now, two extrema of atomic mobility have been discussed. It has been shown, that resonant absorption is negligible for unlimited atomic mobility of free atoms in gases and fluids, while it is dominant for the most solids at ambient temperatures. The missing region of intermediate atomic mobility, which can be found, e.g., in ferrofluidic or nanorheological systems, as they are studied in this thesis, will be discussed in detail at the end of the current section in terms of Brownian diffusive motion.

Hyperfine interactions

Due to its high energy resolution, Mössbauer spectroscopy allows one to analyze variations in nuclear energy levels on the scale of neV, visible by shifts of the Mössbauer absorption lines, caused by electronic and magnetic interactions (hyperfine interactions) of the iron nucleus with its local surrounding. The main three types of hyperfine interactions, namely the isomer shift, quadrupole interaction and Zeeman splitting, will be elucidated here explicitly and are illustrated in figure 3.4. This figure shows the energy scheme of absorber materials experiencing different types of interaction and the corresponding Mössbauer spectra. The increased linewidth $2\Gamma_{nat}$ in the schematic Mössbauer spectra is caused by the folding of the source emission line of natural linewidth Γ_{nat} and the absorption line of the same width. Accordingly, the lower limit of experimentally observable linewidths is fixed to twice the natural linewidth of the excited state of the given Mössbauer isotope.

The interaction energy E of the ^{57}Fe nucleus with the electrostatic potential $V(\vec{r})$ of its surrounding is given by equation (3.10). Here, $\rho(\vec{r})$ is the spatial charge distribution of the nucleus and $\int d\tau$ represents the integration over space. Expanding the potential $V(\vec{r})$ to a Taylor series, one obtains equation (3.11).

$$E = \int \rho(\vec{r})V(\vec{r})d\tau \tag{3.10}$$

$$\approx V(0)\int \rho(\vec{r})d\tau + \sum_i V_i \int X^i \rho(\vec{r})d\tau + \frac{1}{2}\sum_{ij} V_{ij}\int X^i X^j \rho(\vec{r})d\tau + ... \tag{3.11}$$

The first term is independent of material parameters, wherefore it is identical in source and absorber and does not create a shift in line position, while the second term contains the electric dipole moment of the nucleus, which vanishes due to parity conservation [85]. The third contribution represents the interaction of the nuclear quadrupole moment tensor Q_{ij} and the electric field gradient tensor V_{ij} at the nucleus' position, which can be split in two contributions

as follows:

$$\frac{1}{2}\sum_{ij} V_{ij}\int X^i X^j \rho(\vec{r})d\tau = \underbrace{\frac{1}{6}\left[\sum_{i=1}^{3} V_{ii}\right]\int r^2\rho(\vec{r})d\tau}_{E_{mono}} + \underbrace{\frac{1}{6}\sum_{i,j=1}^{3} V_{ij}Q_{i,j}}_{\epsilon}, \tag{3.12}$$

$$Q_{ij} = \int (3X_iX_j - \delta_{ij}r^2)\rho(\vec{r})d\tau, \tag{3.13}$$

$$V_{ij} = \left(\frac{\partial^2 V}{\partial X_i \partial X_j}\right) \tag{3.14}$$

The first term in equation (3.12) can be simplified to (3.15) using the Poisson equation, representing the Coulomb interaction of the iron nucleus of mean square radius $\overline{r^2}$ with its electronic surrounding described by the electron density at the nucleus' position $|\varphi(0)|^2$. This energy contribution, denominated as the isomer shift, is dominated by the interaction with s-electrons, due to their high electron density in proximity to the nucleus. However, information on valence electron densities, i.e., valence state and chemical bonding, can be estimated directly from the isomer shift, due to electronic screening effects influencing the s-electron density $|\varphi_s(0)|^2$. Also, because of the direct proportionality of δ on $|\varphi(0)|^2$, an estimation of the electron density can be made based on the isomer shift. In this context, a decrease in isomer shift δ reflects an increase in the s-electron density of the absorber material. In iron-bearing samples, this would correspond to an increase in electronegativity of the adjacent non-iron elements.

$$E_{mono} = -\frac{Ze^2}{6\epsilon_0}|\varphi(0)|^2\overline{r^2} \tag{3.15}$$

$$\delta = E_{mono,e} - E_{mono,g} = -\frac{Ze^2}{6\epsilon_0}|\varphi(0)|^2(\overline{r_e^2} - \overline{r_g^2}) \tag{3.16}$$

$$\delta = \delta_{em} - \delta_{abs} \propto Ze^2\Delta r(|\varphi_{abs}(0)|^2 - |\varphi_{em}(0)|^2) \tag{3.17}$$

Mean square nuclear radii of ground state and excited states of the iron nucleus deviate by $\Delta r^2 = \overline{r_e^2}$ - $\overline{r_g^2}$, which leads to an overall shift E_{mono} of the corresponding absorption or emission line. Since the isomer shift takes place in the emitter as well as in the studied absorber material, one never observes experimentally the isomer shift δ_i of a single material, but instead the difference in isomer shift of emitter and absorber, as given by equation (3.17). For that reason, a calibration of the absolute line position is needed, to compare values of the isomer shift to experimental results or literature values obtained with different source materials. The most common method is to determine the isomer shift between the utilized source material and an α-iron calibration foil at room temperature, and to display isomer shifts in subsequent experiments relative to this calibration spectrum.

As explained above, the isomer shift, in its classical sense, originates from interaction of the nucleus with its electronic surroundings and, therefore, provides valuable information on valence

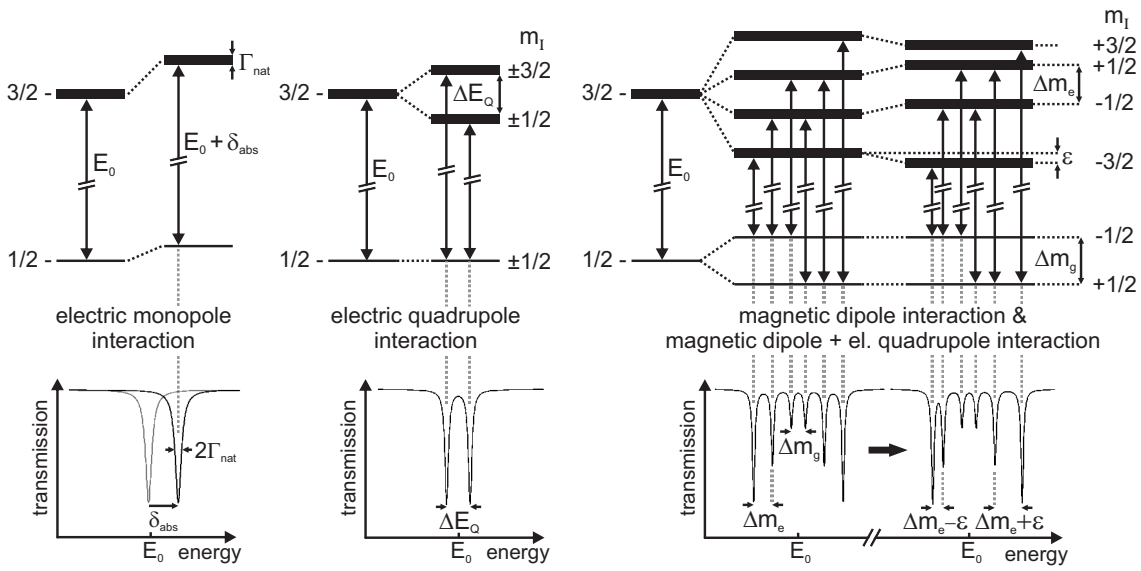

Figure 3.4: Hyperfine interactions within the absorber material and the resulting schematic Mössbauer spectrum.

state, atomic coordination number etc. However, there is a second phenomenon of different origin leading to a shift in line position, wherefore both terms are generally not resolved in common literature. This energy shift is caused by the vibration of the iron nucleus with the mean square velocity $\overline{v^2}$, resulting in a Doppler shift δ_{SODS} in line position given by equation (3.18). Applying the Debye model to determine $\overline{v^2}$, one finds equation (3.19) as an approximation of the temperature dependence of the second order Doppler shift (SODS), often in excellent agreement with experimental observation [88].

$$\delta_{SODS} = \frac{\overline{v^2}}{2c^2} E_\gamma \tag{3.18}$$

$$\approx -\frac{9 k_B E_\gamma}{16 M c^2} \left[\theta_D + 8T \left(\frac{T}{\theta_D} \right)^3 \int_0^{\theta_D/T} \frac{x^3 dx}{exp(x) - 1} \right]. \tag{3.19}$$

δ_{SODS}, calculated by equation (3.19), is displayed in figure 3.5 for Debye temperatures θ_D of 0 - 450 K, showing an almost linear decrease in temperature above θ_D and saturation in the low temperature limit $T \ll \theta_D$. By comparing this theoretical temperature dependence to a series of Mössbauer spectra, one cannot only estimate a sample's Debye temperature, but also use δ_{SODS} as an internal temperature sensor at temperatures in the linear regime. This approach is used, e.g., in chapter 7 to verify the correctness of the temperature calibration in case of Mössbauer spectra of polymer compounds. One has to mention that this calibration method can only be applied, if the 'classical' isomer shift δ does not display a considerable variation in temperature itself. However, $\partial\delta/\partial T$ is found to be negligibly small (ca. 1%) compared to $\partial\delta_{SODS}/\partial T$, so this condition is met in most experiments [88].

The second type of electric hyperfine interaction, namely the nuclear quadrupole interaction,

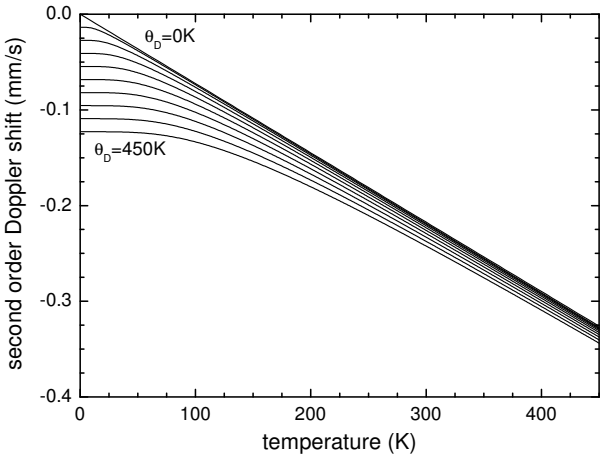

Figure 3.5: Temperature dependence of the second order Doppler shift (SODS), calculated from equation (3.19) for Debye temperatures θ_D in equidistant steps between 0K and 450K.

is given by the second term in equation (3.12). Assuming the nucleus' charge distribution to be cylindrical, the nuclear quadrupole moment Q is a scalar quantity and the expression can be simplified to

$$\Delta E_Q = \frac{eQV_{zz}}{4I(2I-1)}(3m_I^2 - I(I+1))\sqrt{1+\frac{\eta^2}{3}}, \eta = \frac{V_{xx}-V_{yy}}{V_{zz}} \tag{3.20}$$

with V_{zz} being the z-component of the diagonalized electrical field gradient (EFG) tensor. Following equation (3.20), the presence of an EFG as well as of a nuclear quadrupole moment is required to result in a non-zero energy contribution. Furthermore, ΔE_Q is proportional to m_I^2, which is why the $m_I = \pm 3/2$ and $\pm 1/2$ states remain degenerate. Consequently, a doublet structure is displayed in the ^{57}Fe Mössbauer spectrum, corresponding to the energy scheme shown in figure 3.4, with a quadrupole splitting of ΔE_Q of $\frac{eQV_{zz}}{2}\sqrt{1+\frac{\eta^2}{3}}$.
In addition to electric interactions, a splitting of the nuclear energy levels into (2I+1) sublevels can be observed in the presence of an external magnetic field or in the case of magnetically coupled samples (nuclear Zeeman splitting), created by the interaction between the nuclear magnetic dipole moment $\vec{\mu}$ and the magnetic field $\vec{B}$. The splitting between two energy levels characterized by the nuclear magnetic quantum numbers m_{I2} and m_{I2} by the magnetic hyperfine interaction is

$$E_{magn} = -gB\mu_N(m_{I2} - m_{I1}), \mu_N = \frac{e\hbar}{2m_p}. \tag{3.21}$$

Here, g is the nuclear g-factor, μ_N the nuclear magneton and m_p the proton mass. Considering the limitation of the magnetic quantum number to m_I = -I, -I-1 ... I, one finds a splitting of the ^{57}Fe $I_{3/2}$ state into four and of the ground state into two equidistant sublevels. By the selection rules of dipole radiation only transitions of Δm = 0, $\pm$ 1 are allowed. Therefore, only six of the eight possible transitions take place, as they are shown in figure 3.4, not considering minor effects of higher order, leading to the characteristic sextet structure often visible in Mössbauer spectra.

Also, as ground and excited ^{57}Fe state exhibit different nuclear g-factors of $g_g \approx 0.0906$ and $g_e \approx -0.1549$, substates of m < 0 are energetically favorable in the excited I $= 3/2$ state, while in the I $= 1/2$ ground state, it is the m $= +1/2$ substate. Furthermore, as can be seen in figure 3.4, the difference in nuclear g-factor causes a non-equidistant separation of line positions, where the separation between lines 3 and 4 is proportional to $g_g - |g_e|$, while it is proportional to g_e for each other pair of adjacent sextet lines.

Being proportional also to the local magnetic field, the large nuclear Zeeman splitting, observed in an abundance of magnetically ordered materials, implies the existence of an enormous effective magnetic field $B_{eff} > 10$ T. This is strongly suggesting that B_{eff} cannot be ascribed to classical mechanisms of magnetism only, as contributions of the local field, originating only from an applied magnetic field H_{appl} and the corresponding demagnetization field H_{dem}, seldom exceed about 1 T. The dominant contribution to the effective field is the so-called hyperfine magnetic field of electronic origin, whose contributions are outlined in equation (3.22).

$$\vec{B}_{eff} = \underbrace{\vec{B}_{appl} + \vec{B}_{dem}}_{\vec{B}_{loc}} + \underbrace{\vec{B}_{orb} + \vec{B}_{dip} + \vec{B}_{fermi}}_{\vec{B}_{hf}} \tag{3.22}$$

The first term of B_{hf}, B_{orb}, represents the contribution of orbital magnetic moment of unpaired electrons and depends strongly on the electronic configuration of the individual element, whereby it is the predominant contribution in rare earth materials with high orbital magnetic moments, but of minor importance in 3d-metal-based systems. B_{dip} is the field corresponding to the magnetic dipole-dipole interaction of the Mössbauer nucleus and nearby electrons. The last term in equation (3.22) is the so-called Fermi contact field B_{fermi}, given by uncompensated s-electron spin density at the nucleus position. In some materials this can be directly provided by unpaired s-electrons, while in the case of 3d-metals it originates from partial polarization of s-electrons by unpaired 3d-electrons. B_{fermi} can exceed 50 T and usually is the predominant contribution to the hyperfine magnetic field.

Up to this point, hyperfine interactions have been discussed separately, as complex spectral structures can emerge in case of combined nuclear quadrupole interaction and nuclear Zeeman splitting. However, assuming ΔE_Q to be much smaller than E_{magn}, a feasible estimation of line positions can be obtained by simple superposition of both energy contributions. In that case, a shift of the inner four lines relative to the outer absorption lines by an energy of 2ϵ can be observed, visible, e.g., in figure 6.4 for hematite nanoparticles. 2ϵ is denominated as the nuclear quadrupole level shift and described by equation (3.23) and is dependent on the (paramagnetic) nuclear quadrupole splitting ΔE_Q and the angle θ between the principal axis of the electric field gradient tensor and the spin direction. Considering the direction of the electric field gradient EFG as a characteristic of a system's crystal structure, the nuclear quadrupole level shift 2ϵ

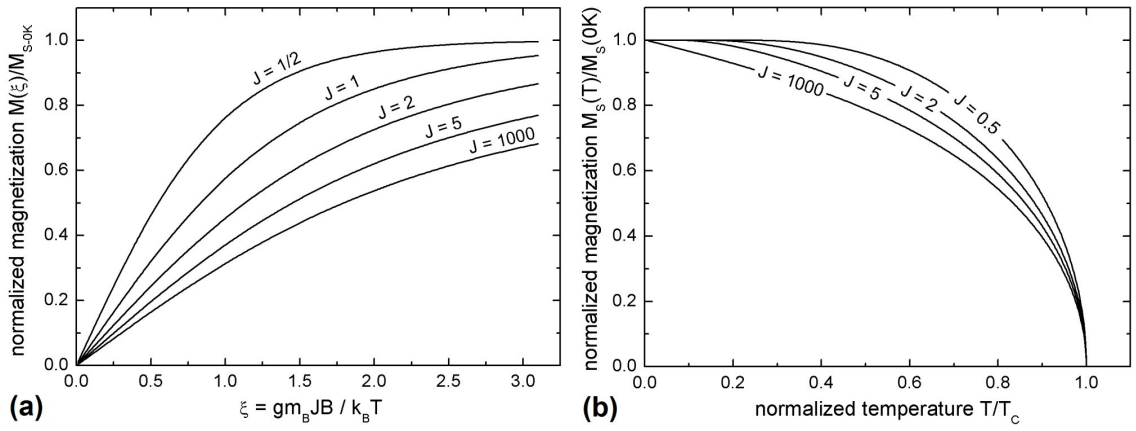

Figure 3.6: Brillouin function , eq. (3.25) versus dimensionless parameter ξ (a), and temperature dependence of saturation magnetization, numerically determined from equation (3.29) (b).

becomes a versatile quantity to study the Fe spin orientation relative to a material's crystal axes. This approach is essential for the analysis of complex spin structures, as, e.g., the discovery of the long range spin cycloid in bismuth ferrite (BFO)-based multiferroics [89, 90, 91].

$$2\epsilon = \Delta E_Q \frac{3\cos(\theta)^2 - 1}{2} \tag{3.23}$$

Disregarding effects of dynamic relaxation or external magnetic fields, which will be discussed in the following paragraphs, the experimentally observed hyperfine magnetic field B_{hf} is expected to be approximately proportional to the absorber's sublattice magnetization, and, therefore, to the saturation magnetization M_S in simple magnetic structures. This makes the hyperfine splitting an additional valuable asset for magnetic characterization. The temperature dependence of B_{hf} can be determined analogously to that of the saturation magnetization: The Brillouin function $B_J(\xi)$, describing the magnetization of an ideal paramagnet with the total angular momentum J, as given in equation (3.25), may be used as a starting point. For $J \gg 1$, i.e., the classical limit approaching macroscopic systems, instead of $B_J(\xi)$ the more simple Langevin equation $L(\xi)$ can be applied.

$$M(\xi) = M_S B_J(\xi) \tag{3.24}$$

$$B_J(\xi) = \frac{2J+1}{2J}\coth\left(\frac{2J+1}{2J}\xi\right) - \frac{1}{2J}\coth\left(\frac{\xi}{2J}\right), \xi = \frac{\mu B}{k_B T} \tag{3.25}$$

$$L(\xi) = \coth(\xi) - \frac{1}{\xi} \tag{3.26}$$

Weiß introduced a so-called molecular field $H_{mol} = \lambda M$, acting on the magnetic dipoles in addition to the external field, in general exceeding its magnitude by far [92]. Assuming $0 \approx H \ll H_{mol}$, the magnetization is primarily generated by the Weiß molecular field, which is,

in turn, proportional to the magnetization. In the most simple case of $J = 1/2$, an intuitive solution of this problem can be obtained by

$$B_{1/2}(\xi) = \tanh(\xi) \Rightarrow M = M_S \cdot \tanh(\xi) \tag{3.27}$$

$$\overset{H\approx 0}{\Rightarrow} M = M_S \cdot \tanh\left(\frac{\mu\mu_0\lambda M}{k_B T}\right) \tag{3.28}$$

$$\Rightarrow m = \tanh\left(\frac{m}{t}\right), m = \frac{M}{M_S}, t = \frac{k_B T}{M_S \mu\mu_0 \lambda} \tag{3.29}$$

With equation (3.29), one reaches a transcendent equation for the dependence of a reduced magnetization m on a reduced temperature t, whose solution can be easily found numerically, as it is displayed for different values of J in figure 3.6. Theoretical reproductions of the temperature dependent saturation magnetization and/or hyperfine magnetic field used in chapter 4 - 7 are performed according to this model. It is apparent that no solution exists above a critical temperature T_C corresponding to $t = 1$, which is the Curie temperature, marking the transition of ferromagnetic to paramagnetic behavior.

Line intensities

While in the previous paragraph the line positions have been discussed, the line intensities will be illustrated here in detail, as they provide valuable information on magnetic orientation and -structure of the studied material. It can be shown that the line intensities I are proportional to the product of the function $\mathrm{F}_{\Delta l,\Delta m}(\theta)$ characterizing the angular dependence of dipole radiation, and the transition probability from ground state $\langle I_g, m_g|$ to excited state $|I_e, m_e\rangle$ [93].

$$I(\theta) \propto |\langle I_g, m_g|M_{M1}|I_e, m_e\rangle|^2 \cdot F_{\Delta l,\Delta m}(\theta) \tag{3.30}$$

$$F_{1,0}(\theta) = \frac{\sin^2(\theta)}{2} \tag{3.31}$$

$$F_{1,\pm 1}(\theta) = \frac{1 + \cos^2(\theta)}{4} \tag{3.32}$$

Here, M_{M1} is the nuclear M1-dipole operator and θ the angle between the spin direction and the direction of the incident γ-ray. Following the Wigner-Eckart-theorem (3.33), one can find equation (3.34) as a description of relative line intensities.

$$\langle I_g, m_g|M_{M1}|I_e, m_e\rangle \propto \begin{Bmatrix} I_g & \Delta l & I_e \\ m_g & e\Delta m & m_e \end{Bmatrix} \cdot \underbrace{\langle I_g|M_{M1}|I_e\rangle}_{const.} \tag{3.33}$$

$$I(\theta) \propto \begin{Bmatrix} I_g & \Delta l & I_e \\ m_g & e\Delta m & m_e \end{Bmatrix}^2 \cdot F_{\Delta l,\Delta m}(\theta) \tag{3.34}$$

The squares of the (3x2) brackets, introduced by Wigner as '3j-symbols' and corresponding to the Clebsch-Gordan coefficients, yield values of 3/12 ($\Delta m = +1$), 2/12 ($\Delta m = 0$) and 1/12

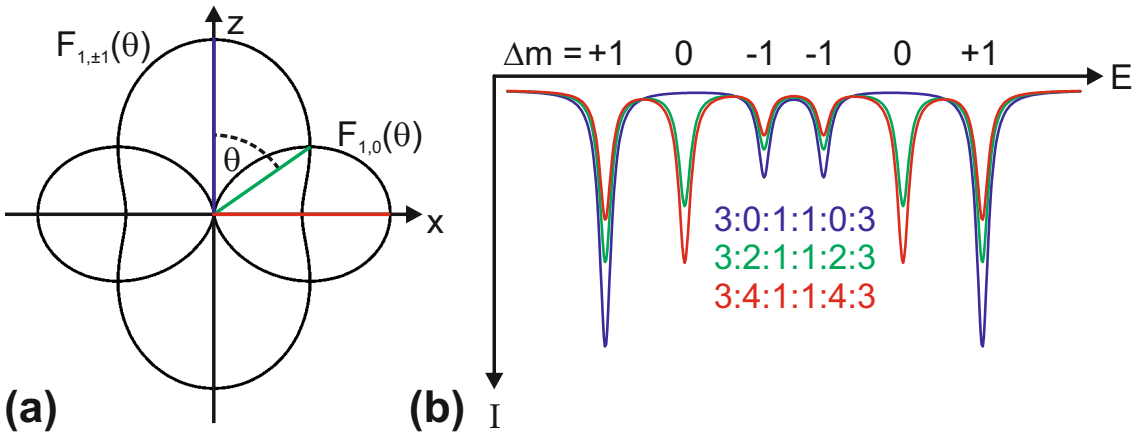

Figure 3.7: (a) Dipole radiation intensity functions $F_{\Delta l,\Delta m}(\theta)$ and schematics of corresponding Mössbauer spectra (b) for angles θ of 0°, 54.7° and 90°.

($\Delta m = -1$). Consequently, a line intensity ratio 3:2:1:1:2:3 is observed if $F_{1,0}(\theta) = F_{1,\pm1}(\theta)$. This is fulfilled for the so-called 'magic angle' of about 54.7°, and is also the average line intensity ratio for a 3D random orientation of spin directions, as is expected, e.g., in powder samples in the absence of external magnetic fields and of crystallographic texture. In general, a relative line intensity ratio of 3:A_{23}:1:1:A_{23}:3 is found, where the line intensity ratio of lines 2 and 3 is defined by

$$A_{23} = \frac{I_2}{I_3} = \frac{4\sin^2(\theta)}{1+\cos^2(\theta)}. \tag{3.35}$$

Obviously, the angle θ between spin- and γ-ray propagation direction can be determined by this method without considering absolute line intensities, allowing the investigation of spin structures. A_{23} approaches 0 in case of Fe spin orientation coaxial to the γ-ray propagation direction, whereby canting angles relative to perfect coaxial alignment can be calculated from values of $A_{23} > 0$. This is demonstrated in the presence of a strong external magnetic field, leading to almost aligned particle magnetic moments in split-coil Mössbauer experiments in chapter 4. $A_{23} \approx 4$, on the other hand, is often observed by Mössbauer spectroscopy in film samples, when the predominant magnetic shape anisotropy gives rise to an in-plane Fe spin orientation. These geometries and resulting spectra are visualized in figure 3.7.

The relative intensities of absorption lines are one of the most significant features in Mössbauer spectroscopy to study spin structures. However, absorption line intensities can be falsified by several effects, based on the geometry of the setup and the characteristics of the absorber, first to mention saturation effects in thick absorbers.

The relevance of this effect is characterized by the so-called 'effective thickness' t_a, where n_a is the density of Mössbauer nuclei, d the sample thickness and σ_0 the maximum resonance absorption cross-section of 2.57 $\cdot 10^{-18}$ cm^2 in case of ^{57}Fe [94]. For $t_a \leq 1$, the sample can

be considered as a thin absorber with Lorentzian lines, while in case of $t_a \gg 1$ self-absorption occurs and a spectral correction by the transmission integral method is required, as illustrated in detail in Ref. [87]. The correction of an experimental spectrum by this approach is described, e.g., in chapter 6.1.

$$t_a = \sigma_0 f d n_a \tag{3.36}$$

The effect can be understood intuitively by replacing a thick sample by several thin ones. Assuming an incident photon intensity constant in energy, reduced intensity at the resonance absorption energy position would already be observed after transmission through the first thin 'layer' of the sample, leading to reduced absorption at these energies in second, third etc. layer of the absorber. Simplified for samples of medium thickness, the effect leads to a reduction in absorption line intensity, which is most pronounced for the absorption lines of highest intensity, resulting in falsified A_{23} ratios.

Spectral modification by Néel relaxation

Superparamagnetism, as it was introduced in chapter 2.3, is the direct result of a nanoparticle's limited volume, leading to fast thermally-induced superspin fluctuation between easy magnetic axes. Mössbauer spectroscopy, being sensitive to magnetic orientation, is known to display changes in its spectral structure dependent on the relaxation rate. However, considerable effort has been made to create theoretical models able to reproduce experimentally recorded spectra and to determine characteristic nanoparticle parameters by doing so.

Some of the first theoretical relaxation models were established by Wickman et al. [95] and Blume and Tjon [96], the latter describing the relaxation process as a dynamic fluctuation with two possible orientations along easy magnetic directions. It has been shown that these two-state models can be applied to fairly reproduce Mössbauer spectra in the region of fast superparamagnetic relaxation. Nevertheless, also at low temperatures, i.e., at slow Néel relaxation, effects on the spectral structure are visible by minor deformations of the absorption lineshape as well as by an apparent decrease in the hyperfine magnetic field. The latter effect was explained in terms of collective magnetic excitations by Mørup [97]. These phenomena correspond to fluctuation of the particle superspin *close* to the easy magnetic direction (figure 2.6), wherefore they cannot be adequately characterized in the limit of a two-state model.

Based on this consideration and in view of the eminent importance of magnetic nanoparticles developing in the 1980s, Jones and Srivastava presented their many-state relaxation model, which can be used to calculate Mössbauer spectra of nanoparticles experiencing slow as well as fast Néel relaxation [72]. As the Jones-Srivastava model is applied in this thesis for that purpose, the basic mechanisms are outlined here:

As a starting point, we assume a magnetic nanoparticle to have the total spin S, leading to 2S+1

possible substates of S_z. Equation (3.37) can be used as a general expression for the lineshape I(ω) of the fluctuating superspin, where $\vec{W}$ describes the equilibrium occupation probabilities. The tensor $\underline{M}$ characterizes the shape of the spectrum, including the line positions ω_i as elements of the diagonal matrix $\underline{\Omega}$, the static linewidth Γ and the transition probabilities. The latter are characterized by the elements P_{ij} of the matrix $\underline{\Pi}$, representing the transition rate from initial state i to the final state j.

$$I(\omega) = 2\Re(\vec{W}\underline{M}^{-1}\vec{1}), \quad \underline{M} = (i\omega + \Gamma)\underline{I} - i\underline{\Omega} - \underline{\Pi} \tag{3.37}$$

The relaxation rates $r_{kk\pm1} = r(S_z, S_z + 1)$ between different adjacent states can then be calculated by equation (3.38) as the square of the transition matrix element, introducing the relaxation parameter R as a measure of the random field assumed to cause the relaxation and determining the absolute rate of relaxation.

$$r(S_z, S_z + 1) = R| < S_z|S_-|S_z + 1 > |^2 = R[S^2 + S - S_z^2 - S_z] \tag{3.38}$$

Using this definition, the elements of the matrix $\underline{M}$ can be expressed as

$$M_{kk} = i(\omega - \omega_k) + \Gamma - M_{kk-1} - M_{kk+1}, \tag{3.39}$$

$$M_{kk\pm1} = -r_{kk\pm1}\exp(\frac{-\Delta E}{k_B T}). \tag{3.40}$$

By calculating the relaxation rate $r_{kk\pm1}$ for S = 1/2, it can be shown that $r_{-1/2\to+1/2} = r_{+1/2\to-1/2} = R$. In this case, the transition matrix element calculated in equation (3.40) corresponds to the expression of the Néel relaxation frequency, with R being equal to the angular attempt frequency in the simple two state model and being inversely proportional to τ_0 for S > 1/2.

As R is expressed, similar to other Mössbauer parameters, like a velocity Δv in units of mm/s, R has to be converted into a representative time τ by usage of equation (3.41). One yields a conversion factor of 1 mm/s $\hat{=}$ 13.7 ns, with τ being inversely proportional to Δv.

$$\Delta E = E_0\frac{\Delta v}{c}, E = \hbar\omega \overbrace{=}^{\tau=\omega^{-1}} \frac{\hbar}{\tau} \Rightarrow \Delta v = \frac{c\hbar}{E_0\tau} \tag{3.41}$$

By analogy with Brownian motion, one finds this general approach to describe the superspin performing a random walk between 2S + 1 sublevels S_z on a spherical surface with a maximum transition rate R and a preferred direction given by the decrease in anisotropy energy upon approaching $S_z = \pm S$. The latter is realized by the exponentially decreasing transition probability for the 'diffusive motion' to a state of higher anisotropy energy $\Delta E = E_i - E_j$ in equation (3.40). However, the computational effort of this method can be impractically large due to the number of required computational steps, increasing for larger spin numbers S. Jones and Srivastava [72] minimized this problem by an efficient solution of the set of appearing differential

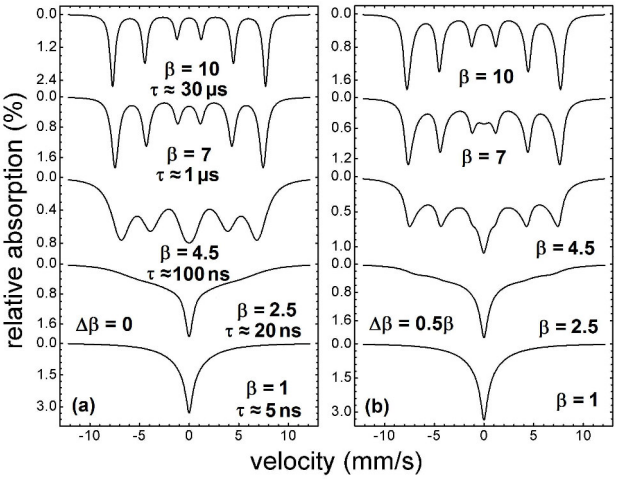

Figure 3.8: Mössbauer relaxation spectra calculated by the many state model for $\beta = E_A/E_{th}$ from 1 - 10, R = 10 mm/s, Γ = 0.6 mm/s and B_{hf} = 50 T for a discrete E_A (a) and an anisotropy distribution of width $\Delta E_A = 0.5 E_A$ (b). Relaxation times τ are calculated from equation (2.6) using an estimation of $\tau_0 \approx 1.37$ ns by converting R to the time scale.

equations. In that way, an application of the many state model with S > 20 can be performed even on home-PC systems, with only small further changes in spectral shape observable upon the usage of even higher spin numbers.

While the many state model is sufficient for the calculation of Néel relaxation in monodisperse particle ensembles, in practical applications one is confronted with the problem of more or less broad distributions in nanoparticle diameters. Due to the exponential dependence between particle volume and relaxation time, it is obvious that there is a huge difference in relaxation times for particles of even slightly different sizes. To consider this, instead of a single spectrum corresponding to a specific value of anisotropy energy E_a, van Lierop and Ryan [98] proposed the application of an anisotropy energy distribution $p(E_A)$, followed by the superposition of subspectra obtained by the many state model for several different values of $E_{A,i}$, weighted by $p(E_{A,i})$. The authors of Ref. [98] applied this approach successfully to frozen ferrofluids with nanoparticle diameters of about 6 nm. In a similar approach, Landers et al. [55] studied relaxation phenomena in nanoparticles affected by magnetic dipole interaction, as described in chapter 4.

Several temperature-dependent calculated spectra are displayed in figure 3.8 to demonstrate the attainable spectral features during the progression of superparamagnetism. Studying figure 3.8, a drawback of the model becomes apparent, since it is not able to explicitly consider effects of quadrupole interaction. This results in the emergence of a central single absorption line in the fast relaxation limit of the calculation, while in most experiments a superparamagnetic doublet is observed. Therefore, to determine an approximation of the correct relaxation state, the spectral area of the calculated single line was matched to that of the experimentally measured superparamagnetic doublet. In the recent years, theoretically valid many state models, including the correct appearance of the superparamagnetic doublet, have been under development by different approaches based on the starting point of the Jones-Srivastava model [99, 100].

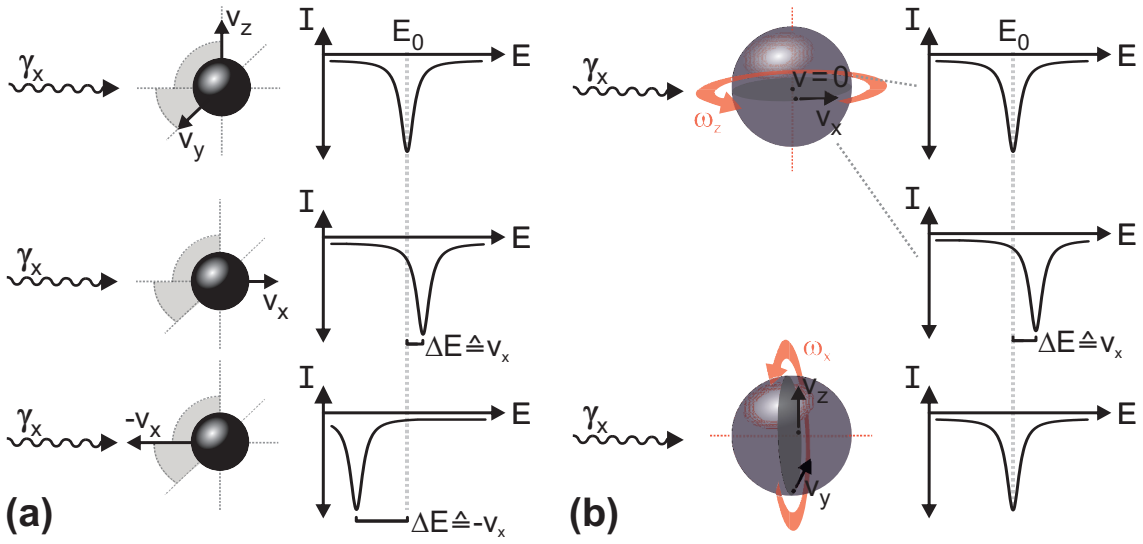

Figure 3.9: Schematic mechanisms leading to line broadening by Brownian movement relative to the γ-ray propagation direction $\vec{\gamma}$: no line shift ΔE by translational motion $v_{y,z} \perp \vec{\gamma}$, ΔE dependent on $|\vec{v}|$ for $v_x \parallel \vec{\gamma}$ (a). Rotational motion results in net movement of iron nuclei perpendicular or parallel to $\vec{\gamma}$, iron nuclei close to the rotation axis display minor line shifts ΔE (b). Combined effects in (a) and (b) result in line broadening of Mössbauer absorption lines.

Effects of Brownian motion

The collapse of the sextet structure to a central superparamagnetic singlet or doublet in case of superspin fluctuation faster than the inverse Larmor frequency ω_{Larmor}, i.e., Néel relaxation, has been discussed above. This effect is directly caused by the averaging of sublevels of different S_z on the Mössbauer time scale, restoring the degeneracy of sublevels otherwise separated by the nuclear Zeeman splitting.

The consequence of Brownian motion on the Mössbauer spectrum of statistically moving particles is fundamentally different. The velocity $\vec{v}$ of each individual particle is accompanied by a shift in resonance energy by the Doppler effect. Possible geometries are visualized in figure 3.9. Only translational movements of an iron atom parallel to the γ-ray propagation direction $\vec{\gamma}$ lead to an energy shift by the linear Doppler effect. Such movements can be realized by translation of the whole particle or rotation about a particle axis, which allows atomic translational movement along $\vec{\gamma}$. Averaging over the whole sample volume and all possible directions of translational and rotational diffusion results in a broadening of the absorption lines instead of a shift in line position.

The first researchers to describe this phenomenon were Singwi and Sjölander in their groundbreaking study on resonant γ-ray absorption under the effect of diffusional motion, which is essential in several research areas up to date [101]. They studied the dependence of the spectral

shape I(ω) on space-time self correlation functions, corresponding to different types of diffusive motion. For pure translational Brownian motion in a liquid, absorption lines were found to remain Lorentzian with an increased total linewidth well described by equation (3.42) and being proportional to the translational diffusion coefficient.

$$\Gamma = \Gamma_{stat} + \frac{2E_0^2}{\hbar c^2} \underbrace{\frac{k_B T}{6\pi\eta R_H}}_{D_t} \tag{3.42}$$

Considering, e.g., the diffusional movement of water molecules with $D_t \approx 10^{-9}$ m^{2}s^{-1}, the line broadening $\Delta\Gamma$ in the range of several hundreds of m/s could not be verified experimentally in Mössbauer spectroscopy, as the absorption line would be indistinguishable from the background intensity already at much lower linewidths. However, for several larger iron-bearing molecules in liquids, as well as for supercooled liquids of increased viscosity, molecular diffusion was studied by means of Mössbauer spectroscopy already in the 1960's and 70's [102, 103, 104, 105]. On the contrary, absorption lines remain measurable for much larger nanoparticles, due to the inverse proportionality of the line broadening on the diameter of the diffusing object, providing information on the particle size or, vice versa, the liquid's viscosity from $\Delta\Gamma$ [106, 107, 108, 109, 110, 111]. Although most of the particles presented in these publications were spherical, more complex particle shapes can be studied, as long as deviations in the anisotropic diffusion coefficients relative to the spherical case are considered, as is illustrated in chapter 6 and explained in more detail in appendix A.7.

Obviously, the particle rotation is not considered in the theory of line broadening presented above. The fact that this process is of minor importance in the mentioned publications on diffusional nanoparticle movement can be intuitively understood by the fact that iron nuclei in a position close to the particle's current rotational axis will create negligible line broadening due to their limited velocity. Accordingly, a relevant Doppler shift in line position only remains for nuclei close to the particle surface, as shown in figure 3.9 (b). However, models for the line broadening by rotational Brownian motion have been established, yielding a potentially non-Lorentzian lineshape [112, 113]. It should be noticed that even for fast particle rotation, Brownian motion cannot be confused with Néel relaxation, as rotational frequencies comparable to the nuclear Larmor frequency would be required to result in a collapse of the spectral sextet structure in case of magnetically ordered particles. Sufficiently fast particle rotation could be created, e.g., by incorporation of ca. 1 nm particles in water, which would result, however, in unmeasurably broad absorption lines, following the above mentioned consideration.

By simplifying the rotational motion to translational movement of the nucleus on a plane perpendicular to the radius vector $\vec{r}$ relative to the center of the particle, Heilmann et al. [112] were able express the rotational line broadening $\Delta\Gamma_{rot}$ by equation (3.43), with Γ_{rot} being

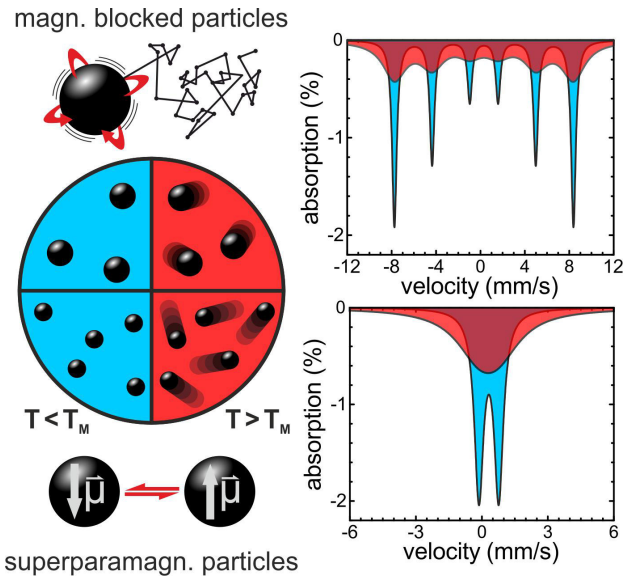

Figure 3.10: Schematic effect of Brownian motion on Mössbauer spectra of ferrofluids of large particles (top), displaying line broadening by Brownian motion, or small particles (bottom) performing relaxation processes, showing also the transition to a superparamagnetic doublet by Néel relaxation. Spectra are shown with and without line broadening below respectively above the fluid's melting point T_M. (Adapted from [111]).

proportional to the rotational diffusion coefficient in accordance to equation 3.42 describing translational motion. Here, θ is the angle between $\vec{r}$ and the incident γ-ray $\vec{\gamma}$. By integration of this expression over the particle volume, the contribution of $\Delta\Gamma_{rot}$ to the total diffusional line broadening can be found to be less than 20%. Therefore, rotational motion is not explicitly included in the evaluation of broadened Mössbauer spectra in chapter 5 - 7, while it can be neglected in hydrogels discussed in chapter 6 due to the particles' strongly elongated shape combined with the containment by the polymer network. Combined effects of line broadening by rotational and translational Brownian movement are independent of the Néel relaxation process. The analysis of particle diffusion and its superspin fluctuation can be performed simultaneously, as the line broadening occurs in the magnetically blocked sextet as well as in the superparamagnetic doublet structure, as displayed schematically in figure 3.10.

$$\Delta\Gamma_{rot} = \frac{E_0^2}{\hbar c^2} \underbrace{\frac{k_B T}{8\pi\eta R_H^3}}_{D_{rot}} \vec{r}^2 \sin(\theta)^2 \tag{3.43}$$

The broadening of absorption lines is for sure the most prominent effect of diffusional motion visible in Mössbauer spectroscopy. Even so, it seems natural to predict that a time dependent change in nuclei position will affect the Lamb-Mössbauer factor, i.e., the spectral area of the spectrum, due to its direct correlation to the mean square displacement $\overline{r^2}$. Indeed, an unexpectedly fast decrease in spectral area was observed in fluid-based systems and is known by now to be a characteristic feature of the diffusion process, similar to the increase in mean square displacement by molecular dynamics [114, 104].

One could be misled by the similarity of the expressions $\overline{x^2}$ in equation (3.7) and $\overline{\Delta x^2}$ in equation (2.11). It has to be mentioned that for the calculation of the Lamb-Mössbauer factor, the mean

square displacement of the vibrating iron nucleus centered at its resting position is considered. In case of Brownian motion it is the diffusional, explicitly time-dependent parameter $\overline{\Delta x^2}$, correlated to the traveled path length. Inserting $\overline{\Delta x^2}$ in equation (3.7) for the Lamb-Mössbauer factor would result in negligibly small line intensity. Instead, an estimation on the decrease in spectral area by Brownian motion ought to be found by analogy to diffusive line broadening. This has been described by J. Jensen, calculating both line broadening and decrease in spectral area A(T) based on the space-time self-correlation function, leading to linearity of $\Delta\Gamma/\Gamma_0$ on $\ln(A(T)/A(0))$ [103], which is noticeable as both parameters are non-linear in temperature. On the contrary, Afanas'ev et al. discussed primarily the rotational diffusion component as the origin of the accelerated decrease in spectral area [113]. To the best of my knowledge, none of these models has been extensively tested. Therefore, while all experimentally determined parameters will be considered for interpretation of ongoing relaxation processes, only the line broadening $\Delta\Gamma$ will be utilized to estimate diffusion parameters and viscosities.

Mössbauer experiments on Brownian motion are not limited to Newtonian fluids. Also, more complex systems of iron-bearing molecules or particles embedded in hydrogels, polymers and liquid crystal solutions were studied to analyze a broad variety of rheological and elastic material parameters [115, 116, 117, 118, 119, 120, 121]. However, the interpretation of such systems requires more sophisticated theoretical models to reflect anisotropic geometries, vibrational contributions and containment effects. To the best of my knowledge, the most appropriate model to describe restricted diffusional movement was established by Nadler et al., where the interaction with the confining 'walls' was treated as a generalized potential [122]. While this approach could be successfully applied to ultrafine nanoparticles [123, 124], it seems inadequate for the ferrohydrogel samples discussed in chapter 6, due to the highly anisotropic character of the embedded hematite nanospindles and their length of about 400 nm, wherefore a qualitative interpretation of Mössbauer data will be presented instead [125].

Experimental setups and Mössbauer techniques

When referring to Mössbauer spectroscopy in the literature, one often means the most frequently applied transmission geometry, as displayed schematically in figure 3.11 and discussed in this paragraph in detail. γ-quanta are emitted by a radioactive source consisting of ^{57}Co atoms embedded in a matrix material, which is Rhodium in the present results. The source is mounted on a driving unit, moving periodically back and forth with a maximum velocity v_{max}, which usually is in the range of some mm/s. By this method the discrete photon energy from the source is tuned via the Doppler effect, as described by equation (3.44). This provides the ability to 'scan' the energy regime of about 1μev around the resonance position to study shifts in the line positions originating from interaction of the ^{57}Fe nucleus with its local surroundings.

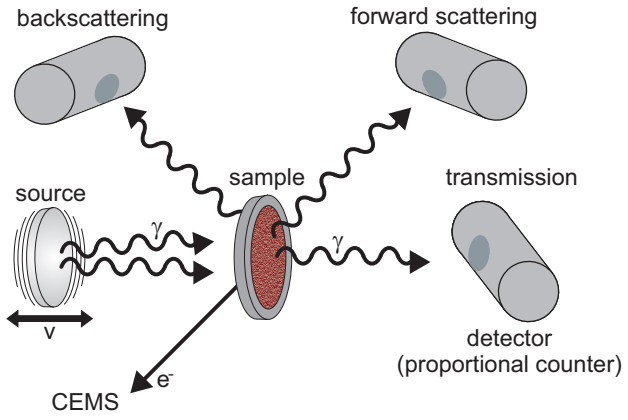

Figure 3.11: Scheme of common Mössbauer geometries: transmission, forward- and backscattering and conversion electron Mössbauer spectroscopy (CEMS)

Different velocity functions v(t) can be applied. A triangular velocity function, often referred as 'constant acceleration mode', results in the same number of data points in each velocity region, whereby spectra from this method are easiest to analyze. A sinusoidal velocity function exhibits no discontinuities in driving unit acceleration, leading to smaller deviations between intended and actual motion of the Mössbauer source, but also to the measurement of a high number of data points in the wings of the spectrum.

$$E(v) = E_0 + \frac{E_0 \cdot v}{c} \Rightarrow E(10\ \text{mm/s}) \approx E_0 + 480\ \text{neV} \tag{3.44}$$

In transmission geometry, a detector, e.g., a proportional counter, registers the rate of γ-quanta transmitted through the sample. This signal at time t is then correlated to the velocity of the driving unit v(t), leading to the characteristic Mössbauer spectrum by plotting the detected γ-ray intensity versus velocity v. Scintillator or semiconductor devices can be used as detectors, depending on the parameters of the individual experiments, i.e., the energy the γ-quanta, the sample geometry, the required time resolution etc.

Further Mössbauer setups include forward- and backscattering geometries [126, 127], Mössbauer spectroscopy of conversion electrons (CEMS), and more sophisticated, but less frequently used techniques like synchrotron experiments [128, 129, 130], each providing unique advantages. CEMS, e.g., is often applied to thin film samples due its surface sensitivity and its ability for depth-selective (DCEMS) studies in more complex setups [131, 132, 133]. In case of ^{57}Fe, most of the conversion electrons exhibit an energy of about 7.3 keV, leading to a penetration depth of about 100 nm [134]. Mössbauer backscattering, on the other hand, has the benefit of being more independent regarding the sample geometry. Therefore, it can be used to study surfaces without the requirement of external sample preparation, as demonstrated by the MIMOS II setup during the Mars expedition [135, 136].

Apart from some test spectra, all Mössbauer results discussed in this thesis were obtained in transmission geometry and constant acceleration mode. However, to study individual sample characteristics, several modified transmission setups were employed:

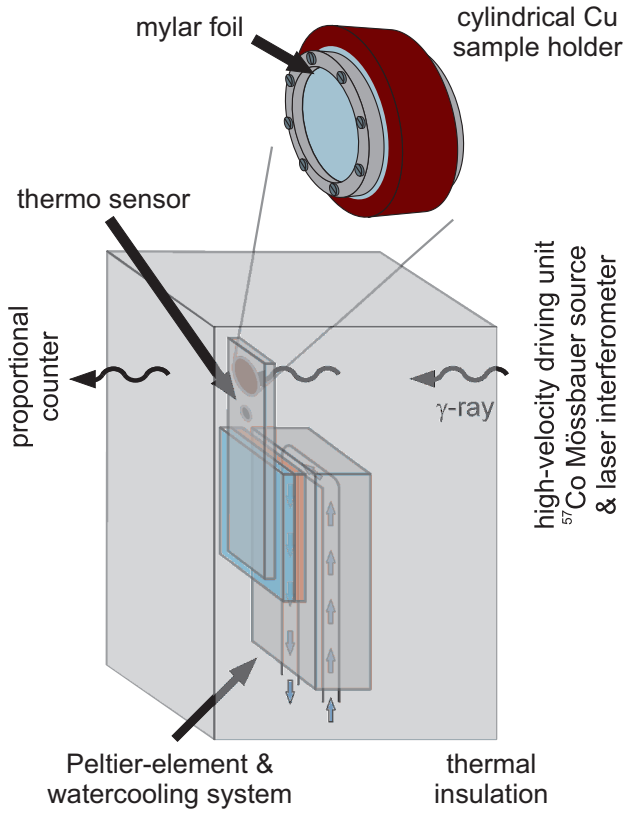

Figure 3.12: Schematic Mössbauer setup. A Peltier heating/cooling element is integrated in the sample holder, to provide precise temperature control up to 60 K above/below room temperature. The liquid/gel sample is sealed tightly in a copper cylinder capped with mylar foil. The sample temperature is monitored by a PT100 thermo sensor mounted near the sample position. Adapted from [125].

- To examine relaxation effects far below ambient temperature, Mössbauer spectra at 4.2 K - 300 K were obtained using liquid nitrogen/helium bath cryostats. To get further insight in spin structure and orientational behavior of magnetic nanoparticles, a l-He cryostat-setup was used, containing superconducting coils in Helmholtz (split-coil) geometry, providing magnetic fields up to 5 T.

- As the main interest in this thesis includes the analysis of Brownian dynamics, detailed studies at tunable temperature close to 300 K are inevitable. For that purpose two new sample holders were designed by Dipl.-Ing. U. von Hörsten, which are shown schematically in figure 3.12. Since standard powder sample holders could not be used in case of water-based ferrohydrogels or even ferrofluids, the actual samples were sealed watertightly within a copper cylinder capped with Mylar foil, to ensure good thermal conduction. First experiments were conducted using aluminum cylinders capped with Al foil, instead of Mylar, resulting in small additional central features in the spectrum caused by minor amounts of iron in the Al foil. This cylindrical sample holder is mounted in direct proximity to a PT100 temperature sensor on top of a Peltier element, reaching temperatures down to about 240 K. For even lower temperatures, a double stacked Peltier-setup was used. The hot back side of the Peltier element is connected to a water-cooled metal block attached to the actual mounting station. The whole setup is embedded in a styrofoam box for thermal insulation, which is transparent for γ-rays. To prevent the condensation of water

on the cooled surfaces of the sample holder, the styrofoam box is in turn sealed in plastic foil. Although the setup was optimized for precise temperature control, small deviations between measured and actual sample temperature have to be expected, since the temperature is not directly measured *in* the composite sample, but only in its proximity. To estimate the error in temperature control, the signal of the PT100 temperature sensor was compared to the temperature *within* the copper cylinder for several samples, measuring the thermo-voltage between these two positions using a NiCr/Ni/NiCr thermocouple. This was, however, not feasible during the actual Mössbauer experiment. By this method, the deviation of both signals was determined to be linear in temperature, reaching a value of about 3 - 7 K at the lowest attainable temperature of about 225 K, depending on the sample volume and the used Peltier sample holder. Subsequently, this offset function was used to calibrate the temperature measurement. Calibration measurements performed are illustrated in more detail in section A.2 of the appendix.

- A similar setup was utilized to study the behavior of polymer compound samples in proximity to and above the melting region, discussed in chapter 7. The above mentioned copper cylinder, holding the sample material, was mounted in proximity to a metal box, containing a quartz-halogen lamp. Temperatures up to about 400 K were reached using this setup. Temperature calibration was performed as explained for the Peltier element sample holder, yielding a temperature deviation of about 3 K at 380 K.

- The quartz-halogen lamp setup as well as the Peltier sample holder were designed to fit in an available 1.5 T electromagnet, posing an essential advantage. The combination of a tunable magnetic field and precise temperature control permits a detailed analysis of each sample's dynamic as well as static magnetic orientational behavior, especially interesting in case of anisotropic compound samples. Measurements of the relative absorption line intensity in section 6.5, revealing the orientational mobility of magnetic moments in hematite nanospindle ferrohydrogels, may serve as an example for Mössbauer spectra recorded at different magnetic fields and temperatures.

3.2 SQUID-magnetometry and AC-susceptometry

While Mössbauer spectroscopy is an element-specific technique sensitive to hyperfine interactions of the ^{57}Fe nucleus, standard magnetometry primarily measures a system's net magnetic moment. Doing so, it can detect changes in overall magnetic orientation far too small to be visible by, e.g., a change in Mössbauer line intensity.

Magnetometry measurements presented in chapters 4 - 7 were performed using a Quantum Design MPMS-5S SQUID-magnetometer (Superconducting QUantum Interference Device), capable of a wide spectrum of individual protocols in the temperature range of 2 - 400 K and

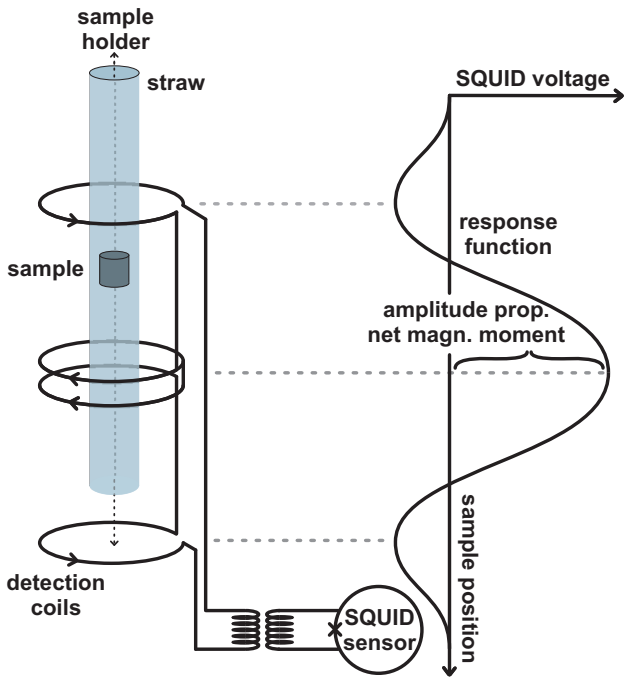

Figure 3.13: Schematic SQUID setup and detection mechanism. Vertical passing of the magnetic sample, mounted at the end of the sample holder, through the detection coils results in an induced voltage signal, which is transferred to the SQUID sensor. The characteristic shape of the response function, from which the net magnetic sample moment is extracted, corresponds to the detection-coil configuration geometry.

magnetic fields up to 5 T and equipped with an integrated option for magnetic AC susceptibility measurements. A SQUID is sensitive to minimal changes in magnetic flux. The SQUID sensor includes a superconductive ring, partitioned by one (AC-SQUID) or two (DC-SQUID) Josephson-junctions of normal-conducting material, thin enough to allow tunneling of Cooper pairs. Due to the quantization of magnetic flux through a ring of superconductive material, an increase in flux directly results in an increase of induced compensation current in steps corresponding to one flux quantum. By connecting both sides of the ring, applying a current and measuring the voltage drop of the circuit, one can determine the compensation current and, therefore, the magnetic flux. In the MPMS-5S, a sample of magnetic material is moved through a coil-set (second order gradiometer) as shown in figure 3.12, resulting in a voltage function of characteristic shape, whose amplitude is determined as it is proportional to the sample's net magnetic moment.

One of the most basic magnetic characterization techniques is the measurement of the field-dependent magnetization M(H), applied before to gain further insight in spin canting effects of particles studied in chapter 4 by means of in-field Mössbauer spectroscopy [26, 137]. To study dynamic relaxation phenomena this method is, however, less suitable, although in some literature reports the application of Sharrock's law on temperature dependent coercivities is reported for estimations of the blocking temperature T_B or the effective magnetic anisotropy K_{eff} of superparamagnetic nanoparticles [138, 139, 140]. Also, to study switching-field distributions closely correlated to anisotropy energies, first-order-reversal-curves of magnetization (FORCs) have been analyzed more regularly in recent years [141]. Instead, to obtain more direct information on relaxation times, measurements of magnetization or magnetic susceptibility under

variation of temperature or frequency are considered more versatile instruments and applied more frequently in literature.

Common protocols for temperature dependent magnetization M(T)

One of the most common methods for the characterization of superparamagnetism in general is the measurement of zero-field cooled (ZFC) and field cooled (FC) magnetization $m_{ZFC,FC}$. For those, the magnetization is measured in an applied magnetic field during warm up, usually small compared to the saturation field and in the range of 10 - 100 Oe, after cooling the sample down either without an applied magnetic field (ZFC) or with the warm-up field already applied (FC).

At sufficiently high temperature, fast fluctuation of the magnetic particle moment between different easy magnetic directions occurs. By cooling the sample in a small magnetic field, net magnetic particle moments align preferentially along easy magnetic axes close to the magnetic field direction, resulting in a relatively high net magnetization. In case of the ZFC magnetization, superspins are aligned randomly relative to field direction, wherefore m_{ZFC} originates from a minimum orientation of particle moments *within* their current anisotropy energy minimum. By reaching the blocking temperature, moments again are able to fluctuate freely, which means that their relaxation time is small compared to the characteristic time window of the detection process, whereby m_{ZFC} and m_{FC} result in the same magnetization curve given by the low field approximation (3.45) of the Langevin equation (3.26).

$$M^{sup}(T) = M_S(T) \cdot L(T) \overbrace{=}^{H \approx 0} \frac{\mu_0 H M_S^2(T) V_{NP}}{3 k_B T} \tag{3.45}$$

One observes a splitting between FC and ZFC magnetizations as illustrated in figure 3.14. Both functions coincide close to the blocking temperature T_B, which is often identified with the maximum in ZFC magnetization T_{max}. The majority of experimentally studied nanoparticle samples cannot, however, be treated in this simple scheme of monodisperse particles with a specific blocking temperature T_B. Considering effects of polydispersity, the characteristic shape of $m_{ZFC,FC}$ can experience considerable broadening depending on the standard deviation of the particle size distribution. Additionally, as elucidated by Madsen et al., the dominating contribution to the net magnetization of the larger particles within the ensemble leads to a shift of the average T_B to lower temperature relative to the maximum T_{max} in ZFC magnetization [142, 143]. Furthermore, m_{ZFC} and m_{FC} do not coincide before exceeding the highest blocking temperature of the nanoparticle ensemble, corresponding to the particles of maximum volume, denominated as the irreversibility temperature.

To describe the FC-ZFC magnetization of a polydisperse nanoparticle ensemble theoretically, a critical blocking volume $V_B(T)$ can be defined by analogy to the blocking temperature $T_B(V)$, as

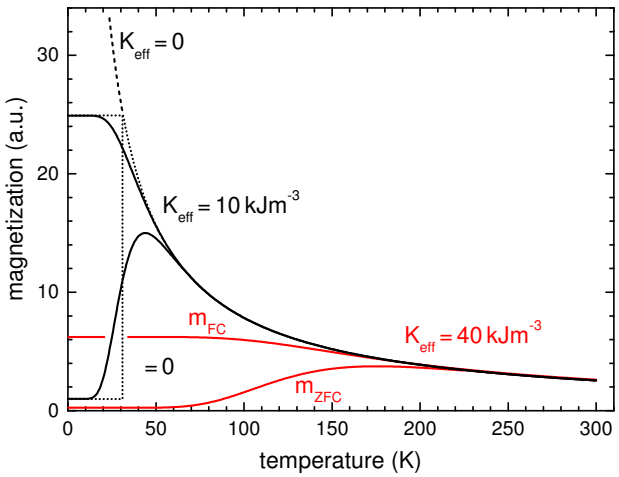

Figure 3.14: ZFC- and FC-magnetization of nanoparticles with 12 nm average diameter and log-normal volume distribution with $\sigma = 0.3$, calculated from equations (3.47) - (3.48) assuming effective anisotropy constants K_{eff} of 40 kJm^{-3} (red), 10 kJm^{-3} (black) and 0 kJm^{-3} (dashed). Dotted lines represent the theoretical trend for monodisperse particles.

given by equation (2.7). As illustrated by Respaud et al. in detail, the magnetic susceptibility in the ZFC respectively FC blocked state can be described by [48, 144, 145]

$$\chi^{bl}_{ZFC}(T) = \frac{M_S^2(T)\mu_0}{3K_{eff}}, \chi^{bl}_{FC}(T) = \frac{M_S^2(T)\Phi\mu_0}{3K_{eff}}. \tag{3.46}$$

Here, Φ is again a parameter characterizing the time window of the applied experimental method. The total magnetization of the ensemble can then be represented by the sum of superparamagnetic and magnetically blocked particles, where the limit of the particle volume integral is the blocking volume $V_B(T)$ normalized by the first moment of the volume distribution $p_V(V)$, which is the average particle volume $\overline{V}$.

$$M_{ZFC}(T) = \frac{H}{\overline{V}} \int_0^{V_B(T)} V p_V(V) \cdot \underbrace{\frac{M_S^2(T)\mu_0 V}{3k_B T}}_{\chi^{sup}(T)} dV + \frac{H}{\overline{V}} \int_{V_B(T)}^{\infty} V p_V(V) \cdot \underbrace{\frac{M_S^2(T)\mu_0}{3K_{eff}}}_{\chi^{bl}_{ZFC}(T)} dV \tag{3.47}$$

$$M_{FC}(T) = \frac{H}{\overline{V}} \int_0^{V_B(T)} V p_V(V) \cdot \underbrace{\frac{M_S^2(T)\mu_0 V}{3k_B T}}_{\chi^{sup}(T)} dV + \frac{H}{\overline{V}} \int_{V_B(T)}^{\infty} V p_V(V) \cdot \underbrace{\frac{\Phi M_S^2(T)\mu_0}{3K_{eff}}}_{\chi^{bl}_{FC}(T)} dV \tag{3.48}$$

As visible in figure 3.14, the splitting between FC and ZFC magnetization is limited to the blocked regime with an abrupt end at the blocking temperature. Therefore it seems natural that the distribution of blocking temperatures $p(T_B)$, closely related to the distribution of anisotropy energies $p(E_A)$, can be inferred from the splitting in magnetization curves $m_{FC} - m_{ZFC}$, as was reported by Hansen et al. [146]. Alternatively, the temperature dependent decay in magnetization upon increasing temperature after field cooling and switching off the field results in a curve comparable to $m_{FC} - m_{ZFC}$. Sometimes, this protocol is denominated as thermoremanent magnetization, whereas instead this name is used to describe the *time* dependent magnetization decay hereafter. This approach stands out by its straightforward access to blocking temperature T_B and magnetic anisotropy energy E_A:

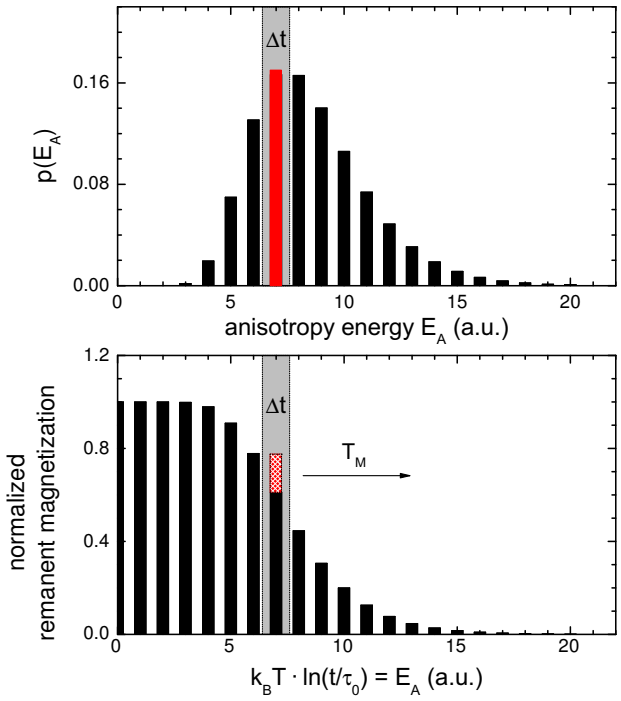

Figure 3.15: Log-normal distribution $p(E_A)$ of anisotropy energies (a) and corresponding universal curve of thermoremanent magnetization (b). Only a small section of anisotropy energies is covered at a certain measurement temperature T_M within a given time interval (marked grey), allowing one to 'scan' the distribution $p(E_A)$ (red), being proportional to the decrease in thermoremanent magnetization.

Measurements of the thermoremanent magnetization (TRM) represent an alternative method to gain comparable information to ZFC-FC magnetization experiments. Unlike the aforementioned techniques, they also allow an approximation of τ_0 independent of further reference measurements [147]. Starting above the highest blocking temperatures in the completely superparamagnetic state of fast superspin fluctuation, the sample is cooled down to a temperature T_M in an applied magnetic field H comparable in amplitude to FC magnetization fields. After waiting a short amount of time to stabilize the sample temperature and to allow the system to reach an equilibrium state, the field is switched off and the time dependent decay in magnetization is recorded. Common measurement times using SQUID magnetometry are t $\approx 10^1 - 10^4$ s. Using fluxgate sensors with considerably shorter measurement time instead, faster relaxation processes with $\tau \gtrsim 1$ ms can be studied, too [148].

One main advantage of this technique can be visualized by studying equation (2.6). Due to the exponential dependence on temperature, an increase in T results in a dramatic decrease in relaxation time τ and, therefore, in a distinct drop in remanent magnetization. On the other hand, the drop in remanent magnetization per second is comparatively small at a constant temperature, which explains the high precision of the TRM method. By measuring $m_{TRM}(t)$ at several different temperatures close to the blocking temperature one can 'scan' a whole set of relaxation times as illustrated in figure 3.15, which allows one to determine anisotropy energies as well as τ_0.

The initial thermoremanent magnetization originates from a (small) preference in magnetic particle moment orientation along easy magnetic axes parallel to the external magnetic field,

which then decreases by randomly directed fluctuations after a time τ. Accordingly, it seems reasonable to assume particles i of anisotropy energy $E_{A,i}$ to display an exponential decrease in magnetization of the form

$$M_i(t) = M_i(0) \cdot \exp(-\frac{t}{\tau_i}) \tag{3.49}$$

As discussed by Battle et al., the thermoremanent magnetization of a nanoparticle ensemble then follows equation (3.50), which can be simplified considering the relaxation times of differently sized particles [1]: At a set measurement temperature T_M and in the studied time interval Δt, e.g., 10 - 1000 s, only particles of a sharply defined anisotropy energy interval will display relaxation visible by a decrease in magnetization, as is labeled in figure 3.15 by the grey region in E_A. Due to the exponential dependence in the relaxation time τ on the anisotropy energy, smaller particles already will be completely in zero-field equilibrium without net magnetization, when the measurement of M(t) is started, while relaxation effects of larger particles are strongly limited by the same reason. Therefore, the decrease in thermoremanent magnetization is directly proportional to the anisotropy energy distribution $p(E_A)$ at the current position $E_{A,i}$, which is used in the aforementioned method intuitively studying $m_{FC} - m_{ZFC}$.

$$M(t) = M(0) \int_0^\infty p(E_A) \cdot \exp(-\frac{t}{\tau(E_A)}) dE_A \tag{3.50}$$

$$\Rightarrow p(E_A) \propto -\frac{\partial M_{TRM}}{\partial(k_B T \ln(t/\tau_0))} \tag{3.51}$$

The most common display of thermoremanent results is to plot m_{TRM} versus $k_B T ln(t/\tau_0)$, corresponding to the anisotropy energy. As magnetization curves measured at different temperatures $T_{M,i}$ will not form a continuous so-called 'master' or 'universal' magnetization curve [149], if a wrong value of the relaxation prefactor τ_0 is used, this scaling of the x-axis allows an estimation of τ_0, which is relatively precise [55, 147]. Further details on applications of TRM for studies of magnetic materials in general, single-domain nanoparticles or paleomagnetism, can be found, e.g., in textbooks of Skomski [150] or Dunlop and Özdemir [19]

AC-susceptometry

AC-susceptometry is an often used technique to analyze dynamical magnetic phenomena and phase transitions. Usually, very small magnetic AC fields are applied, to study the magnetic susceptibility in the low-field approximation, i.e., the quasi-linear section of the Langevin equation. However, some more specialized methods as, e.g., magnetic particle imaging (MPI) utilize the non-linear response to higher magnetic fields to study magnetic dynamics by variation in the amplitude of the higher harmonics of the response function [151, 152].

The dependence of the complex magnetic susceptibility χ on the angular frequency ω_{AC} of the magnetic AC field can be determined according to equation (3.52) in Debye's theory, where χ_0

is the static magnetic susceptibility, N/V the particle density and τ is the relaxation time of a dynamical relaxation process, which can be of Néel, Brownian or other origin [153]. For the most applications, it has been proven to be helpful to separate this expression in contributions of the real component χ' and the imaginary component χ'' of magnetic susceptibility.

$$\chi(\omega_{AC}) = \frac{\chi_0}{1 - i\omega_{AC}\tau}, \chi_0 = \frac{N}{V}\frac{\mu_{NP}^2}{3\mu_0 k_B T} \tag{3.52}$$

$$\chi(\omega_{AC}) = \underbrace{\frac{\chi_0}{1 + \omega_{AC}^2\tau^2}}_{\chi'} - i\underbrace{\frac{\chi_0\omega_{AC}\tau}{1 + \omega_{AC}^2\tau^2}}_{\chi''} \tag{3.53}$$

Equations (3.52) - (3.53) can be applied assuming that the studied nanoparticles possess a specific relaxation time. The latter can be calculated by equation (2.6) or (2.17) in case of Néel relaxation- respectively Brownian rotational times τ_{Neel} and τ_{rot}, or can be approximated by the effective total relaxation time τ_{eff} given by equation (2.20), if both mechanism are relevant. A typical frequency dependent susceptibility signal is displayed in figure 3.16 (a), where fast Néel relaxation and Brownian rotation in the intermediate frequency range are assumed. In principal, three regions (I - III) of different behavior can be identified. At very low angular frequencies $\omega_{AC} = \tau_{AC}^{-1} \ll \tau_{rot}^{-1}$, the particles are considered superparamagnetic (region I), as they can react to very slow changes in magnetic field direction quasi instantaneously, resulting in the saturation value χ_0 of the real component of magnetic susceptibility χ'. At intermediate frequencies, variations in the field direction are too fast to be followed by the rotational Brownian process. Accordingly, the amplitude of χ' in this region is decreased, being limited to contributions of Néel relaxation (region II). In the ultrashort time scale $\tau_{AC} \ll \tau_{Neel}$, neither relaxation mechanism can provide sufficiently fast superspin reorientation, resulting in zero amplitude of the real component of magnetic susceptibility. In this case the particles can be considered magnetically blocked (region III). The transition from one region to the other, i.e., the crossing of τ_{Neel} and τ_{rot}, is marked by a sharp peak in the imaginary magnetic susceptibility χ'', disregarding effects of polydispersity. Therefore, in some publications the analysis of the frequency dependent susceptibility is limited to the function $\chi''(\omega_{AC})$, which can be interpreted more straightforwardly.

As the equations presented above may work to model AC susceptibilities of highly monodisperse particles, they should be improved if distributions $p(D_C, D_{Hyd})$ in core diameters D_C and hydrodynamic diameters D_{Hyd} are taken into account. The distinct variation, especially of the Néel relaxation time, has been discussed in section 2.4 in detail and was illustrated in figure 2.8. To consider size distributions, equation (3.52) can, e.g., be extended to the following expression (3.54), by integrating over D_C by analogy to Ref. [154]. Reasonable approximations, depending on the individual sample material, e.g., assuming a constant core radius or shell thickness, can be helpful to limit the computational effort of these calculations.

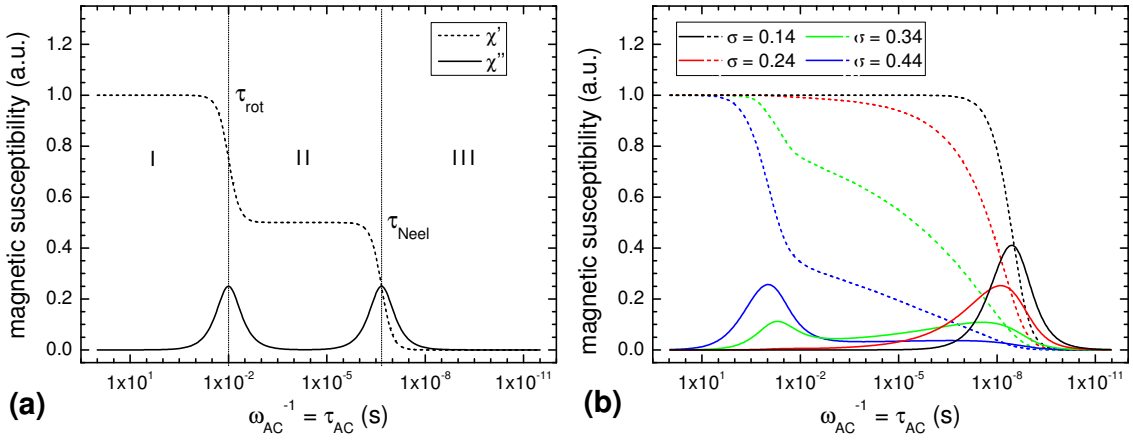

Figure 3.16: Schematic frequency dependence of real (dashed line) and imaginary component (solid line) of AC-susceptibility assuming two discrete relaxation times τ_{rot} and τ_{Neel} of rotational Brownian motion and Néel relaxation, respectively (a), and the calculated AC-susceptibility signal of a log-normal size distribution of bare particles with average diameter D_C = 10 nm, and standard deviation σ = 0.14 - 0.44. Additional parameters were the temperature T = 300 K, dynamic viscosity η = 1 Pas, relaxation prefactor τ_0 = 100 ps and the effective anisotropy energy density K_{eff} = 10 kJ/m^3.

$$\chi(\omega_{AC}) = \frac{\chi_0}{\overline{D_C^6}} \int_{D_C=0}^{\infty} \frac{D_C^6 P(D_C)}{1 - i\omega_{AC}\tau_{eff}(D_C)} dD_C \tag{3.54}$$

As magnetic nanoparticles almost always display one predominant relaxation process, resulting from of the very limited particle-size interval of comparable Brownian and Néel relaxation times, the effort of using distributions in both parameters and the effective relaxation time τ_{eff} to consider both relaxation mechanisms is seldomly made. However, some exemplary calculations on experimental AC-susceptibility data have been reported in Ref. [154, 74]. The effect of particle polydispersity on the AC-susceptibility signal calculated from equation (3.54) is displayed in figure 3.16 (b) for log-normal particle size distributions of average diameter D_C = 10 nm and standard deviations σ = 0.14 - 0.44. There, Néel relaxation behavior is observed for a sharp size distribution $\sigma < 0.2$, while for an increasing standard deviation larger particles in the ensemble are weighted much stronger due to their dominant volume, i.e., total magnetic moment. In that case, intermediate relaxation times are found for a small fraction of particles, and the biggest particles display primarily Brownian rotation. As this effect is clearly visible for standard deviations $\sigma \approx 0.3$, which are still considered as monodisperse, more complex models including effects of the distribution in particle core- and hydrodynamic diameter should be considered for modeling the majority of commercially available nanoparticles.

4 Superspin dynamics of capped nanoparticles: Influence of dipolar interaction on Néel relaxation

Before presenting more advanced methods to analyze Néel and Brownian relaxation mechanisms simultaneously, this chapter will start by giving an insight in Néel relaxation of capped iron oxide nanoparticles. The basic approach here is the synthesis and investigation of magnetite nanoparticles equal in core diameter and capped by silica and/or IGEPAL ligands. By correct choice of the capping material and shell thickness one controls the strength of interparticle magnetic dipole interaction as well as the presence or absence of direct surface contact and, therefore, of exchange interaction between particles. Static as well as dynamic magnetic properties of the particle ensembles showing different magnetic dipole interaction are studied and then compared with Néel relaxation in fluids and complex media in the following chapters.

A basic evaluation of the magnetic properties of this type of capped iron oxide nanoparticles as well as of their oxidation dynamics has already been carried out, supported by Dr. Frank Stromberg, in my preceding diploma thesis 'Mössbauerspektroskopie-Untersuchungen an Fe-Oxid Nanopartikeln' [26]. Main results of the diploma thesis, relevant for the further study of relaxation phenomena, will be outlined briefly within section 4.1. However, as new publications clearly prove the advantages of the extended many-state relaxation model described in section 3.1 [98, 55], selected Mössbauer spectra from Ref. [26] are re-evaluated below using the more adequate model including particle size-distribution effects.

4.1 Particle synthesis and characterization

Iron oxide nanoparticles, as described below, were synthesized by Dr. Masih Darbandi by application of the microemulsion method. To do so, solutions of iron salts $FeCl_2$ and $FeCl_3$ in water, serving as iron precursor materials, are mixed with cyclohexane (C_6H_{12}) and the organic ligands IGEPAL® CO-520. As water barely dissolves in cyclohexane, it will form droplets

Sample	Capping	D_{TEM} (nm)	σ_{TEM} (nm)	D_{XRD} (nm)
M1	bare	6.3±0.1	1.2±0.1	6.2±0.6
M2	IGEPAL	6.3±0.1	0.8±0.1	6.6±0.7
M3	3nm SiO_2 + IGEPAL	6.4±0.1	0.9±0.1	6.5±0.7
M4	6nm SiO_2 + IGEPAL	6.3±0.1	1.0±0.1	6.2±0.6

Table 4.1: Capping method and thickness, and average core diameters D_{TEM} and D_{XRD} and standard deviation of core diameter distribution σ_{TEM} as determined by TEM and XRD [55].

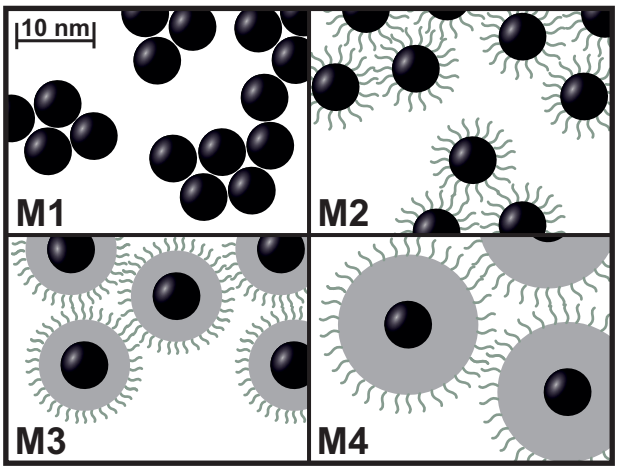

Figure 4.1: Schematic structure of the studied capped iron oxide nanoparticle ensembles M1 - M4, ranging in absolute (hydrodynamic) diameter from 6.3 nm for bare particles in M1 to about 19 nm in double-capped particles in M4.

instantaneously within the mixture due to the peculiar structure of the IGEPAL ligands. The latter exhibit amphiphilic properties, wherefore one end of the IGEPAL molecule will turn to the water droplet and the other to the cyclohexane phase. By this, the ligands form a monomolecular barrier as shown in figure 4.2 (b), which directly implies that the size of the water droplets is determined by the total area of this barrier, i.e., the amount of IGEPAL in the solution volume. By choosing relatively high IGEPAL concentrations, the diameter of the droplets is in the range of several ten nanometers, each serving as nanoreactor for the synthesis of one individual nanoparticle.

To start the formation of nanoparticles from the precursor, ammonium solution is added. For a fixed concentration of iron precursor material, the size of the forming nanoparticles depends on the volume of the nanoreactor, whereby it can be precisely tuned by the number of added IGEPAL molecules. This has been demonstrated by the synthesis of iron oxide nanoparticles of 3 - 9 nm in diameter [155]. Additionally, the size of the particles is influenced by temperature and stirring rate during preparation.

Nanoparticles studied in this chapter are of 6.3 nm in diameter. For sample M1, which is used as a reference with maximum interparticle interaction, particles were precipitated by adding acetone and remaining IGEPAL was removed subsequently, allowing direct surface contact of the nanoparticles, by washing steps using butanol, propanol and ethanol. Sample M2 was redispersed in 3 vol% IGEPAL solution; the thin IGEPAL layer on top of the particle surface may serve well against direct contact and prevent exchange interaction effects. On the other hand, the coating layer is thin enough to create minimum particle separation corresponding to strong magnetic dipole interaction. During the synthesis of samples M3 and M4 different amounts of TEOS (tetraethylorthosilicate) were added, leading to the formation of a silica shell of 3 respectively 6 nm shell thickness in addition to the IGEPAL layer, increasing the minimum core-to-core distance and reducing potential magnetic dipole interaction dramatically. The structure of the four nanoparticle ensembles M1 - M4 is illustrated comparatively in figure 4.1.

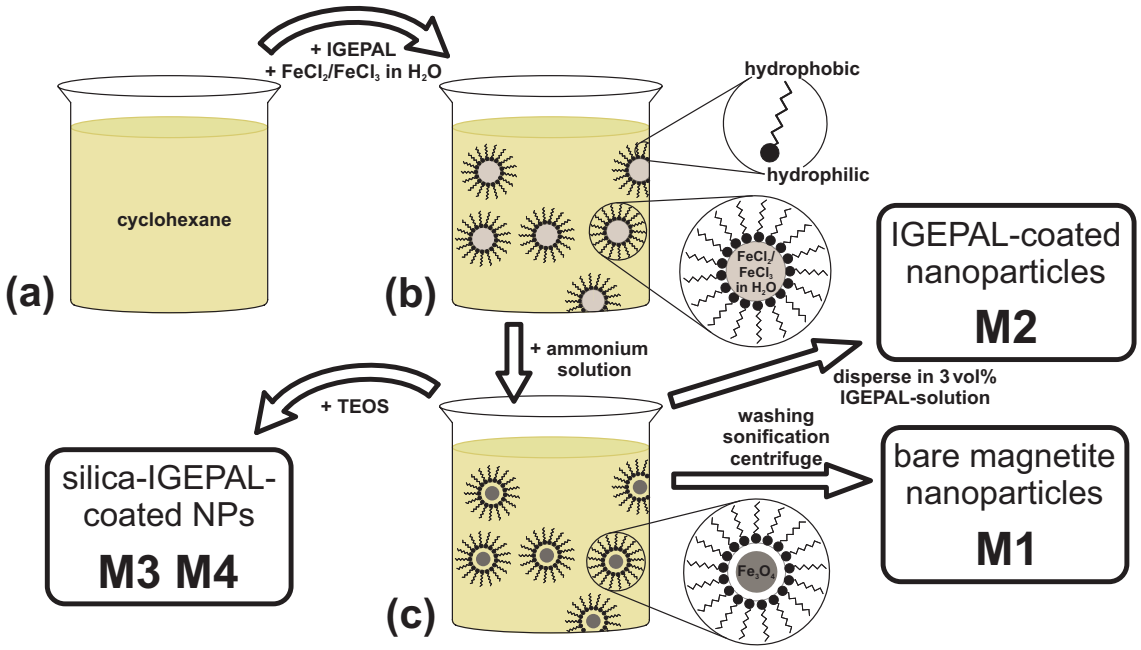

Figure 4.2: Schematic stepwise synthesis procedure of samples M1 - M4 of capped iron oxide nanoparticles.

After preparation, the samples were dried to gain nanoparticle powder.

A meaningful discussion of the dependence of magnetic relaxation phenomena on the strength of interparticle interaction can only be performed, if it can be ensured that the particle sets differ *only* in their effective capping thickness, i.e., their minimum separation, while sharing the same shape, core diameter and structural order. Equal nanoparticle diameters could be verified by transmission electron microscopy (TEM) images, and equal crystal structure could be confirmed by X-ray diffraction (XRD), as shown in figure 4.3. Important sample parameters like capping thickness, capping material and core diameter are listed in table 4.1.

TEM images of the particles show a roughly spherical shape, similar for all samples with some minor irregularities. The silica shell thicknesses of 3 nm (M3) and 6 nm (M4) could be determined directly from TEM images of samples M3 and M4, as the silica material displays a clear difference in TEM contrast compared to the iron oxide particle core. As individual IGEPAL molecules cannot be observed by TEM, their location either on top of the silica shell or at an interface position between particle core and silica material could not be verified, although the letter seems unlikely. However, it should be considered that an additional but invisible IGEPAL layer would increase the effective interparticle distance slightly, which could modify the interaction energy to a minor degree. As the same applies to sample M2 without silica shell, the 'shell thickness' of the IGEPAL surface layer was estimated from the minimum interparticle separation visible in TEM image 4.3 (b) to be about 1.4 nm.

Distributions in core and total 'hydrodynamic' particle diameter $p(R_C)$ and $p(R_{Hyd})$ were de-

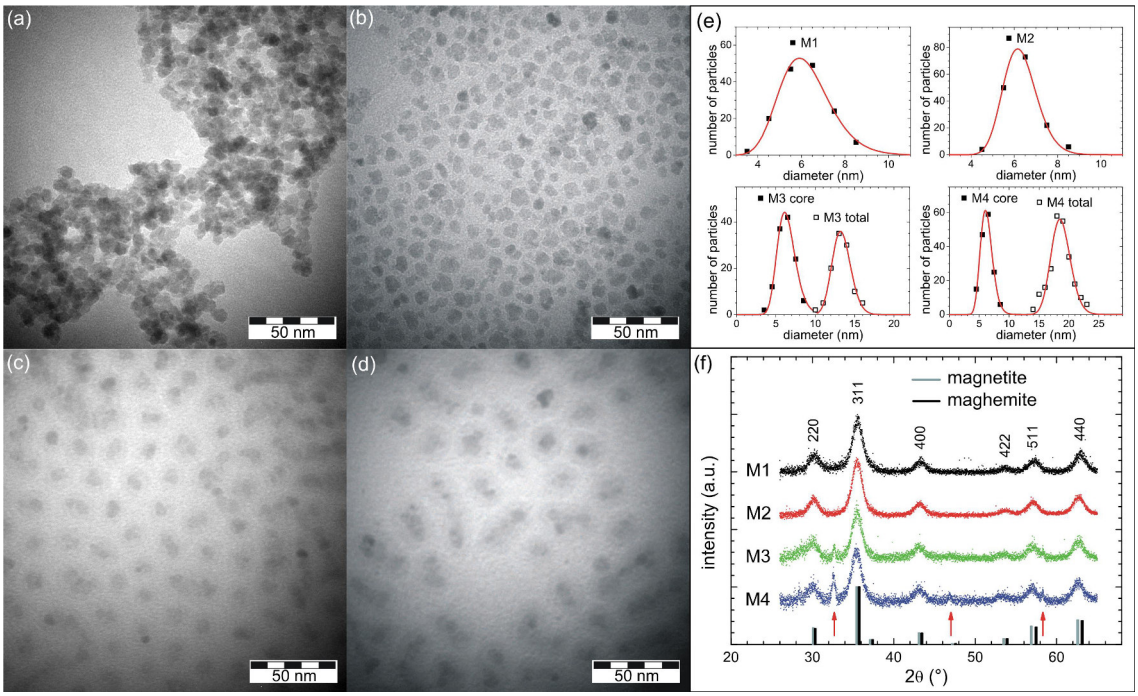

Figure 4.3: TEM images of sample M1 - M4 of capped iron oxide nanoparticles (a - d) and corresponding total particle diameter (open symbols) and core diameter (filled symbols) distributions (e). Experimental XRD-scans of M1 - M4 are compared to theoretical Bragg-peak positions of magnetite and maghemite (f). Red arrows mark additional XRD peaks assigned to ammonium chloride [55].

termined from TEM images of several hundred particles per sample. As the particles are nearly spherical, their diameter was calculated corresponding to a circle of equal area as compared to the ellipsoid formed by the minor and major particle semiaxis. Both types of distributions are shown in figure 4.3 (e) for comparison.

To gain further insight in structure and particle size of the particles, X-Ray diffraction experiments were carried out on nanoparticle powder samples in standard θ-2θ geometry with Cu-K_α radiation using a graphite monochromator. X-ray diffraction pattern of M1 to M4 are displayed in figure 4.3 (f). Bragg peaks of each particle ensemble are consistent with theoretical positions of the ideal magnetite and maghemite (spinel) lattices, which are shown comparatively. From the XRD pattern, the iron oxide phase of the particles cannot be determined without doubt, as Bragg peak positions of magnetite and maghemite are very similar, and as the peaks in the experimental patterns are relatively broad. The broadening of Bragg peaks is expected according to the Scherrer equation (4.1) for particles at the nanoscale, where $\lambda = 154.1$ pm is the wavelength of the X-ray quanta, K the shape factor describing the shape of the crystallites, D_C the diameter of the crystallites and θ the incidence angle of the X-ray. Estimating the crystallite size, i.e., the particle core diameter, from the XRD linewidths using the Scherrer equation,

one yields values identical to sizes determined by TEM within the error margin. Relative error bars of the particle diameter determined by XRD are estimated to ca. 10 %, originating from the rough approximation of the shape factor K = 0.9 in eq. (4.1) for spherical particles.

$$\Delta(2\theta) = \frac{K\lambda}{D_C \cos(\theta)} \tag{4.1}$$

Only particles capped by silica and IGEPAL, i.e., M3 and M4, display additional features in the XRD pattern different from magnetite or maghemite, marked by red arrows in figure 4.3 (f). Positions of these peaks are in good agreement with those of ammonium chloride, which could form as a by-product of the preparation of the silica shell. This seems reasonable to assume, as these contributions are observed only in XRD patterns of samples M3 and M4 with apparently increasing intensity upon higher shell thickness, i.e., higher amount of silica. Traces of ammonium chloride were not found to influence the magnetic or structural properties of the particles in the following experiments. Additionally, as the mass of the capping material relative to the mass of iron oxide within the particle core is not precisely known, this impurity phase prevents a mass normalization to determine, e.g., the absolute values of the particle core magnetization or magnetic susceptibility. Therefore, in this chapter the latter two quantities will be presented normalized to their maximum value for each individual measurement.

In addition to the structural characterization by TEM and XRD, standard magnetometry and in-field Mössbauer spectroscopy were carried out to determine the magnetic saturation moment and magnetic structure of the nanoparticles and to guarantee that they are identical in all but their magnetic interparticle interaction. As mentioned above, the saturation magnetization can only be estimated for bare particles M1, yielding ca. 60 emu/g at an applied magnetic field of 5 T, which is a typical value for iron oxide nanoparticles of this size, but this allows no comparison with the saturation magnetization of M2 to M4 [26]. The shape of the field-dependent magnetization M(H) roughly resembles that of XMCD intensities measured by Dr. A. Warland, from which a site-specific analysis of orientational Fe-spin behavior is principally possible [137, 156]. The latter, however, is no simple task and has been performed here by usage of in-field Mössbauer spectroscopy instead, which is easier to interpret for small variations in site-specific magnetic orientation.

Spectra of samples M1 to M4, recorded at ca. 4.2 K in an external magnetic field of 5 T along the propagation direction of the γ-ray, are shown in figure 4.4. A complete list of hyperfine parameters obtained from these spectra can be found in section A.1 of the appendix. The orientation of the net magnetic particle moment relative to the applied magnetic field B_{appl} results in a variation of the measured effective field B_{eff} of the A- and B-site sublattices, which can be approximated according to equation (4.2) by the vector sum of hyperfine- and external magnetic field B_{hf} and B_{appl} as illustrated in figure 4.5. Here, θ is the site specific canting angle

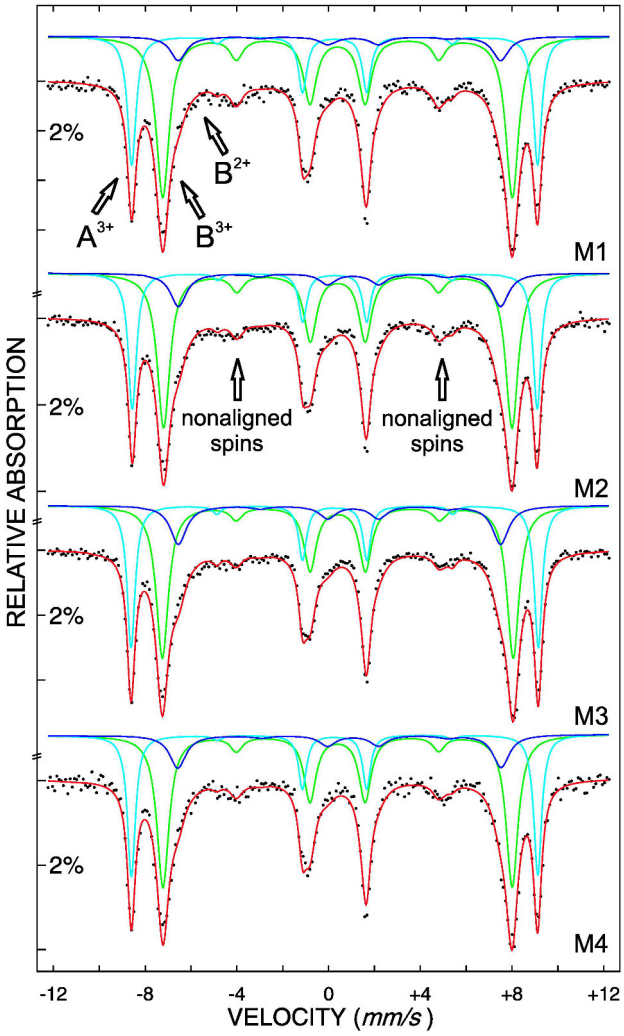

Figure 4.4: Mössbauer spectra of samples M1 - M4 measured at 4.2 K with a magnetic field of 5 T applied parallel to the γ-ray propagation. In addition to experimental data (dots) and to the total least-squares fit (red), three sextet subspectra are shown, corresponding to Fe^{3+} on A sites (cyan) and B-sites (green) and Fe^{2+} on B-sites (blue). Vertical arrows label Mössbauer lines 2 and 5, the relative intensity of which indicates the degree of spin canting [55].

between spin and γ-ray, i.e., the applied field direction. In equation (4.2), $\theta_B > 90°$ is used in agreement with the schematic illustration. However, the canting angle often is defined relative to the ideal ferrimagnetically ordered state $\theta_{B,ideal} = 180°$, wherefore the corresponding angle of 180° - θ_B is used, as it is done below for sake of simplicity. As the hyperfine magnetic field of Fe^{3+} in tetrahedral as well as octahedral surroundings is ca. 52 T, the addition respectively subtraction of about 4 - 5 T results in a pronounced shift in line positions, whereby contributions of A- and B-subspectra now are well resolved as they no longer superimpose.

$$B_{eff}^2 = B_{hf}^2 + B_{appl}^2 + 2B_{hf}B_{appl}\cos(\theta) \overset{\theta\approx 0}{\Rightarrow} B_{eff} \approx B_{hf} + B_{appl} \cdot \cos(\theta) \tag{4.2}$$

Furthermore, the relative intensity of lines 2 and 5 provides information on the sublattice orientation relative to the γ-ray propagation direction, the latter being parallel to the external field direction, as it was explained in detail in section 3.1. Studying the spectrum of bare particles M1, the canting angle θ determined from line intensity ratio A_{23} turns out to be 19° for the B-site sublattice and ca. 13° for the tetrahedral A-site sublattice. Less pronounced canting on the A-site is a common characteristic of magnetite and further members of the spinel

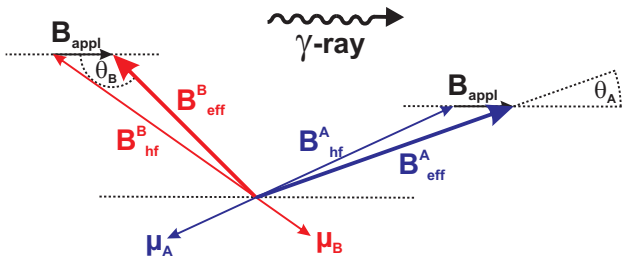

Figure 4.5: Schematic illustration of ferrimagnetic canting angles θ_A and θ_B in external magnetic fields. The alignment of the dominant B-sublattice magnetization results in an increased respectively decreased effective field B_{eff} of the antiparallel sublattices A and B. Adapted from [157]

group. It can be explained by the high B-site exchange constant J_{BB}, which is only slightly smaller than the dominant interlattice exchange constant J_{AB} [158]. As both interactions favor antiparallel alignment, magnetite displays ferrimagnetic ordering with antiparallel sublattice magnetizations and a small disalignment of the B-site moments relative to their ideal coaxial orientation. This can be regarded as an intrinsic origin of spin canting apart from the more dominant surface spin canting as it is typical for small nanoparticles.

As M1 to M4 are of the same core size, no considerable difference in the canting angles is observed, meaning that neither variation of the capping material nor the capping thickness appear to affect the canting behavior strongly, as far as coatings of IGEPAL and silica are concerned. Regarding frustrated surface spins as an effect caused by 'missing bonds' of surface iron atoms, this may indicate a weak bonding of surface atoms to the capping material, the latter not being able to chemically compensate the missing of iron neighbors.

Also, the question arises if bare particles unprotected against oxidation can be directly compared to particles with a protective capping shell, conserving their original state, as the former may exhibit another surface composition (maghemite instead of magnetite). The progression in oxidation from magnetite to maghemite can be observed by the evolution in relative intensity of the Fe^{2+} subspectrum, which stands out by its smaller nuclear Zeeman splitting (smaller hyperfine magnetic field) and the higher isomer shift δ. Spectra shown in figure 4.4 display moderate signs of oxidation with relative Fe^{2+} spectral areas of 10 - 17 %. As 0 % Fe^{2+} should be observed for maghemite and 33 % for ideal magnetite, the existence of a magnetite core of about 4 - 5 nm covered with a maghemite passivation layer can be estimated from these numbers. Theoretical calculations of oxidation rates of magnetite nanoparticles were reported, e.g., by Gallagher et al. [23, 159], while a detailed experimental study was included in the preceding diploma thesis [26], where it has been demonstrated by a study after different aging times that the silica capping conserves a part of the original magnetite phase for several weeks for particles of about 6.3 nm. Further insight was gained by X-ray absorption spectroscopy (XAS) and X-Ray circular dichroism (XMCD) by Dr. Anne Warland [156, 137]. However, the

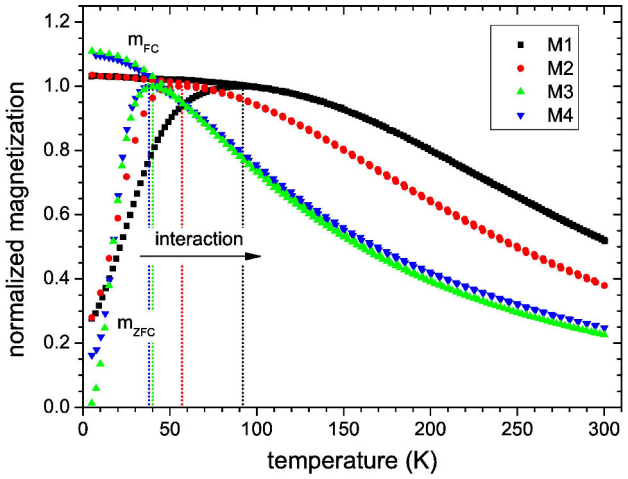

Figure 4.6: Zero-field-cooled (m_{ZFC}) and Field-cooled (m_{FC}) magnetization curves of sample M1 - M4 measured in an applied magnetic field of $\mu_0 H = 10$ mT. Magnetization data are normalized to the maximum value of m_{ZFC} [55].

detection of comparable states of oxidation in capped iron oxide particles again confirms their overall similarity except their interparticle interaction.

4.2 Néel relaxation studied by magnetometry

As a starting point for the basic characterization of magnetic dynamics, measurements of the temperature-dependent magnetization were performed on samples cooled down with and without an applied magnetic field of 100 Oe, in accordance with the zero-field-cooled/field-cooled (ZFC-FC) magnetization protocol, as explained in section 3.2. ZFC-FC magnetization curves, shown in figure 4.6, display the expected change from magnetically blocked to superparamagnetic behavior.

Similar trends are observed for silica capped particles M3 and M4 with a distinct increase in m_{ZFC} up to ca. 30 K, corresponding to blocking temperatures T_B covered by this temperature interval. Above T_B, the magnetic particle moment can freely fluctuate in the superparamagnetic state, as can be seen by the decrease in magnetization being inversely proportional to temperature in agreement with the Langevin equation (3.26). Marking the transition between these two regions, the maximum T_{max} in ZFC magnetization can be used as a characteristic temperature, although it has been outlined in section 3.2 that the first inflection point in m_{ZFC} may represent the blocking temperature more precisely in case of broad distributions of particle diameter.

For samples M3 and M4 with thicker capping, T_{max} is about 40 K, while for smaller coating thickness, i.e., stronger interacting particles, a considerable increase of T_{max} up to 90 K and a broadening of the superparamagnetic transition is observed. Characteristic temperatures of all four samples are listed in table 4.2 together with other parameters of Néel relaxation determined by complementary techniques discussed below. For a direct comparison of parameters in table 4.2, one should remember that the transition from the magnetically blocked to the superparamagnetic state takes place continuously and that blocking temperatures T_B obtained

	TEM	FC-ZFC		TRM		MS	FMR	AC
sample	D (nm)	T_{max}(K)	T_{irr}(K)	τ_0 (ps)	$\overline{E_A}$ (meV)	$\overline{E_A}$ (meV)	$\overline{E_A}$ (meV)	T_0 (K)
M1	6.3(1)	92(2)	102(2)	150(120)	76(2)	69(10)	—	100(2)
M2	7.7(3)	57(1)	85(2)	100(90)	62(3)	54(6)	—	43(2)
M3	13.3(1)	40(1)	70(2)	110(60)	57(1)	43(4)	—	17(2)
M4	18.7(2)	38(1)	68(2)	80(50)	55(1)	39(4)	39(2)	8(2)

Table 4.2: Relaxation parameters obtained from different methods: Core-to-core distance D from TEM. Characteristic temperatures T_{max} and T_{irr} were measured using FC-ZFC-magnetometry and time constants τ_0 were obtained from TRM measurements. Average anisotropy energies $\overline{E_A}$ were determined from TRM, FMR and Mössbauer (MS) results. Interaction energies T_0 from AC-susceptibility were calculated using the Vogel-Fulcher model [55].

by different experimental methods vary according to their time window τ_M, as T_B is defined by the equality of τ_M and the relaxation rate $\tau_{Neel}(T)$.

Further characterization of slow relaxation dynamics in the low temperature regime was performed by the measurement of the thermoremanent magnetization m_{TRM}, as is shown in figure 4.7. As the decay in remanent magnetization m_{TRM} shows a slow variation in time, compared to the pronounced change in FC-ZFC magnetization upon rising temperature, thermoremanent magnetization is a versatile and precise tool to study the nanoparticle anisotropy-energy distribution $p(E_A)$.

The thermoremant magnetization is shown in figure 4.7 as a continuous 'master' curve, plotted versus the normalized product of thermal energy and the logarithmic time factor corresponding to the anisotropy energy, which allows the additional estimation of the relaxation-time prefactor τ_0. This type of plot may be motivated by the consideration that to each temperature corresponds a specific relaxation time $\tau(T)$, wherefore identical decay in magnetization can be realized by different pairs of T_i and $\tau(T_i)$, which are correlated by equation (2.6).

Experimental data points of m_{TRM} were theoretically reproduced using least-squares fitting by the integral of the distribution $p(E_A)$ of anisotropy energies represented by dashed lines, as it has been illustrated in section 3.2. $p(E_A)$ was assumed to be of log-normal shape, where the log-normal standard variation σ, the mean value of anisotropy energy $\overline{E_A}$, marked by dotted lines, and the time factor τ_0 were used as free parameters (see table 4.2).

Good agreement between experimental data and the integrated log-normal fitting routine was found for all four samples by usage of time factors τ_0 of about 10^{-10} s. Upon rising interparticle interaction the mean value of anisotropy energy increases from 55 meV for sample M4 by about 40 % to ca. 76 meV for bare particles M1. In agreement with previously presented results

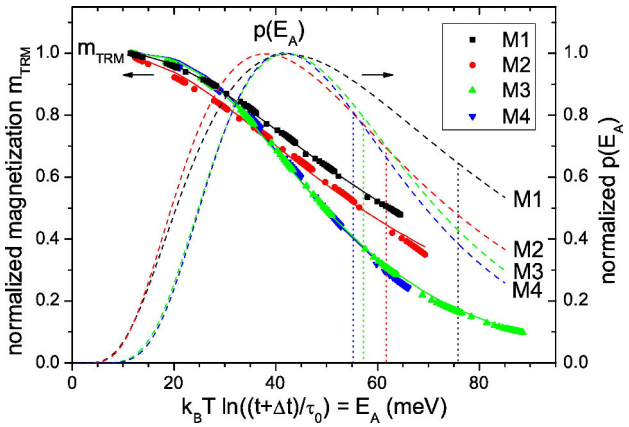

Figure 4.7: Normalized thermoremanent magnetization m_{TRM} of samples M1 - M4 (full symbols) versus relative temperature. Least-squares fit of experimental data m_{TRM} using an integrated log-normal function as described in the text (solid line), dashed lines display the corresponding log-normal distribution $p(E_A)$ of anisotropy energies, vertical lines the corresponding average anisotropy energy $\overline{E_A}$ [55].

from ZFC-FC magnetization, a distinct broadening is observed in addition to the increase in anisotropy energy from M4 to M1. The unbroadened log-normal distribution of sample M4 is characterized by a standard deviation of $\sigma \approx 0.43$. This is an interesting observation, as neglecting the minor size-dependence of K_{eff}, the anisotropy energy measured here is directly proportional to the particle volume. In TEM analysis a diameter standard deviation of 1.0 nm was found for sample M4, corresponding to $\sigma_D \approx 0.15$, or a volume standard deviation $\sigma_V = 3\sigma_D \approx 0.45$, being in good agreement to the width of the anisotropy energy distribution extracted from TRM experiments.

At the starting point of the measurement, i.e., at short times, respectively low temperatures, an accelerated decay in remanent magnetization is detected for samples that experience stronger interaction. This effect could not without doubt be verified by the ZFC-FC magnetization approach, as the zero-field-cooled magnetization can vary strongly due to miniscule remanent fields of the superconducting SQUID magnet. This behavior may be caused by the random spatial configuration of particles within the powder sample:

In general, enhanced magnetic dipole interaction is expected to stabilize the orientation of the magnetic particle moment along a specific direction determined locally by the sum of magnetic stray fields of all particles nearby, which would be in agreement with the observation of increasing average anisotropy energies $\overline{E_A}$ in samples M1 and M2. On the other hand, the accelerated decay at low temperatures may correspond to small particles in a frustrated geometry of larger particles with dominant magnetic moments but without predominant magnetization direction. Such a configuration could superimpose with the small anisotropy energy barrier in smaller particles by additional easy directions given by the magnetization direction of the larger, magnetically blocked particles, which would then result in an increase in the relaxation rate.

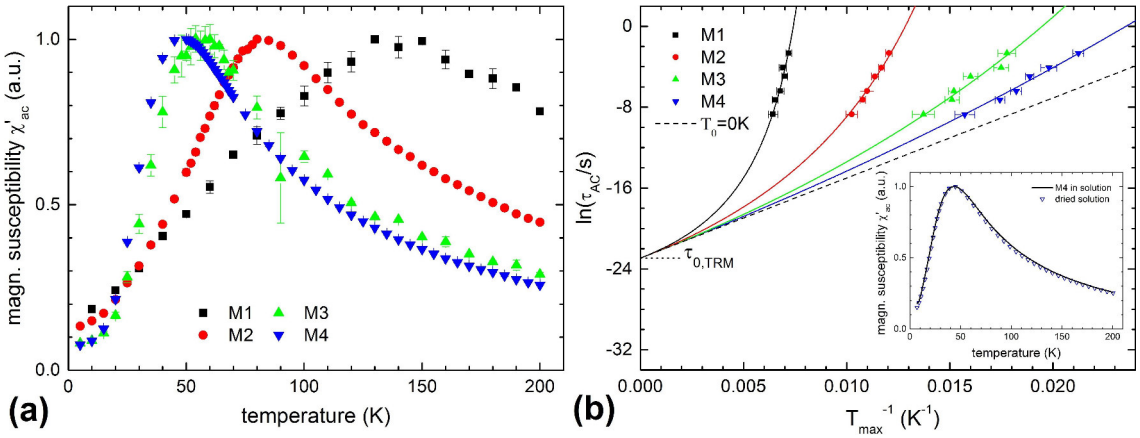

Figure 4.8: Real component χ' of magnetic susceptibility of sample M1 - M4 measured at an AC-frequency of 2.3 Hz and temperatures of 5 - 200 K (a). (b) displays $\ln(\tau_{AC}/s)$ versus the inverse experimental T_{Max} from (a). Solid lines are least-squares fits by Vogel-Fulcher equation (2.8) with $\tau_{0,TRM} = 110$ ps determined from TRM. Free adapted parameters were the anisotropy energy, identical for all samples, and each samples interaction energy analog T_0. The inset displays nearly identical χ' behavior for M4 measured at 11 Hz as a powder and dissolved in isopropanol, adapted from [55].

The approach of analyzing slow relaxation dynamics by means of the decay in remanent magnetization provides an estimation of shape and position of the anisotropy energy distribution. On the other hand, thermoremanent magnetization is still a 'slow' technique with a time window $\tau_M \gg \tau_0$, with τ_M being in the range of seconds to minutes. Because of this, complementary measurements by magnetic AC-susceptometry were carried out, which have the advantage of a smaller and *tunable* τ_M by variation of the frequency of the applied AC magnetic field. This advantage is utilized here to gain a deeper understanding of the influence of interaction effects on the relaxation time and to determine interparticle interaction energies T_0 quantitatively.

Due to the exponential correlation (2.6) of particle volume and relaxation time when assuming a size-independent anisotropy constant K_{eff}, a very broad distribution of relaxation times will be observed even for highly monodisperse nanoparticles, whereby plots of the magnetic susceptibility versus the AC frequency cannot display the full range of relaxation times experienced by the particle moment. Therefore, the temperature dependence of the real component χ' of magnetic susceptibility, measured by applying an AC field amplitude of $H_{Appl} = 4$ Oe, is shown in the range of 5 - 200 K in figure 4.8 (a), instead.

As the basic principle of magnetic moment orientation is comparable in magnetic DC and low-frequency AC fields, it is reasonable to assume that $\chi'(T)$ is proportional to $M_{ZFC}(T)$, as was illustrated in section 3.2, assuming monodisperse and non-interacting particles. Indeed, both curves display strong similarities, although the position of maximum χ' is shifted to higher

temperatures compared to ZFC measurements due to the shorter time window, which can be estimated here as $\tau_M = (2\pi f_{AC})^{-1} \approx 70$ ms.

To utilize the advantage of being able to vary the time window τ_M, the magnetic AC-susceptibility was measured for several frequencies in the range of 2.3 Hz - 1.5 kHz. The resulting decrease in maximum position T_{max} upon rising time factor τ_M displayed in figure 4.8 (b) varies considerably for particles of different shell thickness. Assuming T_{max} to be a feasible approximation of the blocking temperature T_B, the curves can be reproduced by the Vogel-Fulcher law (2.8). As the result of the following analysis strongly depends on the time factor τ_0, that cannot be estimated with sufficient accuracy from the AC susceptibility data alone, a fixed value of $\tau_0 = 110$ ps was used, corresponding to the averaged value of τ_0 obtained from the TRM experiment. In the case of negligible interaction energy T_0, the Vogel-Fulcher equation (2.8) equals the simpler Néel equation (2.6), yielding a linear function in $\ln(\tau)$ versus the reciprocal maximum temperature T_{max}. Upon increasing interparticle interaction, sample M4 to M1 displays stronger deviations from the linear behavior, from which the interaction energy analog T_0 can be extracted, as τ is expected to diverge at T_0 according to the Vogel-Fulcher equation. To reflect the assumption of identical magnetic properties apart from interaction, the four curves in figure 4.8 (b) are least-squares fitted in a simultaneous process with K_{eff} (identical for all samples) and T_0 (adapted individually) being free parameters. For M4 to M1, interaction-energy analogs T_0 of 8 ± 2 to 100 ± 2 K were determined in order of decreasing capping thickness.

4.3 Mössbauer spectra of superparamagnetic particles

Standard magnetometry techniques described above, such as thermoremanent magnetization or ZFC-FC magnetization measurements, may lead to ambiguous interpretations for complex systems, because they are sensitive to the net magnetic moment of the total sample material. However, a specific change in magnetization can originate from a small fraction of particles experiencing fast relaxation dynamics as well as from the majority of particles in the sample displaying low relaxation rates. The advantage of Mössbauer spectroscopy is the ability to detect and quantify different states of magnetic relaxation, i.e., different relaxation times, by their characteristic spectral shape. From the relative spectral area of subspectra that show a specific structure, the particle fraction displaying the corresponding superspin fluctuation time can be determined. For this purpose, results from magnetometry methods were cross-checked by Mössbauer spectroscopy of capped iron oxide nanoparticles M1 - M4, recorded in zero applied magnetic field between 4.2 K and ambient temperature in transmission geometry (figure 4.9). It has to be mentioned here, that raw data of the Mössbauer spectra in figure 4.9 have been analyzed before in the preceding diploma thesis [26]. As it is elaborated below, the development of the more sophisticated many state model that includes a distribution of

anisotropy energies necessitates the re-evaluation of these spectra for cross-checking with new reference data from AC-susceptometry and ferromagnetic resonance (FMR).

Zero-field hyperfine parameters of these spectra are found to be in good agreement with those determined from in-field spectra in section 4.1 and can be well reproduced by application of the same fitting routine. Subspectra of Fe^{2+} on B-sites and Fe^{3+} on both sites can be resolved at low temperatures, whereas upon increasing deformation of the spectral shape by relaxation effects this becomes impossible above ca. 100 K, where the experimental spectrum could be reproduced by only one effective subspectrum of larger linewidth, representing all three iron sites.

At low temperatures up to ca. 20 K the spectra remain completely static, which is indicated by the nearly constant hyperfine magnetic field B_{hf} and the symmetrical absorption lines of the individual subspectra. At 50 - 100 K the manifestation of shoulders at the inner sides of the absorption lines can be observed. These shoulders can be attributed to collective excitations of the particle superspin, accompanied by a decrease of the time-averaged nuclear Zeeman splitting, as it was illustrated in figure 2.6. As the latter is more pronounced for smaller particles with lower anisotropy energy barriers, the log-normal distribution in particle sizes is directly reflected by the shape and fine structure of the absorption line deformation, wherefore the above mentioned many-state relaxation model considering these effects is required to reasonably reproduce experimental spectra.

Collective excitations that cause a decrease in the observed nuclear Zeeman splitting may take place even far below the blocking temperature and can originate from particles of each size. The presence of the superparamagnetic doublet, on the other hand, is a prove of particles being in the superparamagnetic state. The appearance of the first doublet contribution can be directly assigned to the blocking temperature of the particles with the lowest anisotropy energy. Upon heating, the first doublet starts to form at ca. 50 K for silica-capped samples M3 and M4, while it is not detected in stronger interacting particles M1 and M2 before reaching 100 - 150 K.

It becomes apparent that Mössbauer spectra of interacting particles display special characteristics upon further heating. For example, in the spectrum of bare particles M1 at 220 K, a very broad distribution of sextet splittings is visible, indicating a high rate of dynamic fluctuation (figure 4.9). The thermal energy is, however, apparently insufficient to cause completely superparamagnetic behavior, as no considerable doublet structure emerges and the sextet structure is widely conserved instead. This indicates that the interparticle interaction results in a decreased rate of superspin flips between easy magnetic directions, as a fast rate would be reflected in the presence of a central doublet subspectrum and the collapse of the sextet structure. On the other hand, collective thermal fluctuation *within* the current minimum of anisotropy energy seems to take place barely affected by interaction effects, as a very distinct deformation of the

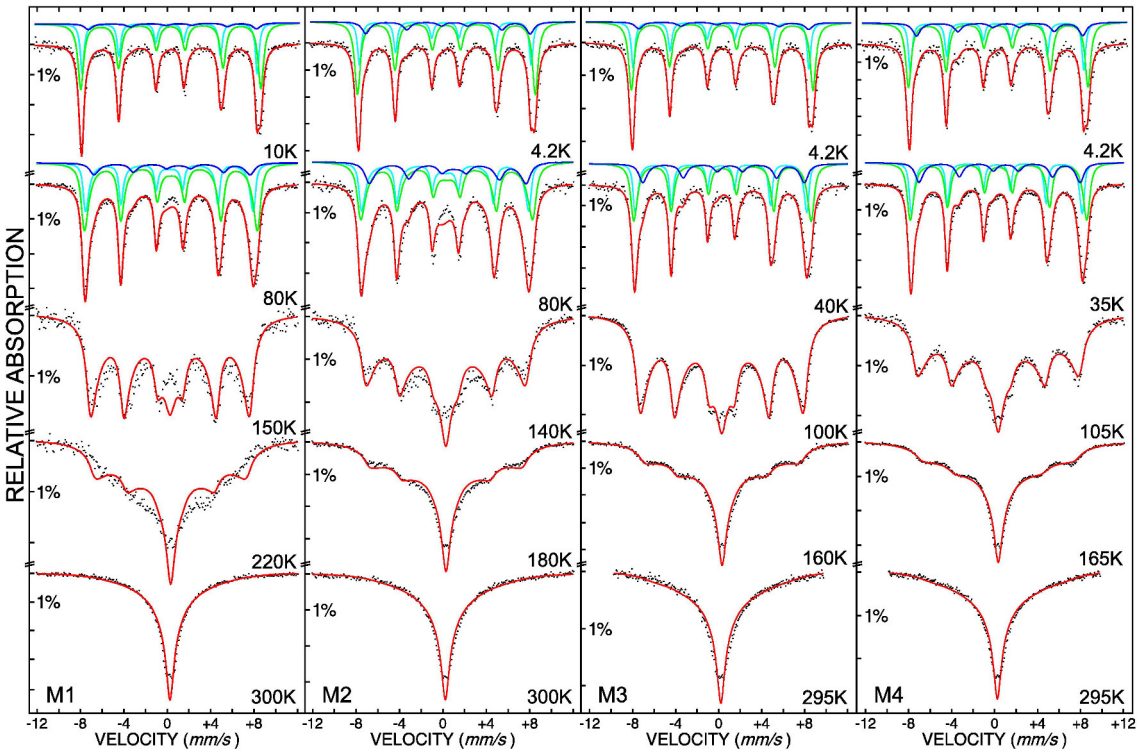

Figure 4.9: Representative spectra of the Mössbauer relaxation study of samples M1 - M4 measured between 4.2 K and ambient temperature. The three subspectra displayed up to 80 K correspond to the fitting model introduced in figure 4.4. Starting at 100 K, only one broadened sextet was used to represent the three superimposed unresolved subspectra, as explained in the text in detail [55].

spectral shape *without* the appearance of a central doublet is observed.

This phenomenon could be explained at least in two ways. It could be possible that the magnetic orientation of smaller particles is, to some extent, coupled to that of nearby bigger particles of dominant magnetic moment by their stray field. This would not hinder fluctuations within a small angular interval close to the preferred orientation, i.e., collective excitations, since these would not be very energetically unfavorable assuming the validity of equation (2.4). However, the superspin would be pinned to this anisotropy axis to prevent disalignment with the dominant next-neighbor particle. This assumption is easy to check, as it would result in a relatively instantaneous collapse of the sextet structure by reaching the highest blocking temperature in the sample, where no 'dominant' pinning neighbors remain. This is in contradiction to the experimental observation of collapsing sextet structure in sample M1 at 200 - 250 K, while in the weakly interacting sample M4 no considerable sextet features are conserved above ca. 160 K, giving an estimation of the highest 'intrinsic' blocking temperatures.

It is more likely for the effect to be of 'collective' origin without dominant larger particles. Assuming a random spatial orientation of the nanoparticles within the powder sample, local

accumulations of several particles sharing a similar direction of anisotropy axes are bound to exist. Although this will not be the case for all particles, the formation of a locally preferred magnetic orientation could prevent spin-flip processes and conserve the sextet spectrum, as the particles 'support' each other mutually. This behavior may characterize the transition regime to a super spin-glass state, observable in strongly interacting particles, in which superspin frustration creates a multitude of metastable states comparable in energy below the glass transition temperature, before relatively abruptly reaching a quasi-superparamagnetic state at elevated temperatures.

Interparticle interactions, apparently resulting in an increase in blocking temperature respectively a deceleration in Néel relaxation dynamics in general, are not implicitly included in the many-state model by Jones and Srivastava [72]. Nevertheless, they are included in the following in an effective average anisotropy energy $\overline{E_A}$, which would result in values of T_B comparable to blocking temperatures enhanced by the interparticle interaction observed in the samples. This effective anisotropy energy combines the net energy barrier created by superposition of magnetocrystalline, shape and surface anisotropy as well as the above mentioned contributions by magnetic dipolar interaction. The latter is denominated as the dipolar energy E_{dip}. Mössbauer spectra were analyzed by this approach to determine the effective anisotropy barrier $\overline{E_A}$, as shown in figure 4.10 (a) in the temperature region starting at the appearance of a first doublet contribution up to the collapse of the sextet structure. As this characteristic temperature region is enhanced upon stronger interaction, evaluated spectra include measurements at about 25 - 180 K for weakly interacting particles M3 and M4 and 80 - 200 K for the bare particles of sample M1.

Average values of the effective anisotropy energy $\overline{E_A}$ obtained are 39 ± 4 meV for sample M4 and are found to increase to 69 ± 10 meV for bare particles M1, which is less than estimated from TRM results. Considering the mean particle diameter and the width of the particle size distribution corresponding to an average particle volume of ca. 140 nm^3, this value can be converted to an effective anisotropy constant of ca. 45 ± 4 kJm^{-3}, which is within the common range for iron oxide nanoparticles of 5 - 8 nm in size [41]. No major changes in effective anisotropy are found in the studied temperature intervals (figure 4.10), which is surprising, as the magnetocrystalline anisotropy constants are known to show strong temperature dependencies. However, as $|K_1|$ is limited to ca. 10 kJm^{-3} in magnetite-maghemite particles, the magnetocrystalline anisotropy may pose the least important component to E_A, which seems to be dominated by the surface anisotropy and, obviously, by contributions of magnetic dipolar interaction, the latter being comparable to the sum of all other anisotropy contributions in case of sample M1. Similar temperature-independent behavior of the anisotropy energy E_A was reported by van Lierop and Ryan using a similar theoretical approach [98].

During the application of the Jones-Srivastava model, three parameters have to be particularly considered, as they directly influence the resulting anisotropy energy E_A. These parameters are the standard deviation of the anisotropy energy distribution, the relaxation parameter R, being a measure of τ_0 as explained in the experimental section 3.1 in detail, and the temperature dependence of the hyperfine magnetic field B_{hf}. While the influence of R on the calculation of the anisotropy energy barrier is self-evident considering its correlation to the relaxation prefactor τ_0, the change in B_{hf} is mainly relevant at low temperatures. There, collective excitations mainly result in a decrease in sextet splitting upon heating, which can superimpose with the temperature-dependent decrease in the intrinsic hyperfine magnetic field, effectively corresponding to the trend in saturation magnetization $M_S(T)$.

To minimize errors by these two sources, the temperature-dependence in $B_{hf}(T)$ measured in zero field has been cross-checked by Mössbauer spectra measured at low temperature in weak external fields, just suppressing relaxation effects, and by comparison with temperature-dependent measurements of the saturation magnetization $M_S(T)$. As the influence of interparticle interaction on R is unclear and presumably small, as the parameter is correlated to the intrinsic relaxation parameter τ_0, the influence of different values of R on the spectra has been tested for samples M3 and M4, and the best agreement between theoretical and experimental spectra could be found for $R \approx 10$ mm/s, whereby this value was applied to all samples. Converting this value of R to the time scale, one finds a corresponding value of $\tau_0 \approx 1.37$ ns as a measure of τ_0. Further effort could have been made to include temperature variation of τ_0, as predicted by theory. The latter was neglected, as the relaxation time correlated to spectral deformation only weakly depends on τ_0 and, therefore, on the parameter R. For the parameters at hand, a variation of R within a factor of two can be expected in the relevant temperature interval, which would modify the calculated anisotropy energy E_A by only 5 - 20 %. For the standard deviation σ of the distribution $p(E_A)$ a value of 0.43 was used, as it has been determined by the integral log-normal fitting of TRM data (figure 4.7), yielding good agreement with experimental spectra of weakly interacting particles in M3 and M4.

By this approach one holds an additional versatile instrument in addition to AC-susceptometry, to obtain a quantitative measure of the strength of interparticle interaction. In the scope of the simple approximation of eq. (2.5) the magnetic dipolar interaction energy E_{dip} is considered as being proportional to the square of the total magnetic particle moment μ_{NP} divided by the cube of the core-to-core distance D^3. As has been thoroughly demonstrated in section 4.1 that particles in sample M1 to M4 deviate only in their capping and exhibit nearly identical magnetic structure, the same value of μ_{NP} can be applied in the calculation for each sample. Again, here it is assumed that the magnetic dipole interaction is inferior to effects of intraparticular exchange interaction, wherefore no considerable effect of next-neighbor stray fields on the degree

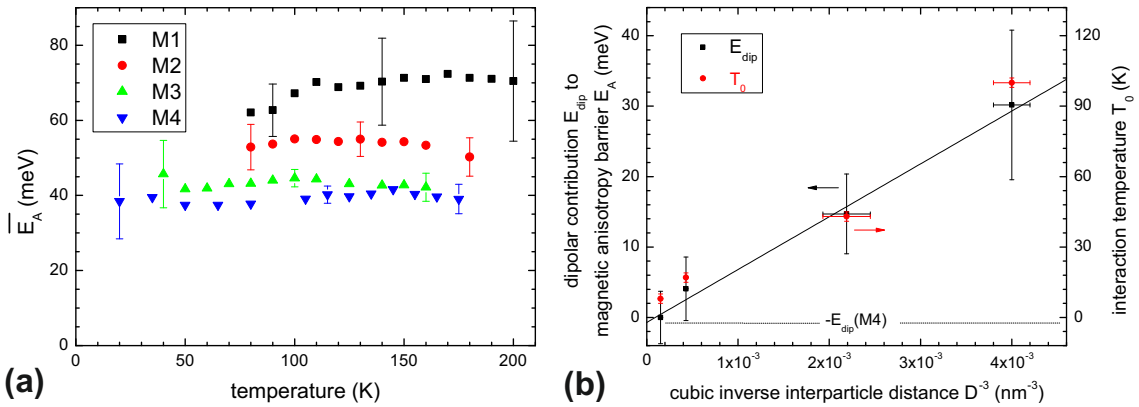

Figure 4.10: Temperature-dependence of the average anisotropy energy $\overline{E_A}$ calculated from Mössbauer relaxation spectra using the many-state relaxation model by Jones and Srivastava (a). Some typical error bars are exemplarily given. (b) displays the contribution of magnetic dipolar interaction to the anisotropy energy barrier E_{dip} (black square) and the interaction energy analog T_0 (red dots) versus the inverse interparticle distances D^{-3}, adapted from [55].

of frustration in surface spins, i.e., spin canting, exists.

To compare results on the interaction energy by both methods, the contribution E_{dip} to the anisotropy energy E_A as calculated from Mössbauer spectra, and the interparticle-interaction analog T_0 are plotted in figure 4.10 (b) versus the inverse cubic interparticle distance D^{-3}. Applied values of D are listed in table 4.2 and determined directly from TEM analysis presented in section 4.1. The interaction-energy analog T_0 is revealed to be approximately linear in D^{-3}, which is in agreement with equation (2.5). For E_{dip} it has to be considered that no Mössbauer spectrum of ideally non-interacting particles is at hand, which could be used to 'calibrate' E_{dip} to zero. Instead, E_{dip} can only be given quantitatively as the difference value between the average anisotropy energy of an individual sample and that of the silica-capped sample M4 showing least interaction effect. From linear interpolation an offset respectively an interaction energy E_{dip}(M4) of ca. 0.7 meV is found. This corresponds to an anisotropy energy $E_A \approx 38$ meV and an effective anisotropy constant $K_{eff} \approx 44$ kJm^{-3} of a theoretical non-interacting particle ensemble.

As can be seen, both data sets in figure 4.10 (b) display approximately linear behavior in D^{-3}, although a higher number of weakly interacting particles of slightly deviating capping thickness would be required to prove this without doubt. However, the evaluation of the present results verifies that quantitative expressions of the interaction energy can be found also by Mössbauer spectroscopy, as has been demonstrated for AC-susceptometry in literature before [160].

The correctness of the determined values of T_0 cannot be proven directly by comparison with interparticle interaction theory. Although an adequate expression can be found by eq. (2.5),

this equation calculates the *maximum* of the angular dependent interaction energy of *two* interacting particles, which is, together with the *number* of interacting particles, different for each configuration of nanoparticles in the powder sample.

As has been shown in section 4.1, the particles can be considered monodisperse, but still exhibit a log-normal standard deviation of $\sigma \approx 0.15$ in the distribution of particle diameters. Additionally, it is known that the interaction energy of a reference particle is proportional to the total magnetic moment μ_{NP} of the associated interacting particle, wherefore it seems reasonable to assume that the dominant contribution to the interaction energy originates from the biggest nearby particle. Following this consideration, the particle moment μ_{NP} can be roughly estimated by assuming the interaction of two relevant particles only, resulting in an average magnetic particle moment of ca. 7300 μ_B by setting in values of T_0 and D^{-3} from figure 4.10 (b) in equation (2.5). Considering the magnetization of the magnetite spinel lattice, this can be translated to a particle core volume of about 130 nm^3 and an average particle diameter of 6 - 6.5 nm, which is in good agreement with particle sizes determined by TEM and XRD analysis. Nevertheless, this is only a rough approximation, as effects of spin canting are also neglected, which lead to a decrease in the net magnetic particle moment acting on nearby particles. From in-field Mössbauer spectra in figure 4.4, a spin-canting angle of about 15° has been extracted at an external magnetic field of 5 T, which means that the net magnetic moment of the particles is severely decreased relative to its saturation moment under zero-field conditions. As this effect directly diminishes the calculated interparticle interaction energy, the agreement between the particle size measured by TEM and that estimated from T_0 by usage of equation (2.5) might be accidental, as the combined interaction of many particles is needed to reach T_0, when spin canting effects on μ_B are considered in the model.

4.4 Ferromagnetic resonance experiments

Studying relaxation effects by different experimental approaches as described above should result in similar values of the anisotropy energies E_A. However, minor differences are evident when comparing results of 'slow' magnetometry techniques, as ZFC-FC and thermoremanent magnetization, with results of Mössbauer spectroscopy being a 'fast' method with a characteristic time window τ_M close to the minimum relaxation time τ_0. To verify, whether this is a result of intrinsic properties of these measurements or an erroneous or misleading analysis of experimental data, complementary 'fast' measurements of the ferromagnetic resonance (FMR) signal have been performed as a reference by Dipl. Phys. Christian Schöppner. Some milligram of double-capped particles M4 were measured in the temperature region of 5 - 300 K at applied magnetic fields of 0 - 1.6 T at a microwave frequency of 9.485 GHz. The derivation of the imaginary part of magnetic susceptibility $\partial\chi''/\partial H$, which has been recorded in the experiment

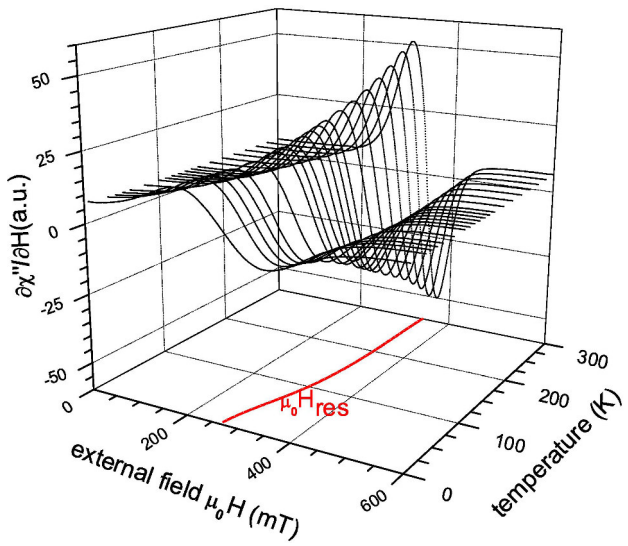

Figure 4.11: FMR spectra of sample M4. The resonance field $\mu_0 H_{res}$ (red line) is defined by the inversion point of the FMR signal (black dotted line) [55].

and is proportional to the absorbed microwave power, is displayed in figure 4.11 as an array of curves measured in temperature steps of about 20 K.

At low temperatures a broad signal with a resonance position, i.e., resonance field H_{res}, of about 270 mT can be observed. The resonance position is defined by the inflection point of the individual curves. Upon rising temperature, the linewidth of the signal decreases considerably and the resonance field increases to about 340 mT at 300 K, in accordance with the paramagnetic resonance field, which could indicate the superparamagnetic state.

The resonance position in general is correlated to the orientation of the magnetic field relative to the magnetization in the studied medium along an easy- or hard magnetic direction. A reasonable assumption is a state of random orientation at low temperatures, which cannot be aligned completely at fields in the region of some 100 mT, leading to a broad distribution of resonance fields H_{res}, each corresponding to an individual angle between easy anisotropy axis and magnetic field direction. In measurements of small numbers of nanoparticles by usage of a micro resonator, which enables one to 'map' anisotropy directions of individual particles, it has been demonstrated that resonance lines of a single particle exhibit linewidths of some mT [161]. Therefore, an alternative explanation apart from a distribution in resonance positions can hardly be found. At elevated thermal energy, at least slow Néel relaxation dynamics can be predicted in the low-field regime for sample M4. This may allow the particle moments to align along their easy magnetic direction, which is the closest to the applied magnetic field direction. This again is accompanied by a distinct decrease in linewidth, as is observed above ca. 200 K by FMR.

According to theory established by Antoniak et al. [139], the anisotropy field $H_A = 2K_{eff}M_S^{-1}$ of a superparamagnetic particle can be extracted from FMR using equation (4.3), where H_{res}^0 is the low temperature limit of the resonance field H_{res} corresponding to the magnetically blocked

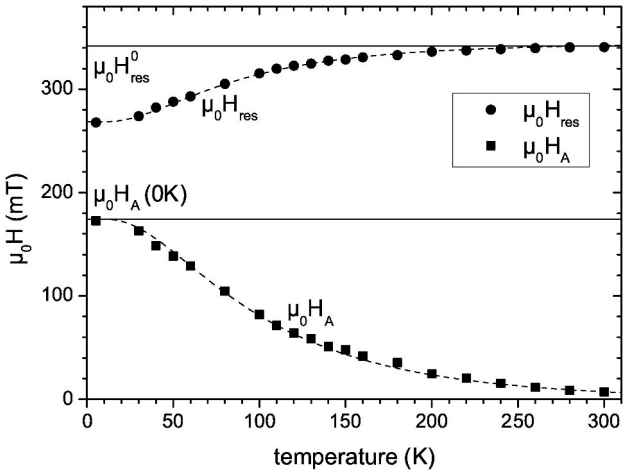

Figure 4.12: Resonance field $\mu_0 H_{res}$ from figure 4.11 (circles) and anisotropy field $\mu_0 H_A$ (squares) calculated by equation (4.3) for sample M4. Dashed lines are guides to the eye [55].

state. The trends in resonance field position as well as the calculated anisotropy field values H_A are compared in figure 4.12.

As the process of superspin fluctuation is not explicitly included in this model, the anisotropy field converges to zero at high fluctuation rates, i.e., high temperatures. This can be understood by analogy to the apparent disappearance of the nuclear Zeeman splitting in the superparamagnetic state observed by Mössbauer spectroscopy. Additionally, the effect of external magnetic fields of up to ca. 300 mT on the Néel fluctuation dynamics is difficult to estimate. By consideration of these two shortcomings, the resonance position at elevated temperatures is not evaluated to further extent. Instead, the analysis will be restricted to the low temperature limit H^0_{res}, where no superspin fluctuations occur.

$$H_{res} = H^0_{res}\left(1 - \left(\frac{H_A}{H^0_{res}}\right)^{1.25}\right)^{0.44} \tag{4.3}$$

According to equation (4.3) a resonance field of $H^0_{res} \approx 265$ mT corresponds to an anisotropy field of 174±6 mT. Presuming that highly frustrated spins at the particle surface do not participate in Néel fluctuations and that, instead, fluctuations are primarily performed by the particle core, where all atomic moments are collinearly aligned, one can approximate the magnetization of the magnetic volume relevant for the Néel relaxation process by the bulk saturation magnetization of magnetite of $M_S \approx 510$ kJm^{-3}. From the definition of the anisotropy field and this magnetization value an effective anisotropy energy density K_{eff} of about 44 ± 2 kJm^{-3} can be calculated in good agreement with values of K_{eff} extracted from Mössbauer spectroscopy (see table 4.2). This comparison contains some daring, but apparently reasonable assumptions, but nevertheless, it appears to substantiate the hypothesis that differences in the anisotropy energy of interacting particles described above originate from the vast difference in the characteristic measurement time of the individual techniques rather than being a measurement artifact.

5 Simultaneous relaxation phenomena in ferrofluids: Study of Brownian and Néel dynamics

The previous chapter discussed the Néel relaxation mechanism in interacting particles intensively. As an extension, the simultaneous occurrence of Néel and Brownian relaxation dynamics is presented hereafter and analyzed comparatively, mainly by Mössbauer spectroscopy and AC-susceptometry methods. AC-susceptometry experiments shown hereafter (chapter 5 - 7) were performed with the assistance of Soma Salamon, M.Sc.

Three commercial glycerol-based ferrofluids, containing capped magnetite nanoparticles of different core diameter, were purchased from Ocean NanoTech. The ferrofluids were modified versions of the standard products SHP5, SHP15 and SHP25 dissolved in a mixture of 70 vol% of glycerol and 30 vol% of water [162]. Magnetic nanoparticles in the ferrofluids are (partially oxidized) magnetite particles of about 5 to 25 nm core diameter, capped with a monolayer of oleic acid and an amphiphilic polymer to prevent agglomeration. Exact particle sizes determined from TEM images and as provided by Ocean NanoTech are included in table 5.1. The particle capping layer is stated by Ocean NanoTech to result in an increase of 8 - 10 nm in hydrodynamic diameter, corresponding to a capping thickness of 4 - 5 nm. This value will be cross-checked independently in section 5.2 by Mössbauer spectroscopy. The ferrofluids exhibit a particle concentration of 10 mg Fe per ml, corresponding to ca. 14 mg magnetite per ml, and displayed excellent stability without observable agglomeration effects within 6 months after purchase.

With core diameters of 5 - 25 nm a wide spectrum of Néel relaxation times is available, corresponding from magnetically blocked to completely superparamagnetic behavior. In parallel, Brownian rotation times do not show such a distinct variation within the interval of hydrodynamic diameters of ca. 15 - 35 nm and lead, in combination with the enhanced dynamic viscosity η by using glycerol-based ferrofluid, to well-measurable frequencies in AC-susceptometry and line broadening in Mössbauer spectroscopy. Dynamic viscosities of 70:30 glycerol solutions are estimated to $\eta_{300K} \approx 25$ mPas down to $\eta_{250K} \approx 1$ Pas in Ref. [66].

5.1 Ferrofluid characterization

Transmission electron microscopy images of the three types of capped iron oxide nanoparticles were measured by Dr. Marina Spasova using a TEM model Tecnai F20, to determine structural properties and particle size distributions $p(D_C)$, which are shown in figure 5.1. For these experiments, a small amount of each ferrofluid has been strongly diluted with water and dropped on a TEM copper grid.

A regular spherical shape has been determined for all three samples. They exhibit core diameter

	phase	D_{ONT} [nm]	D_{TEM} [nm]	T_{max} [K]	T_{irr} [K]
S	maghemite	5±2.5	6.0±0.1	40	60 (Néel)
M	magnetite	15±2.5	14.8±0.1	160	ca. 205 (Brownian)
L	magnetite	25±2.5	26.4±0.1	—	ca. 220 (Brownian)

Table 5.1: Parameters of samples S, M and L obtained from structural and magnetic characterization: Core diameter D_{TEM} determined by TEM, the nanoparticles' iron oxide phase and estimated core diameter D_{ONT} as stated by Ocean NanoTech, the maximum in ZFC magnetization T_{max} and irreversibility temperature T_{irr} as observed by SQUID-magnetometry.

distributions with a standard deviation σ of 0.07 - 0.11, whereby they can be considered as highly monodisperse. This becomes apparent also by the self-organized hexagonal ordering of nanoparticles visible in most of the TEM images. Average core diameters of 6.0 ± 0.1 nm, 14.8 ± 0.1 nm and 26.4 ± 0.1 nm are in very good agreement with the specification by Ocean NanoTech, as listed in table 5.1. According to the distinct variation in the diameter of incorporated particles, the three ferrofluidic samples are denominated as (S)mall, (M)edium and (L)arge, respectively.

As shown in the inset of figure 5.1 in magnification, in addition to the black particle core, the capping layer can be clearly resolved from the background intensity by its considerably diminished, but still visible contrast. A capping thickness of about 4 nm can be determined in accordance with information provided by Ocean NanoTech. While the capping thickness can be estimated from images of the biggest particles, at the same time sample M and L display a smaller interparticle separation compared to 6 nm particles in sample S. It is possible that the ligands within the capping layer are compressed to a lower effective capping thickness by the much higher interparticle magnetic dipole interaction between bigger particles. Assuming a surface separation of 5 nm and the particle diameter as mentioned above, interaction energies of 1.6 meV to 505 meV can be calculated for samples S - L using equation (2.5). The considerable increase in interparticle interaction can be ascribed to its dependence in sixth power on the particle core diameter (D_C^6). In parallel, the number of capping ligands increases only proportionally to the particle surface, i.e., to D_C^2, which could explain minor deformations of capping layers by strong attractive interaction between large ferrimagnetic particles. The latter might contribute, in addition to sedimentation, to enhanced agglomeration and reduced ferrofluid half life of sample L. However, Mössbauer spectra as well as results of AC-susceptometry shown below prove the movement of the particles as individuals in the liquid instead of larger agglomerates. Such agglomerates could have been easily observed by the decrease in diffusive

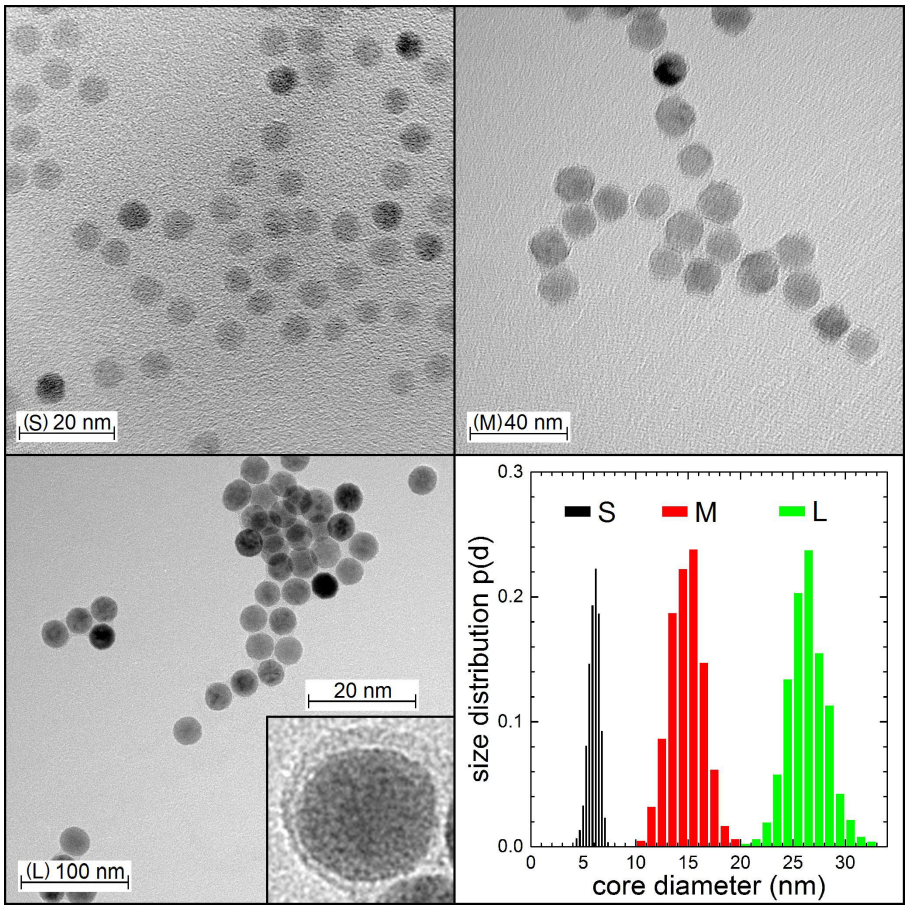

Figure 5.1: From top left to bottom right: TEM images of nanoparticle samples S with $D_{TEM} = D_C$ of about 6 nm, M ca. 15 nm and L ca. 26 nm, and core particle diameter distribution p(D_C). The inset displays diminished contrast of the capping material for the largest particles L in fivefold magnification [111].

motion caused by the enhanced mass of the moving objects.

A basic analysis of Néel and Brownian dynamics has been performed by SQUID ZFC-FC magnetization studies displayed in figure 5.2. Shown is the FC-ZFC magnetization and the difference signal m_{FC} - m_{ZFC}, which can be interpreted in similar manner as the 'master curve' from thermoremanent magnetization measurement, as is illustrated in section 3.2, and corresponds to the blocking temperature distribution p(T_B). All magnetization curves are normalized to the maximum value of low temperature FC magnetization m_{FC}(5K).

For the smallest particles of ca. 6 nm, Néel relaxation is found, as could be also observed for a comparable sample of nanoparticle powder in the previous chapter. The ZFC magnetization reaches its maximum at 40 K, although the difference curve indicates a fluctuation of the majority of magnetic moments already at lower temperatures. The splitting between FC and ZFC magnetization ends at the irreversibility point at ca. 60 K, followed by a Langevin-like

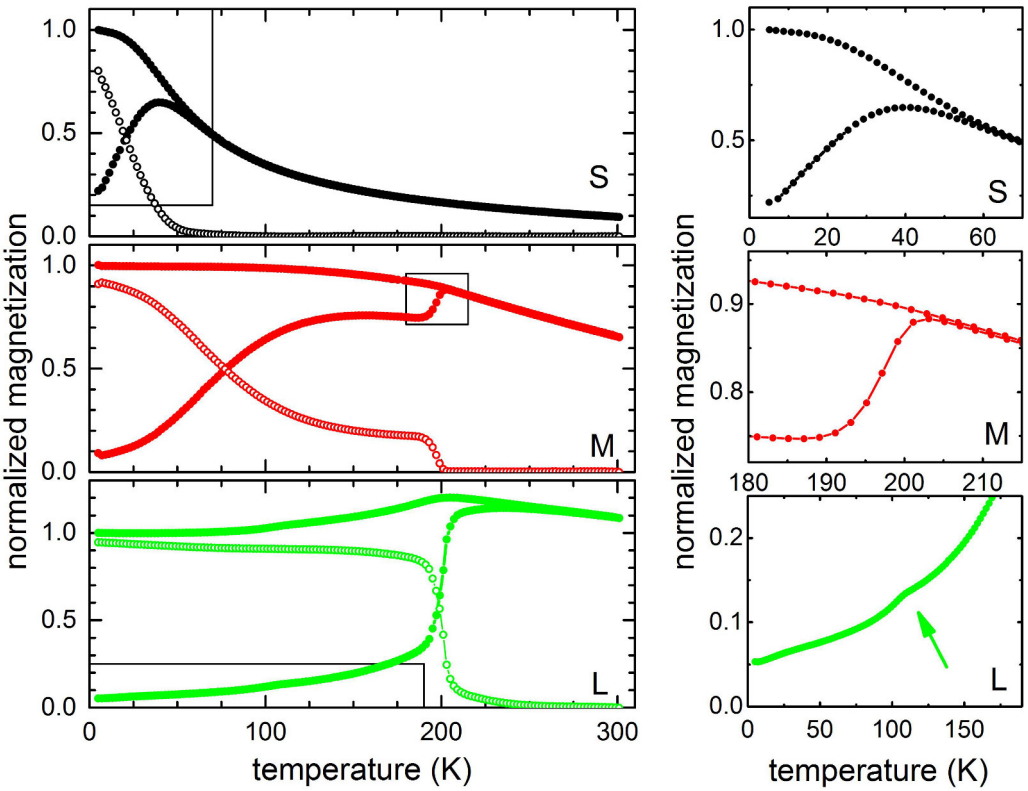

Figure 5.2: Left: Normalized ZFC-FC magnetization curves $m_{ZFC,FC}$ of ferrofluids S, M and L measured in an external magnetic field of μ_0H = 10 mT (dots), and the difference curve m_{FC} - m_{ZFC} (circles). Right: Most relevant regions of dynamic relaxation behavior shown in magnification. Adapted from [111].

behavior at higher temperatures, which translates to a free superspin fluctuation above 60 K on the SQUID time scale of ca. 10 - 100 s. As the particle moments are no longer magnetically blocked, no further change in magnetization behavior by starting Brownian diffusion can be observed upon further heating to the region of moderate ferrofluid viscosities.

Sample M with ca. 15 nm displays higher blocking temperatures with decreasing ZFC-FC splitting up to ca. 200 K. An average blocking temperature of ca. 75 K due to Néel relaxation can be estimated by the inflection point in the FC-ZFC difference curve. It is noticeable that the irreversibility point is not reached below 200 K, where the splitting vanishes relatively spontaneously. The width of this transition is approximately 10 K, deduced from the inset showing this temperature scale in magnification. While apparently the majority of particles already experiences Néel relaxation in this temperature region, the sudden discontinuity can be explained by beginning and rapidly accelerating rotational Brownian diffusion of the larger particles, which remain magnetically blocked up to 200 K by means of the SQUID time scale. This particle fraction, representing about 20 % of the sample's total magnetic moment, also displays superparamagnetic behavior at higher temperatures, presumably due to faster Brownian

motion upon reaching lower viscosities of the glycerol solution.

Even larger particles in sample L display almost completely magnetically blocked behavior in the low-temperature region, which can be recognized by the very small decrease of the difference magnetization curve m_{FC} - m_{ZFC} upon heating. The magnetization exhibits a discontinuity at about 200 K, similar to that observed for sample M, although for sample L a small splitting remains above 200 K that converges to zero at ca. 220 K. The latter may be attributed to beginning agglomeration effects in sample L, resulting in a small number of larger agglomerates with much slower diffusion dynamics. Comparable ZFC-FC magnetization curves were reported before for ferrofluidic systems invented for sealing applications by Schinteie et al., where the discontinuity was explained in terms of the defreezing process of the liquid but unfortunately not discussed in detail [163].

Also visible in magnification in figure 5.2 is a small peak feature in the zero-field-cooled magnetization at ca. 100 - 110 K (green arrow), which indicates the Verwey transition, i.e., the presence of the magnetite phase in sample L with a decreased Verwey temperature compared to the bulk value of $T_{Verwey} \approx 123$ K. It is reasonable to assume a remaining magnetite core in particles of sample L of ca. 26 nm in diameter, conserved by a partially oxidized maghemite passivation shell and the capping layer. To verify the presence of the magnetite phase, Mössbauer spectra of sample S - L were recorded in transmission geometry at temperatures of 80 - 180 K and are shown and discussed in more detail in section A.3 of the appendix. If smaller particles in sample S and M also exhibit a non-oxidized core, the remaining magnetite volume is too small to produce a sufficient feature at the Verwey transition temperature or the signal is broadened too strongly to be detected by a distribution in the size-dependent Verwey transition temperature. Mössbauer spectra of these two samples are likewise inconclusive, as the spectra are widely deformed in the concerning temperature region, which could cover the change in spectral fine structure by electron hopping above the Verwey transition (figure A.2).

The studied solution exhibits are high glycerol concentration of 70 vol% or about 75 wt%. Glassy states have been verified in pure glycerol down to ultralow temperatures of ca. 3 K [164], and glycerol solutions are known to display a glass transition upon decreasing temperature, while a classical freezing process is seldomly observed [66]. Accordingly, it is reasonable to predict the formation of a glass phase below a glass transition temperature T_G, which is extrapolated to ca. 175 K for glycerol solutions in this concentration regime in Ref. [66], without the manifestation of a specific crystalline structure or long range order. In that case, one can model the cooling process by a continuous decrease in molecular mobility or, vice versa, a continuous increase of the dynamic viscosity η during the transition from a highly viscous liquid to an amorphous solid.

If this assumption is correct, the 'onset' of Brownian motion, as it is indicated by the disconti-

nuity at about 200 K in ZFC-FC magnetization curves in figure 5.2, must not be interpreted as a spontaneous change in fluid dynamics. Instead, it is only the crossover from slow to fast diffusive particle rotation compared to the SQUID time constant, caused by the rapid temperature dependent increase in η upon cooling.

This may seem to be a daring presumption, but it can be substantiated by calculations of the low temperature rotation time τ_{rot}. By extrapolation of viscosity literature values in supercooled glycerol solutions one yields an approximate value of $\eta_{200K} \approx 10^4$ Pas [66]. Setting this dynamic viscosity value and the hydrodynamic particle diameter of sample L of about 36 nm into equation (2.17) results in a Brownian rotation time $\tau_{rot} = \omega_{rot}^{-1}$ of about 5 minutes. Present FC-ZFC experiments were performed by applying a constant cooling rate of 2 K/min and displayed a transition region from a partially blocked to the superparamagnetic state of about 10 - 15 K in width, which then translates to a time window of about 5 to 10 minutes, in very good agreement with the aforementioned calculation. This indicates that the distinct feature in the magnetization curve indeed is correlated to a continuous change in dynamic viscosity upon the change from an amorphous solid to the liquid state instead of a melting process, which would presumably result in an even more abrupt change in magnetization.

5.2 Dynamic effects studied by Mössbauer spectroscopy

As mentioned before, the primary objective of this chapter is the simultaneous analysis and quantification of Brownian and Néel relaxation phenomena. In terms of Mössbauer spectroscopy this is possible, as both relaxation mechanisms have completely different influence on the structure of the Mössbauer spectrum.

A sequence of Mössbauer spectra was recorded at 235 - 295 K in steps of ca. 4 K for each of the ferrofluids S, M and L, using a sample holder with an integrated Peltier cooling element, as described in section 3.1 in detail. In figure 5.3, these spectra are shown together with reference spectra measured in a liquid nitrogen cryostat at 150 - 180 K. These reference spectra are used below to determine the spectral structure without effects of Brownian motion due to the solidification of the fluid upon cooling, while Néel relaxation is not expected to show essential changes in relaxation rates between 180 and 235 K.

The reference spectrum of sample L recorded at 150 K consists of only two resolvable sextet subspectra with weakly pronounced inner shoulders implying minimum Néel relaxation. The subspectra correspond to Fe^{+3} on tetrahedral A-sites and an effective $Fe^{+2.5}$ B-site valence state by electron hopping above the Verwey transition. Both subspectra can be well reproduced by usage of the Jones - Srivastava many-state model. The absence of a superparamagnetic doublet and the barely visible asymmetry of subspectra lines indicate a high ratio of anisotropy energy to thermal energy. Calculations by the many state relaxation model yield $\beta = K_{eff}V/k_BT \gtrsim$

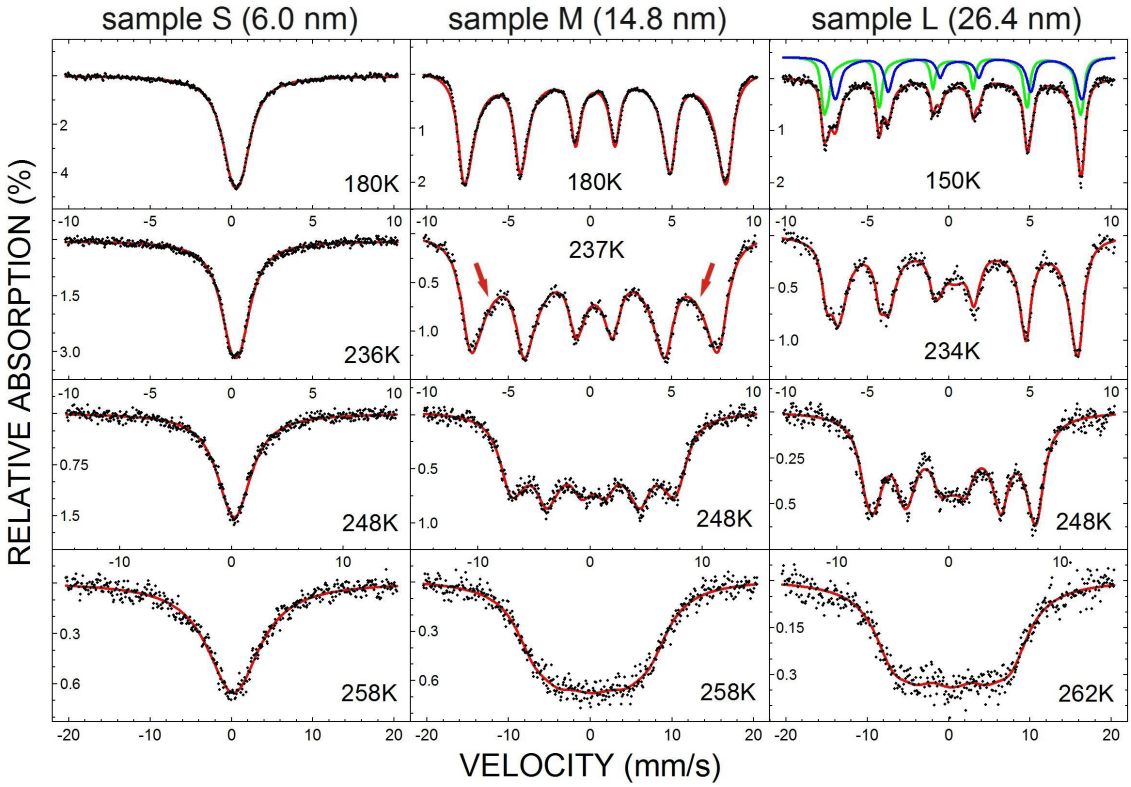

Figure 5.3: Mössbauer spectra of ferrofluidic samples S, M and L measured at 234 - 262 K. Comparatively, low temperature reference spectra of the solidified ferrofluids without Brownian motion are shown on top. Subspectra of iron ions on tetrahedral A-sites (green) and octahedral B-sites (blue) are exemplarily displayed for the reference spectrum of sample L. Inner shoulders visible in spectra of sample M indicate collective excitations (red arrow). Adapted from [111].

20. In this region the model provides no accurate value of the parameter β, i.e., the anisotropy energy E_A, as variations in these parameters have minimum effect on the spectrum. However, by the lower limit approximation of $\beta \gtrsim 20$, $K_{eff} \gtrsim 4\mathrm{kJm}^{-3}$ can be estimated as a lower limit of the effective anisotropy energy density. This value is comparable in magnitude to magnetocrystalline anisotropy constants of $K_1 \approx -12$ kJm^{-3} in bulk magnetite, which is reasonable, as no major contributions by surface anisotropy are expected for 26 nm large particles with highly spherical shape. The nearly spherical shape minimizes shape anisotropy contributions, too.

At 234 K first additional signs of further relaxation appear for sample L, i.e., a slight line broadening that strongly increases upon rising temperature. Above 262 K the sextet structure can no longer be clearly recognized due to severe line broadening $\Delta\Gamma$, which is several times larger than the static linewidth Γ_{stat}. Additionally, an decrease in resonant spectral area occurs, leading to an even faster decrease in spectral intensity by combination with the enhanced linewidth.

Spectra of sample M in figure 5.3 exhibit broadened lines already at 180 K. Even so, the line broadening in this case is a side effect of an increasing asymmetry of the absorption lines, i.e., an apparent distribution in nuclear Zeeman energy splitting, caused by beginning thermal excitation of the superspin within the anisotropy energy minimum of its current easy magnetic direction. It cannot be stated for sure, whether these spectral features originate from collective excitations only or from its combination with beginning superparamagnetic superspin flips. However, as the spectrum does not show any superparamagnetic doublet intensity, a superspin flip rate, if existing, has to be negligible compared to the nuclear Larmor frequency $f_{Larmor} = \omega_{Larmor}/2\pi \approx 30$ MHz. Subspectra of different iron sites cannot be resolved due to this effect and are only noticeable by minor deviations from ideal Lorentzian line shape. Regarding this observation, the spectra were reproduced theoretically using only one subspectrum of a static linewidth $\Gamma_{stat} \approx 0.7$ mm/s in the many state model, the linewidth being enhanced as compared to that of the individual iron-site subspectra of $\Gamma_{stat} \approx 0.45$ - 0.65 mm/s, in the static case.

Here, one has to mention that the definition of the 'static' linewidth $\Gamma_{stat} = \Gamma - \Delta\Gamma$ is restricted to negligible Brownian motion. This means that Néel relaxation, which affects the spectrum by a deformation of the spectral structure itself rather than by a classical line broadening, will also influence the observed linewidth and is still included in Γ_{stat} [72, 100]. To estimate the rate of Brownian motion and, subsequently, the fluids viscosity η, the line broadening by diffusive motion only has to be determined as exact as possible. To assure a fit of experimental data with sufficient quality, an unexpectedly small relaxation parameter of R ≈ 0.01 mm/s had to be applied. For such low values of R, the many state model works in the 'slow diffusion' regime, describing the distribution in the nuclear Zeeman splitting by collective excitation rather than by the superspin flip process itself. Although it is not really feasible to determine anisotropy energies at higher temperatures, the parameter R of 0.01 mm/s is used in the following for spectra of sample M, as it allows a better agreement between experimental data and theoretical spectra and, therefore, a better estimation of Brownian line broadening. To obtain in parallel an approximation of the anisotropy energy, spectra of sample M were alternatively fitted by using a more reasonable value of R ≈ 10 mm/s as described in section A.4 of the appendix, yielding an effective anisotropy energy E_A of about 12.4 $\pm$ 0.5 kJm^{-3}. At elevated temperatures the linewidth in spectra of sample M increases exponentially. In accordance with equation (3.42), $\Delta\Gamma$ is higher than has been found for sample L, due to the smaller hydrodynamic diameter D_{Hyd} of sample M of about 25 nm.

Particles of about 6 nm in sample S are the only ones to display widely superparamagnetic doublet spectra. At 180 K, a transition state similar to a broadened single absorption line is visible, which can be attributed to fluctuation rates in the low GHz regime. The spectrum has been reproduced theoretically by a broadened doublet. In this context, sample S is a particular

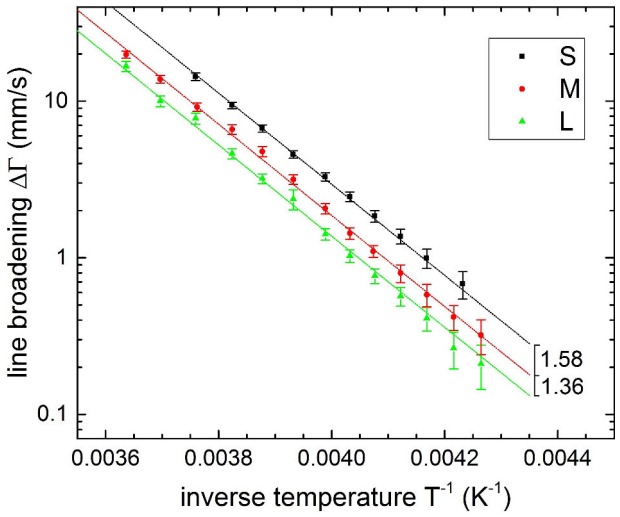

Figure 5.4: Line broadening $\Delta\Gamma$ of Mössbauer absorption lines versus the inverse temperature T^{-1}. Solid lines represent the result of least-squares fitting by the exponential temperature dependence of dynamic viscosity η in accordance with equation (2.18). For ferrofluids S - L the same exponential slope has been used [111].

case, as it displays a considerable change in 'static' linewidth without broadening by Brownian motion, which has not been observed for one of the other ferrofluids so far: Here, a decrease in static linewidth is predicted upon the transition from a broadened singlet-like intermediate state to a well defined superparamagnetic doublet structure at higher thermal energies. This has to be considered carefully, as handling Γ_{stat} as a constant would result in the determination of a negative Brownian line broadening $\Delta\Gamma$ at the lower end of the temperature interval studied. Indeed, the linewidth detected at 236 K is not increased relative to the reference spectrum at 180 K, unlike for ferrofluids M and L of larger particles. In the same manner as it was done for sample L, an upper limit of K_{eff} can be estimated for the 6 nm particles in sample S, based on the calculations by the many state model, as the absence of a superparamagnetic doublet at 180 K indicates an effective anisotropy energy $K_{eff}V \lesssim 3k_BT$, respectively $K_{eff} \lesssim 60$ kJm^{-3}. The line broadening $\Delta\Gamma$ of the three ferrofluids S, M and L, measured in the temperature region of 237 - 273 K, is displayed versus T^{-1} in figure 5.4. Data points of $\Delta\Gamma \gtrsim 20$ mm/s are not shown, because of the difficulty to determine exact linewidths in the absence of a clear sextet structure. Furthermore, large values of $\Delta\Gamma$ are, naturally, accompanied by a considerable loss in spectral intensity, which is additionally decreased by the reduced resonant area at elevated temperatures. A similar problem occurs in the low temperature region. Below 235 K, line broadening of less than 0.2 mm/s is observed. The relative error in $\Delta\Gamma = \Gamma - \Gamma_{stat}$ is, therefore, enhanced, as the accuracy in static linewidths and absolute linewidths is limited to about 0.01 mm/s, depending on the specific sample and spectrum. Due to this fact, and since reference spectra in the liquid nitrogen cryostat had been already measured at about 180 K, recording spectra in the Peltier-cooled setup at temperatures even lower than ca. 237 K was not necessary. The minimum in relative error of $\Delta\Gamma$ can be found at linewidths of about 1 - 8 mm/s, where $\Delta\Gamma$ is already large compared to the static linewidth, but the sextet structure remains clearly visible. Because of this, results in this temperature region will be discussed more thoroughly.

The temperature dependent line broadening displays an exponential increase upon rising temperature with similar slope for all three samples (figure 5.4). In this limited temperature interval the data points can be described very well by an Arrhenius-like function, considering the Andrade equation (2.18) and the correlation of $\Delta\Gamma$ and the dynamic viscosity η by equation (3.42). Therefore, exponential least-squares fits were calculated, which are shown by solid lines in figure 5.4, using the same slope of $m = \frac{-E_{act}}{R}$ for the three data sets. This procedure yields an activation energy density E_{act} of about 55 kJmol^{-1} for all three samples, which is in the expected region between literature values of about 15.5 kJmol^{-1} and 75 kJmol^{-1} of water and glycerol, respectively [165].

Assuming an inversely proportional dependence of line broadening $\Delta\Gamma$ on hydrodynamic radius respectively on hydrodynamic diameter D_{Hyd}, which is based on theoretical predictions as discussed in section 3.1, the ratio of the hydrodynamic diameters between different ferrofluids can be obtained from the offset of the interpolated exponential functions in figure 5.4. The advantage of this method, unlike in calculating D_{Hyd} and capping thickness $s = (D_{Hyd}$ - $D_C)/2$ directly from line broadening, is that systematic errors originating from small deviations in the spherical shape or minor errors in the factor between $\Delta\Gamma$ and D_{Hyd} predicted by theory, contribute to both of the compared interpolated functions in figure 5.4. Therefore, these systematic errors do not affect the calculated particle sizes obtained from the ratio in $\Delta\Gamma$(T). This offset is, as displayed in figure 5.4, 1.58 for sample S to M and 1.36 for sample M to L. Since core diameters D_C are well known from TEM analysis, the average capping thickness s of the nanoparticles is given by equations (5.1) and (5.2). Setting in the above mentioned ratios in this system of equations, the minimum error is achieved for a capping thickness of ca. 5.5 nm. This is in good agreement with the specification from Ocean NanoTech that the hydrodynamic diameter is 8 - 10 nm larger than the core particle diameter.

$$\frac{D_{Hyd,L}}{D_{Hyd,M}} = \frac{D_{C,L} + 2s}{D_{C,M} + 2s} = \frac{26.4\text{ nm} + 2s}{14.8\text{ nm} + 2s} = 1.36 \tag{5.1}$$

$$\frac{D_{Hyd,M}}{D_{Hyd,S}} = \frac{D_{C,M} + 2s}{D_{C,S} + 2s} = \frac{14.8\text{ nm} + 2s}{6.0\text{ nm} + 2s} = 1.58 \tag{5.2}$$

Not only the linewidth, but also the resonant spectral area A_{re} of the Mössbauer spectrum is affected by the Brownian motion of the particles within the ferrofluids. This parameter is usually represented by the Lamb-Mössbauer factor f (also called Debye-Waller factor), that describes the fraction of resonant absorption processes. The decrease in spectral area is illustrated in figure 5.5 (a), comparing spectra obtained in the temperature region of observable Brownian motion above ca. 230 K with several reference spectra at 80 - 180 K. As the Debye-Waller factor exhibits an exponential dependence on the temperature even below the Debye temperature, as has been demonstrated in figure 3.3 of section 3.1, $f(T)$ can be reproduced by a linear function in this logarithmic plot, normalized to $f_{0K} = 1$. Using equation (3.7) the mean

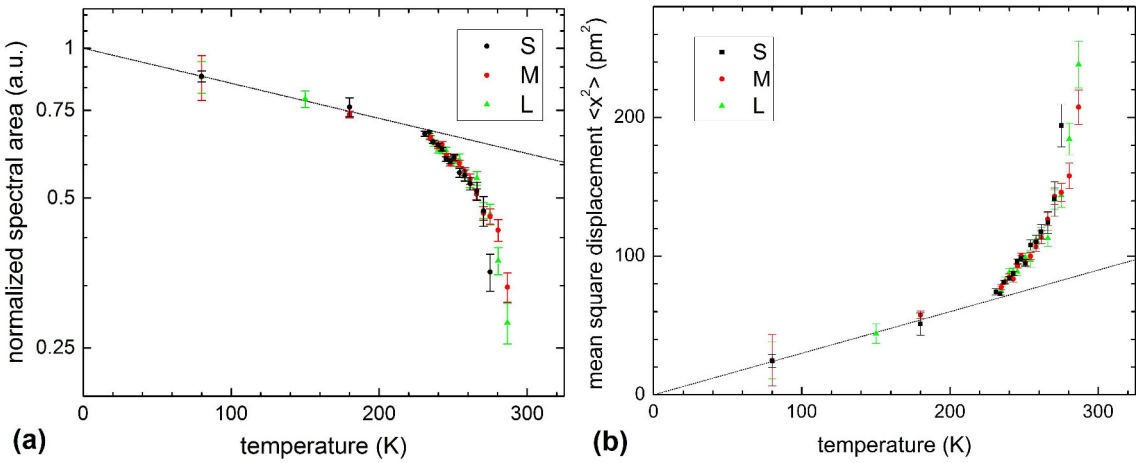

Figure 5.5: Normalized resonant area of Mössbauer spectra of ferrofluids S - L recorded using a bath cryostat at 80 - 180 K respectively a Peltier-cooled setup above 230 K (a) and mean square displacement calculated from equation (3.7). In both graphs, solid lines represent temperature dependent behavior as expected in a solid with a Debye temperature of $\theta_D \approx 290$K, without effects of diffusional Brownian motion.

square displacement by diffusional movement can be determined. This may be not formally correct, since this expression of the Debye-Waller factor has been derived assuming the motion of the iron nucleus close to its ideal lattice position within a harmonic potential. Therefore, as Brownian motion is a process of free diffusion without a defined resting position, calculated values shown in figure 5.5 (b) may be understood as an *effective* mean square displacement in a harmonic potential affecting the resonant spectral area to the same degree as free diffusion at the corresponding temperature.

Experimental data of the ferrofluids coincide well with each other and also with the interpolated exponential functions up to ca. 220 - 230 K, where minor line broadening starts to occur. From the exponential slope $\frac{dln(A_{re})}{dT} \approx 1.7 \cdot 10^{-3}$ K^{-1} in figure 5.5 (a) in the low temperature region a Debye temperature θ_D of about 290 K can be approximated. Debye temperatures of bulk magnetite are reported to be ca. 320 - 330 K [166]. Assuming a minor decrease in θ_D by size effects in nanoparticles of about 15 nm, this is in general agreement with the value of 290 K determined from experimental data.

Above 220 K, the resonant area decreases more rapidly than expected by phononic vibration in the lattice structure of the nanoparticles, as an additional contribution arises by the diffusional movement of the whole particle instead of that of individual atoms. Accordingly, the mean square displacement increases from $\overline{x^2} \approx 60$ pm^2 at 200 K to more than 200 pm^2 at 280 K.

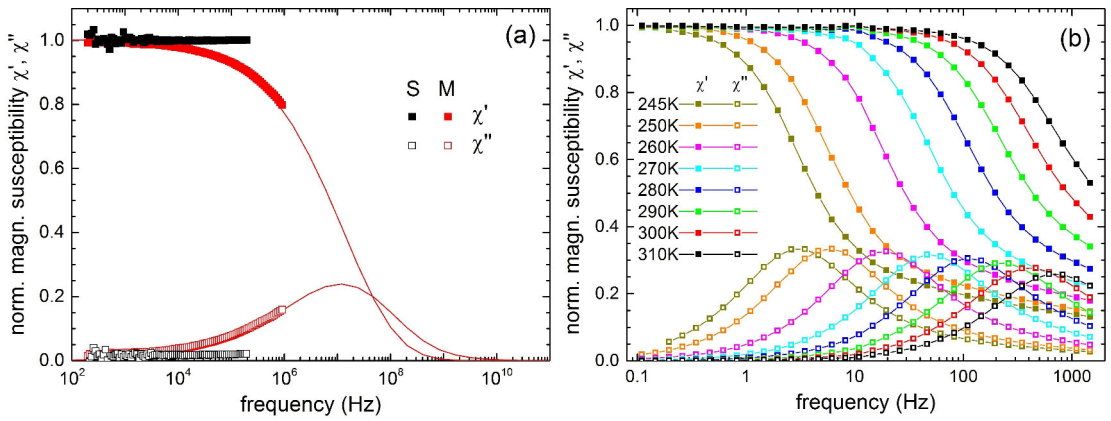

Figure 5.6: Real- (χ', filled symbols) and imaginary component (χ'', empty symbols) of magnetic susceptibility of samples S and M plotted versus the frequency f_{AC} of the external AC magnetic field in the high frequency regime at ca. 300 K (a), and of sample L in the range of 245 - 310 K. Adapted from [111]

5.3 AC-susceptometry

Results of Mössbauer spectroscopy are cross-checked by AC-susceptometry in this section, with focus on the effective anisotropy constants, governing Néel relaxation processes, and dynamic viscosities. It has been explained in section 3.2 in detail that AC-susceptometry is a magnetic measurement technique highly sensitive to changes in net magnetic sample moment, usually working on time scales of milli- to microseconds. While superspin flip processes and diffusional particle motion have different effects on the Mössbauer spectrum, they affect measurements by AC-susceptometry in a very similar fashion through reorientation of the particle magnetic moment. Therefore, it may be difficult to distinguish contributions of both processes in an individual measurement only by considering their relaxation time without further information on the sample. If Brownian and Néel relaxation take place in the same sample in parallel, the usage of an effective relaxation frequency τ_{eff} may be required, but in most cases, Brownian rotation times τ_{rot} and Néel relaxation times τ_{Neel} differ by several orders of magnitudes, whereby only the dominating, i.e., faster relaxation mechanism has to be considered. This could be seen, e.g., in figure 5.2 of section 5.1, where small particles in sample S displayed Néel relaxation only, while predominant superparamagnetism by Brownian motion has been observed by SQUID-magnetometry for 26 nm particles in ferrofluid L. Only sample M, incorporating particles of about 15 nm in diameter, displayed superparamagnetism of mixed origin in FC-ZFC magnetization curves. Regarding these results, AC-susceptometry is applied to obtain a better insight in Néel relaxation effects in sample S, while in sample L reference values of the dynamic viscosity are determined.

In figure 5.6 (a), room temperature measurements of the magnetic AC-susceptibility of sample

S and M are shown in the high frequency regime at $10^2 - 10^6$ Hz. These measurements were carried out by Hilke Remmer, M.Sc., (Braunschweig University of Technology) using a custom-built setup described in Ref. [167] and a field amplitude of 95 μT. For nanoparticles of 6 nm in ferrofluid S no variation in χ' and χ'' is visible in the mentioned frequency range, which indicates that relaxation dynamics of the particle magnetic moments should occur at even higher frequencies. As Brownian rotation frequencies of 1 Hz - 1 kHz are expected for nanoparticles in a high viscosity ferrofluid, these indicated high-frequency relaxation processes have to originate from the Néel relaxation mechanism.

In larger particles in ferrofluid M, beginning Néel relaxation behavior can be observed at frequencies above 10 kHz (figure 5.6 (a)). Experimental data points can be extrapolated by using the Debye relation of the frequency-dependent susceptibility (eq. 3.53) for Néel relaxation times corresponding to the particle core-diameter distribution, which has been extracted from TEM images. The extrapolated function shows a maximum, i.e., an approximation of the average Néel relaxation frequency, at 10 MHz. This value is small compared to the nuclear Larmor frequency, explaining the observation of beginning relaxation effects in the Mössbauer spectra of sample M at ca. 300 K. The best agreement between experimental magnetic susceptibilities and the extrapolation function yields a magnetic anisotropy constant of $K_{eff} = 13.6 \pm 0.7$ kJm^{-3}, using a relaxation prefactor of 20 ps. It should be noticed that this value of the effective anisotropy energy density is very similar to that of 12.4 ± 0.5 kJm^{-3} calculated from Mössbauer spectra using by the many-state relaxation model. Also average blocking temperatures $\overline{T_B}$ determined from difference magnetization curves m_{FC} - m_{ZFC} yield a similar K_{eff} of 15 ± 2 kJm^{-3} in case of ferrofluid M, calculated by equation (2.7), assuming $\overline{T_B} \approx 75$ K and $\Phi = ln(\frac{\tau_M}{\tau_o}) \approx 25$. Estimated values and calculated lower respectively upper limit approximations of anisotropy constants of all samples are listed for comparison in table 5.2.

Also noticeable is the width of the Néel relaxation peak of 4 - 5 orders of magnitude, which is considerably more than observable in case of relaxation by Brownian rotation. However, this behavior is not unexpected, as the Néel relaxation time depends exponentially on the particle volume, wherefore even the highly monodisperse core diameter distribution of the actual sample translates to a very broad distribution of relaxation frequencies. Assuming a similar trend of $\chi(T)$ in ferrofluid S, an average relaxation frequency of at least 1 GHz can be estimated. Lower values would result in a variation of $\chi(T)$ at the limit of observable frequencies of about 1 MHz, caused by fluctuation dynamics of the largest incorporated particles. The lower limit approximation of about 1 GHz would also agree with the doublet-like transition state in Mössbauer spectra of sample S. As Néel relaxation rates in 6 nm particles in sample S are above the observable frequency range, no estimation of K_{eff} can be achieved for this sample by AC-susceptometry. However, approximations of $K_{eff} \leq 60$ kJm^{-3} from Mössbauer spectroscopy

K_{eff} [kJm^{-3}]	ACS	MS	ZFC-FC
S	- - -	$\lesssim 60$	61 ± 7
M	13.6 ± 0.7	12.4 ± 0.5	15 ± 2
L	- - -	$\gtrsim 4$	$\gtrsim 7$

Table 5.2: Effective magnetic anisotropy energy density K_{eff} obtained by Mössbauer spectroscopy (MS), AC-susceptometry (ACS) and ZFC-FC-magnetization curves (ZFC-FC), respectively, as described in sections 5.2 - 5.3.

and ZFC-FC magnetization curves are comparable to anisotropy constants $K_{eff} \approx 40$ - 45 kJm^{-3} determined by several techniques for powder samples of larger non-interacting 6.3 nm particles, as presented in the previous chapter.

For 26 nm particles in sample L, superparamagnetism by diffusional rotation has been observed by ZFC-FC magnetometry, wherefore K_{eff} cannot be determined by AC-susceptometry. However, lower limit approximations of 4 - 7 kJm^{-3} from Mössbauer spectroscopy and ZFC-FC magnetization curves are comparable in magnitude to anisotropy constants of bulk magnetite, which is reasonable since shape anisotropy contributions can be neglected in highly spherical particles and surface anisotropy contributions are of minor importance in particles larger than 15 - 20 nm. In agreement with these observations, no Néel relaxation dynamics are displayed in figure 5.6 (b), and the temperature-dependent magnetic AC-susceptibility has been studied at 245 - 310 K to investigate the variation in Brownian rotation time and the glycerol solution's dynamic viscosity η.

Here, the relaxation peak is almost symmetrical and much sharper than in figure 5.6 (a), as it is of Brownian origin. The average rotational frequency, given by the maximum in χ'' or the inflection point in χ' increases from about 3 Hz at 245 K to ca. 800 Hz at 310 K and is, therefore, in the expected frequency range of rotational motion. Studying the shift between susceptibility curves after equidistant temperature steps of 10 K, one inevitably notices that the increase in f_{rot} is not equidistant, as would be expected from the observed Arrhenius-like temperature dependence of the Mössbauer line broadening (figure 5.4). Additionally, in measurements at, e.g., 245 - 250 K, it can be seen in figure 5.6 (b) that the imaginary susceptibility component χ'' does not decrease to zero, but to a small offset value, which indicates the presence of a minor fraction of Néel relaxation processes at frequencies above 1 kHz.

Based on estimated hydrodynamic particle diameters of 17.0 nm (S), 25.8 nm (M) and 37.4 nm (L) and calculations by equation (2.17), rotational frequencies of the three types of ferrofluids

should not differ by more than a factor of 10. For the biggest particles incorporated in sample L, $f_{rot} \approx 500$ Hz has been observed at ambient temperature, wherefore rotation frequencies of sample S and M have to be in the measurable frequency interval. This is the final verification that their relaxation dynamics are governed by Néel relaxation, as no characteristic features are visible in the above mentioned frequency region. This does not contradict the transition to completely superparamagnetic behavior by Brownian motion as it has been seen in the ZFC-FC magnetization in ferrofluid M (figure 5.2), as the discontinuity observed there occurred at about 200 K. At ambient temperature, even the largest particles in sample M can be expected to display slower Brownian rotation times than Néel relaxation times, as the latter decrease rapidly upon increasing temperature. Comparing predominant Néel relaxation in ferrofluid M and Brownian dynamics in sample L, comparable relaxation frequencies of both mechanisms at room temperature would be expected in ferrofluids containing particles with core diameters of ca. 18 - 20 nm, which would allow more detailed studies on simultaneously occurring relaxation phenomena.

A direct comparison of Brownian dynamics and dynamic viscosities η determined by AC-susceptometry (ACS) and Mössbauer spectroscopy (MS) is limited to ferrofluid L, which is the only sample showing signs of rotational Brownian dynamics only. In AC-susceptometry η can be directly estimated from rotation frequencies using equation (2.17) and hydrodynamic diameters given by $D_{Hyd} = D_C + 2{\cdot}5.5$ nm, since a value of 5.5 nm has been determined for the particle capping thickness by comparison of Mössbauer data of different ferrofluids, as discussed in the previous section. In case of Mössbauer spectroscopy, rotational contributions to line broadening $\Delta\Gamma$ are not considered in a first approximation, wherefore line broadenings from spectra of each sample can be converted in dynamic viscosities by equation (3.42). Dynamic viscosities obtained by these approaches are shown in figure 5.7 between 245 - 310 K (ACS) and 235 - 275 K (MS).

Viscosity data points of different ferrofluids measured by Mössbauer spectroscopy coincide within error margins, if a value of 5.5 nm for the capping thickness is used, as determined from their interpolated line broadening. Furthermore, Mössbauer data display good agreement with results of AC-susceptibility in the region of 245 - 275 K, which is covered by both techniques. In the entire temperature range studied, the viscosity varies from several Pas at 235 K to about 10 mPas at 310 K. This difference of ca. 2 - 3 orders of magnitude in η corresponds, to give an illustrative comparison, to the change from water to motor oil, and is accessible by the combination of both experimental approaches.

In the extended temperature interval of about 235 - 320 K in figure 5.7, the Andrade equation turns out to be only a rough approximation of the temperature dependence of η, while sufficient agreement was found in the smaller temperature interval of about 35 K covered by Mössbauer

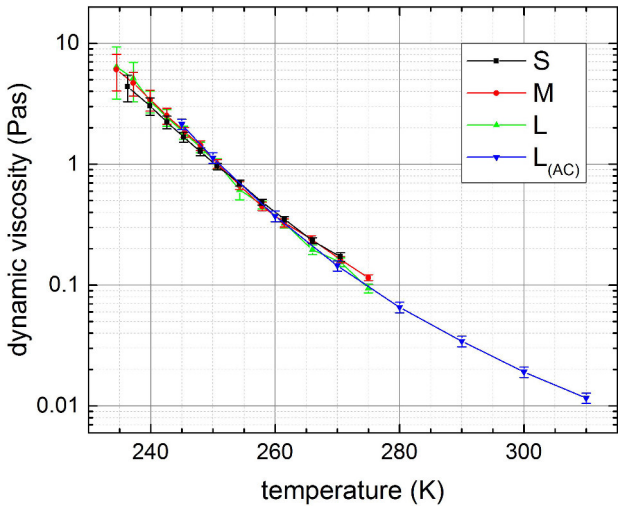

Figure 5.7: Dynamic viscosities η determined from line broadening in Mössbauer spectra for ferrofluids S, M and L and from particle rotation frequencies of sample L observed by AC-susceptometry. All calculations were carried out assuming a particle capping thickness of 5.5 nm. Adapted from [111].

spectroscopy. Instead, η(T) can be described better by the Vogel-Fulcher-Tammann-Hesse (VFTH) equation (2.19). In this model, the Vogel-Fulcher temperature T_{VF} characterizes the point where the viscosity theoretically diverges. In reality, glass-forming liquids adopt solid-like properties at the glass transition temperature T_G, instead. T_G is reported to be ca. 50 K higher than T_{VF} in most cases. For the specific experimental results shown in figure 5.7, T_{VF} cannot be estimated very precisely, as it directly defines the curvature of the $\eta(T)$ function. The latter is difficult to realize, as, e.g., for results of Mössbauer spectroscopy, error margins of the line broadening that are used to determine the viscosity, are at their maximum at the upper and lower limit of the measurable temperature interval, as elaborated before. For that reason, Mössbauer spectroscopy, although it exhibits a comparable overall error margin in η, apparently is the less suitable method compared the AC-susceptibility, when it comes to determining the Vogel-Fulcher temperature T_{VF}, which is found to be ca. 122 $\pm$ 12 K using both data sets in figure 5.7. It is striking that this value is, indeed, about 50 K below the glass transition temperature of ca. 175 K for 70 vol% glycerol solution, theoretically predicted by Gonzales et al. and, therefore, in the expected temperature region [66]. Also comparing the trend in temperature dependent viscosity to literature values shown in figure 5.8, not only general agreement in η(T), but also absolute values of dynamic viscosity matching the region of ca. 75 wt% of glycerol are observed.

All in all it has been demonstrated in this chapter that standard SQUID-magnetometry protocols as well as AC-susceptometry and Mössbauer spectroscopy yield consistent information on Brownian and Néel relaxation phenomena for the three investigated glycerol-based ferrofluids. This may seem obvious, but, as it will be shown in the following chapter in terms of nanoviscosity in nanostructured ferrohydrogels, a local measurement at the atomic scale and at short time scales does not necessarily have to yield identical results compared to macroscopical methods. However, as is shown here, agreement has been observed for three classical Newtonian fluids

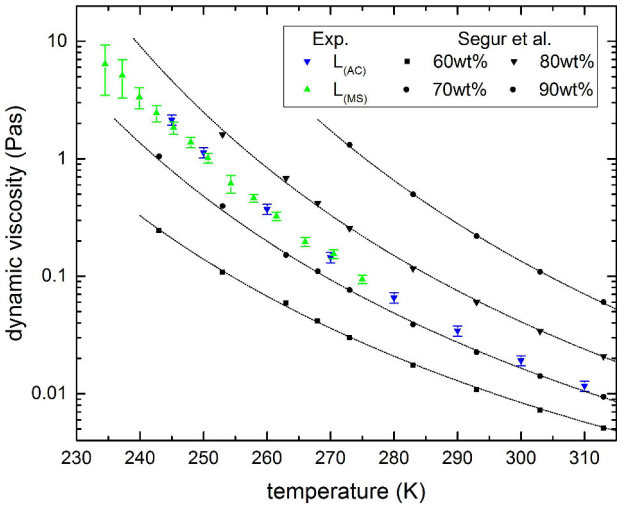

Figure 5.8: Dynamic viscosities η of ferrofluid L calculated from line broadening in Mössbauer spectroscopy (MS) and rotational frequencies from AC-susceptometry (ACS). For comparison, literature values at glycerol concentrations of 60 - 90 wt %, reported by Segur et al., are shown as a reference [168]. Those have been interpolated by the VFTH equation (2.19) assuming continuous variation in parameters η_0 and T_{VF} upon rising glycerol concentration.

studied here.

Estimated values of the effective magnetic anisotropy K_{eff}, as far as they could be determined by ZFC-FC magnetization for a specific sample, are comparable to those determined by Mössbauer spectroscopy. A characteristic increase of K_{eff} upon decreasing particle core diameter from ca. 5 kJm^{-3} for particles of 26 nm to about 60 kJm^{-3} for 6 nm particles was found here. Advantages and disadvantages of the different methods could be evaluated during the determination of the fluid's dynamic viscosity, which was a 70 vol% glycerol solution:

In Mössbauer spectroscopy it is possible to determine parameters of Brownian motion unhindered by possibly existing faster Néel relaxation, which would not be possible by, e.g., AC-susceptometry without further experimental effort. However, at least for the studied set of ferrofluids, evaluation of Mössbauer data yields enhanced error margins in $\eta(T)$ at the upper and lower limit of the measurable temperature limit, which complicates the determination of the Vogel-Fulcher temperature T_{VF} and, i.e., the glass transition temperature T_G. AC-susceptometry, on the other hand, had difficulties to determine the viscosity of these specific ferrofluids, as Néel relaxation is the dominant relaxation effect in two of the samples. Compared to Mössbauer spectroscopy, the ACS method appears to be more straightforward in its interpretation when it comes to Brownian motion, since, e.g., the peak in χ'', marking the average rotation frequency, does not change its shape, whereas Mössbauer spectra at different viscosities can differ widely and require considerably changes in the fitting routine. Furthermore, the effective anisotropy constant K_{eff} could be determined with high precision by AC-susceptometry for sample M, while for sample S no estimation was possible as the relaxation rates were outside of the attainable frequency range. Nevertheless, it has to be mentioned that reasonable values

in agreement with reference measurement could be determined by Mössbauer spectroscopy for the effective anisotropy energy density K_{eff}, the capping thickness s and the ferrofluid's dynamic viscosity η for each sample, and that Mössbauer spectroscopy is capable to determine parameters of both relaxation mechanisms in a single set of spectra, which has been reported in Ref. [111] for the first time as illustrated in detail in the current chapter 5.

6 Nanorheology of ferrohydrogels: Effect of constrained mobility on particle diffusion

In the previous chapter, Brownian dynamics and Néel relaxation of a Newtonian ferrofluid were investigated by Mössbauer spectroscopy and AC-susceptometry experiments. These methods are applied here to study similar processes in nanostructured ferrohydrogels, where particle constraint affects the diffusional motion differently, depending on the locality and time scale of the applied experimental approach. To analyze and quantify this containment effect, AC-susceptometry data are compared with Mössbauer spectra of ferrohydrogels, in which nanoparticles are either embedded in a polymer mesh to hinder particle movement or directly contacted with the polymer strings at their surface. To compare the particle movement with free diffusional motion in a Newtonian liquid, a sucrose-based ferrofluid of identical hematite nanoparticles has been used as a reference system. For each of these two coupling mechanisms, a set of ferrohydrogels was synthesized with different numbers of coupling 'agents', leading to a variation in rigidness of the polymer cages and allowing a more thorough study of the particle-matrix interaction. With the intention to resolve between rotational and translational diffusion, the particles studied are strongly elongated, preventing, e.g., rotation in a tight polymer mesh of the same shape. Additionally, orientational behavior of the ferrohydrogels in external magnetic fields is studied by Mössbauer spectroscopy to analyze magnetic anisotropy constants and the degrees of magnetic and spatial alignment along the field direction.

Utilized hematite nanospindles were prepared by Dr. Lisa Roeder (University of Cologne), by a method originally established by Matijevic et al. [169]. Also ferrofluid and ferrohydrogel samples studied within this chapter containing these particles were synthesized by Dr. Lisa Roeder.

The particle growth takes place in an aqueous solution of ferric chloride $FeCl_3$ (c = 0.02 mol/l) mixed with sodium dihydrogen phosphate NaH_2PO_4. The concentration of the latter can be varied to modify the aspect ratio of the fusiform particles, but was fixed to c = $4.0{\cdot}10^{-4}$ mol/l for particles discussed here. In this way, spindle-shaped hematite nanoparticles were prepared with a length of 387 ± 87 nm and a diameter of 85 ± 15 nm, determined from SEM images as shown in figure 6.1. This corresponds to an aspect ratio p of ca. 4.55. To minimize particle agglomeration in the finalized ferrofluids and ferrohydrogels, the particles have been stabilized electrostatically by treating them with citric acid and tetramethylammonium hydroxide (TMAOH).

0.39 vol% of the prepared nanoparticles were dissolved in 60 wt% sucrose solution under continuous shaking. The dynamic viscosity of similar sucrose solutions is reported to be ca. 20 mPas at ambient temperature, which allows to study relatively slow free diffusive motion and to compare it subsequently with constricted motion in the ferrohydrogels. AC-susceptometry

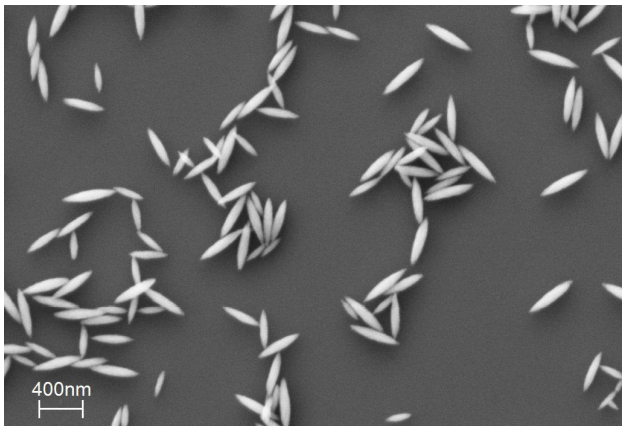

Figure 6.1: SEM images showing hematite nanospindles. An overall identical fusiform shape and size is visible. Particles exhibit an average length of 387 ± 87 nm, a diameter of 85 ± 15 nm and an aspect ratio of p = 4.55 [125].

and Mössbauer spectroscopy results are evaluated in section 6.2 by similar approaches as the glycerol-based ferrofluids discussed in the previous chapter.

Crosslinked ferrohydrogels were prepared from an aqueous solution of hematite nanoparticles, whereto 12.1 vol% acrylamide was added. In parallel to acrylamide, N, N'-methylen (bisacrylamide) (MBA) has been added in different concentrations discussed below, to serve as the crosslinking agent of the forming polymer chains. After cooling this mixture to 277 K, 19.2 μl of each precooled ammonium peroxodisulfate (APDS) and N, N, N', N'-tetramethylethylenediamine (TEMED) were added to start the polymerization reaction after heating the mixture back to room temperature. The process has been performed within a cylindrical polymeric Mössbauer sample holder, to obtain the most suitable sample shape for the planned measurement sequences.

The final ferrohydrogels had a total volume of about 800 μl, reddish color and exhibit a particle concentration of 0.14 vol%, which translates to ca. 0.75 wt%. Three ferrohydrogels of different nanostructure were obtained by tuning the MBA crosslinker concentration, which can be characterized by the mesh size of the forming polymer network geometry. The latter is, in easiest approximation, given by the crosslinking-length ζ_0, which corresponds to the length of the PAAm chain between two MBA nodices and can be approximated by equation (6.1) from the molar fraction $n = n_{MBA}/n_{AAm}$ of MBA to AAm and the monomer size $\alpha \approx 0.58$ nm. This molar fraction has been varied from 10^{-6}, to obtain a weakly crosslinked soft ferrohydrogel, up to $2 \cdot 10^{-3}$, to create a relatively rigid ferrohydrogel, corresponding to mesh sizes of ca. 10 - 400 nm, as listed in table 6.1 in detail. Using mesh sizes much smaller, small, and comparable to the particle dimensions, it should be possible to study different degrees of freedom in translational and rotational particle movement.

$$\zeta_0 = \alpha \sqrt{\frac{n_{AAm}}{2 \cdot n_{MBA}}} = \sqrt{\frac{n \cdot \alpha^2}{2}} \tag{6.1}$$

For the synthesis of particle-crosslinked ferrohydrogels the surface of hematite nanospindles dissolved in water was further functionalized by 3-(Trimethoxysilyl)propyl methacrylate (MTS).

(MBA-)crosslinked ferrohydrogels			particle-crosslinked ferrohydrogels	
sample	molar ratio n	mesh size ζ_0 (nm)	sample	c_{AAm} (wt%)
soft	10^{-6}	410	soft	10.0
medium	10^{-4}	41	medium	16.3
hard	$2 \cdot 10^{-3}$	9.2	hard	22.6

Table 6.1: Synthesis parameters of ferrohydrogels containing hematite nanospindles: molar ratio $n = n_{MBA}/n_{AAm}$ of MBA to AAm and mesh size approximated by the crosslinking length ζ_0 for MBA crosslinked ferrohydrogels [111], which contained 12.1 vol% AAm, each, and AAm mass concentration c_{AAm} in particle-crosslinked ferrohydrogels. Ferrohydrogels were denominated from soft, medium to hard in order of increasing MBA crosslinkage and AAm concentration, respectively.

The preparation of the hydrogel is similar to the above mentioned process: The functionalized hematite nanospindles dissolved in water are mixed with a various amount of acrylamide (AAm), within a Mössbauer sample holder. The samples are cooled down to 277 K and the polymerization process starts after adding APDS and TEMED. As in this case the particles adopt the position as network crosslinkers instead of MBA, now the number of nodices is influenced by the particle concentration, which is comparable to the recipe above.

A constant nanoparticle concentration was used for the preparation of the particle-crosslinked ferrohydrogels, as a variation in particle concentration would also directly affect the intensity of the Mössbauer spectrum. However, the particle mobility on the nanoscale and the macroscopic elasticity, respectively, were adapted here by tuning the overall amount of AAm from 10.0 to 22.6 wt% (see table 6.1). Obviously, a deviant particle mobility could be expected by variation of the basic particle-matrix coupling mechanism from MBA- to particle-crosslinking, although the AAm concentration is comparable for all samples of both sets of ferrohydrogels. They are thoroughly analyzed at the nano- and the macroscale by different experimental methods in section 6.3 - 6.4. A schematic comparison of particle movement and network nanostructure is shown for both types of ferrohydrogels in figure 6.2. A more detailed discussion of the ferrohydrogels' macroscopic shapes and macroscopic texture is presented in the individual sections.

6.1 Antiferromagnetic properties of hematite nanospindles

The canted antiferromagnetic structure of magnetic moments in hematite nanoparticles in combination with the complex magnetocrystalline anisotropy and shape anisotropy contributions due to the elongated shape make a straightforward interpretation of magnetic measurements relatively difficult. Furthermore, additional degrees of directional freedom by spatial orienta-

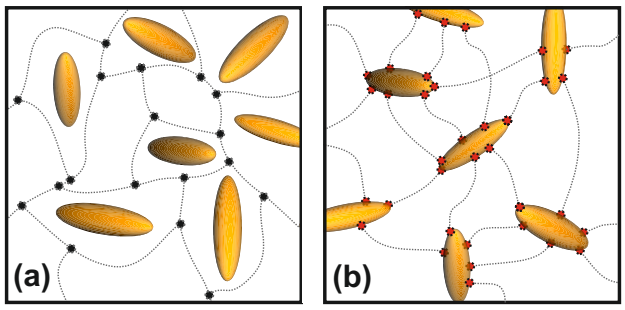

Figure 6.2: Schematic coupling mechanisms in ferrohydrogels realized by (a) particles trapped in network meshes or (b) connected by polymer strings. Nodices of the polymer networks are highlighted by grey (a) and red symbols (b).

tion have to be considered in the ferrohydrogels. To obtain a better insight in particle-matrix interaction and alignment behavior, Mössbauer spectra and in-field orientation of the hematite spindles are studied in this section in form of a nanoparticle powder first, to get a basic understanding of their static and dynamic magnetic properties.

Figure 6.3 displays magnetic hysteresis loops of the nanopowder sample measured by SQUID-magnetometry at 5 and 300 K. Hysteresis loops are visible in the low field regime with coercivities of ca. 50 mT, showing a decrease in area upon heating to 300 K, which may indicate domain wall motion or beginning Néel relaxation. The latter would be surprising, as the particles are large enough to exceed the common definition of ca. 20 - 30 nm as the upper diameter limit for superparamagnetism. However, very small variations in anisotropy energy within the hexagonal basal plane have been reported before, corresponding to a triaxial easy axis system with anisotropy constants in the range of $K_{tri} \ll 1$ kJm^{-3}, corresponding to an anisotropy energy barrier about 3 - 4 orders of magnitudes smaller than the uniaxial anisotropy energy barrier along the c-axis [170]. These may allow collective spin relaxation by the Néel mechanism between triaxial directions within the basal plane even for particles of this size, i.e., a two-dimensional relaxation behavior [34]. A simple approximation of the anisotropy energy barrier by $K_{eff} \cdot V_{NP}$, assuming $K_{eff} \approx 100$ Jm^{-3}, translates to a SQUID blocking temperature of ca. 400 K, which substantiates the aforementioned theory. Additionally, this results indicates that a complete reorientation of the magnetic particle moment within the basal plane may be achieved even in the low field regime, which is in agreement with the saturation of the net magnetization visible in figure 6.3 at ca. 300 - 500 mT. A more detailed evaluation of orientational behavior within and out of the basal plane can be found in section 6.5. The influence of shape anisotropy of the fusiform particles is neglected in the following evaluations, as calculations presented thoroughly in section A.5 of the appendix yield a shape anisotropy constant of $K_{shape} \approx 1$ Jm^{-3}, which is negligible even compared with the triaxial in-plane anisotropy K_{tri}.

In agreement with the net spontaneous magnetization of bulk hematite of ca. 0.38 ± 0.04 Am^2/kg [171], figure 6.3 displays a very small net spontaneous magnetization of about $M_{S,5K} \approx$

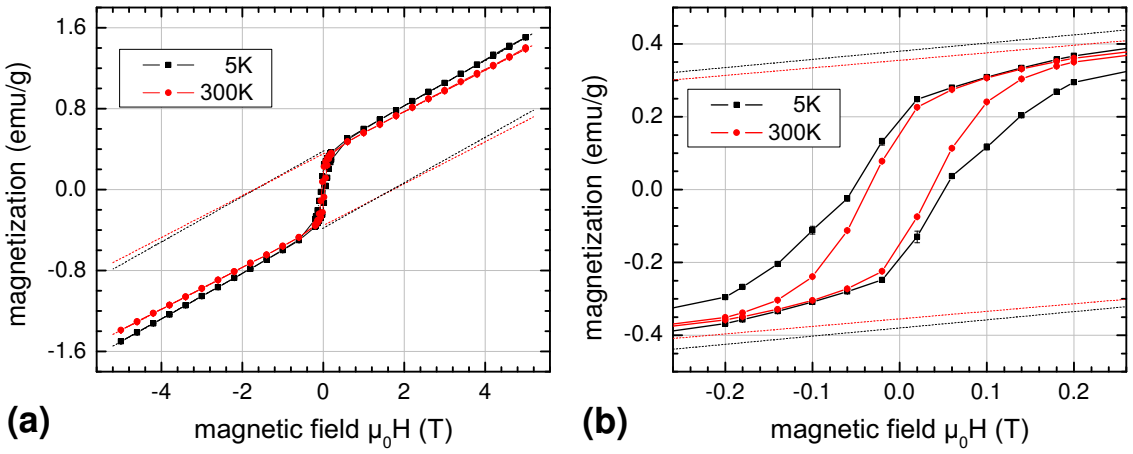

Figure 6.3: Field dependent magnetization M(H) of hematite nanospindle powder (a); the hysteresis loop visible in the low field regime is shown in magnification (b).

0.380 ± 0.005 Am^2/kg at 5 K and $M_{S,300K} \approx 0.355 \pm 0.005$ Am^2/kg at 300 K, obtained from linear extrapolation of the high-field magnetization. These values of the net magnetization correspond to an antiferromagnetic canting angle δ_C of ca. 0.13° relative to the ideal antiparallel alignment of magnetic sublattices. The linear increase at large magnetic fields can be assigned to competing magnetic field energy and antiferromagnetic exchange interaction energy:
The stronger the external magnetic field, the more increases the antiferromagnetic canting angle δ_C, leading to an enhanced net magnetization. The latter is directly given by the vector addition of sublattice magnetizations, wherefore the spontaneous magnetization is found to be $M_S \propto \sin(\delta_C) \propto \delta_C$ for small canting angles. For this approximation one yields $M_{300K,5T} \approx 1.4$ Am^2 and $\delta_{C,300K,5T} \approx 0.48°$ at 300 K at sufficiently large fields. Accordingly, in good approximation one can regard the spins as perpendicular to the net magnetic moment for the evaluation of Mössbauer spectra (shown below).

Another important result of SQUID-magnetometry is the observation of similar net magnetic moments at 5 and 300 K. As the nanospindles are relatively large, one could expect the Morin transition to occur in this temperature interval. Apparently, for the nanospindles no such change in magnetic long range order from canted antiferromagnetism to ideal collinear antiferromagnetism, as has been illustrated in figure 2.2, takes place upon cooling. Thereby, the net magnetic particle moment is almost constant in the whole temperature range studied in this chapter.

Mössbauer spectra of the hematite particle powder are displayed in figure 6.4 for ambient temperature and at 4.3 K without and with a magnetic field of 5 T applied along the γ-ray propagation direction, respectively. Important spectral parameters, obtained from least-squares fitting, are gathered in table 6.2. All spectra show a single sextet of the antiferromagnetically coupled hematite structure without signs of additional iron-bearing phases. At 4.3 K, absorption

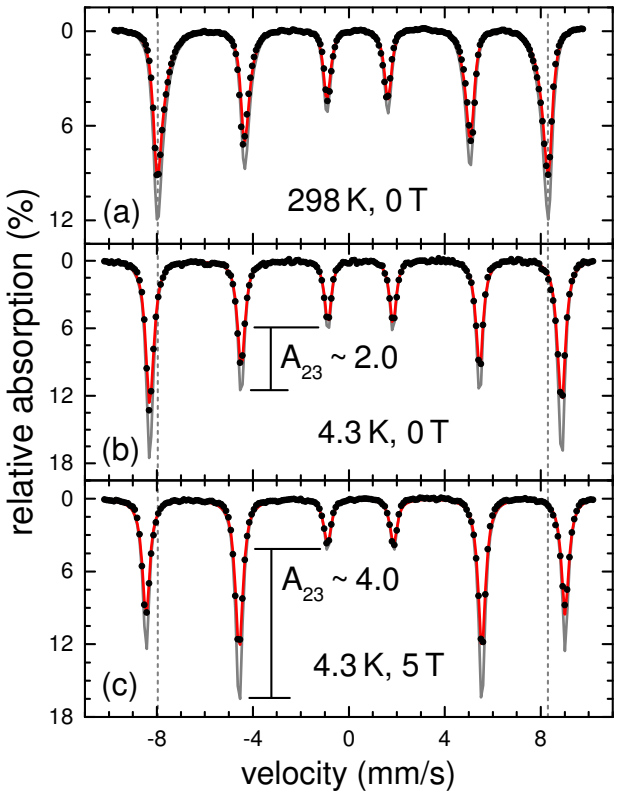

Figure 6.4: Mössbauer spectra of hematite nanospindle powder at room temperature (a), and at 4.3 K without applied field (b), and at 4.3 K in an external magnetic field of 5 T along the γ-ray propagation direction (c). In addition to the least-squares fitted theoretical spectra (red), calculations of the ideal spectrum corrected by means of the transmission integral are shown for comparison (grey).

lines are symmetrical, while at room temperature inner shoulders can be observed, suggesting beginning superspin relaxation by thermal excitation, consistent with the decrease in hysteresis area discussed above (figure 6.3).

All three spectra in figure 6.4 exhibit a similar nuclear quadrupole level shift 2ϵ of about -0.20 mm/s. By comparison with the quadrupole splitting $\Delta E_Q \approx 0.42$ mm/s $\approx -4\epsilon$ an angle of ca. 90° can be found from equation (3.23) between the spin direction and that of the electric field gradient directed along the crystallographic c-axis. In addition to observations by SQUID-magnetometry, this verifies the absence of a Morin transition in the nanoparticles between 5 and 300 K, showing the high-temperature spin configuration of canted antiparallel orientation within the easy magnetic basal plane. From both techniques, it cannot be concluded for certain, whether the Morin transition is suppressed completely or reduced to temperatures below the measurement region. The dependence of the Morin transition temperature T_{Morin} and the particle size has been studied intensively before, and presented comparatively for a large interval of particle sizes in Ref. [47].

Due to the high relative absorption of more than 10 % in the Mössbauer spectra in figure 6.4, a correction of these spectra by the transmission integral method, which is illustrated in section 3.1, is required to obtain a sufficiently precise estimation of spectral line intensities and, i.e., an idea of the spin configuration. These corrected theoretical spectra are represented in figure 6.4 by grey solid lines in addition to the red lines of the original theoretical spectra (least-squares fitted without considering the absorber thickness). Distinct deviations in line intensities of both

	B_{hf} (T)	δ (mm/s)	2ϵ (mm/s)	A_{23}	t_A
298 K, 0 T	49.6(3)	0.370(1)	-0.192(1)	1.94(6)	1.37
4.3 K, 0 T	53.19(1)	0.490(1)	-0.198(1)	1.96(6)	1.32
4.3 K, 5 T	54.16(1)	0.492(1)	-0.205(1)	3.97(9)	1.32*

Table 6.2: Spectral parameters from Mössbauer spectra of hematite nanospindle powder: (average) hyperfine magnetic field B_{hf} (effective field in case of the in-field spectrum), isomer shift δ relative to α-iron at room temperature, nuclear quadrupole level shift 2ϵ, area ratio A_{23} of absorption lines 2 and 3 and effective absorber thickness t_A.

theoretical spectra are visible, proving the necessity of the transmission integral correction. In the 4.3 K zero-field spectrum, the ideal ratio $A_{23} = 2$ of line areas 2 and 3 is expected due to the random particle orientation of the powder sample, allowing a more accurate estimation of the effective absorber thickness t_A to ca. 1.32. This further substantiates the necessity of the spectral correction, as effects of the absorber thickness can be neglected only for $t_A \ll 1$. As the in-field spectrum was recorded subsequently for the identical sample, the same value of t_A has been applied here, yielding a line area ratio of $A_{23} = 3.97 \pm 9$, corresponding to an antiferromagnetic canting angle of $\theta = 86 \pm 4°$ relative to the γ-ray propagation direction, according to equation (3.35) in section 3.1.

Based on the canting angle of almost 90° and the field-independence of the quadrupole interaction, it can be concluded that the particles spatially align perpendicularly to the direction of the external magnetic field. If only the net magnetic moment would change its direction without a spatial reorientation of the particles, this would result not only in the observed increase in line intensity ratio to $A_{23} \approx 4$, but also in a change in the angle between the directions of spin and electric field gradient and, therefore, in the nuclear quadrupole level shift. The peculiar behavior of the hematite particles, to align perpendicular to sufficiently strong magnetic fields has also been verified in subsequent studies by Roeder et al. and Hoffelner et al., by evaluating SEM images of hematite nanospindles, recorded in external magnetic fields of different amplitude [172, 173].

A more precise estimation of the angle between the net magnetic particle moment and the magnetic field direction can be carried out utilizing the increase in effective magnetic field B_{eff} at the ^{57}Fe nucleus detected in in-field Mössbauer spectra. To allow better resolution of the effective magnetic field corresponding to the nuclear Zeeman splitting, the positions of lines 1 and 6 at room temperature in zero external field are marked in figure 6.4 by vertical dashed lines. The increase in hyperfine magnetic field from room temperature to about 5 K is in agreement with the temperature dependence of the Brillouin function. As the spins in the

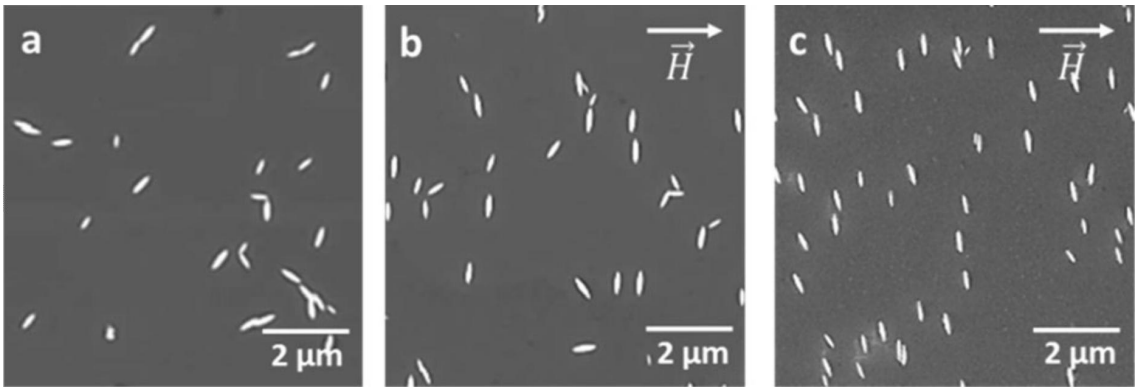

Figure 6.5: SEM images of hematite nanoparticles prepared by the same method and of similar size to those studied by Mössbauer spectroscopy. Drops of nanoparticles dissolved in water were applied and studied, while exposed to external magnetic fields of different amplitudes: (a) H = 0kAm^{-1}, (b) H = 79kAm^{-1}, (c) H = 468kAm^{-1}. The direction of the external magnetic field $\vec{H}$ is indicated by arrows. Figure taken from Ref. [172].

antiferromagnetic hematite particles do not align collinear to field direction, no considerable change in effective field is observed upon raising the field from 0 T to 5 T. Nevertheless, from the small increase from $B_{hf} \approx 53.19$ T to $B_{eff} \approx 54.16$ T, visible in figure 6.4 (b) - (c), a canting angle θ of 81° ± 1° is determined from equation (6.2), which is, essentially, the basic law of cosines. Within error margins this value is consistent with 86° ± 4° determined from the spectral line intensity ratio $A_{23} \approx 3.97 \pm 9$ (table 6.2). It is reasonable to assume that the small deviation between the present canting angles between spin direction and magnetic-field direction relative to the ideal alignment at 90° originates from mechanical frustration of the particles in the powder sample. Incomplete alignment even without mechanical frustration is indicated in SEM images in figure 6.5 (c) of hematite particles ordering on a surface under the influence of an applied magnetic field. Additionally, the intrinsic canting angle of about 1° at 5 T relative to ideal antiparallel orientation has to be considered, as discussed above in terms of SQUID-magnetometry.

$$B^2_{eff,4.3K} = B^2_{hf,4.3K} + B^2_{Appl} + 2B_{hf,4.3K}B_{Appl}\cos(\theta) \Rightarrow \theta \approx 81(1)^\circ \tag{6.2}$$

This method to analyze spin orientation in hematite nanoparticles by comparison of Mössbauer spectroscopy to SQUID-magnetometry is essential for the subsequent study of ferrohydrogels for several reasons. An alternative approach to gain similar information can be realized by optical methods, measuring, e.g., the absorption coefficient in ferrofluids for different particle orientations [16, 174]. By this, the average spatial particle orientation can be determined by the variation in absorbed light in different geometries of the non-spherical particles. However, one has to consider that evaluating the absorption or scattering of light in the visible spectrum usually is limited to transparent samples, whereas highly concentrated ferrofluids and

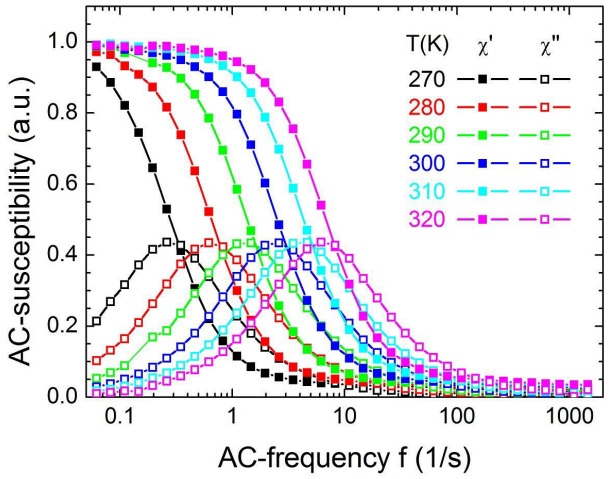

Figure 6.6: Imaginary- (open symbols) and real component (filled symbols) χ' and χ'' of magnetic AC susceptibility of hematite nanospindles in 60 wt% sucrose solution. Measurements were performed using a SQUID-magnetometer with integrated AC-option at 270 - 320 K and 0.05 - 1500 Hz at an AC field amplitude of 4 Oe [125].

ferrohydrogels can be approached more easily by the magnetic techniques discussed here.

Nevertheless, it has been outlined that by in-field Mössbauer spectroscopy at low temperatures combined with data from SQUID-magnetometry as a reference, the spin orientation as well as the spatial particle orientation can be determined relatively precisely exploiting the peculiar crystallographic and magnetic structure of hematite, i.e., the antiferromagnetic ordering of magnetic moments and the orientation of the electric field gradient along the long particle axis, which is identical to the crystallographic c-axis. The same method, which has been carried out successfully for nanoparticle powder here, can be applied to ferrohydrogels in the following, too, if not hindered by severe line broadening, as demonstrated in section 6.5.

6.2 Hematite nanospindles in sucrose solution as a Newtonian reference system

As mentioned before, hematite nanoparticles dissolved in 60 wt% sucrose solution were synthesized as a Newtonian-liquid reference system with measurable Mössbauer absorption line broadening and rotation frequencies visible in AC-susceptibility. Directly comparing ferrohydrogels of different coupling mechanism, it will be studied, whether the particle mobility on the nanoscale is comparable to free diffusion in a medium of enhanced viscosity, as it is the sucrose-based ferrofluid, or whether a more sophisticated theoretical model is required.

In a first attempt to tackle this question, the magnetic AC-susceptibility of the sucrose-based hematite ferrofluid has been measured at various temperatures between 270 K and 320 K and frequencies of 0.05 - 1500 Hz, as displayed in figure 6.6. Due to the suppression of the melting point in sucrose solutions, no freezing in the ferrofluid is expected in this temperature interval even without considering supercooling effects [175]. In general, results of these measurements are comparable to those of glycerol-based ferrofluids of similar viscosity, incorporating smaller particles, which have been discussed in the previous chapter, wherefore their discussion is limited to the most relevant aspects. Imaginary- and real components of the magnetic susceptibility

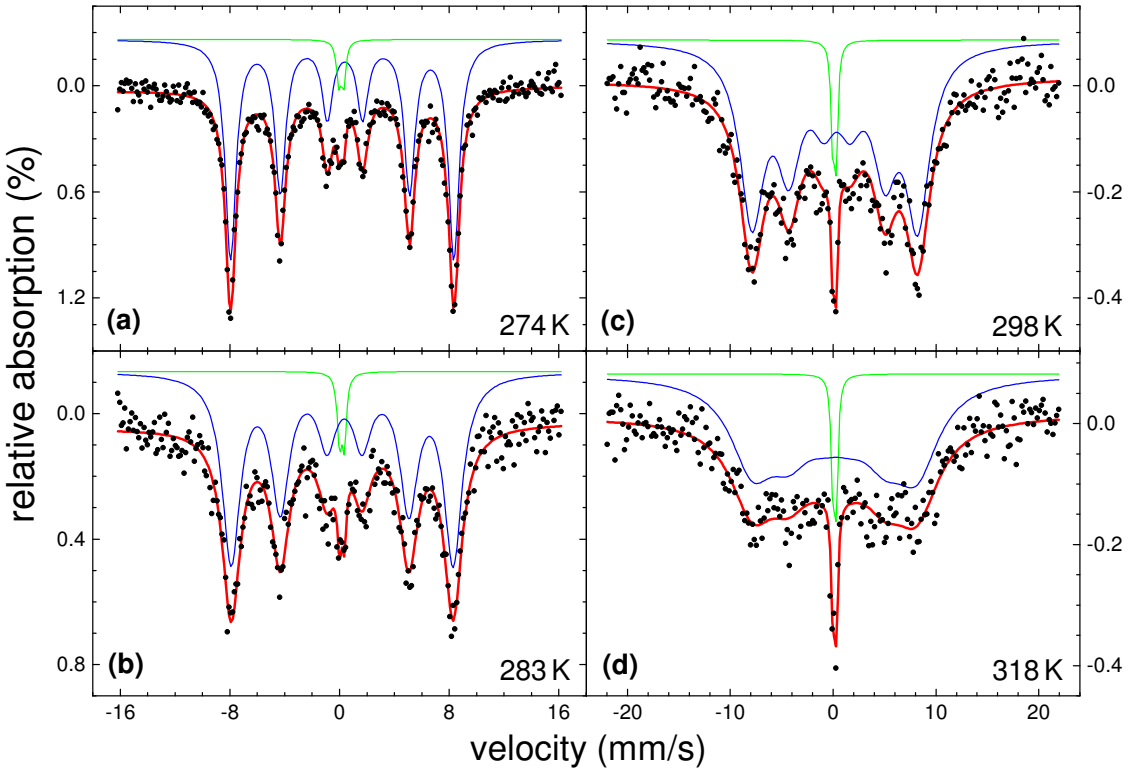

Figure 6.7: Mössbauer spectra of spindle-shaped hematite nanoparticles in 60 wt% sucrose solution recorded at 274 - 318 K. Subspectra correspond to hematite nanoparticles (blue) and minor iron impurities in the aluminum foil used as a reference (green). The broadening of spectral structures by Brownian nanoparticle motion is reproduced by enhanced absorption line width in the least-squares fitting.

have been normalized to the low frequency saturation value of χ'. Peaks of χ'' display a constant normalized amplitude of ca. 0.43, which is close to the ideal value of 0.5, suggesting a minor broadening of the curve due to a distribution in rotation frequencies and particle size, in agreement with the monodisperse character of the hematite nanospindles observed in SEM images (figure 6.1). Maxima in χ'', i.e., Brownian rotation frequencies, shift from ca. 0.3 Hz at 270 K to 8 Hz at 320 K. Despite similar dynamic viscosities η as in the glycerol-based ferrofluids, average rotation frequencies are considerably lower here, which can be assigned to the superior size of the hematite nanospindles as compared to the previously discussed capped spherical magnetite particles.

At low temperatures, Mössbauer spectra of the sucrose-based ferrofluid, shown in figure 6.7, display a structure very similar to that of the hematite nanopowder. Their main component is a symmetrical sextet (blue) corresponding to the antiferromagnetic hematite phase, showing a distinct increase in linewidth up to $\Gamma \approx 5$ mm/s upon decreasing viscosity, i.e., at higher temperatures. An additional central doublet (green) is visible at the center of the spectrum. It can be assigned to minor amounts of iron in the aluminum foil that covered the sample

holder. In the following, this doublet is used as a reference spectrum to the hematite sextet subspectrum, as it can be clearly resolved from the sextet in the whole temperature range and obviously does not display any line broadening $\Delta\Gamma$ by Brownian motion. Thereby, its linewidth is measured at each temperature to check for variations of other origins, e.g., inaccurate velocity calibration or additional broadening caused by the Mössbauer driving unit. Errors from such effects could happen more frequently, as the velocity amplitude of the driving unit is changed often within a series of spectra and is also considerably higher than in conventional Mössbauer experiments. Fortunately, a variation of the doublet linewidth above the error margins has never been observed, which indicates that all reported broadenings of the absorption lines can be assigned to particle relaxation dynamics only.

By analogy to chapter 5, the viscosity of the sucrose solution is estimated from rotational frequencies (AC) and absorption line broadening (MS) using equations (2.17) and (3.42). As these models presume spherical particle shape, some modifications have to be carried out for modeling the hematite nanospindles. From calculations of diffusion coefficients of non-spherical particles, illustrated in more detail in section A.7 of the appendix, it can be seen that the diffusion of an elongated particle can be described by the aforementioned spherical model, using an effective particle diameter corresponding to a spherical particle of similar surface area as the nanospindles, experiencing comparable friction by surrounding fluid molecules.

Squares in figure 6.8 represent values of the dynamic viscosity calculated using an effective particle diameter of $2 \cdot R_{eff} = 140$ nm. By this method, one yields deviating results from both techniques, with viscosities determined by Mössbauer spectroscopy being higher than AC-susceptibility results by a factor of two. This is a surprising result, as very consistent viscosities have been calculated from both methods in the previous chapter for spherical capped magnetite nanoparticles in 70 vol% glycerol solution. It is reasonable to assume the origin of this deviation to be the spindle shape of the hematite particles with distinct elongation, characterized by the aspect ratio of about 4.55. The simple model based on the calculation of an effective diameter apparently is insufficient for particles that deviate considerably from the ideal spherical shape.

To the best of my knowledge, no model has been reported and tested sufficiently to reproduce theoretically Mössbauer spectra of non-spherical particles experiencing free diffusive motion. However, a more appropriate approximation should be accessible using the translational friction coefficient of spheroidal objects and introducing it to equation (2.13). The calculation of translational and rotational friction and diffusion coefficients of spheroidal particles is described in section A.7 in detail, and the approximation of the spindle shape by a spheroid of similar aspect ratio seems reasonable. Using average length and diameter of the nanospindles as extracted from SEM images, the more realistic spheroidal model yields modified rotational and translational diffusion coefficients, influencing the interpretation of the line broadening $\Delta\Gamma$ and

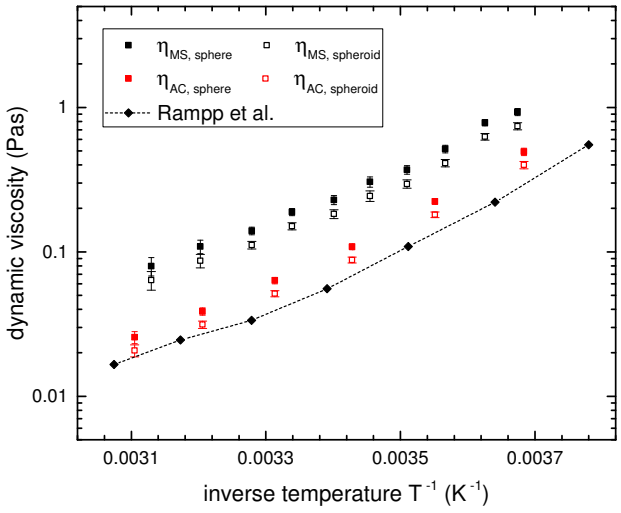

Figure 6.8: Dynamic viscosity η of sucrose-based ferrofluid calculated from Mössbauer line broadening $\Delta\Gamma$ (black symbols) and rotation frequencies f_{rot} from AC-susceptometry (red symbols), modeling the nanospindles by spheres of comparable surface area (squares) or, more precisely, by elongated spheroids (open squares). Macroscopic measurements of η by Rampp et al. from Ref. [176] are shown comparatively (diamonds).

of the rotation frequency f_{rot}. As visible in figure 6.8, dynamic viscosities derived from this model reveal to be smaller compared to those of the spherical model by about 25 %, caused by an increased friction coefficient in elongated particles averaged over all relevant axes of motion, as the model is no longer based on an isotropic body.

Compared to literature reports of the macroscopic viscosity η of comparable sucrose solutions, both Mössbauer spectroscopy and AC-susceptibility yield larger values of η, although it has to be mentioned that rotation frequencies from AC-susceptibility result in a better agreement to macroscopic reference data [176]. Furthermore, for both methods calculated values of η are closer to those determined macroscopically using the spheroidal instead of the spherical model. This may suggest the superiority of the spheroidal model to describe the diffusional movement of the nanospindles for data analysis, although some deviation to literature values remains even in this approach. It is possible that the missing front area perpendicular to the preferred direction of diffusional motion of the hematite spindles, compared to the modeled spheroidal shape, gives rise to a substantial contribution to the translation diffusion coefficient, which affects Mössbauer spectroscopy results only, explaining the larger deviation to literature values seen here. If so, precise measurements of the dynamic viscosities on the nanoscale could be obtained even for highly elongated objects by improved theoretical modeling of more realistic diffusion and friction coefficients, respectively.

In general, one should keep in mind that both techniques yield correct trends in the temperature dependence and magnitude of the dynamic viscosity for fusiform particles of high aspect ratio. This should allow to use the results on sucrose-based ferrofluids discussed in this section as a Newtonian-liquid reference system for comparison with nanoviscosity phenomena in ferrohydrogels hereafter.

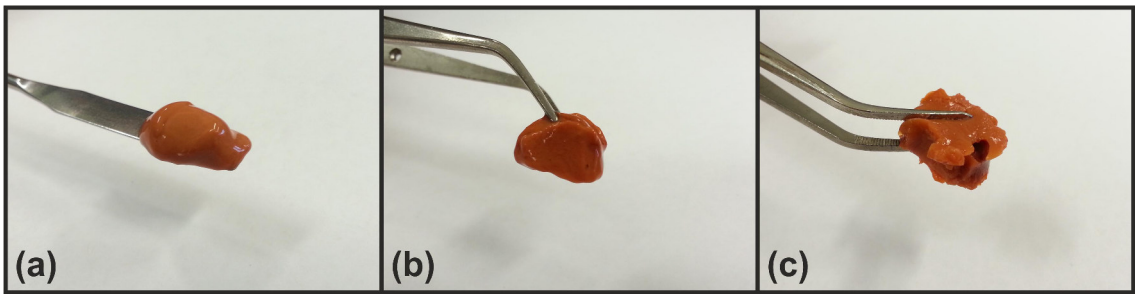

Figure 6.9: Photographs of crosslinked ferrohydrogels with crosslinking densities of $n = n_{MBA}/n_{AAm} = 10^{-6}$ (a), 10^{-4} (b) and $2 \cdot 10^{-3}$ (c). The volume of the displayed sample material used for Mössbauer spectroscopy is about 600 - 700 μl. Highly crosslinked ferrohydrogels exhibit a defined shape and elastic properties, samples of low MBA concentration are in the viscoelastic regime.

6.3 Nanorheology of crosslinked ferrohydrogels

Crosslinked ferrohydrogels have been prepared by the synthesis procedure illustrated above. The macroscopic nature of three samples of identical nanoparticle and acrylamide (AAm) concentration $c_V = 0.14$ vol% and $c_{AAm} = 12.1$ vol% with modified concentration in the methylenbisacrylamide (MBA) crosslinking agent is compared in photographs in figure 6.9. The reddish color of the ferrohydrogels originates from the orange to red coloring of the embedded hematite nanoparticles, while comparable PAAm-hydrogels without incorporated nanoparticles are colorless and mainly transparent [58].

The crosslinking density of this type of ferrohydrogels is characterized by the ratio of MBA to AAm monomers $n = n_{MBA}/n_{AAm}$. The weakly crosslinked sample with the lowest MBA concentration of $n = 10^{-6}$ displays no defined shape in figure 6.9 (a). Experiencing shearing forces it is easily deformed without entirely returning to its original shape. Therefore, its behavior is in the viscoelastic regime, i.e., the intermediate state between an elastic solid and a viscous liquid. Ferrohydrogels of higher crosslinking density shown in figure 6.9 (b)-(c) adopt the shape of the Mössbauer sample holder they are synthesized in and return to this shape after experiencing shearing forces, indicating completely elastic behavior on the macroscale. Additionally, a noticeable hardening of the ferrohydrogel is observed by increasing the crosslinking density from intermediate ($n = 10^{-4}$) to high ($2 \cdot 10^{-3}$) values.

Transmission Mössbauer spectra of the three crosslinked ferrohydrogels in figure 6.10 were recorded in the Peltier-cooled sample holder at temperatures ranging from ca. 240 - 293 K. Up to ca. 270 K, hematite nanospindles embedded in the ferrohydrogel are represented by a nearly symmetric sextet of static linewidth of about 0.4 mm/s. Hyperfine interaction parameters, i.e., isomer shift, nuclear quadrupole level shift and hyperfine magnetic field, are comparable to those of the hematite-nanoparticle powder sample and the sucrose-based ferrofluid at sim-

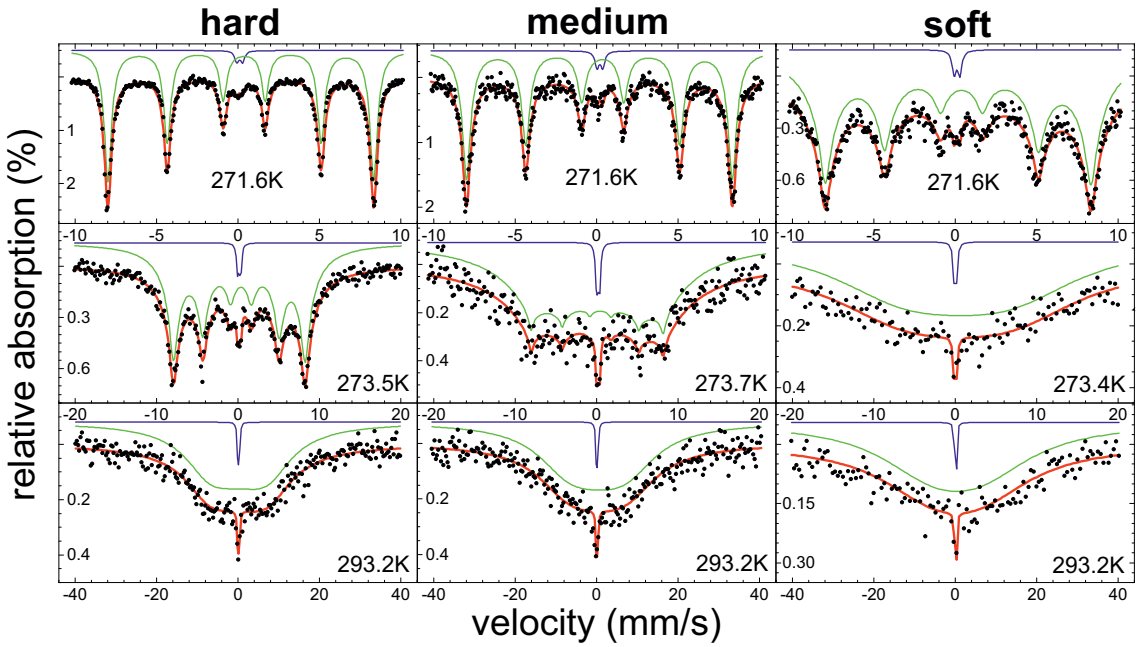

Figure 6.10: Mössbauer spectra of hematite nanospindles (green sextet) embedded in crosslinked ferrohydrogels shown exemplarily between ca. 272 - 293 K. These spectra are reproduced using a linewidth distribution to reflect different degrees of diffusional freedom of the embedded particles. The minor doublet subspectrum (blue) originates from iron impurities in the Al foil covering the sample holder and is used as a reference for linewidth determination. Adapted from [125].

ilar temperatures, within error margins. At about 273 K, a relatively instantaneous increase in linewidth occurs, unlike the quite continuous line broadening $\Delta\Gamma$ with rising temperature displayed by the sucrose-based ferrofluid discussed in the previous section. Additionally, the spectra can no longer be reproduced successfully by a sextet structure of a specific enhanced linewidth Γ. Instead, a distribution $p(\Gamma)$ of linewidths has to be applied to achieve agreement with the experimental spectrum. This effect is exceptionally noticeable in the spectrum of strongly crosslinked ferrohydrogels at about 273 K, where sharp sextet peaks and very pronounced outer peak 'tails' can be simultaneously observed. As sharp peaks of the absorption lines correspond to an almost static linewidth, while the slow decrease in line intensity far away from the peak position originates from considerably broadened spectral components, this indicates states of highly different particle mobility. When discrete values of the linewidth Γ or the line broadening $\Delta\Gamma$ are presented hereafter, these are mean values of the applied linewidth distribution $p(\Gamma)$.

The variation in linewidth Γ upon rising temperature is shown for the three crosslinked ferrohydrogels in figure 6.11. Again, an almost static linewidth may be noticed up to 269 - 271 K, following by a rapid line broadening in the temperature interval of 270 - 274 K, with a

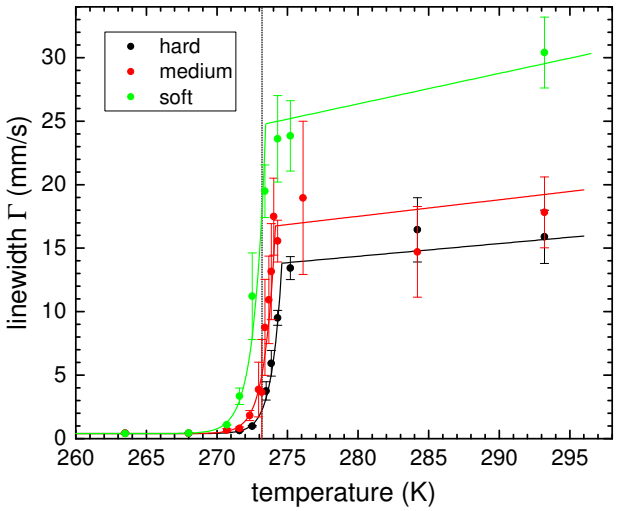

Figure 6.11: Mössbauer linewidth Γ of conventionally (MBA-) crosslinked ferrohydrogels. A distinct increase in linewidth is found close to the water melting point T_{melt}. Also visible are enhanced values of Γ in the liquid ferrohydrogel state for lower crosslinking density. Solid lines are a guide to the eye, the vertical dashed line marks T_{melt}. Adapted from [125].

maximum curvature close to the water melting point. In addition to the calibration of the Peltier sample-cooler illustrated in section A.2, this abrupt change in linewidth may be usable to determine minor differences between the intrinsic sample temperature and the reading of the temperature sensor attached in proximity to the sample, as visualized in figure 3.11.

It should be emphasized, that unlike ferrofluids of particles dissolved in pure water that show a spontaneous freezing process, the ferrohydrogels, although containing 88 vol% of water, display this rapid, but still continuous transition in linewidth and particle mobility, corresponding to a 'melting region' instead of a specific melting temperature. Above the melting region, one would expect that the motion of an approximately free particle is governed by the temperature trend of the dynamic viscosity. For water, being the major component of the hydrogel, the dynamic viscosity decreases from 1.79 to 1.00 mPas for a temperature increase from 273 K to 293 K [177]. An increase in linewidth matching these value does not appear in the measured linewidths. Instead, an increase of only ca. 20 % is detected in the mentioned temperature interval (figure 6.11). The reduced increase in linewidth compared to the trend in dynamic viscosity of water is an indicator of accelerating (upon rising T), but still hindered, motion of the particles in the polymer network structure.

Absolute values of the linewidth in the 'liquid' ferrohydrogel state span from about 25 - 30 mm/s for the weakly crosslinked ferrohydrogel to ca. 15 mm/s for the strongly crosslinked sample, indicating decreasing particle mobility *similar in magnitude* upon rising the crosslinkage by a factor of about 10^3. This relatively minor change in linewidth, i.e., particle mobility on the Mössbauer time scale upon a dramatic change in crosslinking density is surprising and noticeable and may provide additional valuable insight in short-time particle dynamics in combination with further considerations outlined below:

Values of the line broadening $\Delta\Gamma$ in the range of 20 mm/s, representing the major contribution to absolute linewidth Γ above the melting region, are comparable to those measured for sucrose-

based ferrofluids at elevated temperatures. Due to this fact, the ferrofluid can be considered as an adequate reference system to the ferrohydrogels, where the particle mobility is reduced by enhanced viscosity of the Newtonian liquid instead of mechanical particle containment, but resulting in similar particle mobility on the spatial- and time scale of the Mössbauer experiment. Without further knowledge of the nanostructure of the ferrohydrogels it seems reasonable to predict consistent results from experimental methods of different locality and time scale, as it has been demonstrated in the case of the sucrose-based ferrofluids in the previous section.

For comparison with Mössbauer spectroscopy data, the imaginary component of the magnetic AC susceptibility χ'' of the ferrohydrogels measured at 300 K is displayed in 6.12 (a). The reference signal from the sucrose-based ferrofluid is shown complementary, normalized to the same amount of nanoparticles. In contradiction to the hypothesis proposed above, the susceptibility signal of each ferrohydrogel is hardly measurable and negligible in comparison to that of the ferrofluid, showing neither a peak maximum in a similar frequency range close to 3 Hz, nor any other noticeable features. Additionally, no trend in the χ'' signal is visible on variation of the crosslinking density, which is a surprising observation. Although the particle movement presumably is strongly constricted in the more or less rigid polymer mesh surrounding the particle, effectively hindering particle rotation about the short particle axis, a rotation about the long particle axis should not be restricted in principal. The latter would, as mentioned before, result in a variation of the orientation of the magnetic particle moment due to the peculiar magnetic hematite structure, which is, however, not visible by any feature in the observed frequency range.

In the low frequency range, a slight increase in χ'' occurs, which presumably is not caused by spatial orientation of the particles, as it apparently does not depend on the crosslinking density, but rather by a small number of Néel relaxation processes instead, creating a minor and almost constant background in χ''. These processes may be restricted to superspin relaxation within the hematite basal plane, i.e., they may be of two-dimensional character, which, however, cannot be verified here due to the random spatial orientation of the hematite nanospindles within the ferrohydrogel volume. It can be clarified, on the other hand, whether the background signal is caused by Néel relaxation. For that purpose, measurements of χ'' of the medium-crosslinked hydrogel at several temperatures between 230 K and 330 K have been performed as shown in figure 6.12 (b). χ'' increases continuously upon rising temperature in this region, without sudden discontinuities, which would indicate a correlation to the rapid change in line broadening observed near 273 K or additional degrees of freedom attainable at higher temperatures. Thus, it can be concluded that the steady increase in χ'' substantiates its Néel relaxation origin, whereby no considerable signal by Brownian particle rotation in the ferrohydrogels is observable at all in the studied frequency interval.

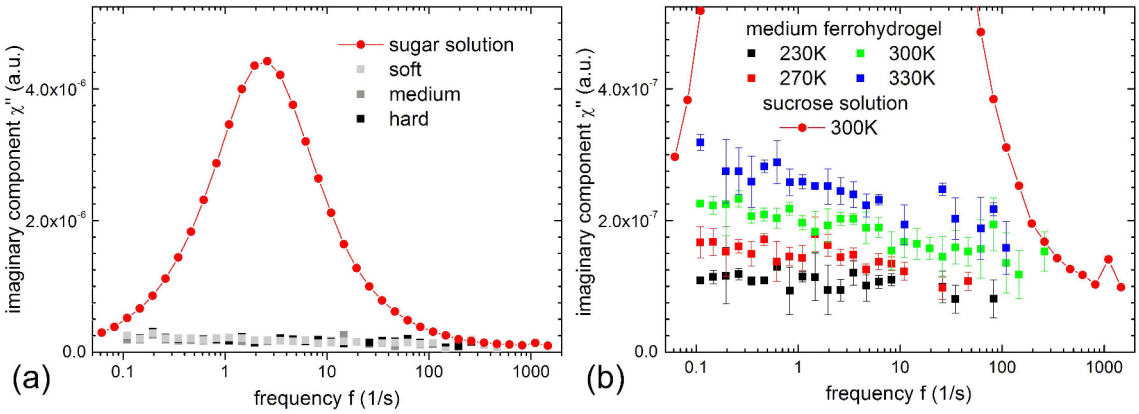

Figure 6.12: Imaginary component χ'' of magnetic AC susceptibility in the frequency range of 0.05 - 1500 Hz: susceptibility signals of ferrohydrogels of different crosslinkage compared to the ferrofluid reference signal (a), adapted from [125], and measured for the sample of medium crosslinkage at different temperatures for comparison (b).

How can this apparent contradiction of distinct line broadening in Mössbauer spectroscopy and negligible χ'' signal in AC susceptometry be explained? In the initial discussion of experimental methods, it has been outlined that Mössbauer spectroscopy exhibits a short characteristic time scale and is a technique sensitive to very local parameters, while the line broadening is primarily caused by translational particle motion. AC-susceptometry, on the other hand, is sensitive to variations in the net magnetic moment on longer time scales by particle rotation, as translational particle motion does not result in a change in the net magnetic particle moment, i.e., the voltage signal induced by the particles detected by the SQUID sensor. Therefore, the explanation for contradicting observations on the particle mobility has to be connected to either the type of motion that is detected, i.e., translational or rotational movement, or to the different time- or length scale of the applied experimental approach, or by a combination of these.

As has been demonstrated in chapter 5, consistent viscosity data have been extracted from both methods studying ferrofluids of spherical monodisperse particles moving in a Newtonian liquid. In sucrose-based ferrofluids, discussed in the previous section, consistent results could be obtained from both methods, too, although absolute numbers of the estimated dynamic viscosity varied, whereby the contradiction between Mössbauer spectroscopy data and those of AC susceptometry cannot be caused by the change in the studied particle shape alone. Thus, the reason for the contradiction in results observed here has to be connected directly to the nanostructure of the crosslinked ferrohydrogels.

Two possible explanations of this phenomenon may be found intuitively: On the one hand, the network structure of the ferrohydrogel could eliminate some degrees of freedom completely, e.g., rotation about or translation along a specific axis, as suggested in the discussion of figure 6.12 (b). Alternatively, the spatial confinement of the particles could limit the free particle motion

to specific short time scales. The motion of gas molecules moving in a defined volume may be an adequate example of such trapped diffusion, as it has been schematically illustrated in figure 2.9. The particles may display free diffusion at the beginning but have to be considered as trapped on longer time scales, where the transition time from trapped to free behavior depends on the diffusional velocity of the particles and the length scale of the free volume.

To some degree, this question can be tackled considering the principle detection mechanism of the applied techniques. In Mössbauer spectroscopy the line broadening has been introduced in correlation to the diffusive particle movement on the timescale of the half life of the excited $I_{3/2}$ state of the ^{57}Fe nucleus of about 100 ns, sensing primarily the translational particle motion due to geometrical reasons, as visualized in figure 3.9. Because of these intrinsic properties, Mössbauer spectroscopy poses a method well suited for the very local study of translational movement of the iron nucleus, which is tightly embedded in the particle in this case, on time scales comparable to 100 ns. One can estimate the mean-square displacement of diffusive motion for the hematite nanospindles in pure water to approximate free movement in the ferrohydrogel, if no 'chains' of the polymer network block the path of the nanoparticle. According to calculations in the spheroidal model in appendix A.7, one yields a friction coefficient of ca. $1.65 \cdot 10^{-9}$ kg s^{-1}. Using this parameter and the viscosity of water at ambient temperature of 1 mPas one can estimate $\overline{\Delta x^2} \approx 0.50$ nm^2 and $\sqrt{\overline{\Delta x^2}} \approx 0.71$ nm within a time interval defined by the half life of the $I_{3/2}$ state of ^{57}Fe.

The average separation between particle surface and the structural units of the polymer network is not known exactly. However, this distance can be reasonably assumed to be only a fraction of the theoretically estimated mesh size ζ_0 and should be correlated to this parameter closely and, therefore, also to the total polymer concentration and the crosslinking density. Basing on these assumptions and considerations, one would predict the observation of distinct line broadening corresponding to quasi-free particle movement within the Mössbauer time scale, if the path of the nanospindle is not blocked on a length scale characterized by $d_{free} \gg 0.71$ nm. The line broadening for completely free motion of the hematite spindles dissolved in water yields about 360 mm/s from equation (A.15) of the spheroidal model. Such large values of the line broadening were not detected, not even in measurements of the hematite particles dissolved in water for reference studies of the agglomeration behavior in section A.6 of the appendix, where maximum values of $\Delta\Gamma \approx 60$ mm/s were reported. Nevertheless, compared to these values, the line broadening in the 'liquid' ferrohydrogels above 273 K of 15 - 30 mm/s are strongly reduced, which implies that the estimation of $d_{free} \gg 0.71$ nm is not valid in the ferrohydrogel nanostructure.

To gain insight in the system by another approach, rotational degrees of freedom can be studied more closely, affecting primarily the AC-susceptometry signals, which are, again, not influenced

by particle translation. However, the above mentioned estimations of geometries and ferrohydrogel length scales, i.e., the particle-surface-to-polymer separation, may be relevant for the resulting rotational motion. For example, experimental data shown in figure 6.12 were recorded at frequencies of ca. 0.05 - 1500 Hz, which translate to relaxation times of about 100 μs to 1 s. On this time scale, the particle diffusionally turns by an average angle of $\sqrt{\overline{\Delta\theta^2}} \gtrsim 0.2 \mathrel{\hat{=}} 10°$ according to equation (2.16). Considering the strongly elongated particle as a cylinder of negligible thickness in easiest approximation, the 'free' angle of rotational motion about the short axis of the nanospindle can be calculated to ca. 0.2° from a radian measure of 0.71 nm and the long half axis a $\approx$ 195 nm as the radius of the rotating object. Hence, free rotation of the spindles about this axis should be possible within the mesh of the polymer network only on time scales much shorter than those accessible by the SQUID setup. The rotation about the long particle axis should, on the other hand, not be restricted, as it does not result in a change in sample volume occupied by the particle, i.e., in contact to the mesh 'walls' by motion of the particle surface. This type of rotation thereby would result in a measurable AC-susceptibility signal, if being in the accessible range of rotation frequencies. Assuming free particle rotation in water on short time scales, an averaged rotation frequency of about 100 Hz would be expected based on equations (2.15) and (A.17), while pure rotation about the long particle axis would correspond to higher frequencies of ca. 300 - 400 Hz according to calculations in section A.7. Nevertheless, no indication of particle rotation about any axis is found in the AC-susceptibility signal.

Of cause, the estimations of length scales in the ferrohydrogel proposed here were carried out assuming a rigid 'wall' of constant position. This is a very simple model for the nanostructure of the polymer network, as the polymer network structure is not a static one, but experiences deformation and movement in water as its surrounding medium. Therefore, approximations of the particle-polymer separation stated above can only be of time- and directional-averaged character. Furthermore, the type of particle constraint has not been defined clearly, which could be realized in the ferrohydrogel, e.g., by a restoring force transferred on the particle in contact with the polymer confinement depending on the current configuration (linear, meandered) of the polymer segment at hand. Assuming that an adequate model of particle constraint could be applied, particle-matrix interactions discussed above still include purely mechanical interactions only. Further indirect interactions acting from particles on the polymer network and vice versa as, e.g., the surrounding medium of water molecules transferring forces on the polymer network as well as on the nanoparticles, have to be considered for a deeper understanding of dynamics in the studied ferrohydrogel geometry. However, hydrodynamic interaction and further types of complex particle-matrix interactions are well beyond the framework of this thesis, dealing primarily with the experimental aspect of nanoparticle relaxation dynamics.

As a final remark, one should keep in mind the proposed explanation, although not being proven thoroughly: Strong line broadening visible in Mössbauer spectroscopy is caused by widely unhindered translational motion, but only on short time scales, as particles come in contact to the 'walls' of the confinement at longer times t. This can be considered as a 'shivering' motion, where the mean-square displacement $\overline{\Delta x^2}$ increases linearly in t, according to the free-diffusion model, while converging to an almost constant value at longer t, which is determined by the polymer content, crosslinking density and geometry of the ferrohydrogel. Because of the high aspect ratio $p > 4$, rotation about the short particle axis is restricted by the shape of the polymer mesh formed around the nanospindle. In combination with the longer time window of the SQUID measurement process, this prevents the detection of any considerable signal of particle rotation by AC-susceptometry.

6.4 Nanorheology of particle-crosslinked ferrohydrogels

In contrast to conventional ferrohydrogels analyzed above, realized by embedding magnetic nanoparticles in meshes of the MBA crosslinked polymeric network, the second set of *particle-crosslinked* ferrohydrogels exhibits a fundamentally different particle-matrix coupling mechanism. While particle-matrix interactions in the first type are restricted to intermittent contact and transfer of momentum between the particles and the confinement represented by network meshes, here the AAm chains are contacted directly to the functionalized surface of the hematite nanospindles. This leads to a restoring force acting on the particle as a reaction on every motion relative to its resting position in the ferrohydrogel network. However, an overall similar macroscopic nature of the ferrohydrogel samples is observed, when compared to the conventionally crosslinked ferrohydrogel of different network structure discussed in the previous section.

Mössbauer spectra of particle-crosslinked ferrohydrogels shown in figure 6.13 display a structure similar to those of the aforementioned conventionally crosslinked ferrohydrogels. Again, a sextet of static linewidth is observed at low temperatures up to ca. 268 K. Close to the water melting point a fast increase in linewidth occurs, which is most pronounced in the ferrohydrogel of the lowest AAm-concentration for a given temperature T, visible exemplarily at ca. 272 K. As discussed in the previous section, the hematite sextet contains contributions of small and large linewidth, representing particles with inequivalent restriction of diffusional movement. This effect could be assigned to random geometries of the individual particle positions, to minor inhomogeneities in the coupling strength within the ferrohydrogel volume, or to intrinsic processes as described by Plachinda et al. [115].

Independent of the actual interpretation, experimental spectra imply that a convenient fitting model needs to include a distribution $p(\Gamma)$ of linewidths, which was realized here by a relatively variable Beta-distribution. The high number of tunable parameters, i.e., width, skewness etc.

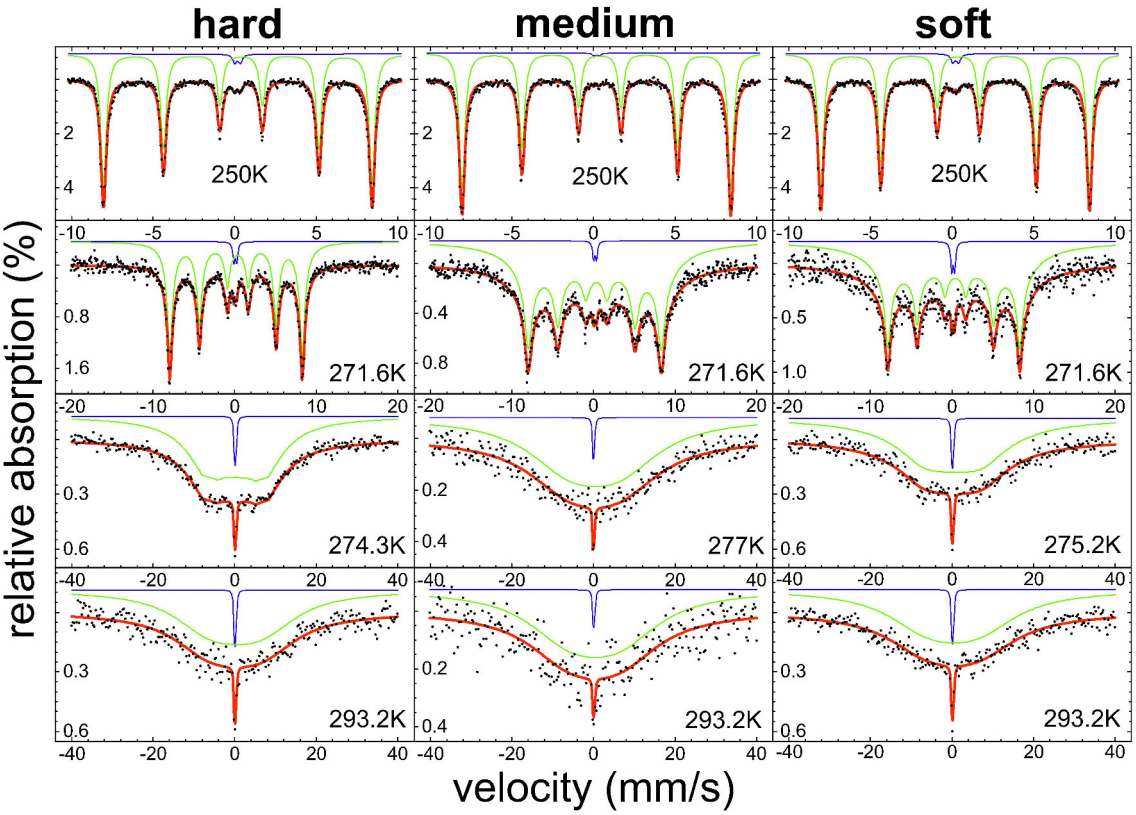

Figure 6.13: Mössbauer spectra of particle-crosslinked ferrohydrogels of different polymer content (soft: 10.0 wt%, medium: 16.3 wt%, hard: 22.6 wt%) recorded at 250 - 293 K. The spectra were theoretically reproduced by analogy to figure 6.10.

of the distribution results in the relatively large error margin visible in figure 6.14, showing the temperature dependent average linewidth. Modifying the Beta-distribution parameters in the model indicates a minor influence of these on $\Delta\Gamma$, wherefore the error margins can be considered as an upper limit approximation here.

As an interesting side effect, a supercooled ferrohydrogel state has been observed when measuring Mössbauer spectra of the ferrohydrogel of medium polymer concentration upon decreasing the sample temperature. Corresponding data points are marked by squares in figure 6.14 and display clearly enhanced linewidths *below* the water melting point. However, for 269 K and especially 263 K, measured linewidths are far below those observed above 273 K. Apparently, by supercooling the dynamic viscosity of the water content is enhanced far enough to be visible in the effective particle mobility, even being already constrained by the attached polymer chains. This poses a promising method to tune the viscosity of the liquid component in gel samples for experimental study, as fluids usually exhibit a strong increase in viscosity below their freezing point in the supercooled state. However, as the minimum size of crystal seeds required for freezing decreases with temperature, the metastable supercooled ferrohydrogel phase could still be maintained at temperatures below 263 K, but showed spontaneous crystallization before a

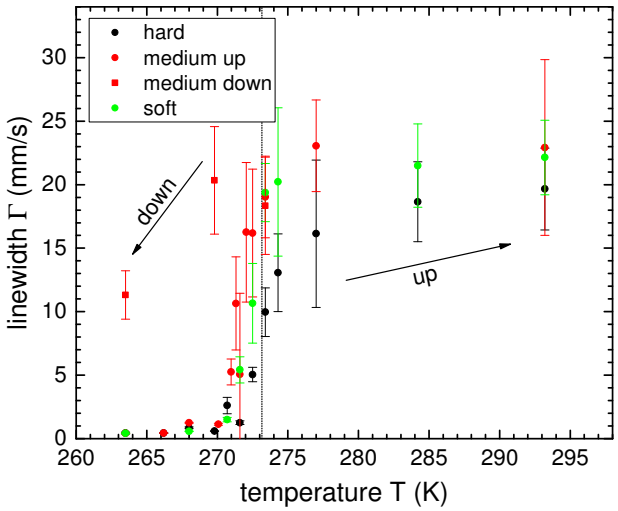

Figure 6.14: Linewidth Γ of particle-crosslinked ferrohydrogels: Series of spectra measured upon rising (circles) and decreasing (squares) temperature. The latter was performed only for gels of intermediate AAm-concentration to study the supercooled ferrohydrogel state. The water melting point T_{melt} is marked by the vertical dashed line.

Mössbauer spectrum of sufficient signal-to-noise ratio could be obtained.

Linewidths of the ferrohydrogels in the 'liquid' state span from ca. 15 - 25 mm/s showing less variation with polymer content compared to the more pronounced dependence in the conventionally crosslinked ferrohydrogels on the MBA crosslinking density. A larger difference in maximum linewidth could have been expected for concentrations c_{AAm} of 10.0 - 22.6 wt%, as the AAm-chains represent the amount of network material stabilizing the ferrohydrogel structure. On the contrary, one could argue that in the particle-crosslinked ferrohydrogels the particles represent the network nodices comparable to MBA-nodices in the conventionally crosslinked ones. In that case, a correlation between the particle mobility and the mesh size characterized by the number of nodices has been demonstrated, the latter being approximately constant in the samples of identical nanoparticle concentration discussed here. Furthermore, as the tuned parameter in this series of samples is the polymer concentration or, vice versa, the water content, an exact quantification of these parameters should have been performed before starting the experiments, since evaporation of water in the ferrohydrogels occurs during longer periods between Mössbauer experiments, which was not known at this time. Due to this effect, the precise AAm concentration, known from the synthesis process, could have been falsified to some extent, as the samples were not measured in parallel, but sequently, whereby different losses of water by evaporation are possible.

To study the dependence of particle mobility on the polymer concentration, and to quantify the error margin by water evaporation, an additional series of reference measurements was performed subsequently, tuning the water content of the medium ferrohydrogel sample. For that purpose, the sample was warmed up to about 45°C and put in a desiccator for 1 - 30 minutes to evaporate a fraction of the incorporated water, before recording a Mössbauer spectrum. The sample needs to be prewarmed to accelerate the evaporation process due to the rapid cooling caused by the drop in air pressure in the desiccator, which can even freeze the ferrohydrogel.

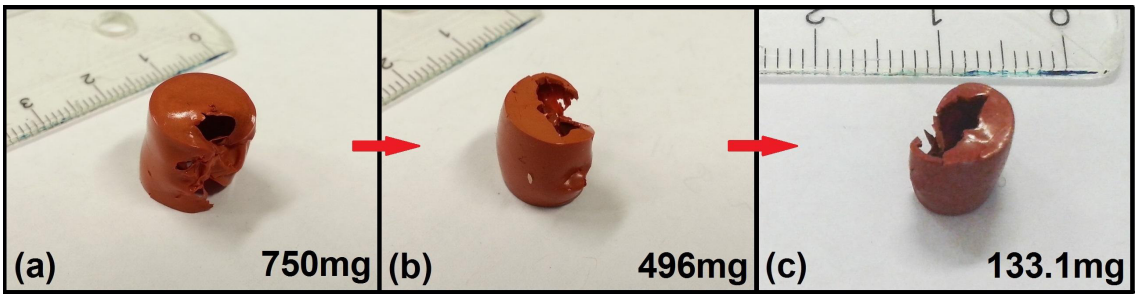

Figure 6.15: Photographs of the medium particle-crosslinked ferrohydrogel during different stages of increasing water evaporation (a) and (b); (c) shows the completely dried sample.

By this method the sample mass was reduced from ca. 750 mg stepwise to a minimum value of 133.1 mg as illustrated in figure 6.15, where photographs during different stages of water evaporation are shown. Upon progressive water extraction, the sample loses most of its volume, and is no longer elastically soft, but instead hard and brittle. The deformed shape of the sample visible in the photographs results from the attachment of the deformable sample volume to the inside walls of the cylindrical sample holder, resulting in the formation of a hole in the center of the sample. Afterwards, the sample adopted the shape of a hollow cylinder irreversibly. The latter has, however, no effect on the measured Mössbauer spectrum, as it modifies the macroscopic shape of the sample, but not its nanoscopic network structure.

Repeated treatment of the sample at a remaining mass of 133.1 mg did not result in a further weight decrease, whereby the ferrohydrogel consisted almost completely of acrylamide and hematite nanospindles at this step of the sample treatment. Subtracting the particle mass of 4.6 mg, calculated from the known particle volume concentration and the density of hematite of about 5300 kg/m^3, a polymer mass of 128.5 mg remains, which can then be used to determine the water respectively polymer content of sample masses achieved during stepwise water evaporation.

Linewidths Γ, respectively the line broadenings $\Delta\Gamma$ of absorption lines in the recorded Mössbauer spectra, are shown in figure 6.16, where the interval of AAm concentrations originally covered by the three prepared particle-crosslinked ferrohydrogels is marked in grey, representing the starting point of the series of spectra upon water evaporation. Above this range, no considerable decrease in line broadening takes place before reaching polymer concentrations of about 50 %, which explains the almost negligible difference in linewidths of the three particle-crosslinked ferrohydrogels observed at ambient temperature in the liquid ferrohydrogel state. From 50 - 70 %, where the particle mobility is strongly reduced by the enhanced density of polymer chains in proximity to the particles, a distinct decrease in linewidth occurs. At even higher concentrations of 70 - 100 % the linewidth converges relatively fast to the static value

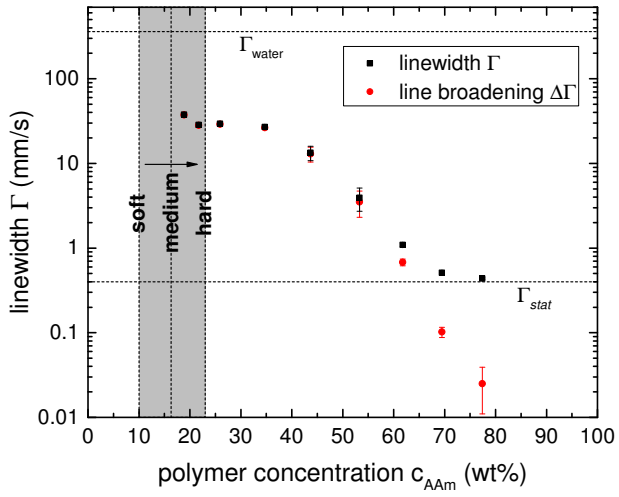

Figure 6.16: Linewidths of medium particle-crosslinked ferrohydrogels) measured at c_{AAm} = 18 - 75 wt%. Horizontal lines mark the theoretical linewidth $\Gamma_{water} \approx 360$ mm/s of spheroidally modeled nanospindles moving in water and the static linewidth Γ_{stat}. The regime of initial polymer concentration of the three ferrohydrogels is highlighted.

of about 0.4 mm/s. In this region, the motion of the particle may be modeled more precisely by a vibration within an elastic solid.

The other 'direction' towards lower concentrations of acrylamide in figure 6.16 could not be studied. However, the experimental data points apparently do not indicate a trend to the theoretical value of about 360 mm/s in linewidth. Possibly such a value cannot be achieved as long as the polymer chains are attached to the particle surface or the curve would have to show a new region of functional behavior below 10 - 15 %, alternatively corresponding to widely free motion of particles still connected by a very small number of polymer chains. Obviously the variation in polymer concentration in particle-crosslinked ferrohydrogels has a minor effect on the particle mobility at Mössbauer time scales as compared to tuning of the concentration of the MBA crosslinking agent in conventionally crosslinked ferrohydrogels.

6.5 Field-induced particle orientation in viscoelastic matrices

The primary objective by embedding magnetic nanoparticles in viscoelastic and elastic matrices is twofold. On the one hand, the nanoparticles may serve as a magnetic probe for the elastic or viscous properties of the surrounding medium, as has been extensively demonstrated in the previous sections. On the other hand, by the orientation of preferably non-spherical particles tightly coupled to the matrix material in sufficiently high external magnetic fields, a designed deformation of the matrix material is achievable. To tune the matrix-volume deformation at a specific field, exact knowledge of the deformation in the vicinity of the particle is extremely helpful, and can be determined by measuring the direction of the particle moment μ_{NP}. However, the effective magnetic anisotropy energy of the particle has to be considered here, too, as the partial alignment of μ_{NP} can be obtained by a particle rotation from its resting position by an angle of φ_1, accompanied by a presumably elastic deformation of nearby matrix material, as well as by orientation of μ_{NP} by an angle φ_2 relative to its easy magnetic direction. In most

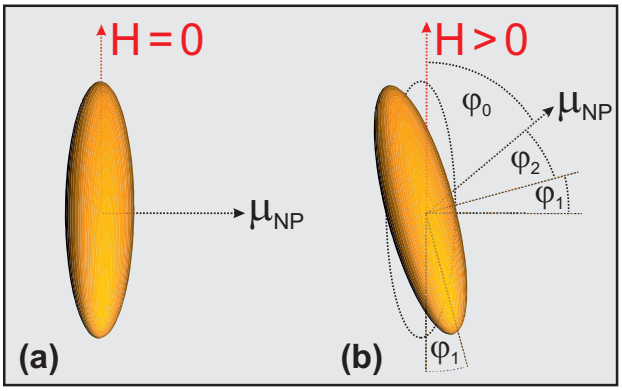

Figure 6.17: Schematic orientation process of the magnetic particle moment μ_{NP} in a deformable medium by a magnetic field H: For H = 0, there is a random orientation of μ_{NP} relative to the magnetic field direction (a). For H > 0, μ_{NP} obtains partial alignment along H, turning by an angle φ_2 relative to the particle's easy magnetic axis, and by spatial particle reorientation by an angle φ_1.

cases, a compromise of the relevant energy contributions is found by nonzero angles φ_2 and φ_1, as illustrated by figure 6.17, where φ_1 is limited by the elasticity of the matrix material and φ_2 by the particles magnetic anisotropy energy. The overall misalignment angle φ_0 relative to the field position is relatively easy to estimate from the deviation of net magnetization along field direction from saturation magnetization by standard magnetometry. On the other hand, some effort has to be made to determine the individual angles φ_1 or φ_2, e.g., by combining magnetometry with optical absorption experiments in external fields [16], the ladder being hindered in opaque ferrohydrogels and comparable compound materials. However, due to the peculiar magnetic structure of the hematite nanospindles used in this series of experiments, it is possible to determine the spin orientation relative to a specific particle axis *and* to the field direction in principle. This has been exemplarily demonstrated in the most simple case of nanospindle powder in section 6.1 by the study of hyperfine interaction parameters from in-field Mössbauer spectra.

To reproduce this successful experiment in the more complex system of hematite nanospindles incorporated in a ferrohydrogel, Mössbauer spectra were recorded in transmission geometry with external magnetic fields of up to 950 mT applied perpendicular to the γ-ray propagation direction. As the setup including the utilized electromagnet does not allow transmission along the field axis, this geometry was used instead. The experiments were carried out on the particle-crosslinked ferrohydrogel of highest polymer concentration of $c_{AAm} \approx 22.6$ wt% and the strongly MBA-crosslinked ferrohydrogel mounted in the sample holder with an integrated Peltier cooling element. The experiment was performed at about 263 K as a starting point, where alignment of the magnetic particle moment μ_{NP} is only possible by its orientation relative to the lattice structure, as the particle itself is pinned in its position by the frozen surrounding matrix, and, thus, cannot rotate. Further spectra were recorded at ca. 272 K, where beginning line

broadening indicates some degree of particle mobility in the hydrogel matrix.
Typical spectra from this series of measurements are shown in figure 6.18. Upon increasing the applied field amplitude, the main effect in the spectrum is a variation in the line intensity ratio A_{23}, which is correlated to the average canting angle θ between spin and γ-ray propagation direction. The trend of A_{23} on the field amplitude is displayed in figure 6.20 (a). The ratio in spectral line area A_{23} decreases from 2 at zero field, which translates to a random spin orientation, roughly linearly to ca. 1.35 at 300 mT, followed by a further slow decrease to about 1.3 at the maximum applied field of 950 mT. The intrinsic reorientation processes are relatively complex, wherefore they are illustrated schematically in figure 6.19 and described in detail in section A.8 of the appendix to provide a thorough understanding of the complete mechanism. There, it is demonstrated that an A_{23} ratio of 4/3 corresponds to an alignment of the net magnetic particle moment μ_{NP} along the field direction as far as possible *within* the easy magnetic basal plane of the hematite structure. This means, that the direction of μ_{NP} is identical to the projection of the applied field direction on the basal plane of each individual particle. This leads to partial alignment of the spins, which are perpendicular to the net magnetic moment, along the γ-ray propagation direction, which is, again, perpendicular to the external magnetic field. Therefore, it can be assumed that the magnetic particle moment turns towards the specified projected direction at fields up to 300 mT. This value will then represent a maximum value for particles, in which the field direction is far off from the easiest magnetic direction the particle moment adopted. This assumption is further substantiated by the observation that the saturation moment of the canted antiferromagnetic structure is reached at about 200 - 300 mT as observed by SQUID-magnetometry studying the nanoparticle powder. Neglecting higher orders of uniaxial anisotropy energy E_{uni}, one can assume the anisotropy in hematite in first approximation to be given by [34]

$$E_A = V_{NP} \cdot \left(-\frac{K_{u1}}{2}(\cos^2(\alpha_1) + \cos^2(\alpha_2)) + \frac{K_{tri}}{2}(\sin^6(\alpha_1)\cos(6\beta_1) + \sin^6(\alpha_2)\cos(6\beta_2)) \right) \quad (6.3)$$

Here, K_{u1} is the uniaxial anisotropy constant, α_i the polar angle between the spin direction of sublattice i and the c-axis, K_{tri} the triaxial anisotropy constant, β_i the azimuthal angles of sublattice i, respectively, with $\vec{s_1}$ and $\vec{s_2}$ being almost antiparallel. For the more simple case of an alignment within the basal plane, the first part of the equation can be neglected, wherefore a combined anisotropy energy barrier of $4 \cdot E_A = 4K_{tri}V_{NP}$ has to be exceeded for alignment of the particle moment by the magnetic energy $E_{mag} = \mu_0 H \mu_{NP} = BM_S V_{NP}$. In this simple approximation, the triaxial anisotropy in the basal plane can thereby estimated by the identity of both energies (E_A and E_{mag}) at the average magnetic field, at which the magnetic particle moment is aligned in the basal plane along the projected field direction. Using an average required magnetic field of ca. 150 mT, the hematite density of $\rho_{hem} \approx 5300$ kg/m^3 and

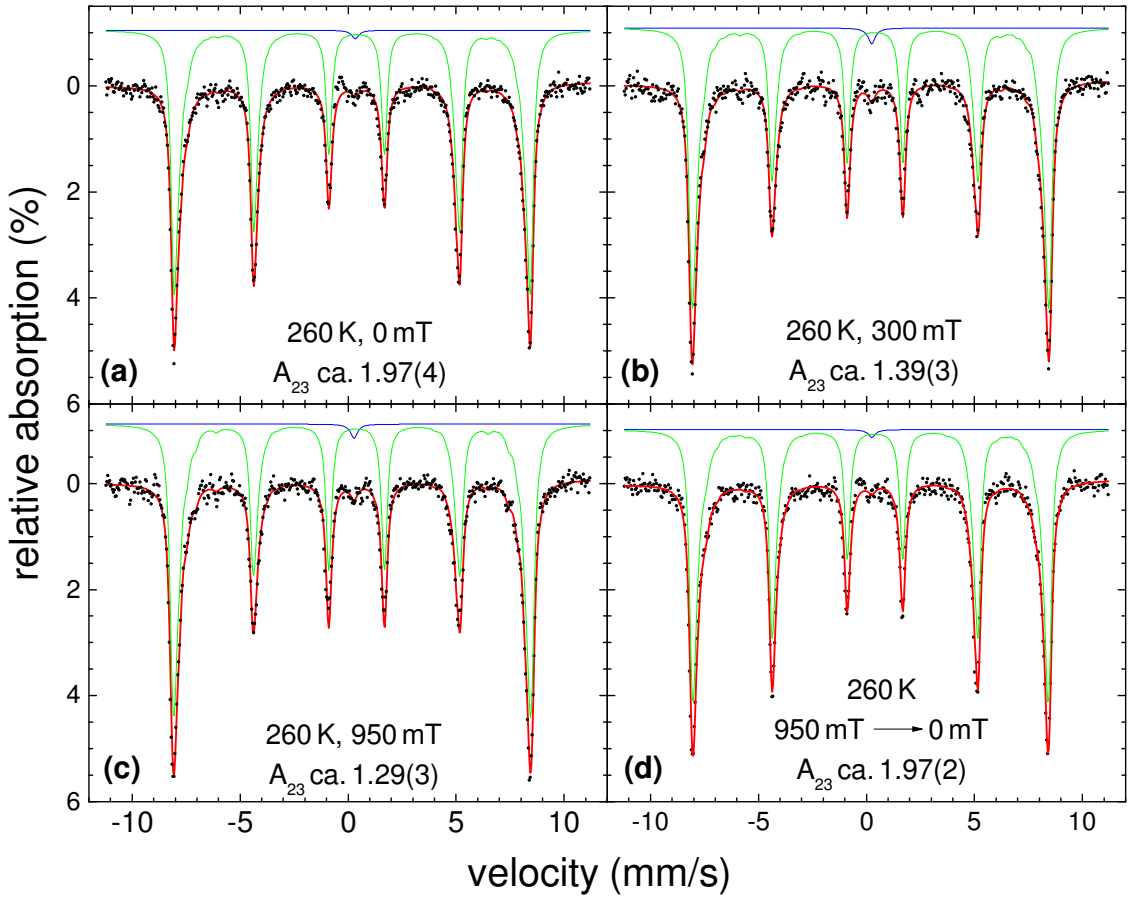

Figure 6.18: Typical Mössbauer spectra of the strongly particle-crosslinked ferrohydrogel measured at 263 K and at (a) 0 mT, (b) ca. 300 mT, (c) ca. 950 mT and in remanence at 0 mT recorded subsequently to spectrum (c). A relatively sharp hyperfine field distribution p(B_{hf}) was used to reproduce minor spectral deformations by collective excitations.

the hematite saturation magnetization of 0.355 Am^2/kg at room temperature from SQUID-magnetometry, shown in figure 6.3, one yields a triaxial anisotropy constant K_{tri} of about 70 J/m^3 from this consideration. This is comparable to reported values from magnetic torque experiments on bulk samples [32].

To check if the orientation process of magnetic particle moments is reversible, magnetic fields of 300 mT respectively 950 mT were applied to the sample and decreased to zero again, to measure the remanence Mössbauer spectrum of the ferrohydrogel. These two data points are marked by red arrows in figure 6.20 (a). Almost no deviation to the line ratio $A_{23} = 2$ of random orientation is observed in remanence, meaning that the orientation within the easy basal plane is a reversible one, *or* that the magnetic particle moment μ_{NP} can perform two-dimensional fluctuation relatively freely within the basal plane by Néel relaxation due to the minimal anisotropy barrier between the triaxial directions [34]. As a similar behavior is observed at the beginning of the melting region at ca. 272 K, this general model of the magnetic

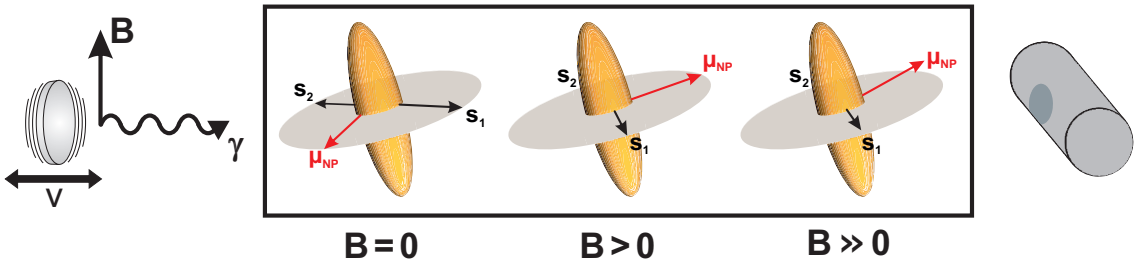

Figure 6.19: Schematic illustration of magnetic orientation in hematite nanospindles: The magnetic field is aligned perpendicular to the propagation direction of the γ-ray. Alignment of the particle magnetic moment μ_{NP} within the easy magnetic plane is obtained first, followed by the development of an out-of-plane component of μ_{NP} at higher field amplitudes. The particle is assumed to be fixed in its spatial orientation, matching observations from Mössbauer experiments in and below the melting region of the ferrohydrogel.

reorientation process seems to be valid not only assuming a fixed particle in a frozen matrix, but also in rigid matrices allowing relatively small deviations of the particle from its original resting position and orientation.

As the line intensity ratio A_{23} slowly decreases above 300 mT to values smaller than 4/3, which cannot be explained by orientation within the basal plane only, one has to assume an additional orientation process, which could be a minor misalignment with respect to the easy magnetic plane, i.e., partial alignment along the very hard magnetic direction of the hexagonal c-axis. This can be clarified by studying the field-dependence of the nuclear quadrupole level shift 2ϵ, shown in figure 6.20 (b), which is coupled to the angle θ between spin direction and c-axis according to equation (3.23). Indeed, a minimum decrease in the absolute value of 2ϵ is found. By linear interpolation the following approximative function is obtained

$$2\epsilon(H) = -0.201 \pm 0.001 + (0.0053 \pm 0.0023)\frac{\mu_0 H}{T} \tag{6.4}$$

Obviously, this linear approximation is valid only in the small field regime, while 'small' means negligible magnetic energy as compared to the uniaxial anisotropy energy barrier. For example, an angle θ of 84.7° ± 1.7° instead of the expected 90° relative to the c-axis can be estimated from equation (3.23) and $2\epsilon(950\text{ mT}) \approx -0.196$ mm/s at the maximum external magnetic field of 950 mT. This indicates partial alignment along the hard magnetic c-axis in sufficiently strong external magnetic fields, which supports the above mentioned hypothesis on magnetic orientation behavior.

In conclusion, by the analysis of the line intensity ratio A_{23} and the nuclear quadrupole level shift 2ϵ, some insight in the orientation process of the magnetic particle moment was won. However, most of these experiments were performed on the frozen ferrohydrogels before reaching the completely 'liquid' ferrohydrogel state, wherefore the question could not be clarified in detail to

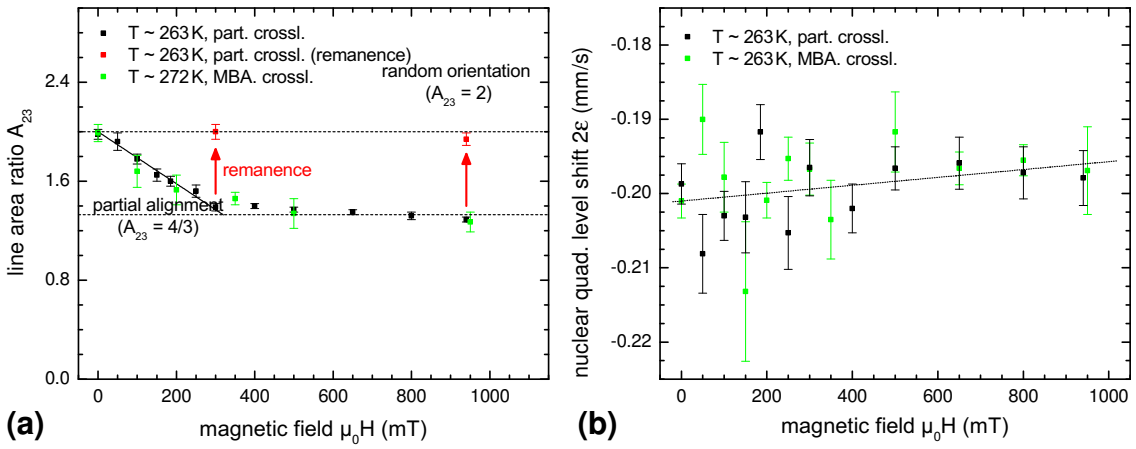

Figure 6.20: Line intensity ratio A_{23} (a) and nuclear quadrupole level shift 2ϵ (b) of the hard particle-crosslinked ferrohydrogel (black) and the strongly conventionally (MBA) crosslinked ferrohydrogel (green) in external magnetic fields perpendicular to the γ-ray propagation direction. Additional measurements were performed in remanence (red) and indicate nearly complete reorientation to the initial state.

which degree the particles rotate spatially and to which degree the moments align within the particles, to gain minimum total energy in an applied magnetic field. It has to be mentioned that this series of experiments represents only a starting point for more extensive studies in the 'liquid' ferrohydrogel state above the water melting temperature. The reason for the restriction to frozen ferrohydrogels here originates from the vast line broadening of ca. 15 - 25 mm/s at room temperature, which prevents any accurate determination of A_{23} and especially 2ϵ. Thereby, experiments as designed above would be limited to ferrohydrogels of larger particles or more rigid gels of, e.g., minor water content, showing smaller line broadenings even in their liquid state, as both spectral parameters can be extracted with sufficient accuracy from spectra with linewidths in the range of 3 - 5 mm/s. Similar experimental setups may be promising candidates for the investigation of the particle mobility in magnetorheological fluids affected by external magnetic fields, i.e., for the measurement of the magnetoviscous effect, too.

7 Relaxation effects in solid matrices: Raspberry particles in meltable polymer-composites

In addition to intrinsic relaxation effects, which are discussed in the previous chapters, parameters of a magnetic hybrid system, first of all the temperature, can also be varied by externally driven processes. Examples of crucial interest, e.g., for medical applications, are magnetic hyperthermia and related techniques. These methods utilize AC- or rotating magnetic fields to change the orientation of the magnetic particle moment in ferrofluids or soft matter compounds, either by reorientation of the particle magnetic moment relative to the particle crystal lattice or by rotational motion of the whole particle, experiencing a torque in the magnetic field:

Considering Néel relaxation only, the net magnetic particle moment μ_{NP} is provided to overcome the anisotropy energy barrier periodically by the external AC magnetic field, followed by relaxation of μ_{NP} to the equilibrium state of minimum energy, whereby the invested energy will dissipate and result in local warming of the compound material. Heating can also be obtained for particles, magnetically blocked in terms of Néel relaxation, by field-driven rotational Brownian motion of the particle in a liquid medium, caused by friction of the particle surface with fluid molecules [9]. In addition to Néel relaxation and Brownian motion, a third method of magnetization reversal is induced domain wall motion in magnetic polydomain particles, also resulting in local heating, which is proportional to the area of the magnetic hysteresis loop and the frequency of the applied magnetic AC field. The latter effect is not considered in the current chapter, as the studied particles are clearly below the critical size limiting monodomain behavior.

The heating of magnetic compound materials has the advantage of being very localized and tunable in transmitted heating power. Therefore, it can be exploited not only for cancer treatment, but also for the external control of other temperature driven phenomena. The system studied in the current chapter consists of polycrystalline iron oxide nanoparticles capped by oleic acid and embedded in dextran ester to form biopolymer compounds (biocomposites), being solid at ambient temperature. By heating in an external AC magnetic field of limited amplitude, remote melting, i.e., the melting of the compound material and a decrease in the dynamic viscosity upon further heating, is intended. In this state active pharmaceutical ingredients (APIs) incorporated in the composite material would be released, wherefore the system could be applied as a magnetic field controlled reservoir for drug delivery [178]. To optimize the heating ability of the particles for a specific magnetic field amplitude, the particles' magnetic relaxation behavior as well as their diffusive motion in the molten polymer as an intrinsic measure of its dynamic viscosity are examined by Mössbauer spectroscopy and magnetometry methods. Amongst other open issues, an essential question is, whether the particles move as

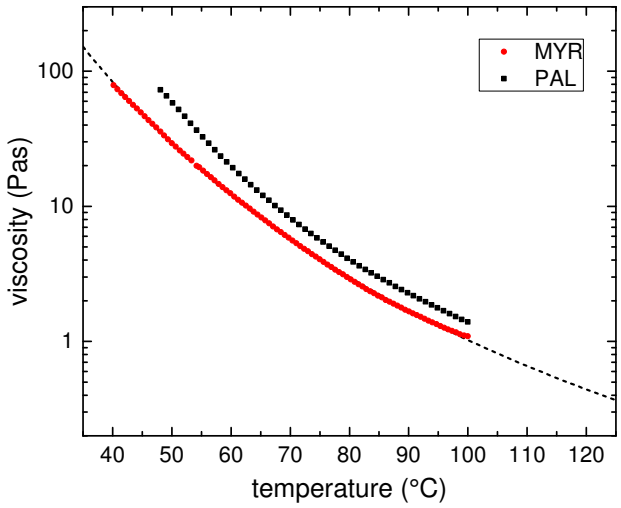

Figure 7.1: Dynamic viscosity η measured macroscopically in the range of the melting point up to ca. 100 °C. Viscosity interpolation functions were determined for polymers MYR and PAL according to the VFTH equation (2.19) and are shown exemplarily for sample MYR [179].

particle clusters, larger agglomerates or individual objects in the polymer melt, which critically affects their energy uptake, respectively their heating ability, by rotational Brownian motion.

7.1 Structure of raspberry particle - polymer compounds

The temperature dependent properties of the matrix material, representing the dominant component of the biopolymer compound, can be tuned by the length and geometry of the chosen polymer chains. Variation in these two parameters results in an increase in polymer melting temperature from room temperature up to about 130°C, as reported by Zhou et al. [178]. Two types of biocomposites are studied in the scope of this chapter, which were synthesized by Mengbo Zhou, M.Sc., (University of Jena) based on dextran myristate ester (MYR) and dextran palmitate ester (PAL), denominated accordingly MYR and PAL for sake of simplicity. Measurements by differential scanning calorimetry subsequently carried out were used to estimate the polymer melting temperature and were crosschecked by direct observation using a hot stage microscope [178]. Melting temperatures were found to be 40 - 45 °C for the myristate-based polymer and 45 - 50 °C for palmitate-based material. It has been demonstrated in Ref. [178] that these polymer compounds can be transferred to the liquid state above the melting point by magnetic AC heating.

Macroscopic measurements of the dynamic viscosity η of molten polymers MYR and PAL without incorporated nanoparticles, externally heated by conventional methods, have been carried out by Dr. Dimitry Borin (Dresden University of Technology) from the melting temperature up to about 100 °C. Figure 7.1 indicates relatively high dynamic viscosities of 1 - 100 Pas in this temperature region, with a slightly higher viscosity observable for sample PAL compared to MYR. For calculations using theoretical models of AC-susceptibility and Mössbauer spectroscopy data shown below, the viscosity curves are approximated by interpolation functions shown exemplary by the dashed line. These obey the Vogel-Fulcher-Tammann-Hesse

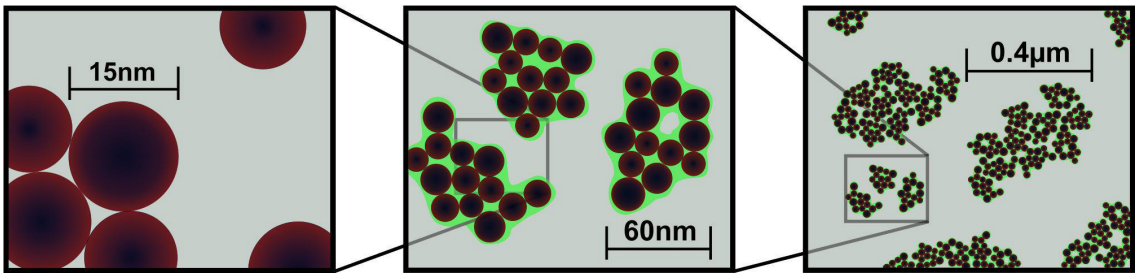

Figure 7.2: Architecture of 'raspberry' particles embedded in polymer compounds on different length scales: (a) Individual monocrystalline and monodomain nanoparticles of partially oxidized magnetite with an average diameter of 15 nm, (b) clusters of several particles as shown in (a) coated with oleic acid with a length of about 60 nm and (c) larger agglomerates of several particle clusters.

(VFTH) formula (2.19), valid for the description of dynamic viscosities close to the glass transition point, and reproduce the experimental data points well, which display, obviously, no simple exponential decrease in viscosity as predicted by the Andrade equation (2.18). These exceptionally large values in η make a direct study of the (rotational) particle motion quite difficult, as rotational frequencies visible in AC-susceptometry, as the most common method for this purpose, are shifted to ultralow frequencies $f_{rot} \ll 1$Hz, which are not accessible by common AC-susceptometry setups designed for the high frequency regime. This problem is even more pronounced due to the high hydrodynamic diameter of the polycrystalline particles, whose structure is illustrated in detail in figure 7.2, and is tackled by the combination of AC-susceptometry at elevated temperatures in the low frequency region, supported by Mössbauer spectroscopy.

'Raspberry' particles, incorporated in composite materials MYR and PAL described above, were synthesized by a precipitation method similar to that proposed by Dutz et al., and are reported to yield convenient specific absorption rates [180], leading to considerable local heating upon externally driven magnetization reversal. The particles were covered with oleic acid to reduce agglomeration effects. The mixture of particles and oleic acid was ball-milled during the coating process to minimize the fraction of large agglomerates. As elucidated in more detail in section 7.2 by means of in-field Mössbauer spectroscopy, the particles presumably exhibit a maghemite passivation layer. Clusters of coated particles of about 50 - 70 nm are visible in TEM images subsequently to this procedure, motivating the intuitive term of a 'raspberry' structure, as illustrated in figure 7.2 (b). Therefore, Brownian relaxation dynamics of separated particles are unlikely to be observed in follow-up experiments, while the question remains whether the cluster size is stable in the biocomposite or if their hydrodynamic diameter will deviate in the polymer melt respectively after repeated melting/solidification cycles.

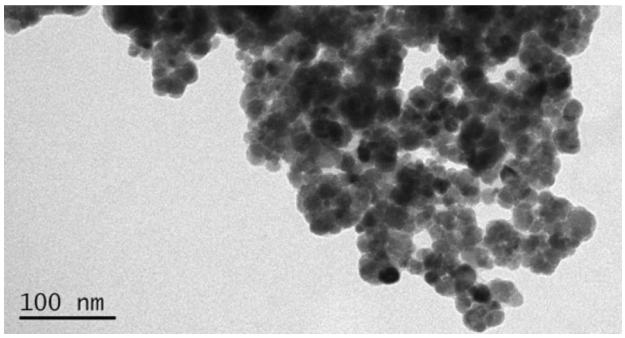

Figure 7.3: TEM image of oleic-acid coated magnetic nanoparticles. Clusters of several particles are visible subsequently to the coating procedure. Figure taken from Ref. [178].

Polymer composites were prepared from 1 wt% of monodomain magnetite crystallites, relative to the total polymer mass. The raspberry structure has been studied after the coverage with oleic acid, showing not only 'individual' clusters but also larger agglomerates with a size up to 2 μm, shown in figure 7.3 and displayed in comparison to separate clusters schematically in figure 7.2.

The latter observation raises a critical question: 'Do the raspberry particles perform diffusion as individual particles or as larger agglomerates?' As below the polymer-compound melting point particle position and orientation are fixed, the energy uptake primarily occurs by induced Néel relaxation, i.e., the driven magnetization reversal without spatial motion of the particle. Thus, the energy uptake in this temperature region will be strongly influenced by the particles' effective magnetic anisotropy. In the liquid polymer above the melting point, the absorption rate may vary due to the onset of rotational Brownian motion as an alternative heating effect. The latter is determined by the hydrodynamic diameter of rotating objects in addition to the dynamic viscosity of the polymer melt. Considering this, a further improvement in the heating ability of the polymer compound may be yielded by modifying the synthesis procedure to tune the size of resulting raspberry particles and particle cores, and to control or prevent the formation of agglomerates, respectively. Therefore, it is one of the primary objectives of the next sections to find an answer to the question regarding the hydrodynamic diameter of particles in the polymer melt.

7.2 Spin structure of raspberry particles

In a first attempt to evaluate the magnetic structure of the raspberry particles, Mössbauer spectra of sample MYR and PAL have been recorded at 4.3 K without an applied magnetic field and in presence of an external magnetic field of 5 T along the γ-ray propagation direction. The resulting spectral shape, as displayed in figure 7.4, is qualitatively comparable to those of capped 6.3 nm iron oxide nanoparticles discussed in chapter 4. Therefore, the same fitting routine could be applied in principle, including one subspectrum each for Fe^{2+} on octahedral B-sites and Fe^{3+} and B- and tetrahedral A-sites. Additionally, a small central doublet contribution

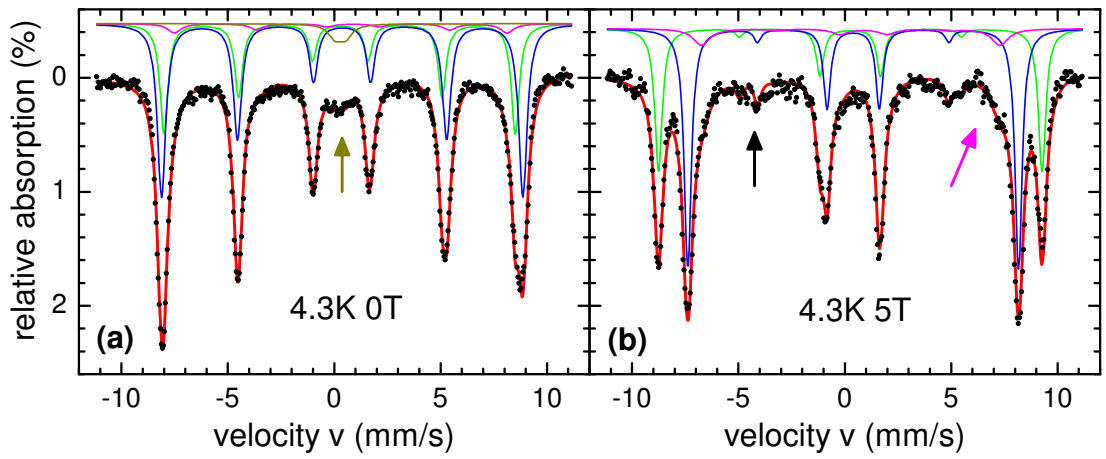

Figure 7.4: Typical Mössbauer spectra of myristate ester-based polymer compound MYR recorded at 4.3 K in zero field (a) and with an external magnetic field of 5 T along the γ-ray propagation direction. Arrows mark the effects of a minor (super)-paramagnetic phase (brown), of remaining intensity of $\Delta m = 0$ transitions due to spin canting (black), and of the subspectrum of B-site Fe^{2+} (purple). Adapted from [181]

is observed at 4.3 K and zero field in figure 4 (a) (brown), indicating the presence of a minor iron-bearing paramagnetic phase or a small number of particles showing superparamagnetic behavior even at very limited thermal energy.

The B-site Fe^{2+} subspectrum displayed in purple exhibits a relatively low spectral area and is visible in the experimental data primarily by a small shoulder at the inner side of lines 1 and 6 only, also visible in the in-field spectrum in figure 7.4 (b). This could imply that the individual iron oxide crystallites are created as a magnetite-maghemite phase mix during the synthesis or, more likely, that reduced amounts of Fe^{2+} indicate oxidation of 15 nm magnetite nanoparticles.

Spin canting effects of the myristate ester-based polymer compound MYR, i.e., the remaining intensity of lines 2 and 5 corresponding to nuclear transitions of $\Delta m = 0$, which are marked by the black arrow in figure 7.4 (b), are relatively small. Averaging over all iron sites yields a mean canting angle (relative to the external field direction) of about 16°. Although this value is not surprising for particles of 15 nm, considering average canting angles of about 20° in capped 6.3 nm iron oxide particles analyzed in chapter 4, one has to consider that surface spin canting is not the only possible explanation for the observation of pinned magnetic moments. It may not be clearly visible in TEM images of the raspberry particles in figure 7.3, but obviously individual crystallites within the coated particle clusters are in direct surface contact. Thus, exchange interaction of surface spins of adjacent magnetite crystallites may be present as an additional source of surface spin frustration. Also, poor crystallinity has been found to be an origin of enhanced surface spin canting [182]. Thereby, the observation of a limited degree of surface

spin canting may imply, despite the direct surface contact of the 15 nm particles, a rather well ordered lattice- and magnetic structure of the particles. Still, when discussing effects of static magnetic orientation, one has to consider that no magnetic field is applied during the coating process, wherefore magnetite crystallites within the same raspberry particle are expected to show a random, non-parallel orientation of easy magnetic directions. As a consequence, particle clusters are bound to display low net magnetic moments in the absence of strong magnetic fields.

7.3 Magnetometry in the melting region

To investigate magnetization dynamics of the nanoparticle compound, field dependent magnetization and ZFC-FC magnetization curves were measured using a SQUID-magnetometer. Curves of M(H) recorded at 5 K and close to the melting temperature are compared in figure 7.5 to illustrate the temperature dependent variation of the compounds' magnetic reorientional behavior in the solid and liquid phases. At 5 K, a pronounced magnetic hysteresis is detected with coercive fields of about 40 mT. At 0.5 T a magnetization of the compound of about $M_{0.5T}$ $\approx$ 0.6 emu/g is measured. Considering the concentration of iron oxide of ca. 1 wt% within the compound material, this translates to a particle magnetization $M_{0.5T} \approx 60$ emu/g, which compares well with the common saturation magnetization reported on magnetite nanoparticles of similar size, especially when considering that M_S may exceed $M_{0.5T}$ considerably due to spin frustration [183].

At 300 K the sample is known to be still in the solid state, as its melting point was determined to about 40 - 45 °C $\approx$ 315 K. Therefore, the noticeable decrease in hysteresis area proving partial superparamagnetic behavior is caused very likely by Néel relaxation processes, indicating an average blocking temperature below 300 K on the SQUID-magnetometry time scale. However, studying the low field regime magnified in figure 7.5 (b), the hysteresis remains slightly opened at temperatures of 300 - 340 K. From 300 K to 320 K, by exceeding the polymer compounds melting temperature, the shape of M(H) displays a minor change, most recognizable at 5 - 20 mT, which could indicate additional contributions of Brownian motion to relaxation dynamics. However, these do not result apparently in a major change of magnetic reversal behavior up to 340 K. Furthermore, the observation of an open hysteresis loop above the melting temperature indicates slow Brownian motion of the particle clusters, being insufficient to cancel the remanent magnetization on the SQUID time scale. The latter could be assigned to the high dynamic viscosity of the polymer melt even far above the melting region or to particles being present as large agglomerates, accordingly leading to slow rotational dynamics.

The exact origin of the above mentioned remaining opening of the hysteresis loop may be easier to clarify by studying ZFC-FC magnetization curves, shown in figure 7.6. At very low

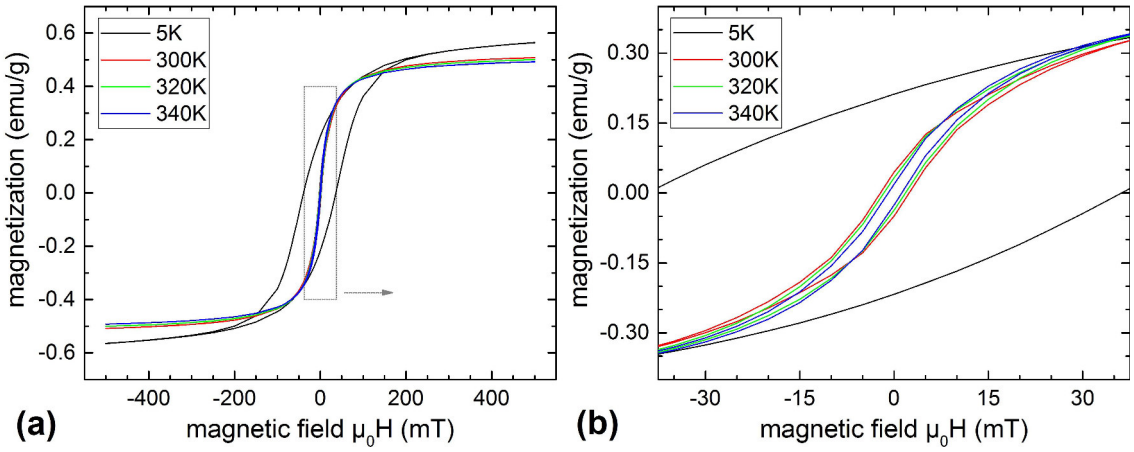

Figure 7.5: Field-dependent magnetization below and above the melting region of polymer compound MYR, displayed up to 0.5 T (a) and in the low field regime shown in magnification (b).

temperatures of T < 20 K, small features in m_{ZFC} are observable, which may correspond to the minor doublet contribution visible in Mössbauer spectra at 4.3 K. Above 20 K, the ZFC- and FC magnetization curves display a relatively constant splitting up to about 250 K. A better insight on Néel relaxation dynamics may be obtained from the difference magnetization curve m_{FC} - m_{ZFC} instead, which is a measure of the distribution of blocking temperatures. This difference curve of magnetizations displays a slow decrease, which is slightly more pronounced in palmitate ester-based polymer compound PAL, indicating a lower Néel blocking temperature and, presumably, a slightly smaller average diameter of the individual magnetite nanoparticles. In the region of the melting temperature at ca. 315 K, a relatively sudden increase in ZFC magnetization respectively a decrease in the difference curve is observed. Such variation in magnetization can be assigned to the onset of Brownian motion in a similar way as discussed for ZFC-FC magnetization curves in chapter 5. From the inflection point of this magnetization curve an estimation of the melting temperature $T_M \approx 318$ K may be found in compound MYR and 330 K in sample PAL, which is widely consistent with values of T_M found by differential scanning calorimetry in [178]. The jump in ZFC magnetization is noticeably higher in sample MYR, implying that a higher number of particles reaches the superparamagnetic state at this point. The latter could indicate slightly larger particles in sample MYR, as suspected before, or could be correlated to the difference in dynamic viscosity of MYR and PAL at a given temperature.

Above T_M an accelerated decrease in ZFC-FC splitting is detected in both polymer melts. This presumably translates to a higher number of particles reaching the superparamagnetic state now by combined Néel and Brownian superspin dynamics. However, even at the maximum temperature of 390 K covered in this experiment, the irreversibility temperature is still not

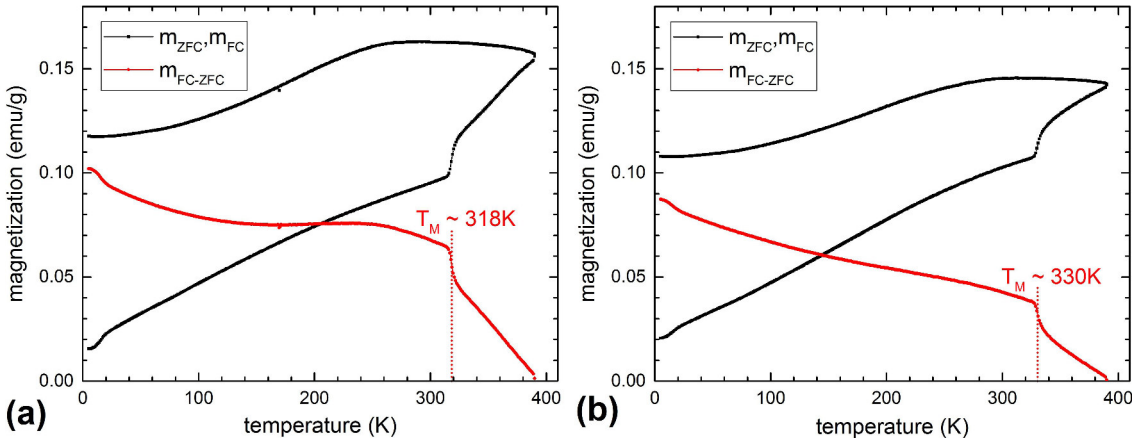

Figure 7.6: ZFC-FC magnetization of polymer compounds MYR (a) and PAL (b), measured in an external magnetic field of 10 mT (black). The difference curve $m_{FC} - m_{ZFC}$ is displayed in red, dotted lines mark the melting temperature T_M of the polymer compounds, here defined by the inflection point of the difference curve.

reached, as no joint ZFC-FC curve is found showing a decrease in magnetization according to the Langevin equation. Therefore, some blocked magnetic moments have to be conserved up to 390 K in agreement to the observation of a small opening in the hysteresis curve above the melting temperature.

7.4 AC-mapping of relaxation times

At room temperature, measurements of field- and temperature dependent magnetization, as shown above, reveal mainly Néel relaxation of the particles incorporated in the polymer compounds. However, they allow no direct estimation of relaxation frequencies of these dynamic processes beyond the fact that they have to be fast compared with the time constant τ_{Squid} of the SQUID magnetometry mechanism at least for a fraction of the incorporated nanoparticles. The exact knowledge of the Néel relaxation time, especially in direct comparison to the Brownian rotation frequency, may be essential for the understanding of the complete relaxation mechanism of the raspberry particles and for optimization of the specific energy absorption rate. For this reason real- and imaginary component χ' and χ'' of the magnetic AC susceptibility were determined above and below the melting region of the polymer. Utilizing the AC-option of the applied SQUID setup, τ_{Neel} and τ_{rot} were mapped frequency- as well as temperature dependent at about 5 - 390 K and 0.017 - 1500 Hz to cover a wide range of relaxation dynamics. 3D-maps and corresponding 2D-projections of the magnetic AC susceptibilities of polymer compounds MYR and PAL are gathered in figure 7.7.

Studying χ'(T), a trend comparable to those of the ZFC magnetization can be observed for both polymer compounds. While both samples display a relatively continuous increase upon rising

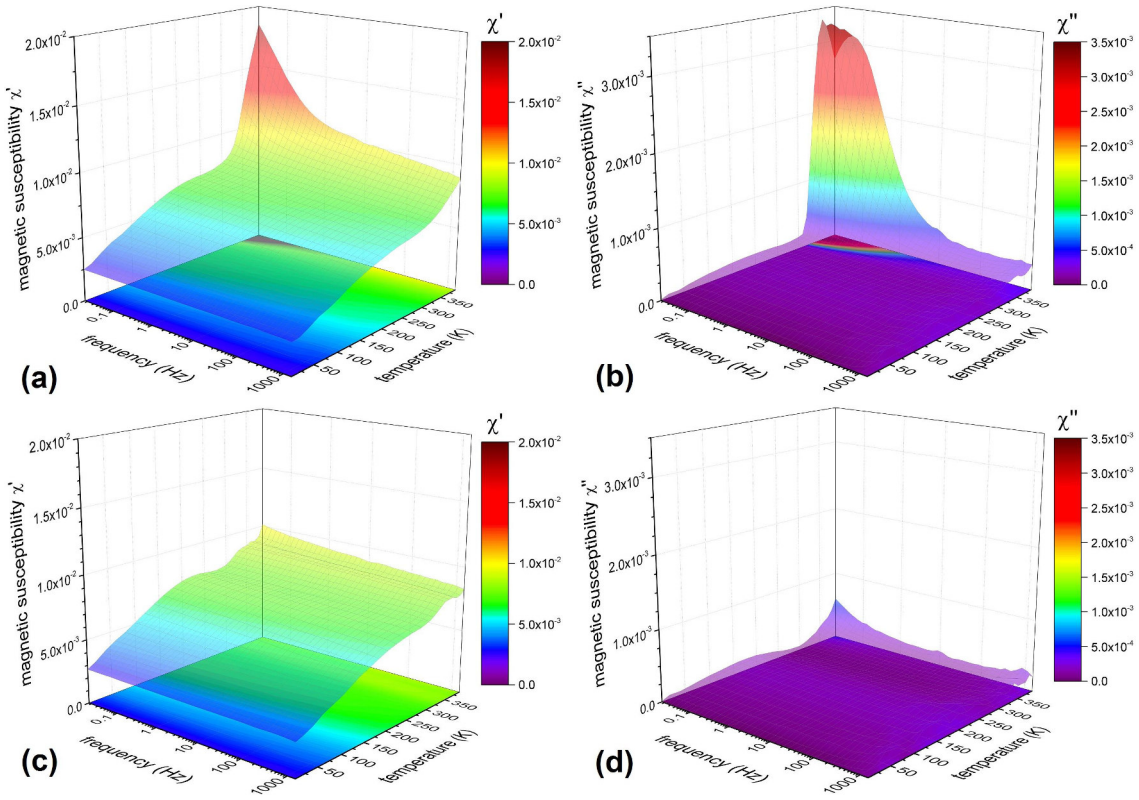

Figure 7.7: Real- and imaginary component χ' and χ'' of magnetic AC-susceptibilities of samples MYR (a,b) and PAL (c,d), recorded with an AC-field amplitude of 1 Oe at temperatures of 5 - 390 K and frequencies of 0.017 - 1500 Hz.

temperature at frequencies above 10 Hz, the AC-map of the myristate ester-based polymer exhibits an additional peak at the lowest measurable frequencies above the melting point. The latter can be assigned to orientational processes by Brownian diffusion, which seem to be absent or shifted to the immeasurable frequency region in sample PAL.

As described in section 3.2, the imaginary component χ'' of magnetic AC-susceptibility displays a peak feature at the frequency position marking relaxation dynamics, wherefore it is easier to analyze and to interpret. At 5 - 300 K, the polymer compound is still solid and the relaxation restricted to Néel superspin fluctuation, whereby the almost constant small background intensity in χ'' indicates a very broad distribution of Néel relaxation frequencies. The latter corresponds to the slow frequency-dependent decrease in χ' at a given temperature. Barely recognizable, χ'' exhibits a broad maximum in both compounds at about 150 - 200 K, which could reflect the average blocking temperature of particles in the sample, adopting superparamagnetic behavior by Néel relaxation alone. As the individual magnetite particles within the raspberry-type clusters are not assumed to be highly monodisperse, the very wide-spanning range of Néel relaxation frequencies is not unexpected.

Above 310 K, a much sharper maximum appears in χ'' of the polymer compound MYR and shifts

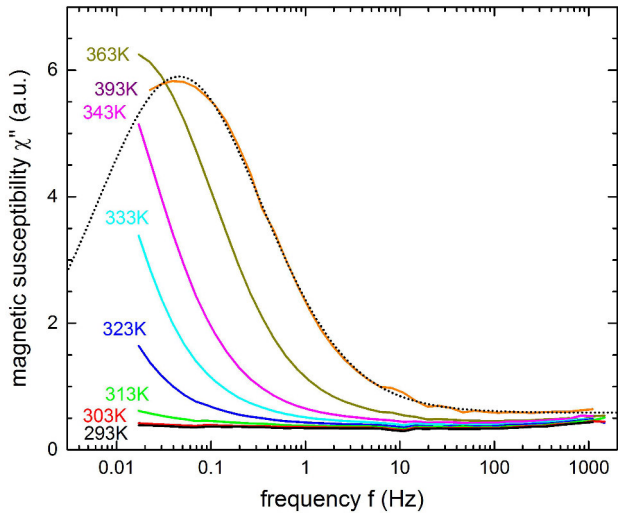

Figure 7.8: Imaginary component χ'' of magnetic AC susceptibility of myristate ester-based polymer compound MYR close to the melting point. The dashed line represents the theoretical reproduction of experimental data of sample MYR at 393 K using an extended Debye model corresponding to equation (3.54) [181].

to higher frequencies upon further heating. As this feature for sure originates from Brownian dynamics and is, therefore, directly correlated to the hydrodynamic size of the particles and the viscosity of the polymer melt, it is shown in more detail in figure 7.8 and discussed accordingly below. Assuming the validity of the Stokes-Einstein relation in the region of ultralow rotation frequencies, the peak position in χ'' is found to match rotation frequencies predicted by equation (2.17) for viscosities displayed in figure 7.1 and hydrodynamic diameters of 50 - 70 nm of the raspberry-type particle clusters. The validity of the Stokes-Einstein relation seems to be a reasonable assumption, as it has been demonstrated down to the glass temperature, where diffusional dynamics are remarkably slow [184].

The peak height in χ'' of the Brownian feature is about 10 times higher than the background of Néel origin, which suggests that Brownian motion represents the dominant relaxation mechanism in the polymer melt of MYR. In sample PAL, only the very beginning of a peak similar to that in the myristate ester-based compound is visible up to 393 K. This is in agreement with the less pronounced increase in superspin relaxation upon the transition to the liquid polymer state reported in ZFC-FC magnetization measurements. However, the question remains, if this effect stems primarily from the higher viscosity in sample PAL, or from larger hydrodynamic diameter of the incorporated particles compared to MYR.

A closer inspection of the imaginary component χ'' of magnetic AC susceptibility is possible in figure 7.8. For polymer compound MYR, a constant background signal of Néel origin is visible at 293 - 303 K, which are both measurements in the solid polymer state. By reaching the liquid state, an additional contribution is found at very low frequencies of about 0.01 - 0.1 Hz, which proves their origin to be the diffusional Brownian motion. Upon rising temperature, the maximum in χ'' shifts into the accessible frequency range. Here, it has to be mentioned that the majority of commercially available AC-susceptometers are designed for the high-frequency regime and exhibit a lower-limit frequency of about 1 - 10 Hz, whereas the AC-option of the

utilized SQUID magnetometer can drive stable AC magnetic fields at frequencies even below 10^{-2} Hz. At the highest studied temperature of 393 K, the maximum of the peak feature is positioned in the measured frequency region, which allows a quantitative discussion of rotation frequencies and the determination of hydrodynamic radii:

Yielding relatively good agreement to experimental data, the frequency-dependent χ'' signal at 393 K has been reproduced according to an extended Debye relation including a distribution of hydrodynamic diameters, corresponding to equation 3.54. A dynamic viscosity of about 0.5 Pas was used in this model, obtained by extrapolation of viscosity data in figure 7.1 to 393 K = 120 °C. The resulting χ''-signal is represented in figure 7.8 (a) by the dashed line. A distribution of core diameters for determination of the Néel contribution to χ'' is explicitly not included based on two considerations: Not only is the Néel background signal almost without structure on five orders of magnitude in frequency, making an estimation of Néel relaxation parameters very difficult, but also no reference measurement of the distribution in particle-core diameter is available, which could be used to cross-check results from such a calculation. However, the fitting routine of Brownian rotation frequencies applied to the experimental data in figure 7.8 yields an average hydrodynamic diameter of the raspberry particle clusters of 64 nm with a standard deviation of 36 nm. The shift in peak position upon decreasing temperature matches the increase in dynamic viscosity from macroscopic reference measurements, as shown in figure 7.1. Thus, the results indicate a relatively broad size distribution of the particle clusters. As a minor drawback it has to be considered that in this model the raspberry particles are regarded as a large individual particle of relatively small net magnetic moment and not as an assembly of smaller particles with random magnetic orientation instead, which would be more adequate. It is unclear to what degree the calculations performed in the model are obscured by individual particles in the raspberry structure already experiencing orientational freedom by Néel superspin fluctuation.

The number of coated single-core magnetite nanoparticles apparently is relatively limited, as no additional Brownian contribution is visible at higher rotation frequencies corresponding to smaller hydrodynamic diameters. One could assume that these cannot be observed, as the amplitude of the susceptibility signal is proportional to the square of the total magnetic particle moment and, therefore, much smaller than the signal of the larger raspberry particles. However, this would be a false assumption: In particle clusters of the 'raspberry' structure, the net magnetic moment should be strongly reduced due to the random orientation of easy magnetic directions in the particle ensemble, while in an individual particle all magnetic moments would be aligned relatively well and collinearly, wherefore the net magnetization in such a particle would exceed that of a raspberry particle cluster by far.

Following this consideration, the absence of susceptibility signals at higher frequencies proves

the absence of individual smaller particles. On the other hand, the presence of large agglomerates and particle clusters of higher hydrodynamic diameter cannot be disproved completely, as they would rotate more slowly at considerably lower frequencies, which cannot be studied by AC-susceptometry up to temperatures of about 390 K. Therefore, Mössbauer spectra of both polymer compounds have been recorded at temperatures comparable to those of the AC experiments. As the broadening of the Mössbauer absorption lines is, according to equation 3.42, inversely proportional to the hydrodynamic diameter of the studied particles, a high number of larger agglomerates of raspberry clusters would result in the observation of a striking sharp spectral component, whose spectral area would correspond to the amount of agglomerates relative to the total particle mass of the sample.

7.5 Relaxation dynamics in polymer melt studied by Mössbauer spectroscopy

Mössbauer spectra of myristate and palmitate ester-based polymer compounds MYR and PAL were recorded, with assistance of Samira Webers, B.Sc., in transmission geometry from ambient temperature up to ca. 400 K. For these experiments, the composite material was mounted into the halogen-lamp heated sample holder described in section 3.1. To ensure sufficient spectral intensity the sample thickness was chosen to about 9 mm by melting the polymer material by moderate warming and filling the liquid into the copper cylinder of the sample holder before solidification. Considering the iron oxide concentration in the nanoparticle polymer composite, this geometry corresponds to an effective density of 8 - 10 mg iron oxide particle powder per cm^2.

The room temperature spectrum of composite PAL shown in figure 7.9 (a) exhibits the expected sextet structure and minor effects of relaxation, i.e., minor asymmetry in line shape by collective excitations or beginning Néel fluctuations, while no superparamagnetic doublet is visible. This spectral shape may be surprising, as one remembers the primarily superparamagnetic behavior in field- and temperature dependent magnetization measurements. Obviously, relaxation effects take place at room temperature on a time scale fast compared to SQUID-magnetometry but still barely affecting the Mössbauer spectrum.

As the deformation of the spectrum relative to the static line shape is relatively small, no exact value of the effective anisotropy barrier can be obtained, but an estimation based on the Jones-Srivastava many-state model, which is described in section 3.1 and used in the theoretical reproduction of the spectra, yields an effective anisotropy energy E_A of about 200 meV. Taking into consideration the approximation of the particle core diameter to be about 15 nm, this translates to $K_{eff} \approx 20$ kJm^{-3}, which is slightly enhanced relative to $K_{eff} \approx 14$ kJm^{-3} for the highly monodisperse 15 nm iron oxide nanoparticles of ferrofluid M in chapter 5. As no detailed information on type and strength of interparticle interaction in the raspberry particles

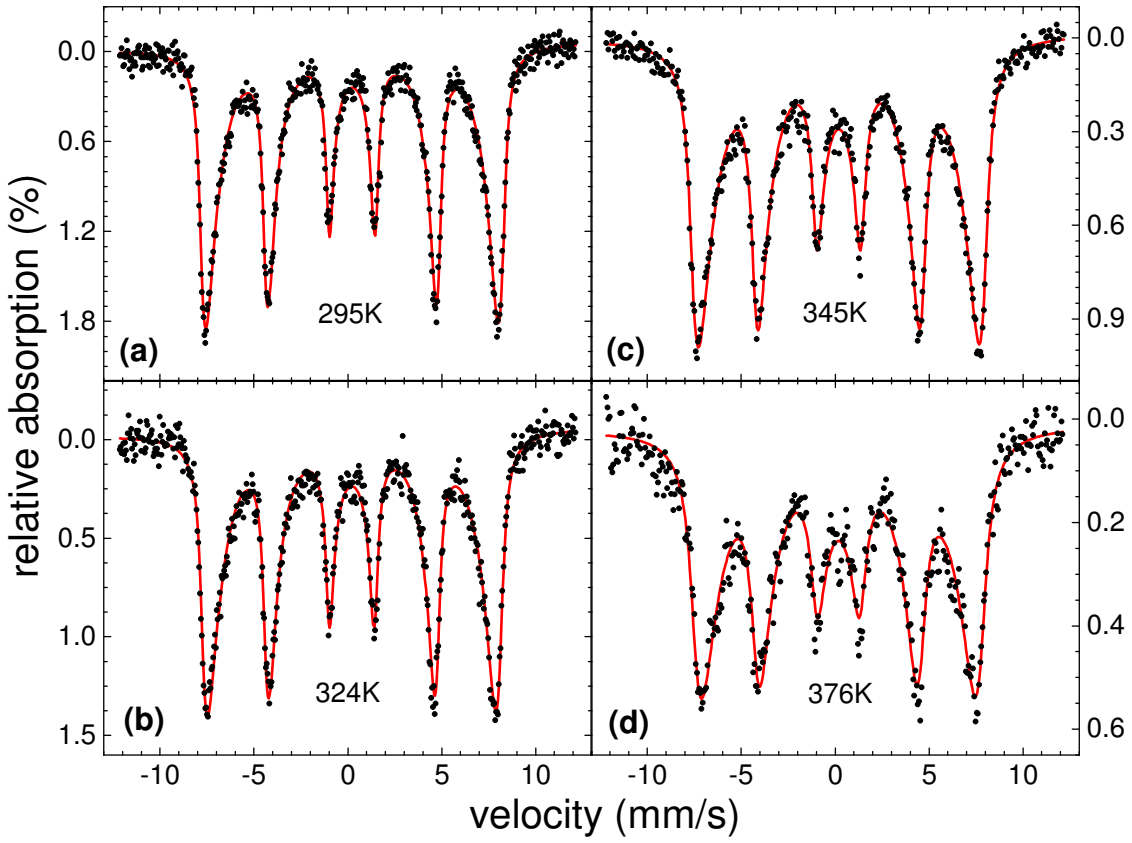

Figure 7.9: Mössbauer spectra of palmitate ester-based polymer compound PAL recorded from room temperature up to 376 K.

is provided, modifications of the effective interaction energy, as illustrated in chapter 4, are included in this estimation and may explain the enhanced value of K_{eff}, since the particle separation by the oleic acid coating is relatively small and the particles of 15 nm in diameter exhibit a considerable net magnetic moment.

Starting at temperatures close to the melting region at ca. 330 K, the onset of line broadening by Brownian motion is detected. Calculated linewidths determined from Mössbauer spectra of both polymer compounds are compared in figure 7.10. Upon heating the polymer melt, further increase in line broadening is observed. However, the maximum of observed linewidths is about 1 mm/s, whereby the line broadening $\Delta\Gamma$ is comparable in magnitude to the static linewidth Γ_{stat} of about 0.4 mm/s. Considering values of $\Delta\Gamma$ of 20 mm/s and more, reported for ferrofluids and ferrohydrogels in the previous chapters, this underlines the high viscosity of the polymer melt.

To compare linewidths determined by Mössbauer spectroscopy with results from the AC-mapping shown above, the theoretical trend in $\Delta\Gamma$(T) was calculated from equation (3.42), using dynamic viscosities from figure 7.1 and the size distribution of raspberry particles from AC experiments with a mean particle diameter of 64 nm. To consider the distribution of par-

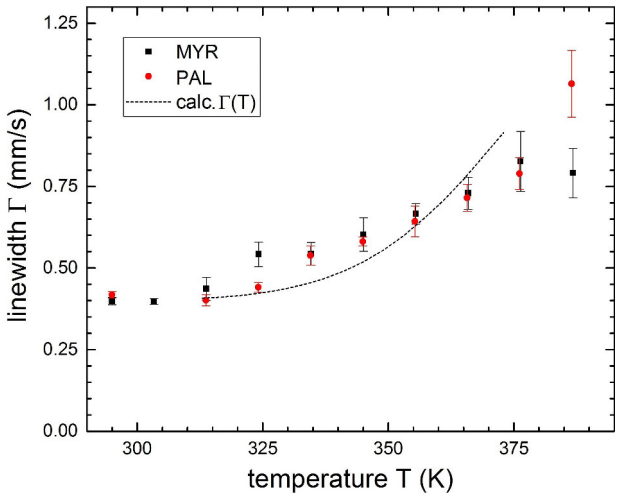

Figure 7.10: Linewidth Γ of Mössbauer absorption lines of polymer compounds MYR and PAL determined between room temperature and about 400 K. The dashed line shows the temperature dependence of Γ(T), as calculated from AC-susceptometry reference data and the interpolated viscosity function $\eta(T)$ of polymer MYR. Adapted from [181].

ticle diameters, the size-dependent line broadening was weighted by the particle volume, i.e., the number of iron atoms showing the corresponding linewidth, and subsequently averaged to yield the dashed line visible in figure 7.10. Here, it has to be mentioned, that this line does not represent a theoretical reproduction of the experimental data points of linewidths determined by Mössbauer spectroscopy, but a pure theoretical trend calculated from parameters determined by an independent technique. Nevertheless, good agreement of the dashed line and the Mössbauer linewidths is found, which indicates the correctness of the size distribution parameters $\overline{D_{Hyd}} = 64$ nm and $\Delta D_{Hyd} = 36$ nm extracted from rotation frequencies measured by AC-susceptometry. Apparently, no spectral components of static linewidth are present in the high-temperature Mössbauer spectra, further substantiating the assumption that the majority of the iron oxide in the polymer compounds is included in particle clusters of the raspberry structure, while no considerable indication of larger agglomerates is observable.

As the primary result of this study one should keep in mind, that extensive AC-susceptibility studies provided a detailed insight in the onset and development of Brownian motion in the polymer melt as well as in the underlying background of Néel relaxation processes. While the evaluation of these detailed AC-maps represents a more clear and straightforward tool to obtain absolute numbers of, e.g., particle rotation frequencies, contributions of both relaxation mechanisms can be resolved more easily using Mössbauer spectroscopy. As effective magnetic anisotropies, rotation frequencies and the distribution of hydrodynamic diameters could be estimated, optimization of the specific absorption rate by tuning the nanoparticles' field- and temperature-dependent behavior is in reach, using combined results from Mössbauer spectroscopy and AC-susceptometry as a starting point.

8 Conclusion and Outlook

Soft matter compound systems containing magnetic nanoparticles exhibit peculiar and versatile properties tunable by the magnetic structure of the particles, the matrix material and the type and coupling mechanism leading to the particle-matrix interaction. These include variations in Néel and Brown relaxation behavior determined by their local environment, e.g., interparticle interaction of nearby particles, and the reduction of particle mobility by the nanostructured surrounding. The surrounding matrix medium, vice versa, can be influenced by external stimuli, first of all magnetic fields, using the particles as transferring agents to allow remote melting of nanoparticle composites as well as viscosity tuning in magnetorheological fluids.
These phenomena highly depend on the mobility of the nanoparticles' magnetic moments and their orientation in external magnetic fields. For this reason, magnetization dynamics as well as static magnetic structure have been examined in this thesis utilizing Mössbauer spectroscopy in combination with AC-susceptometry and further reference techniques. Especially in ferrohydrogels in the viscoelastic regime, magnetic relaxation phenomena and particle mobility are primarily governed by the nanostructure of the matrix material in direct proximity of the particle. Thus, the investigation of the particle by experimental methods of different detection mechanism, locality and time scale, is a promising approach to yield a more thorough understanding of particle-matrix interaction.
The most important insights obtained in this thesis following this consideration are outlined here shortly, while a more detailed description addressing the questions raised in the introduction is presented on the next pages on each of the studied systems individually, whose structures are displayed schematically in figure 8.1.

I The analysis of capped iron oxide nanoparticles led to the finding of widely altered Néel relaxation behavior depending on the strength of interparticle interaction. Observed effects could be modeled in first approximation by an enhanced effective anisotropy energy barrier, increasing proportionally to the magnetic dipolar interaction energy.

II Studying ferrofluids containing iron oxide nanoparticles of different core diameter, the simultaneous quantitative analysis of Néel relaxation and Brownian motion could be demonstrated for the first time using Mössbauer spectroscopy. Determined values of the particles' effective magnetic anisotropy and the fluid's dynamic viscosity were in excellent agreement with reference data from AC-susceptometry, proving the accuracy of these experiments.

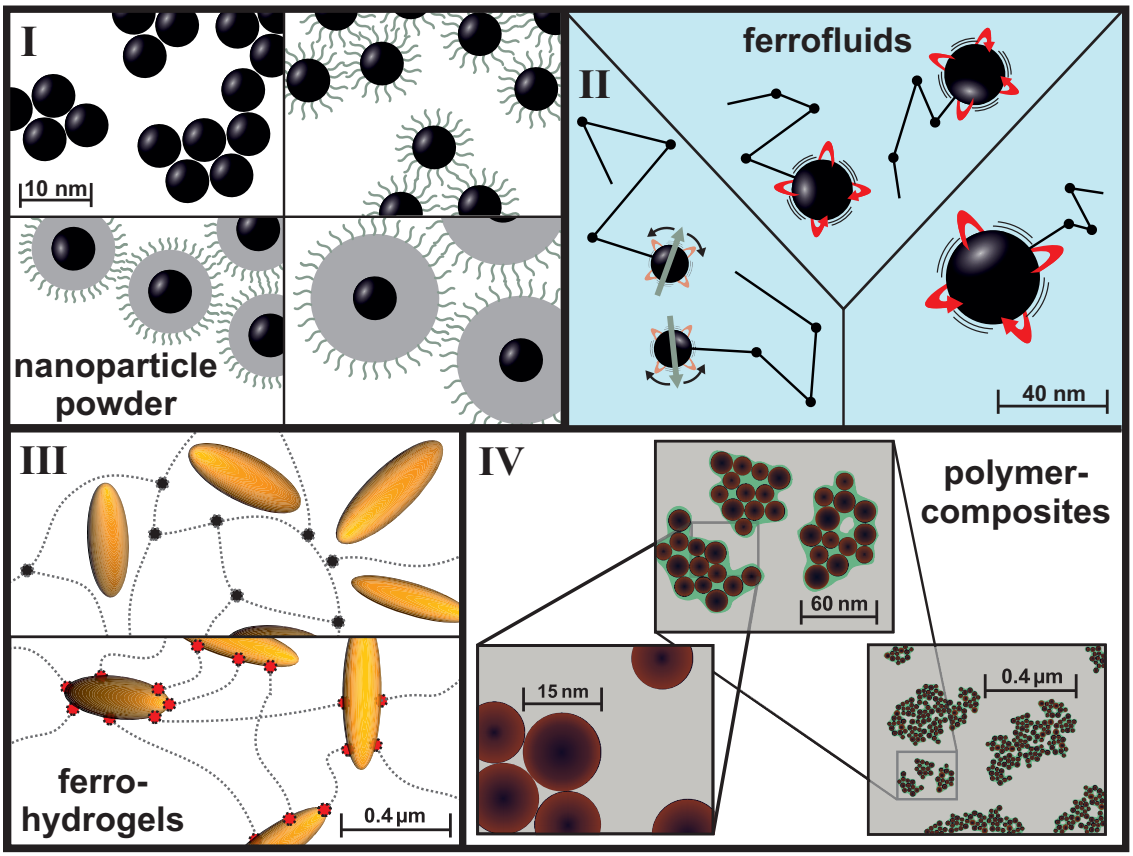

Figure 8.1: Schematic illustration of all studied composite systems. **I**: Capped 6.3 nm iron oxide nanoparticles studied in chapter 4 regarding the influence of interparticle interaction on Néel relaxation. **II**: Ferrofluids containing capped magnetite particles of different size, where relaxation is dominated by Brownian motion in larger particles and by Néel relaxation in smaller particles (chapter 5). **III**: Schematic structure of MBA- and particle-crosslinked ferrohydrogels. The variation in particle mobility on the hydrogels internal structure was analyzed in chapter 6. **IV**: Particle clusters coated with oleic acid in dextran based polymers, whose temperature dependent dynamic magnetic behavior was examined in chapter 7.

III Investigating the particle mobility in ferrohydrogels of different internal structure on the nanoscale using Mössbauer spectroscopy, considerable particle movement was observed on short timescales. The absence of a corresponding AC-susceptibility signal was interpreted in terms of particle containment, preventing rotational particle movement especially on longer timescales.

IV In nanoparticle biocomposites designed for remote melting applications, a thorough understanding of relaxation mechanisms was gained by frequency- and temperature dependent AC-mapping, covering Néel as well as Brownian relaxation times.

Néel relaxation influenced by magnetic dipole interaction

has been analyzed using 6.3 nm magnetite nanoparticles of different capping thicknesses, ranging from bare particles to particles capped with IGEPAL and an additional silica shell of about 6 nm, tuning the strength and type of interaction experienced by the particles. By in-field Mössbauer spectroscopy, negligible influence of the capping on the particles' magnetic structure, including the spin canting angle of ca. 20°, has been demonstrated. The availability of tunable capping thicknesses without a resulting change in the particles' magnetic structure was the critical prerequisite for studying relaxation phenomena affected by interparticle interaction. Magnetic relaxation by the mechanism of Néel superspin fluctuation was widely modified under the influence of interparticle interaction. Basic ZFC-FC magnetization protocols as well as more sophisticated measurements of the thermoremanent magnetization (TRM) displayed a broadening of the transition to superparamagnetic behavior and a distinct increase in the particles' blocking temperature. TRM experiments also allowed the determination of the anisotropy energy distribution and an estimation of the relaxation time factor τ_0 of 80 - 150 ps. Temperature analogs T_0 of the interaction energy of 5 - 100 K could be extracted from AC-susceptometry showing a considerable increase upon decreasing particle capping thickness.

As a direct reference method, Mössbauer spectra of the four types of particles have been recorded at temperatures of 5 - 300 K, as Mössbauer spectroscopy allows to disentangle the subspectra of particles in different states of Néel relaxation by analyzing the progression from magnetically blocked sextets to superparamagnetic doublets. Spectra have been reproduced theoretically using a many-state relaxation model, whereby an anisotropy energy density of $K_{eff} \approx 45 \pm 4$ kJm^{-3} was found in double capped particles experiencing minimal interaction, in excellent agreement to reference values of 44 ± 2 kJm^{-3} obtained from ferromagnetic resonance experiments. By comparison with values of T_0 from AC-susceptometry, it is revealed that the interparticle interaction energy, leading to a decrease in the relaxation rate, is already comparable to the total anisotropy energy resulting from magnetocrystalline-, surface- and shape anisotropy contributions, in case of strongest interparticle interaction observable for bare particles. This implies a dramatic influence of interparticle interaction on Néel relaxation times in ensembles of larger particles with superior magnetic moment.

A linear correlation of dipolar anisotropy contributions E_{dip} from Mössbauer spectroscopy and T_0 from AC-susceptometry data to the interparticle separation D^{-3} has been found, matching theoretical predictions. This also demonstrates the capability of Mössbauer spectroscopy to estimate interaction energies. The latter is a critical issue, as the study of magnetorheological fluids and composites including a high concentration of relatively large nanoparticles leads inevitably to strong magnetic dipole interaction.

Brownian and Néel dynamics simultaneously accessible by Mössbauer spectroscopy

Ferrofluids of magnetic nanoparticles in a Newtonian fluid are the most simple system allowing relaxation of the particle moment not only by the Néel fluctuation mechanism, but also by spatial reorientation of the whole particle driven by thermal energy and limited by the friction with fluid molecules. To study combined effects of both processes, capped magnetite nanoparticles with 6 - 26 nm core diameter were added to 70 wt% glycerol solution. The excellent monodispersity of the particles has been verified by TEM images.

Particles of different diameter displayed fundamentally different magnetic relaxation dynamics in magnetometry experiments. The smallest particles exhibited Néel-type superparamagnetism with blocking temperatures below 50 K, while 15 nm and 26 nm particles displayed higher blocking temperatures and a fraction of magnetic moments still blocked up to the onset of sufficiently fast Brownian motion at ca. 200 K. Investigating the width of the superparamagnetic transition, a fast but continuous decrease in viscosity was concluded, indicating a glass transition. Calculations of the Brownian rotation times substantiated this assumption. The distinct variation in magnetic relaxation in particles of different size is a convenient proof of their tunability. By choosing an adequate particle size, Brownian and Néel relaxation can be tailored to match the requirements of the individual application.

A surprising and important finding regarding this issue, reported here, to the best of my knowledge, for the first time, was the ability of Mössbauer spectroscopy to resolve and quantify effects of both relaxation phenomena, as each has its characteristic influence on the spectral shape. The Néel relaxation process is detected by the apparent time-averaged canceling of the nuclear Zeeman splitting, while diffusional motion results in Doppler-broadened absorption lines. From series of Mössbauer spectra of the ferrofluids an estimation of effective magnetic anisotropies of the incorporated particles, as well as the thickness of the particle coating and the dynamic viscosity of the solution could be extracted.

As a method capable of analyzing both relaxation phenomena, AC-susceptometry has been utilized to cross-check data from Mössbauer experiments. While AC-susceptometry in general displays the total relaxation frequency, which is primarily determined by the dominating relaxation process, effective magnetic anisotropies of 15 nm particles of $K_{eff} \approx 13.6 \pm 0.7$ kJm^{-3} were found to be in good agreement to those determined by Mössbauer spectroscopy. Furthermore, dynamic viscosities calculated from Brownian rotation times of the largest particles, which were blocked in terms of Néel relaxation, were identical to those determined from the Doppler-broadening of Mössbauer absorption lines within errors margins. These results verify the ability of Mössbauer spectroscopy to provide access to both main mechanisms of magnetic particle relaxation, wherefore it can be regarded as a versatile approach for a thorough analysis of relaxation phenomena in ferrofluids and soft matter nanoparticle composites.

Nanorheology in ferrohydrogels: The effect of containment on particle mobility has been studied by increasing the complexity of the model system by two further steps, switching from isotropic to elongated particles and from Newtonian fluids to nanostructured ferrohydrogels: Hematite nanospindles were embedded in elastic and viscoelastic matrices to restrict their diffusional movement to an extent controlled by the type of particle-matrix interaction and the crosslinkage of the network structure. For that purpose three MBA-crosslinked ferrohydrogels have been analyzed, where the nanospindles are trapped in polymer network meshes varied in size from 10 nm to 400 nm. Here, the anisotropic particle shape allowed not only an evaluation of translational motion, but also of restricted rotation about specific particle axes. In another approach, the particles' surfaces were contacted with polymer chains, leading to a direct force-transferring mechanism in particle-crosslinked ferrohydrogels. Their elasticity could be tuned by the total amount of acrylamide in the samples, which was about 10, 16 and 22 wt% in the three particle-crosslinked samples. To compare findings on these nanostructured ferrohydrogels to those discovered for glycerol-based ferrohydrogels, a Newtonian reference sample was prepared by adding the hematite nanospindles to 60 wt% sucrose solution.

Magnetization dynamics in these reference samples were similar to those in glycerol based ferrofluids. Comparable trends in the temperature dependent viscosity were observed by AC experiments and Mössbauer spectroscopy, although a notable deviation to literature values was found for both. The latter is likely to originate from the inaccurate spherical-nanoparticle model applied, wherefore a more appropriate spheroidal model was introduced, yielding better agreement to literature data.

Studying Mössbauer spectra of crosslinked ferrohydrogels up to room temperature, a rapid increase in the absorption line broadening was visible close to the water melting point, finally reaching 15 - 30 mm/s. The width of this transition was about 3 K, indicating a softening region instead of a specific melting point. Although room temperature linewidths of about 25 mm/s vastly exceed the static linewidth of ca. 0.4 mm/s, they are considerably small compared to theoretical predictions of about 360 mm/s for free particle motion in water, indicating reduced diffusive movement in ferrohydrogels. Comparing room temperature linewidths of the softest (30 mm/s) and hardest ferrohydrogel (15 mm/s), the dependence in particle mobility on the crosslinking density was found to be surprisingly small, considering that this parameter was varied in the ferrohydrogel ensemble by a factor of 2000.

In contradiction to the observation of remaining Brownian motion by Mössbauer spectroscopy, no indication of diffusive motion was found by AC-susceptometry experiments on the crosslinked ferrohydrogels. The imaginary magnetic susceptibility signal was negligibly small and no peak features could be identified, which would mark Brownian rotation frequencies. The contradiction of this finding, compared with considerable particle mobility deduced from Mössbauer

spectroscopy data, could be explained in terms of the local nanostructure of the polymer network and the very short time constant of Mössbauer spectroscopy at the scale of nanoseconds: While the studied ferrohydrogels display elastic or viscoelastic behavior on the macroscale, on the nanoscale they can presumably be visualized by large hematite spindles swimming in ca. 90 wt% of water, trapped by a relatively small amount of polymer chains. At the nanosecond timescales, it seems reasonable to assume that the particles perform widely free diffusive motion before experiencing restoring forces by the confining polymer network. Additionally, the Mössbauer absorption line broadening originates primarily from translational motion, which is less hindered for elongated particles than rotational motion in a cage of similar shape. AC-susceptometry, on the other hand, is studied here on the millisecond regime, where free diffusion of the spindles in water would result in a traveled distance much longer than provided by the network structure. Therefore, and due to its detection mechanism being mainly sensitive to magnetic orientation by particle rotation, a negligibly small signal is found in AC experiments. Although a completely different coupling mechanism is in place in particle-crosslinked ferrohydrogels, controlling the particle-matrix interaction, Mössbauer experiments on these samples are found to display a trend of line broadening with temperature, which is very similar to that of the conventionally (MBA-) crosslinked ferrohydrogels. This may suggest a similar degree of particle confinement, as the range of acrylamide concentrations covered by the particle-crosslinked samples is comparable to those in MBA-crosslinked ferrohydrogels.

On variation of the polymer content in three particle-crosslinked ferrohydrogels, no noticeable difference in line broadening $\Delta\Gamma$ is detected, which could be explained by a constant number of nodices in the polymer network, as the number of particles, serving as crosslinker in these samples, is unvaried. To extend the region of examined polymer concentrations, one of the particle crosslinked ferrohydrogel samples was treated in the desiccator to remove some of the incorporated water, yielding polymer concentrations from 16 - 100 wt%. By this approach, a plateau of relatively constant linewidth was detected at about 16 - 40 wt%, followed by a rapid decrease in particle mobility reaching absolute linewidths that are comparable to the static value at about 70 - 80 wt%, the latter indicating a widely suppressed Brownian motion.

In addition to temperature dependent Mössbauer experiments, the magnetic orientation of the ferrohydrogel was studied upon increasing external magnetic fields. From field-dependent variation in line intensity and position, complete orientation of the particles' magnetic moment in the easy basal plane of the hematite crystal structure could be deduced, combined with a slowly increasing out-of-plane alignment reaching higher field amplitudes. The successful repetition of this experiment close to the hydrogel melting region indicates the applicability of this type of experiment to study the field-dependent orientation of the magnetic moment and the spatial alignment of the particle in the deformable hydrogel matrix at the same time.

Brownian motion in meltable polymer-composites

Focusing on the effect of magnetic heating, Néel and Brownian dynamics of particles incorporated in polymer compounds were analyzed to allow an optimization of the particles' energy uptake and conversion of magnetic energy to heat. A critical question regarding the contribution of Brownian motion to this process is the hydrodynamic size of the moving objects within the polymer melt. The smallest structural unit of those were 15 nm magnetite-maghemite particles, covered with oleic acid. Adjacent particles form particle clusters showing a 'raspberry-type' structure with a length of about 60 nm, which could move in the polymer melt separately or as larger agglomerates, limiting the rotation frequency and influencing the energy uptake.
Magnetometry has been performed on two different nanoparticle polymer compounds of slightly different dynamic viscosities and melting temperatures in the region near 50 °C. These compounds showed superparamagnetic behavior by a mixture of Néel superspin relaxation and Brownian motion, attributed to smaller respectively larger particles of the ensemble. The onset of Brownian motion was clearly visible by discontinuities in magnetization curves close to the melting region.
A more thorough insight in relaxation frequencies was achieved by detailed AC-mapping, meaning the measurement of the complex magnetic AC-susceptibility under variation of the temperature and the frequency of the AC magnetic field. By this method, a very broad distribution of Néel superspin fluctuation was detected, producing a structureless and almost constant background signal. A significant peak feature occurred at temperatures above ca. 50 °C, shifting from ultralow frequencies into the accessible frequency interval. This contribution was very pronounced in the myristate ester-based compound, while in the second sample the peak feature was barely visible as it remained below the measurable frequency range. This difference in relaxation dynamics could point to larger particle diameters in the palmitate based compound, accompanied by much lower rotation frequencies. Reproducing this feature by an appropriate model system, also considering effects of the particle size distribution, resulted in the estimation of the average hydrodynamic particle size, yielding about 64 nm and a standard deviation of 36 nm. Thus, the particles move within the myristate polymer melt primarily as separate raspberry clusters rather than as large agglomerates. Based on this result, particle core size and raspberry structure can be tuned to optimize the specific energy uptake and the heat conversion capability of the polymer compound.

Outlook

Within the scope of this thesis a number of questions regarding magnetic particle dynamics could be answered, while others remain partially unsolved. One of the first main results was the observation of widely unchanged surface spin canting in combination with strongly increased blocking temperatures upon variation of the particle capping thickness. As reports of different surface magnetism can be found for capping showing strong or weak chemical bonding to the surface of the nanoparticle, a promising idea would be the tuning of the particle capping material to achieve a variation in particle-matrix interaction in parallel to designing the desired magnetic structure of the particle. This, however, depends on the applicable capping materials and their suitability as mediating agents transferring particle-matrix interaction.

As Mössbauer spectroscopy has been shown to be a versatile instrument for simultaneous characterization of relaxation dynamics of Néel as well as Brownian origin, testing of this auspicious approach on different types of soft matter compounds would be the logical next step. Mössbauer setups often include coil geometries to apply magnetic fields, whereby a detailed analysis, e.g., of the magnetoviscous effect in magnetorheological fluids would be natural. Doing this, deeper insight in the formation and dynamics of particle chains could be attained using AC-susceptometry as a reference method.

While Mössbauer spectroscopy is capable of studying different relaxation processes in parallel, other techniques could be modified to follow this approach. In recent experiments higher harmonics in the non-linear magnetic response signal of a sample exposed to an external AC magnetic field above the linear low-field region are analyzed. As Néel superspin fluctuation and diffusive Brownian motion show a fundamentally different dependence on the amplitude of external magnetic fields, the study of higher harmonics in ferrofluids and soft matter nanoparticle compounds could also yield, to some degree, resolution of both processes.

Intensifying the research by Mössbauer spectroscopy on particle diffusion, the influence of the aspect ratio on translational and rotational movement could be modeled in more detail, as elongated hematite nanospindles were the only example showing noticeable deviations between results from Mössbauer spectroscopy and AC-susceptometry in absolute numbers, while the detected behavior in general was comparable.

Beyond using iron-bearing particles as a 'passive' sensor for material properties, the main motive for the widespread application of magnetic nanoparticles in composites is the ability to tune these properties 'actively'. Therefore, the study of orientational dynamics in the presence of a magnetic field deserves more attention, including the influence of the particle shape on the resulting deformation of the surrounding matrix material. Especially promising for such experiments are anisotropic particle configurations, which can be obtained by triggering the polymerization process in presence of an applied magnetic field.

A Appendix

A.1 Hyperfine parameters of capped iron oxide nanoparticles

In-field Mössbauer spectra of capped iron oxide nanoparticles shown in figure 4.4 were recorded to determine their magnetic structure and hyperfine parameters and allow a quantitative comparison of particle properties. Hyperfine parameters obtained from least-squares fits of these spectra are listed in table A.1, where isomer shift δ and effective magnetic field B_{eff} of the Fe^{2+} subspectrum were fixed due to their minor spectral area complicating the determination of hyperfine parameters in each spectrum individually. Further details on the theoretical reproductions of the in-field spectra are presented in Ref. [55].

Independent of the applied capping agent or shell material, isomer shifts and effective magnetic fields of the three subspectra were found to be widely similar for all samples. On the other hand, different amounts of Fe^{2+}, corresponding to the fraction of magnetite in the particles, are found for the bare particles M1, while particles coated with IGEPAL (M2) and an additional silica shell (M3 - M4), display larger spectral area of the Fe^{2+} subspectrum, indicating smaller thickness of the maghemite oxidation layer. As the variation in Fe^{2+} from 10 % to 17 % is not very pronounced, only minor differences, e.g., in the particle magnetic moment are expected. Some differences are also visible in the site-specific spin canting angles θ. However, by calculating the *average* canting angle $\overline{\theta}$, i.e., by weighting the subspectra canting angles by the corresponding relative spectral area, one yields values of $\overline{\theta}$ spanning from about $19°\pm1°$ (M1) to $17°\pm1°$ (M3, M4), which implies very similar magnetic surface structure. As the variation in average canting angles is within the error bar, it is unclear if θ is increased to a minor extent by a higher thickness of the oxidation shell or by the applied capping material or if these small differences justify such a detailed interpretation at all. Nevertheless, it should be mentioned that by in-field Mössbauer spectroscopy, an almost identical magnetic particle structure in external magnetic fields was verified.

A.2 Temperature calibration of custom-built Mössbauer sample holders

Liquid or partially fluid samples were mounted in the custom-built sample holder, introduced in section 3.1, inside a copper cylinder, which was sealed tightly using epoxy resin in first experiments and later on sealed by a screw-mountable mylar window. Both geometries do not easily allow to determine the temperature of the liquid inside. For that reason, the measurement temperature was quantified using a PT100 temperature sensor mounted in proximity to the sample position at the surface of the sample holder. However, as small deviations of the nominal sensor temperature relative to the sample temperature are possible, calibration measurements have been performed using a NiCr-Ni-NiCr thermocouple. Connecting the NiCr-Ni contact to the PT100 sensor and putting the Ni-NiCr contact inside the liquid volume of a water

	A^{3+}	B^{3+}	B^{2+}	A^{3+}	B^{3+}	B^{2+}
		M1			M2	
δ (mm/s)	0.37±0.01	0.50±0.01	0.88*	0.38±0.01	0.52±0.01	0.88*
θ (°)	15±3	22±2	13±13	15±3	21±2	0±16
B_{eff} (T)	54.9±0.1	47.3±0.1	43.6*	54.7±0.1	47.1±0.1	43.6*
A (%)	30±1	60±1	10±1	30±1	56±1	14±1
	A^{3+}	B^{3+}	B^{2+}	A^{3+}	B^{3+}	B^{2+}
		M3			M4	
δ (mm/s)	0.38±0.01	0.51±0.01	0.88*	0.38±0.01	0.50±0.01	0.88*
θ (°)	15±2	18±2	20±6	12±3	19±2	20±7
B_{eff} (T)	55.0±0.1	47.4±0.1	43.6*	54.9±0.1	47.2±0.1	43.6*
A (%)	31±1	53±1	17±1	31±1	55±1	15±1

Table A.1: Hyperfine parameters of capped iron oxide nanoparticles M1 - M4 determined by in-field Mössbauer spectroscopy as described in section 4.1: Isomer shift δ relative to α-iron at room temperature, the site-specific canting angle θ, the effective magnetic field B_{eff} and the relative spectral area of the individual subspectra corresponding to Fe^{3+} on tetrahedral A-sites (A^{3+}), and Fe^{3+} or Fe^{2+} on octahedral B-sites (B^{3+},B^{2+}), respectively [55].

reference sample allowed to determine an upper-limit estimation of the error in the measured sample temperature. Water is an adequate reference sample, as most of the other measured compounds are mainly water based with very similar thermal conductivity and thermal capacity. To improve the precision of this reference measurement, it was performed repeatedly for three times with the Ni-NiCr contact mounted at a random position, at the center of the sample space and close to the copper wall of the sample holder. Temperature difference ΔT, being proportional to the measured thermal voltage signal, are shown in figure A.1. Upon lowering the sample temperature, a linear increase in the difference voltage signal is observed with small variation dependent on the individual position of the thermocouple and a mean value of about 10 % of the sample temperature relative to ambient conditions. This calibration was applied, e.g., in Mössbauer experiments on ferrohydrogels presented in chapter 6, where the temperature calibration had limited effect on the nominal sample temperature, as relevant variations in the Mössbauer spectrum where discussed in the region of ca. 273 K, corresponding of a temperature correction of about 2 K. These calibration measurements were performed subsequently to first experiments on ferrohydrogels using the Peltier-cooled sample holder, leading to minor deviations between data in chapter 6 and Ref. [125]. For further experiments on glycerol-based

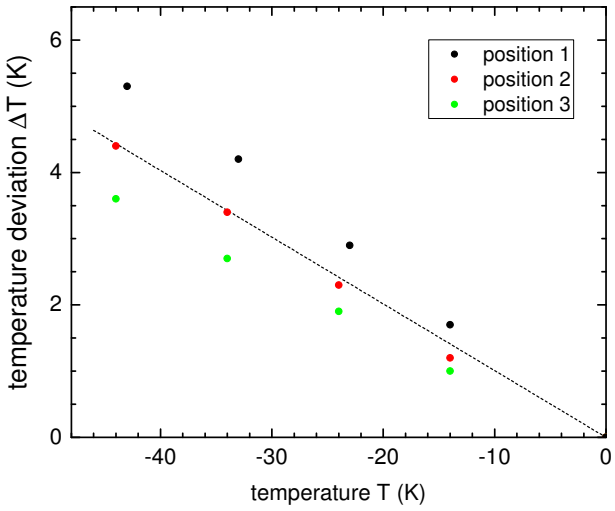

Figure A.1: Temperature deviation ΔT between measurements *within* the liquid sample and in its proximity on the sample holder at measurement temperature T (relative to ambient temperature). The calibration measurement has been performed three times with small variations in the position (1-3) of the thermocouple within the sample volume, the dashed line represents the least-squares linear interpolation.

ferrofluids discussed in chapter 5 a new double-stacked Peltier setup was designed to reach even lower temperatures combined with a better thermal insulation. In this setup $\leq 6\%$ temperature deviation was determined. The quartz-halogen lamp setup introduced for experiments on the polymer compounds in chapter 7 was calibrated by analogy to these measurements, yielding a linear temperature deviation and $\Delta T \approx +3$ K at about 380 K. Results from Mössbauer spectroscopy shown in the scope of this thesis were plotted versus the nominal temperature, calibrated according to the utilized Mössbauer sample holder.

A.3 Verwey transition in glycerol-based ferrofluids

Weakly pronounced peaks in the FC-ZFC magnetization curves of ferrofluidic sample L at ca. 100 - 110 K indicate a Verwey transition and, therefore, the presence of a remaining magnetite core in the incorporated 26 nm iron oxide nanoparticles, as described in section 5.1. Mössbauer spectra of ferrofluids with particles from 6 to 26 nm in core size (sample S, M and L) were recorded in a liquid nitrogen cryostat in the range of 80 - 180 K. For each sample, one spectrum was measured below and one spectrum above the bulk Verwey temperature of 123 K.

The Mössbauer spectrum of sample S at 80 K displays a deformed sextet structure, which could be reproduced theoretically by usage of a hyperfine field distribution $p(B_{hf})$. At 180 K, sample S shows a transition spectrum, similar to a superparamagnetic doublet. In both spectra of sample M, the sextet structure is conserved, corresponding to a magnetically blocked state, although beginning relaxation dynamics, i.e., thermally driven collective excitations, are visible by increasingly asymmetric line shapes upon warming. Accordingly, the spectra have been successfully reproduced by the many-state relaxation model of Jones and Srivastava [72]. For the biggest particles in sample L, clear evidence of the Verwey transition can be observed, in agreement with SQUID-magnetometry results. Only one sextet with a structureless inner

shoulder, marked by a black arrow, is visible at 80 K, which can be assigned to superposition of both Fe^{3+} subspectra (A- and B-sites) and that of Fe^{2+} ions on B-sites. In contrast, the spectrum at 150 K exhibits two well-resolved subspectra, marked by the red arrow. According to Néel's original theory, they can be assigned to a mixed $Fe^{2.5+}$ valence state by electron hopping between different B-site ions, leading to the existence of only one B-site subspectrum (green) with slightly different hyperfine parameters as compared to the tetrahedral A-site (cyan).

As this change in spectral fine structure is very pronounced and comparable to Mössbauer literature reports on the Verwey transition in bulk magnetite, this fact indicates a large magnetite volume fraction in sample L, presumably by conserved magnetite in the particle core. The existence of minor magnetite fractions in sample S and M cannot be clarified here, as their Mössbauer spectra display beginning or striking Néel relaxation features, which could cover the effects discussed above for sample L.

A.4 Alternative MS-fitting model using high relaxation rates

The fitting routine for Mössbauer spectra of ferrofluid sample M, incorporating capped 15 nm magnetite nanoparticles, as described in section 5.2, is well-suited to reproduce the peculiar shape of the spectra and to determine the broadening $\Delta\Gamma$ of the absorption lines relative to the static linewidth. A low relaxation parameters R $\ll$ 10 mm/s corresponds to the slow diffusion limit, i.e., a slow diffusive superspin reorientation, and is usually not adequate to reproduce fast superparamagnetic processes and the correct estimation of the anisotropy energy E_A. In the slow diffusion limit, the effect of Néel relaxation on the spectral shape is limited to a distribution in the nuclear Zeeman splitting, while no superparamagnetic doublet is observable even at low anisotropy energies [72, 100]. To obtain reference values of E_A comparable to that of samples S and L, spectra of sample M were reproduced, in addition to the original fit, using R = 10 mm/s, which is shown in figure A.3. R, which is a measure of the relaxation prefactor τ_0, then translates to $\tau_0 \approx 1.37$ ns, as described in section 3.1 in more detailed. This is roughly comparable to reference values of $\tau_0 \approx 10^{-10}$ s, acquired by thermoremanent magnetization in section 4.2. This new fitting routine yields an anisotropy energy density of $K_{eff} \approx 12.4 \pm 0.5$ kJm^{-3}, being about constant in the temperature interval of 180 - 240 K, where Néel relaxation effects on the spectral shape are clearly visible, whereas the spectrum is smeared out by enhanced Brownian line broadening at higher temperatures, where no magnetic anisotropies can be determined.

Calculated spectra in figure A.3 (red lines) display good agreement with the experimental data. Above 248 K, no difference between the computed and measured broadened spectra is observable any longer. At lower temperatures, a less precise reproduction of line shape in the center of the spectrum, i.e., close to the position of the beginning intensity of the superparamagnetic

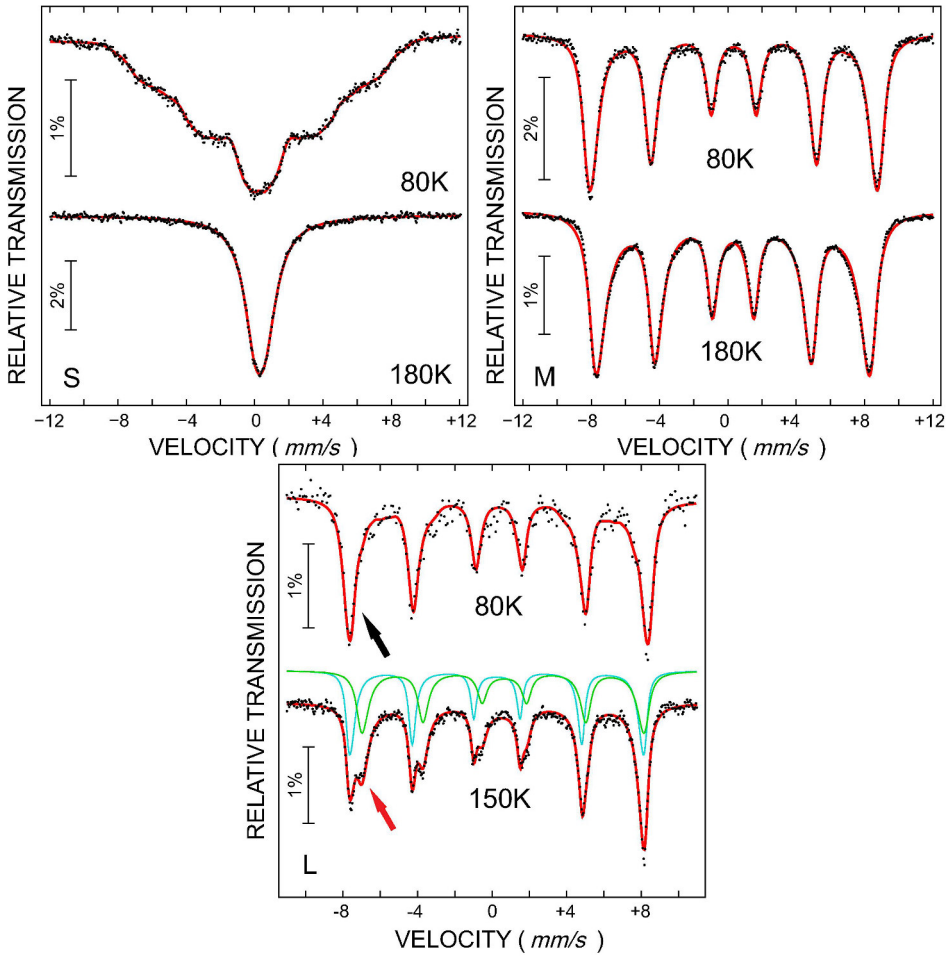

Figure A.2: Mössbauer spectra of ferrofluid sample S, M and L measured below (at 80 K), and above the bulk Verwey temperature (e.g. at 180 K). Spectra of sample S and M display distinct Néel relaxation features. In sample L, the superposition of Fe^{3+} and Fe^{2+} contribution leads to a structureless inner shoulder at 80 K (black arrow). For sample L at 150 K, all B-site atoms contribute to one single subspectrum due to electron hopping, leading to clear changes in the fine structure of lines 1 and 2 (red arrow).

doublet, is revealed by direct comparison to the original fitting routine in figure 5.3. Apparently, for R = 10 mm/s, a small doublet intensity is predicted in this temperature regime, which does not occur in the experimental spectrum. Although the particle concentration in the fluid is relatively low, the particles are of considerable size with large net magnetic moment, compared to the smaller interacting particles discussed in chapter 4. Therefore, they could experience weak magnetic dipole interaction, suppressing the emergence of the superparamagnetic doublet to some degree, as was similarly observed for strongly interacting particles of about 6 nm in diameter in chapter 4.

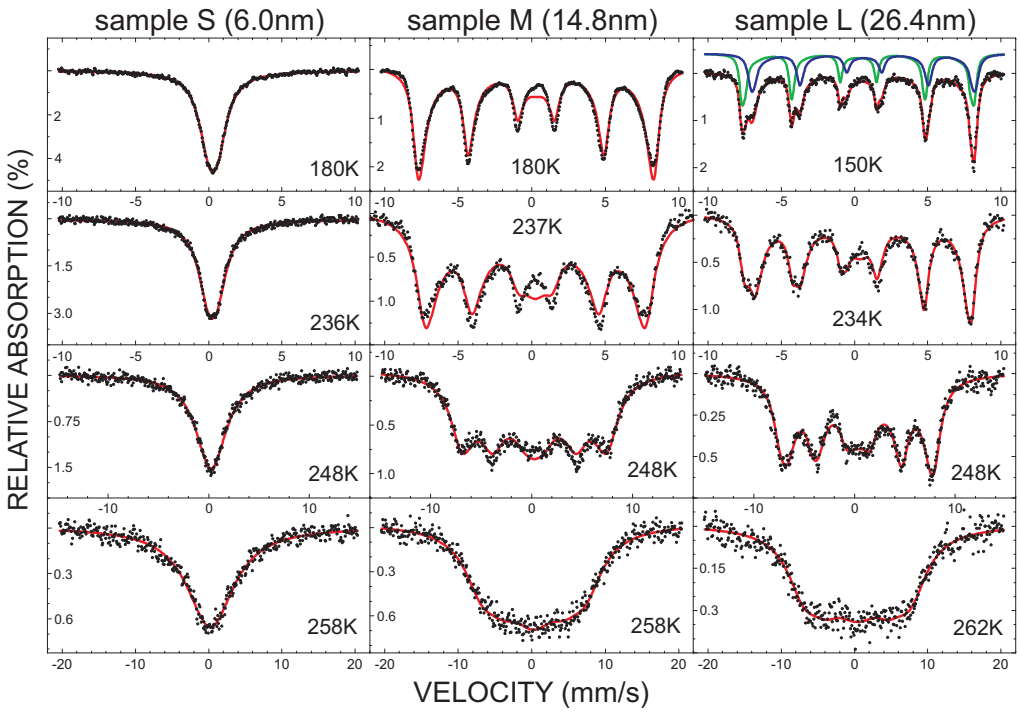

Figure A.3: Mössbauer spectra of 15 nm nanoparticles incorporated in glycerol-based ferrofluid (sample M), calculated using a relaxation parameter R of 10 mm/s by analogy to figure 5.3. Spectra of sample S and L are shown for comparison.

A.5 Shape anisotropy of hematite nanospindles

In chapter 6, the magnetic anisotropy of the hematite nanospindles studied was approximated by a strong uniaxial anisotropy along the hexagonal c-axis and a very weak triaxial anisotropy contribution parallel to the easy magnetic basal plane. With a magnetocrystalline anisotropy constant of ca. 0.1 - 1 kJm^{-3} the latter is so small that contributions of shape anisotropy may lead to a distinct variation in the magnetic orientation behavior of the individual particle. For that reason the contribution by shape anisotropy of spindle-shaped hematite nanoparticles is estimated in the following by approximating the fusiform particle by a spheroid. Then the shape anisotropy energy density is [44]

$$K_{shape} = \frac{\mu_0 M_S^2}{2}(N_c - N_a) \cdot \sin^2(\theta). \tag{A.1}$$

Here N_a and N_c are the demagnetization factors of the spheroid along the long semiaxis a and the short semiaxis b = c, respectively, and θ the angle between the magnetization direction and a. The demagnetization factors of a spheroidal particle with the aspect ratio p = a/c can be well approximated by [150]

$$N_A \approx \frac{1}{p^2-1}\left(\frac{p}{\sqrt{p^2-1}}\text{arccosh}(p) - 1\right). \tag{A.2}$$

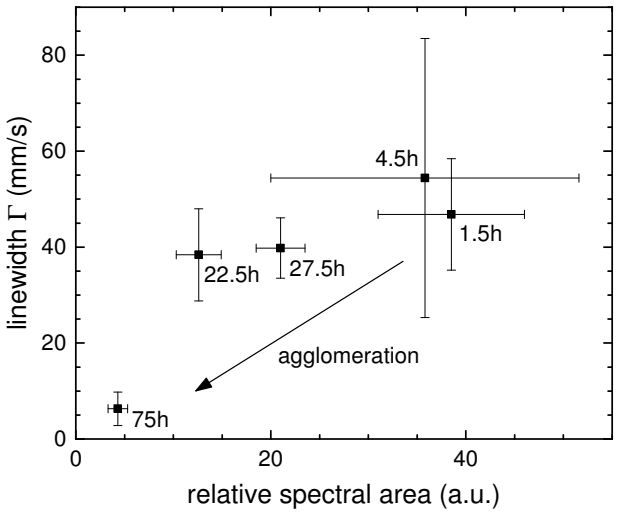

Figure A.4: Linewidths observed in spectra of $c_V \approx 1.3$ vol% hematite nanoparticles in water versus the relative spectral area. Aging times of the ferrofluids are labeled accordingly, showing enhanced agglomeration after several days.

For the hematite nanoparticles at hand, parameters are 2a = 387nm and 2c = 85nm, resulting in p $\approx$ 4.55, $N_a \approx 0.064$ and $N_c \approx 0.468$ according to $\sum N_i = 1$ and $N_b = N_c$. The canted antiferromagnetic structure of hematite above the Morin transition leads to a minor net magnetization of about 2000 A/m, wherefore one yields a maximum in shape anisotropy energy density $K_{shape} \approx 1.0$ J/m^{-3} from the equation above. As expected for particles made from nearly antiferromagnetic material with $M_S \to 0$, the contribution of shape effects to the total anisotropy energy is negligible, even when compared to the very weak magnetocrystalline anisotropy defining the triaxial easy axes within the basal plane.

A.6 Effect of agglomeration on Mössbauer spectra of ferrofluids

Ferrofluids tend to display limited stability due to particle agglomeration and sedimentation. To study the long time stability of hematite nanospindle ferrofluids and the maximum shelf time without measurable changes in particle mobility, Mössbauer spectra were measured for water-based ferrofluids and 60 wt% sucrose solution after waiting times of several hours to days. While sucrose-based ferrofluids exhibit good long time stability, presumably due to the higher viscosity leading to less pronounced sedimentation, agglomeration effects could be observed in hematite nanospindles dissolved in water, as exemplarily demonstrated in figure A.4. Within several hours a considerable decay in average linewidth and spectral area is observed. This could indicate enhanced particle agglomeration followed by sedimentation of the larger, unstable agglomerates to the bottom of the sample holder.

Mössbauer spectra obtained within the first hours of the experiment yield linewidths of about 60 mm/s. This is much higher than maximum linewidths of about 20 mm/s determined in case of sucrose-based ferrofluids or crosslinked ferrohydrogels, proving that this value does not represent the maximum linewidth observable for particles of this size due to their kinematic motion as an upper limit of velocity in Brownian diffusional motion. Mössbauer spectra of

this reference series are not displayed individually, as they exhibit poor signal-to-noise ratio due to the limited measurement time of several hours. In parallel, this could indicate that agglomeration effects start already within the first hours, wherefore even higher linewidths would be observable directly after sample preparation.

A theoretical prediction of the diffusional line broadening may be obtained from equation (2.16) assuming a dynamic viscosity η_{water} of 1 mPas and representing the fusiform particle by a spherical particle of comparable surface, yielding $\Delta\Gamma \approx 400$ mm/s. Due to beginning agglomeration effects the exact line broadening of the nanospindles dissolved in water could not be clarified for comparison with this theoretical value. However, the overall correctness of the applied fitting routines and theoretical models is ensured by the comparison of line broadening determined by Mössbauer spectroscopy with rotation frequencies from AC-susceptometry of spherical particles of ca. 25 nm in hydrodynamic diameter in glycerol-based ferrofluids, presented in chapter 5.

A.7 Calculation of anisotropic diffusion coefficients

Studying slightly elongated particles, is seems reasonable to approximate their Brownian motion by that of a spherical particle experiencing similar friction in contact to the surrounding fluid molecules. However, hematite nanospindles studied in chapter 6 deviate strongly from the spherical shape, wherefore one can predict considerable error resulting from the application of spherical diffusion coefficients. Instead, the spindle shape of the particles resembles more closely to that of a spheroid with long half axis a and short half axis c = b. The most relevant remaining difference of both bodies is the missing front area of the nanospindle perpendicular to the preferred direction of motion.

The friction and diffusion coefficients of spheroidal objects moving in liquids have been analyzed extensively. According to Ref. [185] - [186], translational and rotational friction coefficients of a spheroid parallel and perpendicular to its long half axis are described by the following set of equations.

$$s = \frac{2}{\sqrt{a^2 - c^2}} \ln\left(\frac{a + \sqrt{a^2 - c^2}}{c}\right) \tag{A.3}$$

$$\gamma_t^{\parallel} = 16\pi\eta \frac{a^2 - c^2}{(2a^2 - c^2)s - 2a} \tag{A.4}$$

$$\gamma_t^{\perp} = 32\pi\eta \frac{a^2 - c^2}{(2a^2 - 3c^2)s + 2a} \tag{A.5}$$

$$\gamma_r^{\parallel} = \frac{32\pi\eta}{3} \frac{a^4 - c^4}{(2a^2 - c^2)s - 2a} \tag{A.6}$$

$$\gamma_r^{\perp} = \frac{32\pi\eta}{3} \frac{(a^2 - c^2)c^2}{2a - c^2 s} \tag{A.7}$$

	sphere	spheroid
$\gamma_t^{\parallel}$	$2.64 \cdot 10^{-8}$ J m^{-2} s	$2.73 \cdot 10^{-8}$ J m^{-2} s
$\gamma_t^{\perp}$	$2.64 \cdot 10^{-8}$ J m^{-2} s	$3.58 \cdot 10^{-8}$ J m^{-2} s
$\gamma_r^{\parallel}$	$1.72 \cdot 10^{-22}$ Js	$7.14 \cdot 10^{-22}$ Js
$\gamma_r^{\perp}$	$1.72 \cdot 10^{-22}$ Js	$1.25 \cdot 10^{-22}$ Js

Table A.2: Spheroidal translational- (t) and rotational (r) friction coefficients for motion parallel ($\parallel$) and perpendicular ($\perp$) to the spheroids long half axis a in sucrose solution of $\eta_{300K} \approx 0.02$ Pas. For calculation of the spheroidal approximation parameters 2a = 387 nm and 2c = 85 nm of the hematite nanospindles have been applied, and for those of the simpler spherical approximation an estimated effective radius of 70 nm was used.

The broadening $\Delta\Gamma$ of Mössbauer absorption lines is correlated directly to the mean square displacement within the time scale of the measurement technique, characterized by the half life of the excited ^{57}Fe $I_{3/2}$ nuclear state of about 100 ns. An approximation assuming spheroidal geometry may, therefore, be found by estimating an averaged translational diffusion coefficient. For the isotropic motion of a spherical object, $\overline{\Delta r^2}$ is given by equation (2.14). Accordingly, equation (A.9) is an expression of the movement averaged over all directions, parallel as well as perpendicular to the long particle axis. Friction coefficients of a spheroid with long- and short axis lengths 2a = 387 nm und 2c = 85 nm, identical to that of the hematite nanoparticles, are listed in table A.2 in comparison with values determined from the spherical model.

$$\overline{\Delta r^2} = \sum_{i=1}^{3} \overline{\Delta r_i^2} \tag{A.8}$$

$$\overline{\Delta x^2} = \overline{\Delta y^2} = \overline{\Delta z^2} \quad \Rightarrow \quad \overline{\Delta r^2}_{Kugel} = 3 \cdot \overline{\Delta x^2} \tag{A.9}$$

Following equations (2.13) and (3.42) a correlation of line broadening $\Delta\Gamma$ inversely proportional to the friction coefficient γ can be predicted. Thereby, an averaged 'isotropic' line broadening may be estimated from the harmonic mean value of translational friction coefficients parallel and perpendicular to the spheroidal long particle axis by analogy to Ref. [187], as described by equation (A.10). For length and diameter of the hematite nanospindles, one yields a parameter $K(\gamma_t^{\parallel}, \gamma_t^{\perp}) \approx 1.65 \cdot 10^{-6}$ m.

$$\overline{\gamma_t} = \left(\frac{\gamma_t^{\parallel -1} + 2\gamma_t^{\perp -1}}{3} \right)^{-1} \tag{A.10}$$

$$K(\gamma_t^{\parallel}, \gamma_t^{\perp}) = \frac{\overline{\gamma_t}}{\eta} \tag{A.11}$$

To determine the dynamic viscosity η directly from experimentally measured linewidths, respectively the corresponding averaged translational diffusion coefficient, the parameter $K(\gamma_t^{\parallel}, \gamma_t^{\perp})$

can be defined. In the spherical model, K represents the geometrical factor $6\pi R_{Hyd}$ and converges to this value for spheroids of aspect ratio p $\rightarrow$ 1. Using this parameter in the formula of the energy variation by the Doppler effect, one yields an expression for the line broadening in case of spheroidal particles

$$\Delta v = \frac{\Delta E c}{E_0}, \qquad \Delta E = 2\hbar D k^2, \tag{A.12}$$

$$\Rightarrow \Delta v = 2Dk, \qquad D = \frac{k_B T}{\overline{\gamma_t}} \tag{A.13}$$

$$\Rightarrow \Delta v = \frac{2k k_B T}{\overline{\gamma_t}}, \qquad \overline{\gamma_t} = K(\gamma_t^{\parallel}, \gamma_t^{\perp})\eta \tag{A.14}$$

$$\Rightarrow \Delta v(mm/s) = 10^3 \cdot \frac{2k k_B T}{\eta K(\gamma_t^{\parallel}, \gamma_t^{\perp})} \approx 2.01 \cdot 10^{-9} \frac{T}{\eta K(\gamma_t^{\parallel}, \gamma_t^{\perp})} \tag{A.15}$$

By analogy to the translational diffusion coefficient of spheroids derived above as the primary component of line broadening visible in Mössbauer spectroscopy, an estimation of the rotational frequency in AC-susceptibility can be established using the rotational spheroidal friction and diffusion coefficients. As AC experiments on elongated particles in chapter 6 are limited to the frequency range corresponding to the millisecond regime, one can consider translational and rotational motion as decoupled processes. As illustrated by Han et al. [188], elongated particles display diffusional motion preferentially parallel to the long particle axis, which is relevant only on very short time scales before particle rotation leads to averaged motion in all directions on longer time scales. Following this assumption, degrees of freedom in translation have not to be included in the model. The AC-susceptibility signal of elongated particles usually is relatively easy to predict, as the magnetic particle moments $\vec{\mu_{NP}}$ normally are aligned along the long particle axis due to dominating shape anisotropy. In that case, only $\gamma_r^{\parallel}$ would remain in the model, as only the rotation about the short particle axes would result in a change in direction of the particle net magnetic moment.

For the hematite nanoparticles discussed here, the model is more complex, as the shape anisotropy contribution is very small due to the negligible saturation magnetization as illustrated in section A.5 of the appendix, leading to an orientation of the net magnetic moment along a direction within the hexagonal basal plane. Thereby, a change in $\vec{\mu_{NP}}$ can be achieved by rotation about the short *and* the long particle axis. By analogy to the directional averaging of the translational friction coefficients to $\overline{\gamma_t}$, one now can assume independent rotation about the three relevant axes. However, the rotation about the short axis parallel to the magnetic

moment can be neglected, as it does not result in a variation of $\vec{\mu_{NP}}$.

$$\left(\frac{\gamma_r^{\parallel -1} + \gamma_r^{\perp -1}}{2}\right)^{-1} = \overline{\gamma_r} \tag{A.16}$$

$$K_2(\gamma_r^{\parallel}, \gamma_r^{\perp}) = \frac{\overline{\gamma_r}}{\eta} \tag{A.17}$$

Similar to the translational model, one finds a parameter $K_2(\gamma_r^{\parallel}, \gamma_r^{\perp})$ by equations (A.16) and (A.17), converging to the well known term of $8\pi R_{Hyd}^3$ from equation (3.43) for the rotation of spherical objects. Setting in the parameters a and c of the hematite nanospindles, one yields $K_2(\gamma_r^{\parallel}, \gamma_r^{\perp}) \approx 1.06 \cdot 10^{-20}$. Thus, the rotational friction coefficient is, similar to the translational friction coefficient, enhanced relative to that of the spherical reference object, resulting in a decrease in calculated dynamic viscosity from a specific rotation frequency in the AC-experiment. For the spheroidal model presented here, calculated viscosity values are displayed comparatively with those from the spherical model in figure 6.8, revealing a decrease of ca. 25 % in η by Mössbauer spectroscopy as well as by AC-susceptometry.

A.8 Orientation of hematite nanospindles in external magnetic fields

In section 6.5, the effect of an external magnetic field, applied perpendicular to the γ-ray propagation direction, on the Mössbauer spectrum of a viscoelastic ferrohydrogel is investigated. One of the key issues is which conclusions can be drawn from this experiment on the magnetic orientation of the superspin within the hematite nanoparticles or on the spatial orientation of the nanospindles within the ferrohydrogel. This question will be discussed here in more detail under usage of suitable theoretical models:

In the literature, reports of negligible triaxial magnetic anisotropy within the hematite basal plane perpendicular to the hexagonal c-axis can be found [32]. In the studied hematite nanospindles, the c-axis corresponds to the long particle axis due to the particle growth mechanism. The primary component of the electric field gradient tensor V_{zz}, relevant for the Mössbauer analysis discussed below, is also aligned parallel to the hexagonal c-axis in hematite. Based on this magnetic structure, one would predict an orientation of the magnetic particle moment $\vec{\mu_{NP}}$ along one of the three triaxial easy directions in the basal plane in zero external field. At moderate external field amplitudes, an orientation along magnetic field direction as far as possible within the basal plane could be expected, as the dominating uniaxial anisotropy does not allow considerable orientation in the direction of the c-axis. This complex geometry is illustrated in figure 2.4 in chapter 2.

The prediction of the spin orientation, i.e., the sublattice magnetization, relative to the propagation direction of the γ-ray, which determines the line intensity ratio A_{23} in the resulting Mössbauer spectrum, is not a trivial matter. Assuming complete alignment of the particle

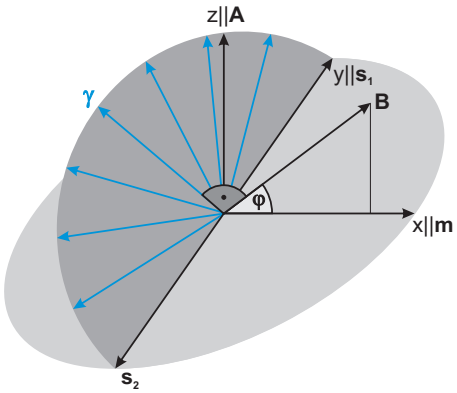

Figure A.5: Schematic view of the antiparallel spin orientation of $\vec{s_1}$ and $\vec{s_2}$, perpendicular to the net magnetization $\vec{m}$, in the applied magnetic field $\vec{B}$ relative to the γ-ray propagation directions (blue). For this schematic model, a complete orientation of the net magnetic particle moment *within* the easy magnetic basal plane is assumed.

magnetic moment along the magnetic field direction within the easy magnetic plane, a simple model can be found by a fixed particle orientation and a number of γ-ray propagation directions, representing the possible orientations of the randomly aligned particles relative to the γ-ray in the sample:
By defining the vector $\vec{A}$, corresponding to the direction of the long particle axis along the z-axis in cartesian coordinates, the easy magnetic basal plane is automatically represented by the x-y-plane. As the particle magnetic moment will turn within the easy magnetic plane along the magnetic field direction $\vec{B}$, we can define $\vec{B}$ as situated in the x-z-plane. In consequence, the γ-ray, which is perpendicular to $\vec{B}$, is represented here by a plane of possible directions perpendicular to $\vec{B}$. As this geometry may be confusing, important directions are illustrated in figure A.5.
Now, the average line intensity ratio A_{23} can be determined by integrating over all possible geometries, but it can also be obtained by the three following and relative simple considerations:

- As $\vec{B}$ is in the x-z-plane and spin directions $\vec{s_{1,2}}$ will, per definition, turn perpendicular to $\vec{B}$ within the x-y-plane, $\vec{s_{1,2}}$ are aligned coaxial to the y-direction.
- Thus, possible canting angles θ between $\vec{s_{1,2}}$ and γ can be described by a constant distribution in the angular interval of 0° - 180°.
- As the function A_{23} is symmetrical in 90° intervals, one yields an average angle of 45°.

Obviously, the more complex integral calculation can be avoided by this approach. However, this integration has been carried out as a reference, yielding the same average canting angle of 45°, which translates to a ratio in spectral area of lines 2 and 3 of $\overline{A_{23}} = 4/3$. This is consistent

with line intensity ratios of 4/3 observed in Mössbauer spectra at about 300 mT, proving the complete alignment of the magnetic particle moment within the easy magnetic plane. Further studies on the out-of-plane orientation can be performed in terms of the nuclear quadrupole level shift, as reported in section 6.5.

By analogy to this geometry, the same model can be utilized to predict the line intensity ratio in case of a magnetic field *parallel* to the γ-ray propagation direction, yielding an intuitive value of $A_{23} = 4$, corresponding to spins aligned perpendicular to the field direction. This geometry has been realized testwise by attaching a set of NdFeB-rings to the sample holder, providing a static magnetic field of ca. 340 mT in the required direction. From a measured reference spectrum, the predicted value of $A_{23} = 4$ has been verified, proving again the complete orientation of the net magnetization within the easy magnetic plane.

Bibliography

[1] X. Batlle and A. Labarta. Finite-size effects in fine particles: magnetic and transport properties. *J. Phys. D: Appl. Phys.*, 35:R15, 2002.

[2] S. Mørup, E. Brok, and C. Frandsen. Spin Structures in Magnetic Nanoparticles. *J. Nanomater.*, 720629, 2013.

[3] A.-H. Lu, E. L. Salabas, and F. Schüth. Magnetic Nanoparticles: Synthesis, Protection, Functionalization, and Application. *Angew. Chem. Int. Ed.*, 46:1222, 2007.

[4] D. H. Wang and W. H. Liao. Magnetorheological fluid dampers: a review of parametric modelling. *Smart Mater. Struct.*, 20:023001, 2011.

[5] H. S. Lee and S. B. Choi. Control and Response Characteristics of a Magneto-Rheological Fluid Damper for Passenger Vehicles. *J. Intell. Mater. Syst. Struct.*, 11:80, 2000.

[6] K. Raj and R. Moskowitz. Commercial applications of ferrofluids. *J. Magn. Magn. Mater.*, 85:233, 1990.

[7] R. Moskowitz. Dynamic Sealing with Magnetic Fluids. *A S L E Transactions*, 18:135, 1975.

[8] A. S. Lübbe, C. Alexiou, and C. Bergemann. Clinical Applications of Magnetic Drug Targeting. *J. Surg. Res.*, 95:200, 2001.

[9] A. B. Saluhnke, V. M. Khot, and S. H. Pawar. Magnetic Hyperthermia with Magnetic Nanoparticles: A Status Review. *Curr. Top. Med. Chem.*, 14:572, 2014.

[10] T. Neuberger, B. Schöpf, H. Hofmann, M. Hofmann, and B. von Rechenberg. Superparamagnetic nanoparticles for biomedical applications: Possibilities and limitations of a new drug delivery system. *J. Magn. Magn. Mater.*, 293:483, 2005.

[11] L. Lanotte, G. Ausanio, C. Hison, V. Iannotti, C. Luponio, and C. Luponio Jr. State of the art and development trends of novel nanostructured elastomagnetic composites. *J. Optoelectron. Adv. M.*, 6:523, 2004.

[12] K. Zimmermann, V. A. Naletova, I. Zeidis, V. Böhm, and E. Kolev. Modelling of locomotion systems usig deformable magnetizable media. *J. Phys.: Condens. Matter*, 18:S2973, 2006.

[13] R. L. Snyder, V. Q. Nguyen, and R. V. Ramanujan. Design parameters for magneto-elastic soft actuators. *Smart Mater. Struct.*, 19:055017, 2010.

[14] D. Kuckling, A. Richter, and K.-F. Arndt. Temperature and pH-Dependent Swelling Behavior of Poly(*N*-isopropylacrylamide) Copolymer Hydrogels and Their Use in Flow Control. *Macromol. Mater. Eng.*, 288:144, 2003.

[15] S. B. Dierker, R. Pindak, R. M. Fleming, I. K. Robinson, and L. Berman. X-Ray Photon Correlation Spectroscopy Study of Brownian Motion of Gold Colloids in Glycerol. *Phys. Rev. Lett.*, 75:449, 1995.

[16] T. Klein, A. Laptev, A. Günther, P. Bender, A. Tschöpe, and R. Birringer. Magnetic-field-dependent optical transmission of nickel nanorod colloidal dispersions. *J. Appl. Phys.*, 106:114301, 2009.

[17] P. C. Fannin, B. K. P. Scaife, and S. W. Charles. New technique for measuring the complex susceptibility of ferrofluids. *J. Phys. E: Sci. Instrum.*, 19:239, 1986.

[18] L. von Bogdandy and H.-J. Engell. *The Reduction of Iron Ores*. Springer-Verlag, Berlin, 1971.

[19] D. J. Dunlop and Ö. Özdemir. *Rock Magnetism*. Cambridge university Press, 1997.

[20] B. D. Cullity and C. D. Graham. *Introduction to magnetic materials*. John Wiley & Sons, Inc., Hoboken, New Jersey, 2. edition, 2009.

[21] A. H. Hill, F. Jiao, P. G. Bruce, A. Harrison, W. Kockelmann, and C. Ritter. Neutron Diffraction Study of Mesoporous and Bulk Hematite, α-Fe_2O_3. *Chem. Mater.*, 20:4891, 2008.

[22] Z. Somogyvári, E. Sváb, G. Mészáros, K. Krezhov, I. Nedkov, I. Sajo, and F. Bourée. Vacancy ordering in nanosized maghemite from neutron and X-ray powder diffraction. *Appl. Phys. A*, 74:S1077, 2002.

[23] K. J. Gallagher, W. Feitknecht, and U. Mannweiler. Mechanism of Oxidation of Magnetite to γ-Fe_2O_3. *Nature*, 217:1118, 1968.

[24] W. Wu, Q. He, and C. Jiang. Magnetic Iron Oxide Nanoparticles: Synthesis and Surface Functionalization Strategies. *Nanoscale Res. Lett.*, 3:397, 2008.

[25] P. Kanninen, C. Johans, J. Merta, and K. Kontturi. Influence of ligand structure on the stability and oxidation of copper nanoparticles. *J. Colloid Interface Sci.*, 318:88, 2008.

[26] J. Landers. *Mössbauerspektroskopie-Untersuchungen an Fe-Oxid Nanopartikeln*. diploma thesis, Universität Duisburg-Essen (2011).

[27] E. J. W. Verwey. Electronic Conduction of Magnetite (Fe_3O_4) and its Transition Point at Low Temperatures. *Nature*, 144:327, 1939.

[28] W. Kündig and R. S. Hargrove. Electron hopping in magnetite. *Solid State Commun.*, 7:223, 1969.

[29] D. J. Huang, H.-J. Lin, J. Okamoto, K. S. Chao, H.-T. Jeng, G. Y. Guo, C.-H. Hsu, C.-M. Huang, D. C. Ling, and W. B. Wu et al. Charge-Orbital Ordering and Verwey Transition in Magnetite Measured by Resonant Soft X-Ray Scattering. *Phys. Rev. Lett.*, 96:096401, 2006.

[30] F. J. Morin. Magnetic Susceptibility of αFe_2O_3 and αFe_2O_3 with Added Titanium. *Phys. Rev.*, 78:819, 1950.

[31] A. H. Morrish. *Canted Antiferromagnetism: Hematite*. World Scientific, Singapore, 1994.

[32] P. J. Flanders and W. J. Schuele. Anisotropy in the Basal Plane of Hematite Single Crystals. *Philos. Mag.*, 9:485, 1964.

[33] G. Cinader, P. J. Flanders, and S. Shtrikman. Magnetization and Mössbauer Studies of the Field Dependence of the Morin Transition in Hematite. *Phys. Rev.*, 162:419, 1967.

[34] F. Bødker, M. F. Hansen, C. B. Koch, K. Lefmann, and S. Mørup. Magnetic properties of hematite nanoparticles. *Phys. Rev. B*, 61:6826, 2000.

[35] S.-H. Gee, Y.-H. Hong, J. C. Sur, D. W. Erickson, M. H. Park, and F. Jeffers. Spin Orientation of Hematite (α-Fe_2O_3) Nanoparticles During the Morin Transition. *IEEE Trans. Magn.*, 40:2691, 2004.

[36] Y. Syono and Y. Ishikawa. Magnetocrystalline Anisotropy of $xFe_2TiO_4 \cdot (1\text{-}x)Fe_3O_4$. *J. Phys. Soc. Japan*, 18:1230, 1963.

[37] Z. Kąkol and J. M. Honig. Influence of deviations from ideal stoichiometry on the anisotropy parameters of magnetite $Fe_{3(1-\delta)}O_4$. *Phys. Rev. B*, 40:9090, 1989.

[38] D. Fiorani (ed). *Surface Effects in Magnetic Nanoparticles*. Springer, New York, 2005.

[39] D. Lin, A. C. Nunes, C. F. Majkrzak, and A. E. Berkowitz. Polarized neutron study of the magnetization density distribution within a $CoFe_2O_4$ colloidal particle II. *J. Magn. Magn. Mater.*, 145:343, 1995.

[40] R. H. Kodama, A. E. Berkowitz, E. J. McNiff Jr., and S. Foner. Surface Spin Disorder in $NiFe_2O_4$ Nanoparticles. *Phys. Rev. Lett.*, 77:394, 1996.

[41] A. Demortière, P. Panissod, B. P. Pichon, G. Pourroy, D. Guillon, B. Donnio, and S. Bègin-Colin. Size-dependent properties of magnetic iron oxide nanocrystals. *Nanoscale*, 3:225, 2011.

[42] J. Park, E. Lee, N.-M. Hwang, M. Kang, S. C. Kim, Y. Hwang, J.-G. Park, H.-J. Noh, J.-Y. Kim, and J.-H. Park et al. One-Nanometer-Scale Size-Controlled Synthesis of Monodisperse Magnetic Iron Oxide Nanoparticles. *Angew. Chem. Int. Ed.*, 117:2932, 2005.

[43] A. G. Roca, M. P. Morales, K. O'Grady, and C. J. Serna. Structural and magnetic properties of uniform magnetite nanoparticles prepared by high temperature decomposition of organic precursors. *Nanotechnology*, 17:2783, 2006.

[44] S. Mørup, M. F. Hansen, and C. Frandsen. Magnetic Nanoparticles. *Comprehensive Nanoscience and Technology*, 1:437, 2011.

[45] S. P. Gubin (ed.). *Magnetic Nanoparticles*. WILEY-VCH Verlag, Weinheim, 2009.

[46] S. Mørup and H. Topsøe. Magnetic and electronic properties of microcrystals of Fe_3O_4. *J. Magn. Magn. Mater.*, 31:953, 1983.

[47] Ö. Özdemir and D. J. Dunlop and T. S. Berquó. Morin transition in hematite: Size dependence and thermal hysteresis. *Geochem., Geophys., Geosyst.*, 9:Q10Z01, 2008.

[48] E. C. Stoner and E. P. Wohlfarth. A Mechanism of Magnetic Hysteresis in Heterogeneous Alloys. *Phil. Trans. Roy. Soc.*, 240:599, 1948.

[49] L. Néel. Théorie du trainage magnétique des ferromagnétiques en grains fins avec application aux terres cuites. *Ann. Geophys.*, 5:99, 1949.

[50] W. F. Brown, Jr. Thermal Fluctuations of a Single-Domain Particle. *J. Appl. Phys.*, 34:1319, 1963.

[51] W. T. Coffey, P. J. Cregg, and Yu. P. Kalmykov. On the theory of Debye and Néel relaxation of single domain ferromagnetic particles. *Adv. Chem. Phys.*, 83:263, 1993.

[52] J. Dieckhoff, D. Eberbeck, M. Schilling, and F. Ludwig. Magnetic-field dependence of Brownian and Néel relaxation times. *J. Appl. Phys.*, 119:043903, 2016.

[53] J. L. Dormann, L. Spinu, E. Tronc, J. P. Jolivet, F. Lucari, F. D'Orazio, and D. Fiorani. Effect of interparticle interactions on the dynamical properties of γ-Fe_2O_3 nanoparticles. *J. Magn. Magn. Mater.*, 183:L255, 1998.

[54] O. Iglesias and A. Labarta. Magnetic relaxation in terms of microscopic energy barriers in a model of dipolar interacting particles. *Phys. Rev. B*, 70:144401, 2004.

[55] J. Landers, F. Stromberg, M. Darbandi, C. Schöppner, W. Keune, and H. Wende. Correlation of superparamagnetic relaxation with magnetic dipole interaction in capped iron-oxide nanoparticles. *J. Phys.: Condens. Matter.*, 27:026002, 2015.

[56] S. Mørup and E. Tronc. Superparamagnetic Relaxation of Weakly Interacting Particles. *Phys. Rev. Lett.*, 72:3278, 1994.

[57] S. Bedanta and W. Kleemann. Supermagnetism. *J. Phys. D: Appl. Phys.*, 42:013001, 2009.

[58] L. Roeder, M. Reckenthäler, L. Belkoura, S. Roitsch, R. Strey, and A. M. Schmidt. Covalent Ferrohydrogels Based on Elongated Particulate Cross-Linkers. *Marcomolecules*, 47:7200, 2014.

[59] A. Einstein. Über die von der molekularkinetischen Theorie der Wärme geforderte Bewegung von in ruhenden Flüssigkeiten suspendierten Teilchen. *Ann. Phys.*, 17:549, 1905. (English translation in: Investigations on the theory of the Brownian movement, Methuen, London, 1926).

[60] M. von Smoluchowski. Zur kinetischen Theorie der Brownschen Molekularbewegung und der Suspensionen. *Ann. Phys.*, 21:756, 1906.

[61] M. P. Langevin. Sur la théorie du mouvement brownien. *C. R. Acad. Sci. (Paris)*, 146:530, 1908. (English translation: P. Langevin (1997) On the Theory of Brownian Motion, *Am. J. Phys.*, 65:1079).

[62] A. Einstein. Zur Theorie der Brownschen Bewegung. *Ann. Phys.*, 19:371, 1906. (English translation in: Investigations on the Theory of the Brownian Movement, Methuen, London 1926).

[63] R. Edgeworth, B. J. Dalton, and T. Parnell. The pitch drop experiment. *Eur. J. Phys.*, 5:198, 1984.

[64] Viskosität, *https://de.wikipedia.org/wiki/Viskosität*, 07.04.2016.

[65] W. Kauzmann. The nature of the glassy state and the behavior of liquids at low temperatures. *Chem. Rev.*, 43:219, 1948.

[66] J. A. T. González, M. P. Longinotti, and H. R. Corti. The Viscosity of Glycerol-Water Mixtures Including the Supercooled Region. *J. Chem. Eng. Data*, 56:1397, 2011.

[67] H. Vogel. Das Temperaturabhängigkeitsgesetz der Viskosität von Flüssigkeiten. *Phys. Z.*, 22:645, 1921.

[68] G. S. Fulcher. Analysis of recent measurements of the viscosity of glasses. *J. Am. Ceram. Soc.*, 8:339, 1925.

[69] G. Tammann and W. Hesse. Die Abhängigkeit der Viscosität von der Temperatur bei unterkühlten Flüssigkeiten. *Z. Anorg. u. allg. Chem.*, 156:245, 1926.

[70] J. Ferry. *Viscoelastic Properties of Polymers*. Wiley, New York, 1980.

[71] J. Rault. Origin of the Vogel-Fulcher-Tammann law in glass-forming materials: the $\alpha - \beta$ bifurcation. *J. Noncryst. Solids*, 271:177, 2000.

[72] D. H. Jones and K. K. P. Srivastava. Many-state relaxation model for the Mössbauer spectra of superparamagnets. *Phys. Rev. B*, 34:7542, 1986.

[73] R. M. Ferguson, A. P. Khandar, C. Jonasson, J. Blomgren, C. Johansson, and K. M. Krishnan. Size-Dependent Relaxation Properties of Monodisperse Magnetite Nanoparticles Measured Over Seven Decades of Frequency by AC Susceptometry. *IEEE Trans. Magn.*, 49:3441, 2013.

[74] S.-H. Chung, A. Hoffmann, K. Guslienko, S. D. Bader, C. Liu, B. Kay, L. Makowski, and L. Chen. Biological sensing with magnetic nanoparticles using Brownian relaxation. *J. Appl. Phys.*, 97:10R101, 2005.

[75] A. Mukhopadhyay and S. Grannick. Micro- and nanorheology. *Curr. Opin. Colloid. Interface Sci.*, 6:423, 2001.

[76] E. Roeben, L. Roeder, S. Teusch, M. Effertz, U. K. Deiters, and A. M. Schmidt. Magnetic particle nanorheology. *Colloid. Polym. Sci.*, 292:2013, 2014.

[77] G. M. Bancroft, A. G. Maddock, and R. G. Burns. Applications of the Mössbauer effect to silicate mineralogy - I. Iron silicates of known crystal structure. *Geochim. Cosmochim. Acta*, 31:2219, 1967.

[78] F. E. Fujita. *in 'Mössbauer Spectroscopy'*. U. Gonser (ed.), Springer Verlag, Berlin, 1975.

[79] F. E. Wagner and A. Kyek. Mössbauer Spectroscopy in Archaeology: Introduction and Experimental Considerations. *Hyp. Interact.*, 154:5, 2004.

[80] D. R. Cousins and K. G. Dharmawardena. Use of Mössbauer Spectroscopy in the Study of Ancient Pottery. *Nature*, 223:732, 1969.

[81] C.E. Weaver, J. M. Wampler, and T. E. Pecuil. Mössbauer Analysis of Iron in Clay Minerals. *Science*, 156:504, 1967.

[82] G. Klingelhöfer, B. Fegley Jr., R. V. Morris, E. Kankeleit, P.Held, E. Evlanov, and O. Priloutskii. Mineralogical analysis of Martian soil and rock by a miniaturized backscattering Mössbauer spectrometer. *Planet. Space Sci.*, 44:1277, 1996.

[83] C. L. Herzenberg and D. L. Riley. Mössbauer Spectrometry of Lunar Samples. *Science*, 167:683, 1970.

[84] R. B. Scorzelli. Application of the Mössbauer effect to the study of meteorites - A review. *Hyp. Interact.*, 66:249, 1991.

[85] D. Barb. *Grundlagen und Anwendungen der Mössbauerspektroskopie*. Akademie-Verlag, Berlin, 1980.

[86] F. L. Shapiro. The Mössbauer effect. *Soviet Physics Uspekhi*, 3:881, 1961.

[87] Y.-L. Chen and D.-P. Yang. *Mössbauer effect in Lattice Dynamics*. Wiley-VCH Verlag, Weinheim, 2007.

[88] Y. Hazony. 3d Density Distribution and the Intrinsic Temperature Dependence of the Mössbauer Isomer Shift in Iron Compounds. *Phys. Rev. B*, 7:3309, 1973.

[89] C. Blaauw and F. van der Woude. Magnetic and structural properties of $BiFeO_3$. *J. Phys. C: Solid State Phys.*, 6:1422, 1973.

[90] D. Sando, A. Agbelele, D. Rahmedov, J. Liu, P. Rovillain, C. Toulouse, I. C. Infante, A. P. Pyatakov, S. Fusil, E. Jacquet, and et al. Crafting the magnonic and spintronic response of $BiFeO_3$ films by epitaxial strain. *Nature Mat.*, 12:641, 2013.

[91] J. Landers, S. Salamon, M. Escobar Castillo, D. C. Lupascu, and H. Wende. Mössbauer Study of Temperature-Dependent Cycloidal Ordering in $BiFeO_3$ Nanoparticles. *Nano Lett.*, 14:6061, 2014.

[92] P. Weiß. L'hypothèse du champ moléculaire et la propriété ferromagnétique. *J. Phys. Theor. Appl.*, 6:661, 1907.

[93] G. Schatz and A. Weidinger. *Nukleare Festkörperphysik: Kernphysikalische Messmethoden und ihre Anwendungen*. Teubner-Verlag, Stuttgart, 3. edition, 1997.

[94] T. C. Gibb. *Principles of Mössbauer Spectroscopy.* Chapman and Hall, London, 1976.

[95] H. H. Wickman, M. P. Klein, and D. A. Shirley. Paramagnetic Hyperfine Structure and Relaxation Effects in Mössbauer Spectra: Fe^{57} in Ferrichrome A. *Phys. Rev.*, 152:345, 1966.

[96] M. Blume and J. A. Tjon. Mössbauer Spectra in a Fluctuating Environment. *Phys. Rev.*, 165:446, 1968.

[97] S. Mørup. Magnetic hyperfine splitting in Mössbauer spectra of microcrystals. *J. Magn. Magn. Mater.*, 37:39, 1983.

[98] J. van Lierop and D. H. Ryan. Mössbauer spectra of single-domain fine particle systems described using a multiple level relaxation model for superparamagnets. *Phys. Rev. B*, 63:064406, 2001.

[99] M. A. Chuev. Mössbauer spectra of single-domain particles in a weak magnetic field. *J. Phys.: Condens. Matter*, 20:505201, 2008.

[100] M. A. Chuev. Multi-level relaxation model for describing the Mössbauer spectra of single-domain particles in the presence of quadrupolar hyperfine interaction. *J. Phys.: Condens. Matter*, 23:426003, 2011.

[101] K. S. Singwi and A. Sjölander. Resonance Absorption of Nuclear Gamma Rays and the Dynamics of Atomic Motions. *Phys. Rev.*, 120:1093, 1960.

[102] A. J. F. Boyle, D. St. P. Bunbury, C. Edwards, and H. E. Hall. The Mössbauer Effect in Tin from 120°K to the Melting Point. *Proc. Phys. Soc.*, 77:129, 1961.

[103] K. Højgaard Jensen. Mössbauer Effect and Molecular Motion in Condensed Systems with Diffusion. *Phys. kondens. Materie*, 13:273, 1971.

[104] D. C. Champeney and D. F. Sedgewick. Investigation of molecular motion in some organic glasses and supercooled liquids by Mössbauer scattering. *J. Phys. C: Sol. State Phys.*, 5:1903, 1972.

[105] S. Mørup and J. E. Knudsen. Molecular dynamics and spin-lattice relaxation of Fe^{3+} in a supercooled liquid. *J. Phys. C: Solid State Phys.*, 18:2943, 1985.

[106] T. Bonchev, P. Aidemirski, I. Mandzhukov, N. Nedyalkova, B. Skorchev, and A. Strigachev. A study of Brownian motion by means of the Mössbauer effect. *Sov. Phys. JETP*, 23:42, 1966.

[107] K. P. Singh and J. G. Mullen. Mössbauer Study of Brownian Motion in Liquids: Colloidal Cobaltous Hydroxy Stannate in Glycerol, Ethanol-Glycerol and Aqueous-Glycerol Solutions. *Phys. Rev. A*, 6:2354, 1972.

[108] H. Keller and W. Kündig. Mössbauer studies of Brownian motion. *Sol. State Common.*, 16:253, 1975.

[109] G. von Eynatten, T. Ritter, H. E. Bömmel, and K. Dransfeld. Diffusive Motion of Iron Microcrystals Studied by Mössbauer Spectroscopy. *Z. Phys. B Cond. Mat.*, 65:341, 1987.

[110] P. Fornal and J. Stanek. Mobility of Hematite Submicron Particles in Water Solutions of Sugar. *Acta Phys. Pol. A*, 114:1667, 2008.

[111] J. Landers, S. Salamon, H. Remmer, F. Ludwig, and H. Wende. Simultaneous Study of Brownian and Néel Relaxation Phenomena in Ferrofluids by Mössbauer Spectroscopy. *Nano Lett.*, 16:1150, 2016.

[112] I. Heilmann, B. Olsen, and J. Højgaard Jensen. Non-Lorentzian diffusion-broadened Mössbauer lines. *J. Phys. C: Sol. State Phys.*, 7:4355, 1974.

[113] A. M. Afanas'ev, P. V. Hendriksen, and S. Mørup. Influence of rotational diffusion of the Mössbauer spectrum of ultrafine particles in a supercooled liquid. *Hyp. Interact.*, 88:35, 1994.

[114] F. G. Parak and K. Achterhold. Protein dynamics on different timescales. *J. Phys. Chem. Sol.*, 66:2257–2262, 2005.

[115] A. S. Plachinda, V. E. Sedov, V. I. Khromov, L. V. Bashkeev, and I. P. Suzdalev. Bound diffusion of ultrafine particles in generalized anharmonic potential. *Hyp. Interact.*, 56:1483, 1990.

[116] J. Stanek and P. Fornal. Mobility of inorganic nanoparticles in soft matter. *Hyp. Interact.*, 190:75, 2009.

[117] K. Konik, P. Fornal, D. Okla, and J. Stanek. Microstructure and Dynamics of Magnetic Iron Nanoparticles Aggregates in Protein Gels. *Acta Phys. Pol. A*, 121:457, 2012.

[118] E. W. Knapp, S. F. Fischer, and F. Parak. The influence of protein dynamics on Mössbauer spectra. *J. Chem. Phys.*, 78:4701, 1983.

[119] L. Khenkin, T. Baluyan, A. Novakova, I. Rebrin, and E. Makhaeva. Iron complexes embedding influence on PMAA hydrogel. *IOP Conf. Ser.: Mater. Sci. Eng.*, 38:012029, 2012.

[120] D. L. Uhrich, J. M. Wilson, and W. A. Resch. Mössbauer investigation of the smectic liquid crystalline state. *Phys. Rev. Lett.*, 24:355, 1970.

[121] W. J. LaPrice and D. L. Uhrich. A Mössbauer temperature study of a cold nematic liquid crystal: Nematic glass-supercooled nematic. *J. Chem. Phys.*, 71:1498, 1979.

[122] W. Nadler and K. Schulten. Generalized Moment Expansion for the Mössbauer Spectrum of Brownian Particles. *Phys. Rev. Lett.*, 51:1712, 1983.

[123] A. S. Plachinda, V. E. Sedov, V. I. Khromov, L. V. Bashkeev, and I. P. Suzdalev. Bound diffusion of ultrafine particles in a generalized potential: a Mössbauer study. *Chem. Phys. Lett.*, 175:101, 1990.

[124] A. S. Plachinda, V. E. Sedov, V. I. Khromov, I. P. Suzdalev, V. I. Goldanskii, G. U. Nienhaus, and F. Parak. Mössbauer studies of bound diffusion in a model polymer system. *Phys. Rev. B*, 45:7716, 1992.

[125] J. Landers, L. Roeder, S. Salamon, A. M. Schmidt, and H. Wende. Particle-Matrix Interaction in Cross-Linked PAAm-Hydrogels Analyzed by Mössbauer Spectroscopy. *J. Phys. Chem. C*, 119:20642, 2015.

[126] F. Wagner. Applications of Mössbauer Scattering Techniques. *J. Phys. Colloques*, 37:C6–673, 1976.

[127] D. C. Champeney. The scattering of Mössbauer radiation by condensed matter. *Rep. Prog. Phys.*, 42:1017, 1979.

[128] S. L. Ruby. Mössbauer experiments without conventional sources. *J. Phys. Colloques*, 35:C6–209, 1974.

[129] W. Sturhahn, T. S. Toellner, E. E. Alp, X. Zhang, M. Ando, Y. Yoda, S. Kikuta, M. Seto, C. W. Kimball, and B. Dabrowski. Phonon Density of States Measured by Inelastic Nuclear Resonant Scattering. *Phys. Rev. Lett.*, 74:3832, 1995.

[130] M. E. Gruner, W. Keune, B. Roldan Cuenya, J. Landers, S. I. Makarov, D. Klar, M. Y. Hu, E. E. Alp, J. Zhao, and M. Krautz et al. Element-Resolved Thermodynamics of Magnetocaloric $LaFe_{13-x}Si_x$. *Phys. Rev. Lett.*, 114:057202, 2015.

[131] E. Kankeleit. Untersuchung von Konversionselektronen beim Mößbauer-Effekt am Wolfram-182 mit einem magnetischen Spektrometer. *Z. Phys.*, 164:442, 1961.

[132] K. Nomura, Y. Ujihira, and A. Vertes. Applications of conversion electron Mössbauer spectrometry (CEMS). *J. Radioanal. Nucl. Chem.*, 202:103, 1996.

[133] W. Keune. Surface magnetism by depth-selective CEMS. *Hyp. Interact.*, 27:111, 1986.

[134] D. Liljequist, T. Ekdahl, and U. Bäverstam. Analysis of the electron transport in conversion electron Mössbauer spectroscopy (CEMS). *Nucl. Instr. Meth.*, 155:529, 1978.

[135] G. Klingelhöfer, B. Bernhardt, J. Foh, U. Bonnes, D. Rodionov, P. A. de Souza, C. Schröder, R. Gellert, S. Kane, and P. Gütlich et al. The Miniaturized Mössbauer Spectrometer MIMOS II for Extraterrestrial and Outdoor Terrestrial Applications: A Status Report. *Hyp. Interact.*, 144/145:371, 2002.

[136] G. Klingelhöfer, R. V. Morris, B. Bernhardt, C. Schröder, D. S. Rodionov, P. A. de Souza Jr., A. Yen, R. Gellert, E. N. Evlanov, and B. Zubkov et al. Jarosite and Hematite at Meridiani Planum from Opportunity's Mössbauer Spectrometer. *Science*, 306:1740, 2004.

[137] A. Warland. *Röntgenabsorptionsspektroskopie an Fe-Oxid-Nanopartikeln.* Ph.D thesis, Universität Duisburg-Essen (2013).

[138] M. P. Sharrock. Time dependence of switching fields in magnetic recording media. *J. Appl. Phys.*, 76:6413, 1994.

[139] C. Antoniak, M. E. Gruner, M. Spasova, A. V. Trunova, F. M. Römer, A. Warland, B. Krumme, K. Fauth, S. Sun, P. Entel, M. Farle, and H. Wende. A guideline for atomistic design and understanding of ultrahard nanomagnets. *Nature Comm.*, 2:528, 2011.

[140] B. Kuerbanjiang, U. Wiedwald, F. Häring, J. Biskupek, U. Kaiser, P. Ziemann, and U. Herr. Exchange bias of Ni nanoparticles embedded in an antiferromagnetic IrMn matrix. *Nanotechnology*, 24:455702, 2013.

[141] M. Jamet, W. Wernsdorfer, C. Thirion, D. Mailly, V. Dupuis, P. Mélinon, and A. Pérez. Magnetic Anisotropy of a Single Cobalt Nanocluster. *Phys. Rev. Lett.*, 86:4676, 2001.

[142] D. E. Madsen, M. F. Hansen, and S. Mørup. The correlation between superparamagnetic blocking temperatures and peak temperatures obtained from ac magnetization measurements. *J. Phys.: Condens. Mat.*, 20:345209, 2008.

[143] J. I. Gittleman, B. Abeles, and S. Bozowski. Superparamagnetism and relaxation effects in granular Ni-SiO_2 and Ni-Al_2O_3 films. *Phys. Rev. B*, 9:3891, 1974.

[144] E. P. Wohlfarth. The temperature dependence of the magnetic susceptibility of spin glasses. *Phys. Lett.*, 70:489, 1979.

[145] M. Respaud, J. M. Broto, H. Rakoto, A. R. Fert, L. Thomas, B. Barbara, M. Verelst, E. Snoeck, P. Lecante, and A. Mosset et al. Surface effects on the magnetic properties of ultrafine cobalt particles. *Phys. Rev. B*, 57:2925, 1998.

[146] M. F. Hansen and S. Mørup. Estimation of blocking temperatures from ZFC/FC curves. *J. Magn. Magn. Mater.*, 203:214, 1999.

[147] A. Labarta, O. Iglesias, Ll. Balcells, and F. Badia. Magnetic relaxation in small-particle systems: T $\ln(t/\tau_0$ scaling). *Phys. Rev. B*, 48:10240, 1993.

[148] F. Ludwig, E. Heim, S. Mäuselein, D. Eberbeck, and M. Schilling. Magnetorelaxometry of magnetic nanoparticles with fluxgate magnetometers for the analysis of biological targets. *J. Magn. Magn. Mater.*, 293:690, 2005.

[149] J. J. Prejean and J. Souletié. Two-level-systems in spin glasses: a dynamical study of the magnetizations below TG, application to CuMn systems. *J. Phys. (Paris)*, 41:1335, 1980.

[150] R. Skomski. *Simple Models of Magnetism*. Oxford university Press, 2008.

[151] B. Gleich and J. Weizenecker. Tomographic imaging using the nonlinear response of magnetic particles. *Nature*, 435:1214, 2005.

[152] N. Gehrke, A. Briel, F. Ludwig, H. Remmer, T. Wawrzik, and S. Wellert. *New perspective for MPI: A toolbox for tracer research* in Magnetic Particle Imaging, vol. 140 Springer Proceedings in Physics, Springer-Verlag, Berlin. 2012.

[153] P. Debye. *Polar molecules*. The Chemical Catalog Co., Reprinted by Dover Publications, New York, 1929.

[154] B. Fischer, B. Huke, M. Lücke, and R. Hempelmann. Brownian relaxation of magnetic colloids. *J. Magn. Magn. Mater.*, 289:74, 2005.

[155] M. Darbandi, F. Stromberg, J. Landers, N. Reckers, B. Sanyal, W. Keune, and H. Wende. Nanoscale size effect on surface spin canting in iron oxide nanoparticles synthesized by the microemulsion method. *J. Phys. D: Appl. Phys.*, 45:195001, 2012.

[156] A. Warland, C. Antoniak, M. Darbandi, C. Weis, J. Landers, W. Keune, and H. Wende. Effect of silica capping on the oxidation of Fe_3O_4 nanoparticles in dispersion revealed by x-ray absorption spectroscopy. *Phys. Rev. B*, 85:235113, 2012.

[157] S. Ammar, N. Jouini, F. Fièvet, Z. Beji, L. Smiri, P. Moliné, M. Danot, and J.-M. Grenéche. Magnetic properties of zinc ferrite nanoparticles synthesized by hydrolisis in a polyol medium. *J. Phys.: Condens. Matter*, 18:9055, 2006.

[158] Y. Yafet and C. Kittel. Antiferromagnetic Arrangements in Ferrites. *Phys. Rev.*, 87:290, 1952.

[159] P. S. Sidhu, R. J. Gilkes, and A. M. Posner. Mechanism of the low temperature oxidation of synthetic magnetites. *J. Inorg. Nucl. Chem.*, 39:1953, 1977.

[160] J. L. Dormann, D. Fiorani, and E. Tronc. On the models for interparticle interactions in nanoparticle assemblies: comparison with experimental results. *J. Magn. Magn. Mater.*, 202:251, 1999.

[161] A. Terwey, R. Meckenstock, B. W. Zingsem, S. Masur, C. Derricks, F. M. Römer, and M. Farle. Magnetic anisotropy and relaxation of single Fe/Fe_xO_y core/shell- nanocubes: A ferromagnetic resonance investigation. *AIP Adv.*, 6:056119, 2016.

[162] Ocean NanoTech, Products » Iron Oxide Nanoparticles Suspension in Water (5-30 nm) » SHP, *http://www.oceannanotech.com/product.php?cid=69&pid=122*, 12.05.2016.

[163] G. Schinteie, P. Palade, L. Vekas, N. Iacob, C. Bartha, and V. Kuncser. Volume fraction dependent magnetic behaviour of ferrofluids for rotating seal applications. *J. Phys. D: Appl. Phys.*, 46:395501, 2013.

[164] Y. Akagi and N. Nakamura. Tunneling molecular motion in glassy glycerol at very low temperatures as studied by ^{1}H SQUID nuclear magnetic resonance. *J. Phys.: Condens. Matter*, 12:5155, 2000.

[165] A. I. Sulatskaya, A. A. Maskevich, I. M. Kuznetsova, V. N. Uversky, and K. K. Turoverov. Flourescence Quantum Yield of Thioflavin T in Rigid Isotropic Solution and Incorporated into the Amyloid Fibrils. *PLoS ONE*, 5:e15385, 2010.

[166] G. A. Sawatzky, F. van der Woude, and A. H. Morrish. Recoilless-Fraction Ratios for Fe^{57} in Octahedral and Tetrahedral Sites of a Spinel and a Garnet. *Phys. Rev.*, 183:383, 1969.

[167] F. Ludwig, A. Guillaume, M. Schilling, N. Frickel, and A. M. Schmidt. Determination of core and hydrodynamic size distributions of $CoFe_2O_4$ nanoparticle suspensions using ac susceptibility measurements. *J. Appl. Phys.*, 108:033918, 2010.

[168] J. B. Segur and H. E. Oberstar. Viscosity of Glycerol and Its Aqueous Solutions. *Ind. Eng. Chem. Res.*, 43:2117, 1951.

[169] M. Ozaki, S. Kratohvil, and E. Matijević. Formation of monodispered spindle-type hematite particles. *J. Colloid Interface Sci.*, 102:146, 1984.

[170] P. J. Besser, A. H. Morrish, and C. W. Searle. Magnetocrystalline Anisotropy of Pure and Doped Hematite. *Phys. Rev.*, 153:632, 1967.

[171] P. J. Flanders and J. P. Remeika. Magnetic properties of Hematite single crystals. *Philos. Mag.*, 11:1271, 1965.

[172] L. Roeder, P. Bender, M. Kundt, A. Tschöpe, and A. M. Schmidt. Magnetic and geometric anisotropy in particle-crosslinked ferrohydrogels. *Phys. Chem. Chem. Phys.*, 17:1290, 2015.

[173] D. Hoffelner, M. Kundt, A. M. Schmidt, E. Kentzinger, P. Bender, and S. Disch. Directing the orientational alignment of anisotropic magnetic nanoparticles using dynamic magnetic fields. *Faraday Discuss.*, 181:449, 2015.

[174] B. M. I. van der Zande, G. J. M. Koper, and H. N. W. Lekkerkerker. Alignment of Rod-Shaped Gold Particles by Electric Fields. *J. Phys. Chem. B*, 103:5754, 1999.

[175] L. Slade and H. Levine. Non-equilibrium behavior of small carbohydrate-water systems. *Pure & Appl. Chem.*, 60:1841, 1988.

[176] M. Rampp, C. Buttersack, and H.-D. Lüdemann. Self-Diffusion of Sucrose in Molasses. *Ind. Eng. Chem. Res.*, 39:4400, 2000.

[177] J. Hallett. The Temperature Dependence of the Viscosity of Supercooled Water. *Proc. Phys. Soc.*, 82:1046, 1963.

[178] M. Zhou, T. Liebert, R. Müller, A. Dellith, C. Gräfe, J. H. Clement, and T. Heinze. Magnetic Biocomposites for Remote Melting. *Biomacromolecules*, 16:2308, 2015.

[179] pricate communication with Mengbo Zhou, M.Sc., University of Jena.

[180] S. Dutz, W. Andrä, R. Hergt, R. Müller, C. Oestreich, C. Schmidt, J. Töpfer, M. Zeissberger, and M. E. Bellemann. Influence of dextran coating on the magnetic behaviour of iron oxide nanoparticles. *J. Magn. Magn. Mater.*, 311:51, 2007.

[181] R. Müller, M. Zhou, T. Liebert, J. Landers, S. Salamon, S. Webers, A. Dellith, T. Heinze, and H. Wende. Mobility Investigations of Magnetic Nanoparticles in Biocomposites. *submitted to Mater. Chem. Phys.*, 2016.

[182] M. P. Morales, C. J. Serna, F. Bødker, and S. Mørup. Spin canting due to structural disorder in maghemite. *J. Phys.: Condens. Matter*, 9:5461, 1997.

[183] G. F. Goya, T. S. Berquó, F. C. Fonseca, and M. P. Morales. Static and dynamic magnetic properties of spherical magnetite nanoparticles. *J. Appl. Phys.*, 94:3520, 2003.

[184] S. Gupta, J. Stellbrink, E. Zaccarelli, C. N. Likos, M. Camargo, P. Holmqvist, J. Allgaier, L. Willner, and D. Richter. Validity of the Stokes-Einstein Relation in Soft Colloids up to the Glass Transition. *Phys. Rev. Lett.*, 115:128302, 2015.

[185] F. Perrin. Mouvement brownien d'un ellipsoide - I. Dispersion diélectrique pour des molécules ellipsoidales. *J. Phys. Radium*, 5:497, 1934.

[186] M. A. Charsooghi, E. A. Akhlagi, S. Tavaddod, and H. R. Khalesifard. A MATLAB program to calculate translational and rotational diffusion coefficients of a single particle. *Comput. Phys. Common.*, 182:400, 2011.

[187] J. Wagner, C. Märkert, B. Fischer, and L. Müller. Direction Dependent Diffusion of Aligned Magnetic Rods by Means of X-Ray Photon Correlation Spectroscopy. *Phys. Rev. Lett.*, 110:048301, 2013.

[188] Y. Han, A. M. Alsayed, M. Nobili, J. Zhang, T. C. Lubensky, and A. G. Yodh. Brownian Motion of an Ellipsoid. *Science*, 314:626, 2006.

List of Figures

Publications

Peer reviewed articles

1. **Nanoscale size effect on surface spin canting in iron oxide nanoparticles synthesized by the microemulsion method**
   M. Darbandi, F. Stromberg, J. Landers, N. Reckers, B. Sanyal, W. Keune, and H. Wende
   J. Phys. D: Appl. Phys., 45:195001, 2012

2. **Effect of silica capping on the oxidation of Fe_3O_4 nanoparticles in dispersion revealed by x-ray absorption spectroscopy**
   A. Warland, C. Antoniak, M. Darbandi, C. Weis, J. Landers, W. Keune, and H. Wende
   Phys. Rev. B, 85:235113, 2012

3. **Cobalt Ferrite/Barium Titanate Core/Shell Nanoparticles**
   M. Etier, Y. Gao, V. V. Shvartsman, A. Elsukova, J. Landers, H. Wende, and D. C. Lupascu
   Ferroelectrics, 438:115, 2012

4. **Magnetoelectric Effect in (0-3) $CoFe_2O_4$-$BaTiO_3$ (20/80) Composite Ceramics Prepared by the Organosol Route**
   M. Etier, V. V. Shvartsman, Y. Gao, J. Landers, H. Wende, and D. C. Lupascu
   Ferroelectrics, 448:77, 2013

5. **Effect of particle size on ferroelectric and magnetic properties of $BiFeO_3$ nanopowders**
   M. Escobar Castillo, V. V. Shvartsman, D. Gobeljic, Y. Gao, J. Landers, H. Wende, and D. C. Lupascu
   Nanotechnology, 24:355701, 2013

6. **Mössbauer Study of Temperature-Dependent Cycloidal Ordering in $BiFeO_3$ Nanoparticles**
   J. Landers, S. Salamon, M. Escobar Castillo, D. C. Lupascu, and H. Wende
   Nano Letters, 14:6061 2014

7. **Correlation of superparamagnetic relaxation with magnetic dipole interaction in capped iron-oxide nanoparticles**
   J. Landers, F. Stromberg, M. Darbandi, C. Schöppner, W. Keune, and H. Wende
   J. Phys. Condens. Matter, 27:026002, 2015

8. **Element-Resolved Thermodynamics of Magnetocaloric $LaFe_{13-x}Si_x$**
   M. E. Gruner, W. Keune, B. Roldan Cuenya, C. Weis, J. Landers, S. I. Makarov, D. Klar, M. Y. Hu, E. E. Alp, J. Zhao, M. Krautz, O. Gutfleisch, and H. Wende
   Phys. Rev. Lett., 114:057202, 2015

9. **Measuring the magnetoelectric effect across scales**
   D. C. Lupascu, H. Wende, M. Etier, A. Nazrabi, I. Anusca, H. Trivedi, V. V. Shvartsman, J. Landers, S. Salamon, and C. Schmitz-Antoniak
   GAMM-Mitt., 38:25, 2015

10. **Magnetoelectric coupling on multiferroic cobalt ferrite-barium titanate ceramic composites with different connectivity schemes**
    M. Etier, C. Schmitz-Antoniak, S. Salamon, H. Trivedi, Y. Gao, A. Nazrabi, J. Landers, D. Gautam, M. Winterer, D. Schmitz, H. Wende, V. V. Shvartsman, and D. C. Lupascu
    Acta Mat., 90:1 2015

11. **The role of weak interlayer coupling in the spin-reorientation of perpendicular ultrathin Co-Fe-B/Mg-O-based heterostructures**
    R. R. Gareev, V. Zbarsky, J. Landers, I. Soldatov, R. Schäfer, M. Münzenberg, H. Wende, and P. Grünberg
    Appl. Phys. Lett., 106:132408, 2015

12. **Element-specific electronic structure and magnetic properties of an epitaxial $Ni_{51.6}Mn_{32.9}Sn_{15.5}$ thin films at the austenite-martensite transition**
    B. Krumme, A. Auge, H. C. Herper, I. Opahle, D. Klar, N. Teichert, L. Joly, P. Ohresser, J. Landers, J. P. Kappler, P. Entel, A. Hütten, and H. Wende
    Phys. Rev. B, 91:214417, 2015

13. **Particle-Matrix Interaction in Cross-Linked PAAm-Hydrogels Analyzed by Mössbauer Spectroscopy**
    J. Landers, L. Roeder, S. Salamon, A. M. Schmidt, and H. Wende
    J. Phys. Chem. C, 119:20642, 2015

14. **Multiferroic Clusters: A New Perspective for Relaxor-Type Room-Temperature Multiferroics**
    L. F. Henrichs, O. Cespedes, J. Bennett, J. Landers, S. Salamon, C. Heuser, T. Hansen, T. Helbig, O. Gutfleisch, D. C. Lupascu, H. Wende, W. Kleemann, and A. J. Bell
    Adv. Funct. Mater., 26:2111, 2016

15. **Simultaneous study of Brownian and Néel relaxation phenomena in ferrofluids by Mössbauer spectroscopy**
    J. Landers, S. Salamon, H. Remmer, F. Ludwig, and H. Wende
    Nano Lett., 16:1150, 2016

16. **Planetesimal Formation in the Warm, Inner Disk: Experiments with Tempered Dust**
    C. de Beule, J. Landers, S. Salamon, H. Wende, and G. Wurm
    accepted for publication in *Astrophys. J.*

17. **Molecular design for tailoring single source precursor of bismuth ferrite**
    G. Bendt, R. Schivon, S. Salamon, J. Landers, U. Hagemann, C. Limberg, H. Wende, and S. Schulz
    accepted for publication in *Inorg. Chem.*

18. **Mobility Investigations of Magnetic Nanoparticles in Biocomposites**
    R. Müller, M. Zhou, T. Liebert, J. Landers, S. Salamon, S. Webers, A. Dellith, D. Borin, T. Heinze, and H. Wende
    submitted to *Mater. Chem. Phys.*

Further articles

1. **Synthesis and Magnetic Properties of Cobalt Ferrite Nanoparticles**
   M. F. Etier, V. V. Shvartsman1, F. Stromberg, J. Landers, H. Wende, and D. C. Lupascu
   Mater. Res. Soc. Symp. Proc. Vol. 1398 @ 2012 Materials Research Society

2. **Magnetoelectric Properties of $0.2CoFe_2O_4$-$0.8BaTi0_3$ composite prepared by organic method**
   M. F. Etier, Y. Gao, V. V. Shvartsman, D. C. Lupascu, J. Landers, and H. Wende
   IEEE ISAF-ECAPD-PFM conference 2012, Aveiro

Conference contributions

1. **Correlation of superparamagnetic relaxation with magnetic dipole and exchange interaction in capped iron-oxide nanoparticles**
   J. Landers, F. Stromberg, M. Darbandi, W. Keune, and H. Wende
   Spring meeting of the German Physical Society, Berlin (2012), talk

2. **Correlation of superparamagnetic relaxation with magnetic dipole and exchange interaction in capped iron-oxide nanoparticles**
   J. Landers, F. Stromberg, M. Darbandi, C. Schöppner, W. Keune, and H. Wende
   CENIDE-meeting, Duisburg (2012), poster & talk

3. **Correlation of superparamagnetic relaxation with magnetic dipole and exchange interaction in capped iron-oxide nanoparticles**
   J. Landers, F. Stromberg, M. Darbandi, C. Schöppner, W. Keune, and H. Wende
   International Symposium on Non-ergodic behavior in martensites, Duisburg (2013), poster

4. **Cycloidal spin-structures in Bismuth iron-oxide nanoparticles**
   J. Landers, S. Salamon, W. Keune, M. Escobar, D. C. Lupascu, and H. Wende
   Spring meeting of the German Physical Society, Regensburg (2013), talk

5. **Microscopic understanding of particle-matrix interaction in magnetic hybrid materials using element-specific techniques**
   J. Landers and H. Wende
   1. Colloquium of SPP1681, Benediktbeuern (2013), poster

6. **Measurement of microviscosity in crosslinked polyacrylamide ferrohydrogels by Mössbauer spectroscopy**
   J. Landers, L. Roeder, A. M. Schmidt, and H. Wende
   Spring meeting of the German Physical Society, Dresden (2014), poster

7. **Application of Mössbauer spectroscopy on ferrohydrogels**
   J. Landers and H. Wende
   Group meeting SPP1681, Dresden (2014), talk

8. **Measurement of microviscosity in crosslinked polyacrylamide ferrohydrogels by Mössbauer spectroscopy**
   J. Landers, L. Roeder, A. M. Schmidt, and H. Wende
   14. German Ferrofluid Workshop, Ilmenau (2014), talk

9. **Measurement of microviscosity in crosslinked polyacrylamide ferrohydrogels by Mössbauer spectroscopy**
   J. Landers, L. Roeder, A. M. Schmidt, and H. Wende
   Group meeting SPP1681, Stuttgart (2014), talk

10. **Comparative study of nanoparticle motion by Mössbauer spectroscopy and AC-susceptometry**
    J. Landers, L. Roeder, A. M. Schmidt, and H. Wende
    2. Colloquium of SPP1681, Benediktbeuern (2014), talk

11. **Diffusion effects in different deformable matrices studied by Mössbauer spectroscopy**
    J. Landers, L. Roeder, A. M. Schmidt, H. Wende, C. Kuhlmann, F. Ludwig, M. Zhou, and R. Müller
    Group meeting SPP1681, Berlin (2015), talk

12. **Mössbauer spectroscopy for simultaneous in situ disentanglement of Néel and Brown relaxation phenomena**
    J. Landers, S. Salamon, H. Remmer, F. Ludwig, and H. Wende
    15. German Ferrofluid Workshop, Rostock (2015), talk

13. **Analyzing nanoparticle dynamics by Mössbauer spectroscopy**
    H. Wende, J. Landers, L. Roeder, S. Salamon, H. Remmer, F. Ludwig, and A. M. Schmidt
    3. Colloquium of SPP1681, Benediktbeuern (2015), poster

Acknowledgements

As my field of experience primarily included nanoparticle magnetism some years ago, for me ferrohydrogels and other nanoparticle compounds were fascinating new materials. However, realizing new experimental approaches, adapting sample holder geometries and finding suitable theoretical models was challenging. I was very lucky to be supported by helpful and enthusiastic colleagues, which did not hesitate to offer support and good advice.

- First of all, I would like to thank Prof. Dr. Heiko Wende for supervising and supporting my thesis and adding me to his workgroup back in 2010, where I had the opportunity to get insights in many interesting topic areas in a pleasant work environment.

- I greatly appreciate all the valuable discussions and suggestions from Prof. Dr. Werner Keune and his remarkable enthusiasm in supporting young researchers. His extensive experience with Mössbauer spectroscopy helped me to unriddle several puzzling phenomena.

- I would like to thank Soma Salamon, M.Sc., for years of collegial cooperation, support in magnetometry experiments and his endurance discussing unfamiliar sample behavior.

- Dipl.-Ing. Ulrich von Hörsten I would like to thank for his indispensable support of our laboratory studies, including the programming of new Pi-subroutines. He also took great effort in explaining unfamiliar setups and adapting our equipment to meet the requirements of our new liquid samples.

- Dr. Frank Stromberg did an excellent job introducing me in Mössbauer spectroscopy and nanoparticle magnetism, which was a great help tackling my thesis topic.

- I would like to thank Prof. Dr. Annette Schmidt, Dr. Lisa Roeder and Dipl. Chem. Eric Roeben for the preparation of ferrohydrogel samples and very fruitful and nice discussions during meetings in Cologne, Benediktbeuern and elsewhere, which helped me a lot getting an impression of the synthesis and internal geometries of soft matter systems.

- I appreciate the collaboration with Dr. Frank Ludwig, Dipl.-Ing. Christian Kuhlmann and Hilke Remmer, M.Sc., which not only supported us by high-frequency susceptometry, but also spend a lot of time for discussions on AC-phenomena.

- Dr. Robert Müller and Mengbo Zhou, M.Sc., I would like to acknowledge for providing us with biocompatible nanocomposites and introducing me to the topic of remote melting. I appreciate the support by Samira Webers, B.Sc., when studying these composites using Mössbauer spectroscopy.

- I would like to thank Dipl. Phys. Christian Schöppner for performing FMR experiments on our nanoparticles and Dr. Carolin Antoniak and Alexandra Terwey, M.Sc., for very illustrative explanations of the deeper meaning of FMR-linewidths and geometries.

- Dr. Masih Darbandi I would like to thank for preparing capped magnetite nanoparticles and introducing me to the basics of the microemulsion synthesis procedure.

- To all other members of the AG Wende I am very grateful for stimulating discussions, collegial support and fruitful discussions over several years.

- I would like to acknowledge financial support by the DFG priority program SPP1681 "Field controlled particle matrix interaction".

- Finally, I want to express my heartfelt gratitude to my family for their constant support during my thesis and enduring my enthusiastic introductions to my field of research.